Interdisciplinary Studies on Contemporary Research Practices in Engineering in the 21st Century-III

Editor: Prof. Dr. Kamil Kaygusuz

ÖZGÜR YAYINLARI

Interdisciplinary Studies on Contemporary Research Pratices in Engineering in the 21st Century-III

Editor

Prof. Dr. Kamil Kaygusuz

ÖZGÜR YAYINLARI

Published by
Özgür Yayın-Dağıtım Co. Ltd.
Certificate Number: 45503

15 Temmuz Mah. 148136. Sk. No: 9 Şehitkamil/Gaziantep
+90.850 260 09 97
+90.532 289 82 15
www.ozguryayınlari.com
info@ozguryayinlari.com

Interdisciplinary Studies on Contemporary Research Pratices in Engineering in the 21st Century-III

21. Yüzyılda Mühendislikte Çağdaş Araştırma Uygulamaları Üzerine Disiplinler Arası Çalışmalar -III

Prof. Dr. Kamil Kaygusuz

Language: English - Turkish
Publication Date: 2023
Interior desing by Yeter Yeşilyurt
Cover design by Mehmet Çakır
Cover design and image licensed under CC BY-NC 4.0
Print and digital versions typeset by Çizgi Medya Co. Ltd.

ISBN (PDF): 978-975-447-644-6

DOI: https://doi.org/10.58830/ozgur.pub130

This work is licensed under the Creative Commons Attribution-NonCommercial 4.0 International (CC BY-NC 4.0). To view a copy of this license, visit https://creativecommons.org/licenses/by-nc/4.0/ This license allows for copying any part of the work for personal use, not commercial use, providing author attribution is clearly stated.

Suggested citation:
Kaygusuz, K., (ed) (2023). ***Interdisciplinary Studies on Contemporary Research Pratices in Engineering in the 21st Century-III.*** Özgür Publications. DOI: https://doi.org/10.58830/ozgur.pub130. License: CC-BY-NC 4.0

The full text of this book has been peer-reviewed to ensure high academic standards. For full review policies, see https://www.ozguryayinlari.com/

ÖZGÜR YAYINLARI

Ön Söz

Mühendislik, köprüler, tüneller, yollar, araçlar ve binalar dahil olmak üzere makineler, yapılar ve diğer öğeleri tasarlamak ve inşa etmek için bilimsel ilkelerin kullanılmasıdır. Mühendislik disiplini, her biri uygulamalı matematik, uygulamalı bilim ve uygulama türlerinin belirli alanlarına özel vurgu yapan, geniş bir yelpazede uzmanlaşmış mühendislik alanlarını kapsar. Mühendislik bir ülkenin kalkınmasında ve gelişmesinde çok önemli rol oynayan disiplinler arası ortaklığın meydana getirdiği bir üst bilim dalıdır. Mühendislik, matematiksel ve doğal bilim dallarından, ders çalışma, deney yapma ve uygulama yolları ile kazanılmış bilgileri akıllıca kullanarak, doğanın kuvvetleri ve maddelerini insanoğlu yararına sunmak üzere ekonomik olan yöntemler geliştiren bir meslektir.

Çünkü mühendislik yaklaşımı; işi sorun çözmek olan insan yaklaşımıdır. Mühendislik yaklaşımı içinde bulunan çalışanlar, görülmeyeni görerek, düşünülmeyeni bularak, optimum çözümleri hedefleyip durumdan maksimum faydayı çıkarmayı bilirler. Diğer taraftan mühendislik nedir, sorusu ile aklımıza çok geniş ve detaylı bir tanımlama gelse de genel olarak mühendislik, problemleri çözebilmek için gerekli olan bilim ve matematiğin uygulanmasıdır diyebiliriz. Mühendisler, bir şeylerin nasıl çalıştığını anlar ve bilimsel keşiflerin pratik hayatta kullanımı için yöntemler bulur.

Yayınlanan bu kitap; çeşitli mühendislik dallarında hocalık yapan akademisyenlerin sunmuş olduğu gerek kendi özgün çalışmaları ve gerekse literatürden aktarılan derleme çalışmaların bir araya getirilmiş sunumlarından meydana getirilmiştir. Burada amaç konuyla ilgilenen mühendis ve akademisyenlerin önemli sayılacak mühendislik çalışmalarını bir arada bulmalarıdır. Dolayısıyla kitabın önemli bir boşluğu dolduracağı ve genç araştırmacılara faydalı olacağı kanaatindeyim. Bu bağlamda; kitaba bilimsel katkı sunan, kitabı baskıya hazırlayan kısacası emeği geçen herkese teşekkür ederiz.

Yayımlanan bu kitabın gerek mühendislere ve gerekse genç akademisyenlere faydalı olmasını diler, tüm mühendis ve genç akademisyenlere başarılar dilerim.

Prof. Dr. Kamil KAYGUSUZ
Makine & Kimya Mühendisi ve Enerji Uzmanı
Karadeniz Teknik Üniversitesi Öğretim Üyesi
Türkiye Bilimler Akademisi Asli Üyesi

Preface

Engineering is the use of scientific principles to design and construct machines, structures and other items, including bridges, tunnels, roads, vehicles and buildings. The engineering discipline encompasses a wide range of specialized engineering fields, each with particular emphasis on specific areas of applied mathematics, applied science, and application types. Engineering is a sub-discipline created by the interdisciplinary partnership that plays a very important role in the development and development of a country. Engineering is a profession that develops economical methods to present the forces and substances of nature for the benefit of human beings, using the knowledge gained through study, experimentation and application from the branches of mathematics and natural sciences wisely.

Because the engineering approach; It is the human approach whose job is to solve problems. Employees who take the engineering approach know how to see the unseen, find the unthinkable, target optimum solutions and get the maximum benefit from the situation. On the other hand, although a very broad and detailed definition comes to mind with the question of what is engineering, we can say that engineering is the application of science and mathematics necessary to solve problems. Engineers understand how things work and find ways to use scientific discoveries in practical life.

This book published; It was created from the presentations of both their own original studies and compilation studies from the literature presented by academics who teach in various engineering branches. The aim here is for engineers and academics interested in the subject to find important engineering studies together. Therefore, I believe that the book will fill an important gap and be useful to young researchers. In this context; We would like to thank everyone who contributed scientifically to the book, in short, who contributed to the preparation of the book for printing.

I hope that this published book will be useful to both engineers and young academics, and I wish success to all engineers and young academics.

Prof. Dr. Kamil KAYGUSUZ
Mechanical & Chemical Engineer
Karadeniz Technical University
Energy Expert

Contents

Ön Söz **iii**

Preface **v**

Chapter 1

Influence of T6 heat Treatment on the Mechanical Properties of AA7075 and AA7020 alloys **1**

Uğur Büyük

Emin Çadırlı

Hasan Kaya

Erkan Üstün

Mehmet Gündüz

Chapter 2

The Importance of Energy Storage for Sustainable Heat and Power **17**

Kamil Kaygusuz

Chapter 3

Comparison of Power Performance of Horizontal Axis Wind Turbines with NACA 4412 and NREL S809 Airfoils **39**

Mehmet Bakırcı

Chapter 4

Investigation of Turbulence Models in the Analysis of Two Different Airfoils with Computational Fluid **62**

Mehmet Bakırcı

Chapter 5

Simulation-Based Investigation of Heat Collection in Various Absorber Plate Materials for Solar Water Heating Systems **101**

Mara Niebling

Coskun Firat

Altin Maraj

A. Talat Inan

Chapter 6

Using of Electric Scooters in the Individual Electric Vehicle Category to Improve the Life Quality of Physically Disabled Person: A New Electric Wheelchair Design with Brushless DC Motor and Li-Ion Battery **117**

Taner Çarkıt

Anıl İbrahim Topçular

Mehmet Yılmaz

Türkan Ağır

Gökhan Cumali

Chapter 7

GIS-Based Evaluation of Disaster and Emergency Assembly Areas with AHP in Local Scale **131**

Deniz Arca

Hülya Keskin Çıtıroğlu

Chapter 8

Investigation of the Behavior of Steel-Concrete Composite Structure with Different Design Properties Under Far-Fault and Near Fault Earthquake Records **149**

Serkan Etli

Melek Akgül

Chapter 9

Reflection of Industry 4.0 on Logistics Activities: Logistics 4.0 **179**
Beste Desticioğlu Taşdemir

Chapter 10

Increasing the Efficiency of Composite Materials Manufacturing Productivity by Using Artificial Intelligent Methods **197**
Mehmet Emin Demir
Onur Denizhan

Chapter 11

Solar Irradiance Prediction and Methods Used in Prediction Studies **215**
Erşan Ömer Yüzer
Altuğ Bozkurt

Chapter 12

Consideration of Pumice Sand-Concrete Interface Friction in Pile Modeling **239**
İbrahim Yiğit

Chapter 13

Zararlı Bitkilerin İlaçlanması için Tarımsal bir İnsansız Kara Aracı **251**
Sinan Akdan
İsmail Öner
Nevzat Akdeniz
Ahyet Bingöl
Salih Ensar Şimşek
Emrehan Yavşan

Chapter 14

Yaprak Yaylarda Yorulma Analizi **267**

Güven Ege Erkman

Chapter 15

Minimum Miktarda Yağlama Yöntemi İçin Farklı Uygulama Mesafelerinin ve Farklı Kesme Parametrelerinin St37 Çelik İşlenebilirliğine Etkilerinin İncelenmesi **285**

Üsame Ali Usca

Chapter 1

Influence of T6 heat Treatment on the Mechanical Properties of AA7075 and AA7020 alloys

Uğur Büyük[1]

Emin Çadırlı[2]

Hasan Kaya[3]

Erkan Üstün[4]

Mehmet Gündüz[5]

Abstract

The AA7075 and AA7020 alloys were prepared using a vacuum melting furnace and a casting furnace. Mechanical properties of the alloy samples were investigated as-cast and under heat-treated conditions. To investigate the effect of heat treatment, numerous designed AA7075 and AA7020 samples were homogenized (solution process) in two steps (300 ^{o}C/12h+475 ^{o}C/12h) and then aged under different regimes. The mechanical properties of microhardness (HV), ultimate tensile strength (σ_{UTS}), tensile yield strength (σ_{TYS}), compressive yield strength (σ_{CYS}) and Young's modulus (E) were measured to investigate the effect of heat treatment on mechanical properties. Both alloy systems (AA7075 and AA7020) were compared both within themselves and with each other in terms of mechanical properties depending on how they were subjected to the heat treatment. Depending on the applied heat treatments, 7075 alloy exhibited superior mechanical properties

1 This work was supported by the Erciyes University Scientific Research Project Unit under contract No's: FBA-2021-10981. The authors are grateful for the financial support.

Prof. Dr., Erciyes University, Faculty of Education, Department of Science Education, Kayseri, Turkey, buyuk@erciyes.edu.tr, Orcid: 0000-0002-6830-8349

2 Prof. Dr., Niğde Ömer Halisdemir University, Faculty of Arts and Sciences, Department of Physics, Niğde, Turkey, ecadirli@gmail.com, ORCID: 0000-0002-8085-9733

3 Prof. Dr., Erciyes University, Faculty of Education, Department of Science Education, Kayseri, Turkey, hasankaya@erciyes.edu.tr, ORCID: 0000-0003-3529-9762

4 Dr., Niğde Ömer Halisdemir University, Institute of Science, Niğde, Turkey, erkanustun_07@hotmail.com, ORCID: 0000-0002-7745-396X

5 Prof. Dr., Erciyes University, Faculty of Sciences, Department of Physics, Kayseri, Turkey, gunduz@erciyes.edu.tr, ORCID: 0000-0002-2811-0338

https://doi.org/10.58830/ozgur.pub132.c519

compared to 7020 alloy. A good combination of high microhardness and reasonable tensile strength has been achieved for both alloy systems by sequential and appropriate heat treatment. While the peak σ_{UTS} value reached for the AA7075 alloy was 425 MPa (regime 3), it was determined as 320 MPa (regime 2) for the AA7020 alloy. After the aging process at 150 ^{o}C/24h (regime 2) applied proceeding the homogenization process, the peak HV and σ_{CYS} values for AA7020 alloy were achieved as 1235 MPa and 321.6 MPa, respectively.

1. INTRODUCTION

Due to its high strength/weight ratio and shapeability, Aluminum is used in a wide range of areas from construction applications to structural parts of various vehicles (automobile bodies, engine parts, aircraft bodies, etc.). Due to the low densities of these alloys, besides the energy efficiency they provide, they are preferred in terms of sustainability, which has been emphasized in recent years, as well as their easy recycling properties. Nowadays, intensive studies on alloy properties, heat treatment and forming technologies are carried out in order to increase the existing properties of aluminum. 7xxx alloys are considered to be the most important group among heat treatable aluminum alloys. Depending on the applied heat treatment, there are great increases in mechanical properties (Hatch, 1984). In applications requiring high strength, 7xxx series aluminum alloys, which can be hardened by aging, are preferred (Rometsch, Zhang & Knight, 2014).

The increase in the mechanical properties of the alloy with aging is due to the difficulty of the dislocation movement of the secondary phase precipitates formed by heat treatment in the structure (Tekeli *et al.*, 2019). Aging is a three-stage heat treatment. These consist of solution, quenching and aging stages. In the solution stage, the material is kept at high temperature in order to obtain a supersaturated, single-phase solid-solution rich in alloying elements. In the quenching phase, the material is cooled rapidly and the supersaturated microstructure is preserved at room temperature. In the aging stage, the rapidly cooled alloy is kept at a certain aging temperature for a certain period of time, and the second phase is formed in the structure.

The effects of the heat treatment on the mechanical properties (microhardness, ultimate tensile strength, compressive strength) of the AA7075 (Al-5.5Zn-2.5Mg-1.5Cu wt.%) and AA7020 (Al-4.5Zn-1.2Mg-0.15Cr-0.15Zr wt.%) alloys have not been investigated in a comparative manner. Therefore, the purpose of the present work was to investigate mechanical properties of the AA7075 and AA7020 alloys depending on the heat treatment.

2. EXPERIMENTAL PROCEDURES

2.1. Preparation of the AA7075 and AA7020 cast alloys

Weighed quantities of high purity (99.99 %) Al, Zn, Mg, Cu and other minority metals (Cr, Zr) were used to prepare the AA7075 and AA7020 cast alloys (all compositions are given in wt.% unless otherwise noted). First, Al was placed in a graphite crucible (L:170 mm, OD: 40 mm, ID:30 mm) and melted in a vacuum furnace. After complete melting of Al, the required amount of Zn was placed under the surface of the liquid Al. Three stirrings of the liquid Al-Zn alloy were carried out at five-minute intervals, and then required amount of Mg packed with pure thin Al foil was placed in a graphite cage with many perforations; it was then put under the surface of the liquid Al-Zn alloy in order to avoid Mg burning on the surface of the melt. Finally, Cu and other minority metals (Cr and Zr) required according to the type of alloy were put into the crucible and melted. To get homogeneous cast alloys, the alloys were melted again in the vacuum melting furnace by inverting the billet. After stirrings and allowing time for the melt homogenization, the molten alloys were poured through a funnel into a graphite crucible that was connected with other alumina molds (180 mm in length, 9 mm OD, 6 mm ID) placed in a casting furnace. The furnace had lower and upper heaters at temperatures of approximately 50 ^{o}C and 100 ^{o}C above the melting point of the alloy, respectively. Each sample was stirred with a fine alumina rod and then solidified from bottom to top using a water cold stainless-steel reservoir in order to obtain a complete mixture and directionally solidified homogeneous sample. The average cooling rates through the directionally solidified samples were between 8-2 K/s depending on the position relative to the reservoir. The sample preparation experiments were repeated until the necessary numbers of suitable samples were produced. The upper and lower parts (10 mm) of the sample, which may contain casting defects, were discarded and not used for mechanical testing. The remaining parts of the samples for both alloys were prepared for mechanical tests.

2.2. Heat treatment

First, required amounts of samples (for microhardness, tensile and compressive strength tests) were produced for each alloy (AA7075 and AA7020). The solution treatment (homogenization) and aging processes in different regimes applied within the scope of this study are shown schematically in Fig. 1. To compare alloy samples to be heat treated with samples in as-cast form (Fig. 1a), five of the as-cast (without heat treated, WHT) samples group were not exposed to any heat treatment (HT) and they were stored at a low temperature (-18 ^{o}C) in a freezer in order to avoid the nat-

ural aging of the alloy at room temperature (RT) for microstructure and mechanical tests. The remaining twenty-five samples were exposed to a two-step 300 °C/12h+475 °C/12h solution treatment process (homogenization) and then quenched in water at RT (Fig. 1b). After the solution treatment process, these twenty-five samples were divided into five subgroups. One of these subgroups was preserved as an only homogenized group. In other words, it was not exposed to any aging treatment process. The remaining four subgroups (five samples in each subgroup) were exposed to artificially aging process (T6) in different conditions (regime1- regime4) (Fig. 1c-f). As shown in Fig. 1, five test samples were allocated for each subgroup to increase the reliability of the data.

The solution heat treatments (T6) were conducted in a Protherm PLF 110/45 model muffle furnace. In the two-step solution process, the samples were first kept at 300 °C for 12 hours and then at 475 °C for 12 hours and then quenched in water at room temperature to obtain a supersaturated solid solution α–Al. Then, the process was completed by performing an artificial aging process in four different regimes. As can be seen from Figure 1c-f, regime 1(120 °C/24h) and regime 2 (150 °C/24h) one step regime 3 (120 °C/12h +150 °C/12h) and regime 4 (150 °C/12h +180 °C/12h) consist of two-step heat treatments. The heat treatment (HT) conditions in both solution treatment and aging process are given in Table 1. After the heat treatments, standard metallography, microhardness, tensile strength, and compressive strength were carried out for all the samples (as-cast (WHT), only homogenized and homogenized+aged samples).

Table 1. Heat treatment processes of theAA7075 and AA7020 alloys

Name of sample	Process	Status
WHT	Without heat treatment	As-cast
OH	Only Homogenization	300 °C/12h+475 °C/12h (two-step)
Regime 1	H+artificial aging	300 °C/12h+475 °C/12h→120°C/24h (one-step)
Regime 2	H+artificial aging	300 °C/12h+475 °C/12h→150°C/24h (one-step)
Regime 3	H+artificial aging	300 °C/12h+475 °C/12h→120 °C/12h+150 °C/12h (two-step)
Regime 4	H+artificial aging	300 °C/12h+475 °C/12h→150 °C/12h+180 °C/12h (two-step)

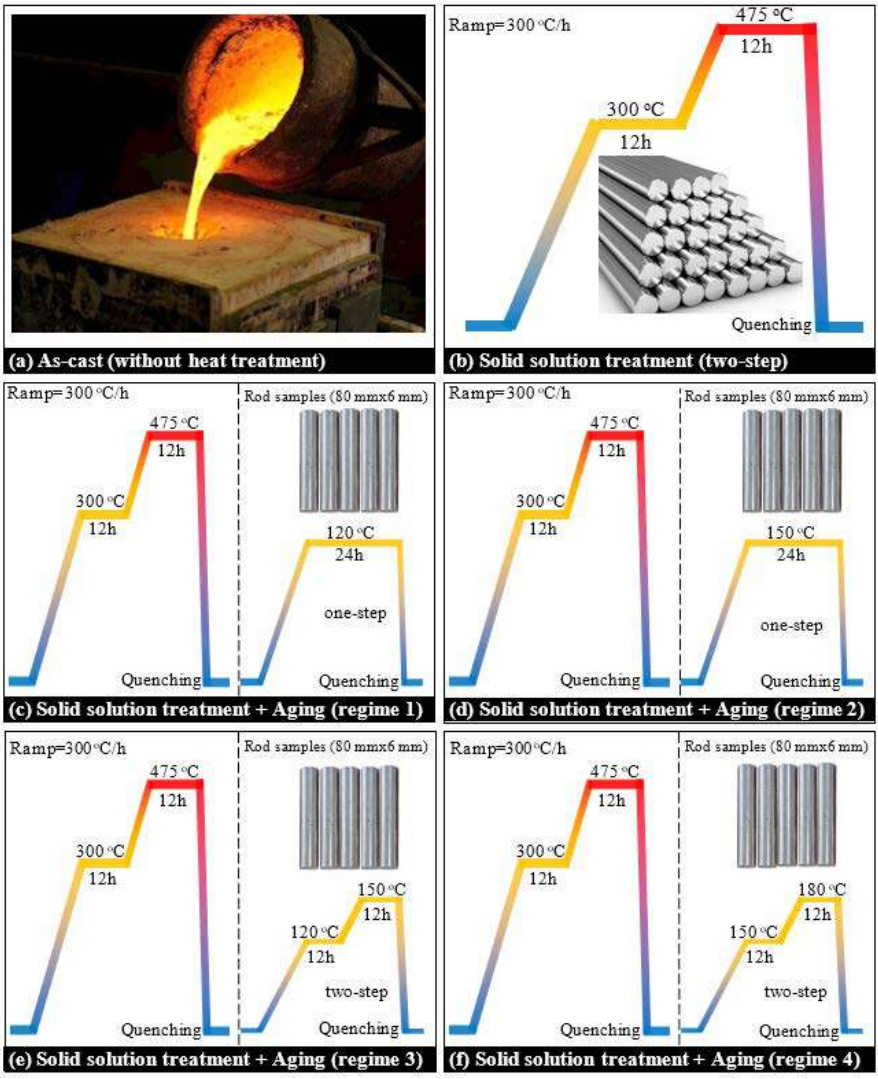

Figure 1. Types of heat treatment process (a) as-cast (without heat treatment WHT) (b) Solution treatment process (300°C/12h+475°C/12h homogenization with two-step) (c) aging regime 1 with one-step (120 °C/24h) (d) aging regime 2 with one-step (150 °C/24h) (e) aging regime 3 with two-step (120 °C/12h +150 °C/12h) (f) aging regime 4 with two-step (150 °C/12h +180 °C/12h)

2.3. Measurement of the microhardness (HV)

Microhardness measurements were conducted at room temperature using a Future-Tech FM−700 model microhardness test apparatus. A 300-gram

load was applied to the sample surface for 10 seconds, and approximately 20-25 readings were taken for each section. The mean values were obtained from the microhardness readings. Even though the measurement process was conducted with utmost care, some errors may have occurred due to surface quality of the sample, phase distribution in the microstructure and uncertainty in the traces. Additionally, a measurement error could be caused by the inability to achieve the required sharpness when measuring the diagonal lengths of the trace developed on the sample surface. The percentage of error obtained in the hardness measurements is acceptable (6%) and is within the systematic measurement error limits of the device.

2.4. Measurement of ultimate tensile strength (σ_{UTS}), tensile yield strength ($\sigma_{TYS)}$, and compressive yield strength (σ_{CYS})

The tensile and compressive strength of the samples were evaluated using a Shimadzu AG-XD testing system. The cylindrical samples for tensile testing had a diameter of 6 mm and a length of 60 mm, while the compressive samples had a diameter of 6 mm and a length of 8 mm. For each test, the strain rate for tensile testing was set to 10^{-3} s^{-1} at room temperature and the deformation rate for compressive testing was 1 mm/min. In order to assure the accuracy of the results, the tests were performed three times and the mean values were taken. It was observed that the error of the measurements was around 5%.

3. RESULTS AND DISCUSSION

3.1. Microhardness

Figure 2 shows the effect of various heat treatments on the microhardness values of AA7075 and AA7020 samples. HV values of the as-cast AA7075 and AA7020 samples without heat treatment are found to be 1835 and 350 MPa, respectively. The highest HV value for AA7075 alloy was obtained as 1920 MPa, for the only homogenized sample (300°C/12h+475°C/12h). This value (1920 MPa) is considerably higher than 1235 MPa, which is the highest value obtained for AA7020 alloy (regime 2). Heat treatments led to a greater increase in microhardness values for the AA7020 alloy. The microhardness of the cast sample increased from 350 MPa to 1235 MPa with the heat treatment called regime 2 (H+150 °C/24h). Results obtained for AA7075 alloy were in agreement with some previous studies in which the peak aged conditions of AA7075 alloy formed by squeeze casting and by extrusion were obtained after aging for 24 h at 120 °C (Kim *et al.*, 2001) and for 48 h at 120 ◦C (Emani *et al.*, 2009), respectively. Maamar (Maamar

et al., 2008) reported that the microhardness value for an AA7075 alloy increased from 1450 to 1850 MPa after applying the aging treatment. By comparing these microhardness values with our microhardness values, it becomes obvious that aging treatment is successful.

3.2. Tensile strength

Figure 3 shows the strength-strain curves of AA7075 and AA7020 alloys (σ_{TYS} and σ_{UTS} points indicated by yellow dot and black dot, respectively). While the samples of AA7075 alloy showed higher tensile strength compared to the samples of AA7020 alloy, the samples of AA7020 alloy reached higher values in terms of ductility. The elongation in the samples of AA7075 alloy varies between 1.1% and 6.6%, and the highest elongation value was obtained in the sample aged with regime 4. It has been determined that the elongation values obtained in the samples of AA7020 alloy are higher than the samples of AA7075 alloy. The elongation values for the samples of AA7020 alloy ranged between 5.1% and 19.6%, and the highest elongation value was obtained in the sample aged with regime 3.

Figure 2. The influence of homogenization and aging treatment on the microhardness for each alloy

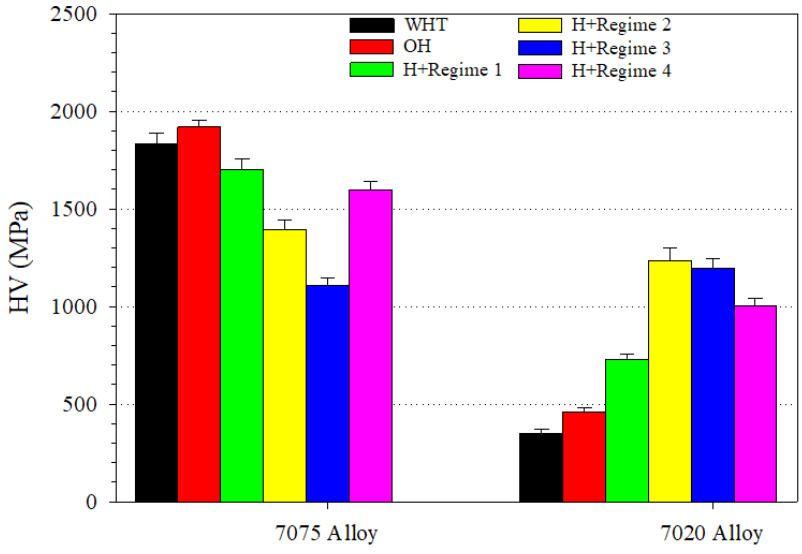

Figure 3. Typical tensile strength-strain curves of the WHT and HT samples (a) AA7075 alloy (b) AA7020 alloy

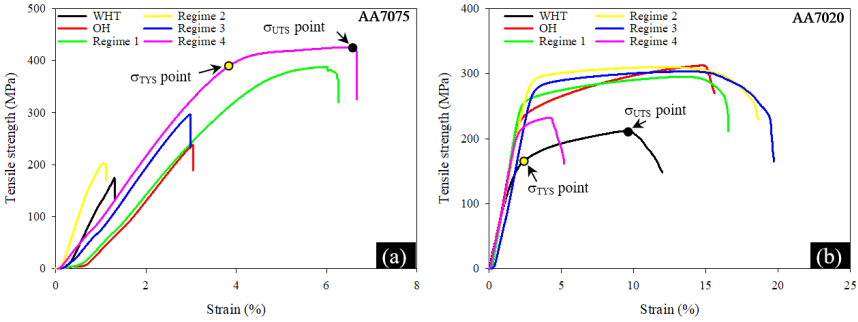

In Fig. 4a, the ultimate tensile strengths (σ_{UTS}) of the samples AA7075 and AA7020 obtained from the curves in Fig. 3 are given. The lowest σ_{UTS} value for the AA7075 alloy was determined as 174.6 MPa for the WHT sample, while the highest σ_{UTS} value was determined as 425.1 MPa for aged sample with regime 4. Peak σ_{UTS} value was obtained as 328 MPa for this aging process (regime 4) and 243% improvement was achieved compared to the σ_{UTS} value of the as-cast sample (WHT). The lowest σ_{UTS} value for AA7020 alloy was obtained as 212.1 MPa for the WHT sample, while the highest σ_{UTS} value was determined as 312.5 MPa for the only homogenized sample (OH). The σ_{UTS} value (425.1MPa) obtained for the AA7075 alloy is considerably higher than the σ_{UTS} value (312.5 MPa) obtained for the AA7020 alloy.

The yield point is the point on a strength-strain curve that indicates the limit of elastic behavior and the beginning of plastic behavior. The tensile yield strength ($\sigma_{TYS)}$ values are shown in Fig. 4b for both alloys. As can be seen in Fig. 4b, while the lowest σ_{TYS} value as 160.1 MPa was determined in the as-cast sample (WHT) without any heat treatment for the AA7075 alloy, the highest σ_{TYS} value as 378.2 MPa was in the aged sample with regime 4. Depending on the applied heat treatments in AA7075 alloy, the change in the σ_{TYS} values shows parallelism with the change in the σ_{UTS} values. In AA7020 alloy, while the lowest σ_{TYS} value as 163.3 MPa was determined in the as-cast sample (WHT) without any heat treatment for the AA7075 alloy, the highest σ_{TYS} value as 293.5 MPa was in the aged sample with regime 2. As can be seen Fig. 4(a-b), the observed parallelism between σ_{TYS} and σ_{UTS}, depending on the heat treatment conditions for the AA7075 alloy, was not observed in the AA7020 alloy. In addition, the highest σ_{TYS} value (378.2 MPa) determined for AA7075 is considerably higher than the highest σ_{TYS} value (293.5 MPa) obtained for AA7020 alloy.

In both alloys, both the σ_{UTS} and σ_{TYS} values improved significantly with aging at different regimes. Similar behaviors on the tensile properties were reported by Mahathaninwong et al. for AA7075 Al alloy (Mahathaninwong *et al.*, 2012), Paulisch *et al*. for AA7020 Al alloy (Paulisch *et al.*, 2015), and Chemingui *et al*. for AA7020 Al alloy (Chemingui *et al.*, 2010). The strengthening mechanism of the aging at T6 for the studied alloy is attributed to the precipitation hardening. In some studies, it is emphasized that the formation of the precipitate is caused by dislocation movement (Chemingui *et al.*, 2010; Chen *et al.*, 2012; Li *et al.*, 2006).

3.3. Compressive strength

Compressive strength-strain curves for AA7075 and AA7020 samples are shown in Fig. 5. Compressive yield strength values were determined from strength-strain curves (σ_{CYS} point indicated by black dot). The values of the σ_{CYS} under different heat treatment processes are shown in Fig. 6. While the lowest σ_{CYS} value was determined as 278.2 MPa for the as-cast sample (WHT) in AA7075 alloy, the highest σ_{CYS} value was determined as 501.6 MPa for the sample aged with the regime 3.

Figure 4. The influence of homogenization and aging treatment on the ultimate tensile strength and tensile yield strength for AA7075 and AA7020 alloys (a) ultimate tensile strength (b) tensile yield strength

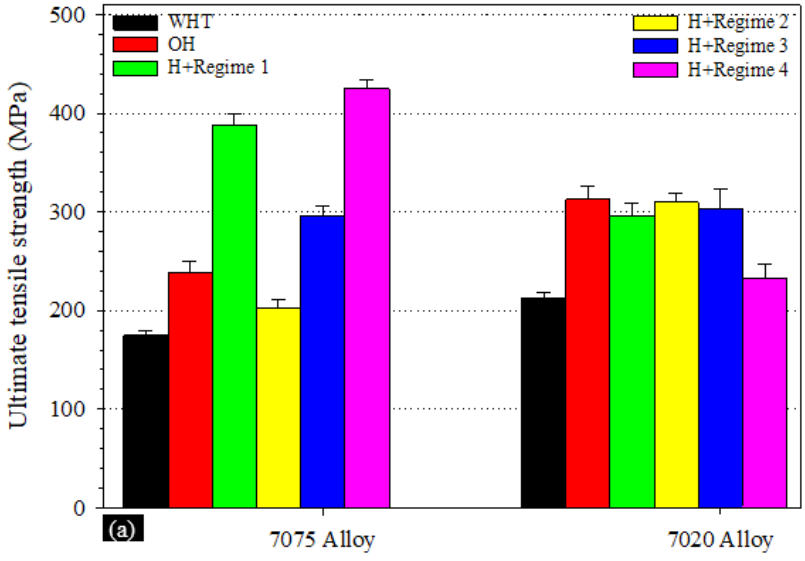

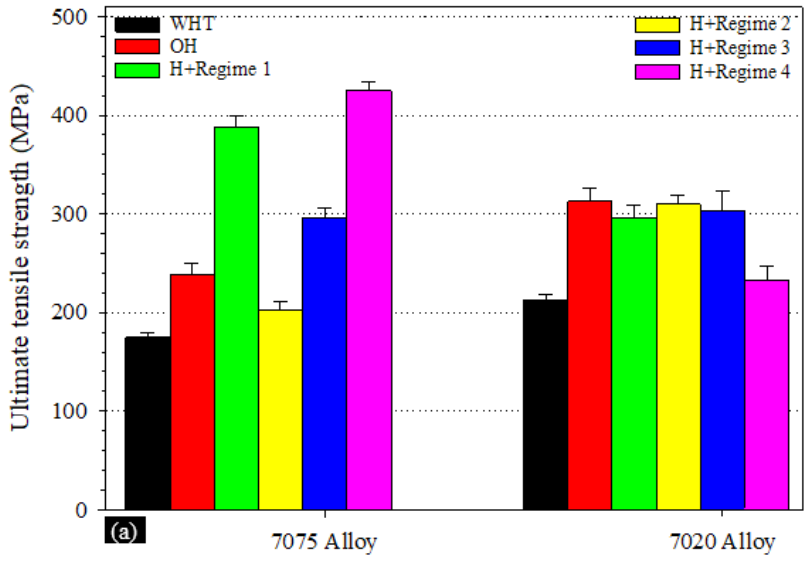

Figure 5. Typical compressive strength-strain curves of the WHT and HT samples (a) AA7075 alloy (b) AA7020 alloy

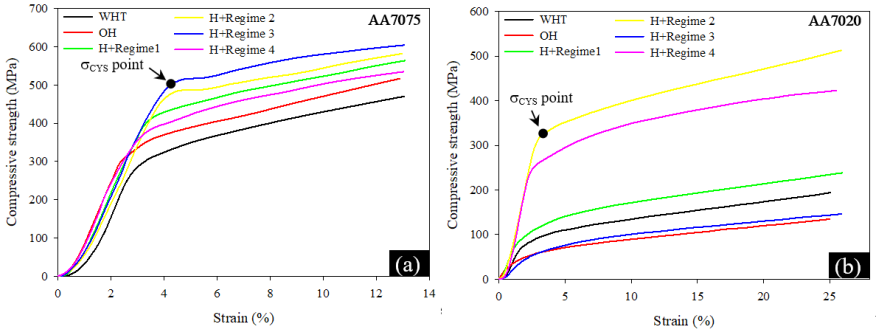

In AA7020 alloy, on the other hand, the σ_{CYS} values (56.6 and 54.1 MPa) obtained in some regimes (OH, regime 3) were below the σ_{CYS} value (84.7 MPa) obtained for the as-cast sample. However, the highest σ_{CYS} value was obtained as 321.6 MPa in the sample aged with the regime 2. When AA7075 and AA7020 alloys were compared, the highest σ_{CYS} value was found to be 501.6 MPa in the sample aged with the regime 3 in AA7075 alloy, while the highest σ_{CYS} value was found as 321.6 MPa in the sample aged with the regime 2 in AA7020 alloy. Thus, in AA7020 alloy, one-step regime

2 emerged as the most optimum HT process in terms of compressive yield strength, while in AA7075 alloy, the most optimum HT process was determined as two-step regime 3. Peak value (321.6 MPa) of σ_{CYS} obtained for AA7020 alloy in this study (H+regime 2) is in very good agreement with values 310 MPa, 300 MPa and 331 MPa obtained by Feng et al. (Feng *et al.*, 2013) at 190 °C/12h aging process after solution treatment (500 °C/3h) for Al-4Cu-1.3Mg alloy, Samuel *et al*. (Samuel *et al.*, 2015) at 200 °C/5h aging process after solution treatment (495 °C/8h) for 220 Al-2Cu based alloy and Zhan et al. (Zhan *et al.*, 2018) at 160 °C/12h aging process for Al-4.26Cu-1.36Mg alloy, respectively.

3.4. Young modulus

Young modulus values (E) defined from strength-strain curves in Fig. 3 is given in Fig. 7. As can be seen in Figure 7, the E values obtained for both AA7075 and AA7020 alloys vary between 68.6-76.3 GPa. Young's modulus values did not show a radical change depending on the applied heat treatments. While the highest E value was determined as 75.6 GPa for AA7075 alloy (OH), the highest E value was determined as 76.3 GPa for AA7020 alloy (regime 1). In summary the peak values of the mechanical properties detected after HT are given in Table 2. Many heat treatments are used in the metal fabrication and processing industry. Considering these studies, there are many factors that affect the heat treatment processes applied after solidification such as microstructure (size, shape and composition of the different constituent phases), presence of precipitates (composition, distribution, size of the particles), and interactions between dislocations.

Figure 6. The influence of homogenization and aging treatment on the compressive yield strength for AA7075 and AA7020 alloys

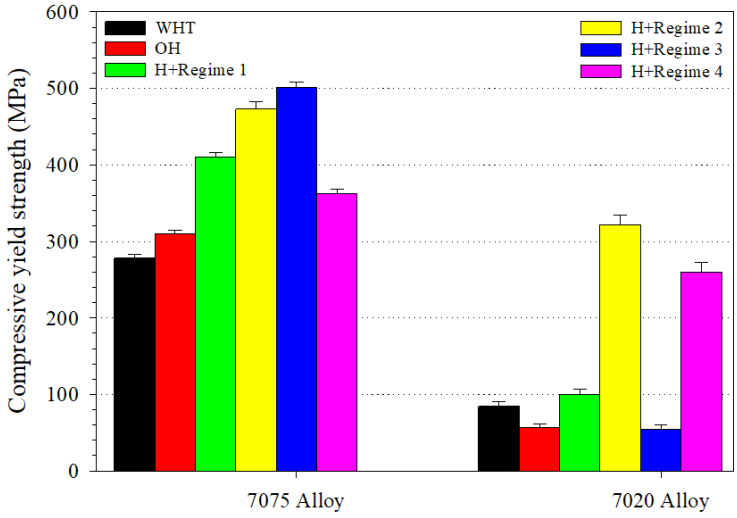

Figure 7. The influence of homogenization and aging treatment on the Young modulus for AA7075 and AA7020 alloys

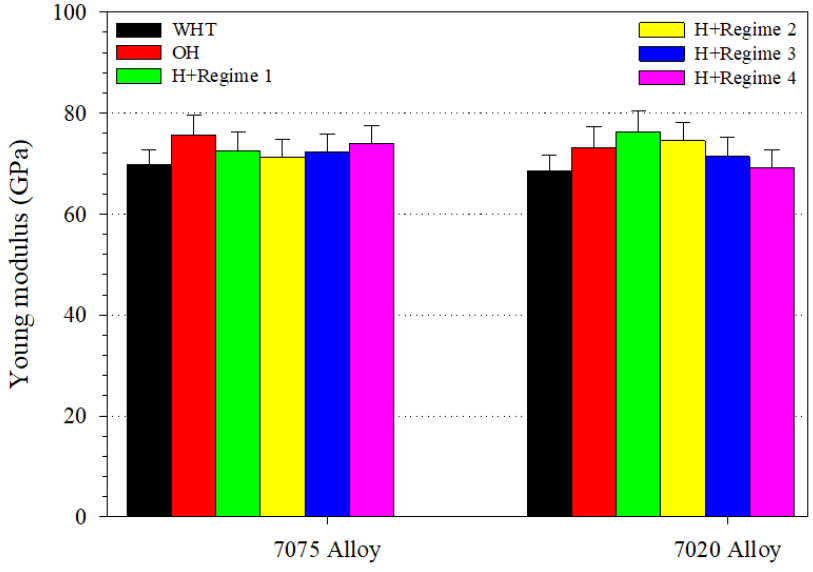

Table 2. Heat treatment (HT) conditions in which the mechanical properties reach peak value

Mechanical properties	Peak Values	Process
Microhardness (AA7075)	1920 MPa	Only Homogenization
Microhardness (AA7020)	1235 MPa	Regime 2
Ultimate tensile strength (AA7075)	425.1 MPa	Regime 4
Ultimate tensile strength (AA7020)	312.5 MPa	Only Homogenization
Tensile yield strength (AA7075)	378.2 MPa	Regime 4
Tensile yield strength (AA7020)	293.5 MPa	Regime 2
Elongation (AA7075)	6.6 %	Regime 4
Elongation (AA7020)	19.6 %	Regime 4
Compressive yield strength (AA7075)	501.6 MPa	Regime 3
Compressive yield strength (AA7020)	321.6 MPa	Regime 2
Young modulus (AA7075)	75.6 GPa	Only Homogenization
Young modulus (AA7020)	76.3 GPa	Regime 1

4. CONCLUSION

AA7075 and AA7020 alloys were produced using the vacuum furnace and the casting furnace. Mechanical properties of as-cast and heat-treated samples were investigated. The key findings are given as follows:

I. Substantial improvements in the microhardness of the AA7075 and AA7020 alloys were attained at different aging processes after solution treatment (300 ^{o}C/12h+475 ^{o}C/12h). Peak hardness values are obtained as 1920 MPa (OH) and 1235 MPa (regime 2), respectively.

II. The highest ultimate tensile strength as 425.1 MPa was obtained for the AA7075 alloy (regime 4). The peak elongation value in the AA7020 alloy (regime 4) reached to 19.6 %. T6 heat treatments (including different conditions and regimes) were improved significantly, both in the microhardness and tensile properties of both alloys. The increased microhardness and tensile strength in the aging treatments were attributed to a finer distribution of precipitates. This high precipitate density slows

the dislocation movement and thus a higher stress is required for its bowing.

III. The compressive yield strength of the AA7075 alloy (regime 3) reached 501.6 MPa with the aging process (120 °C/12h+150 °C/12h) applied after the solution treatment (300 °C/12h+475 oC/12h). The maximum gain of this sample was calculated to be about 80.3%.

IV. There were no radical changes in Young's modulus for either alloy. Depending on the applied HT conditions, values in the range of 68-76 GPa were determined.

ACKNOWLEDGMENTS

This work was supported by the Erciyes University Scientific Research Project Unit under contract No's: **FBA-2021-10981**. The authors are grateful for the financial support.

REFERENCES

J. E. Hatch, Aluminum: properties and physical metallurgy. Metals Park, Ohio: American Society for Metals, 1984. ISBN: 978-0-87170-176-3

P. A., Rometsch, Y. Zhang, S. Knight, Heat treatment of 7xxx series aluminium alloys - Some recent developments. Transactions of Nonferrous Metals Society of China (English Edition), 24 (7), (2014) 2003–2017. https://doi.org/10.1016/S1003-6326(14)63306-9

S.Tekeli, İ. Şimşek, D. Şimşek, D. Özyürek, Effects of different solid solution temperatures on microstructure and mechanical properties of the AAAA7075 alloy after T6 heat treatment. High Temperature Materials and Processes, 38 (1), (2019) 892–896. https://doi.org/10.1515/htmp-2019-0050

S.W. Kim, D.Y. Kim, W.G. Kim, K.D. Woo, The study on characteristics of heat treatment of the direct squeeze cast AA7075 wrought Al alloy, Mater. Sci. Eng. A 304–306 (2001) 721–726. https://doi.org/10.1016/S0921-5093(00)01594-X

S.V. Emani, J. Benedyk, P. Nash, D. Chen, Double aging and thermomechanical heat treatment of AAAA7075 aluminum alloy extrusions, J. Mater. Sci. 44 (2009) 6384–6391. https://doi.org/10.1007/s10853-009-3879-8

H. Maamar, R. Rabah Otmani, T. Fahssi, N. Debbache, D. Allou, Heat treatment and welding effects on mechanical properties and microstructure evolution of 2024 and AA7075 aluminium alloys, Metal 13 (2008) 1–7.

N. Mahathaninwong, T. Plookphol, J. Wannasin, S. Wisutmethangoon, T6 heat treatment of rheocasting AA7075 Al alloy, Mat. Sci. Eng. A 532 (2012) 91–99. https://doi.org/10.1016/j.msea.2011.10.068

M.C. Paulisch, N. Wanderka, M. Haupt, S. Selve, I. Driehorst, W. Reimers, The influence of heat treatments on the microstructure and the mechanical properties in commercial AA7020 alloys, Mat. Sci. Eng. A 626 (2015) 254–262. https://doi.org/10.1016/j.msea.2014.12.040

M. Chemingui, M. Khitouni, K. Jozwiak, G. Mesmacque, A. Kolsi, Characterization of the mechanical properties changes in an Al–Zn–Mg alloy after a two-step ageing treatment at 70° and 135 °C, Mater. Des. 31 (2010) 3134–3139. https://doi.org/10.1016/j.matdes.2009.12.033

S. Chen, K. Chen, G. Peng, L. Jia, P. Dong, Effect of heat treatment on strength, exfoliation corrosion and electrochemical behavior of 7085 aluminum alloy, Mater. Des. 35 (2012) 93–98. https://doi.org/10.1016/j.matdes.2011.09.033

L. Li, T.T. Zhou, H.X. Li, C.Q. Chen, B.Q. Xiong, L.K. Shi, Effect of additional elements on aging behavior of Al-Zn-Mg-Cu alloys by spray form-

ing, Trans. Nonferrous Met. Soc. China 16 (2006) 532–538. https://doi.org/10.1016/S1003-6326(06)60093-9

W. Feng, Z. Yanqi, X. Baiqing, Z. Yongan, L. Xiwu, L. Zhihui, L. Hongwei, Effect of Si addition on microstructure and mechanical properties of Al-Cu-Mg alloy. J Alloys Compd. 585, 474–478 (2013). https://doi.org/10.1016/j.jallcom.2013.08.214

A.M. Samuel, S.A. Alkahtani, H.W. Doty, F.H. Samuel, Role of Zr and Sc addition in controlling the microstructure and tensile properties of aluminum-copper based alloys. Mater. Design. 88, 1134–1144 (2015). https://doi.org/10.1016/j.matdes.2015.09.090

L. Zhan, X. Wu, X. Wang, Y. Yang, G. Liu, Y. Xu, Effect of process parameters on fatigue and fracture behavior of Al-Cu-Mg alloy after creep aging. Metals 8, 298 (2018). https://doi.org/10.3390/met8050298

Chapter 2

The Importance of Energy Storage for Sustainable Heat and Power

Kamil Kaygusuz[1]

Abstract

The impact of energy storage is far-reaching, as not only does it address the issues that have limited renewable energy's penetration, it fundamentally alters the longstanding relationship between utilities and their customers. The disruptive potential of storage is unlike other energy technologies in that it pervasively extends across the value chain in a way that stakeholders will impact and be impacted by its adoption. Energy storage can play an important role in the present, in the short-term and in the medium- term future energy scenario. Both stationary and automotive applications will be considered and the main features required by each of them for an energy storage system will be explained. A very brief description of the proven and most promising storage technologies will be given with the aim of providing an overview of the peculiarities of each one and consequently its better-suited applications. Finally, the state-of-the-art, the opportunities and the barriers to the spread of energy storage systems will be summarized.

1. Introduction

Energy efficient thermal energy storage (TES) system constitutes a crucial instrument in thermal distribution networks today. Due to the thermal management of urban and industrial landscapes becomes increasingly important, so too does the impact of carefully planned and designed TES systems [1-5]. TES systems, for the most part, do not specifically generate nor consume thermal energy and their role in the thermal distribution landscape is essentially analogous to that of a battery or capacitor in a power distribution network. They allow supply to meet demand by bridging the gaps between the two [6-8]. In most manifestations of TES systems, this gap is often a time gap, where the surplus thermal energy generated is preserved in the TES for a future period when the demand for it is greater or more

1 Karadeniz Technical University, Department of Chemistry, Trabzon, Türkiye

Hasan Kalyoncu University, Department of Mechanical Engineering, Gaziantep, Türkiye, kamilk@ktu.edu.tr, Orcid: 0000-0001-8364-2794

https://doi.org/10.58830/ozgur.pub130.c542

appropriate, such as with hot water storage for night-time heating, or even across longer periods of time like seasonal TES systems which store heat during summer and discharge during winter [9-11]. The "storage" phase of the TES is often coined as the "charging" phase in the literature, while the utility phase of the TES process is considered as the "discharging phase". Hence, TES systems play important roles in creating efficient and resilient thermal distribution networks by allowing load matching to take place as needed. Figure 1 illustrates how TES is applied to bridge the gap between demand and supply needs [12-15].

Fig. 1. TES meet load deficits by bridging the time gap between supply-side and demand-side utilities.

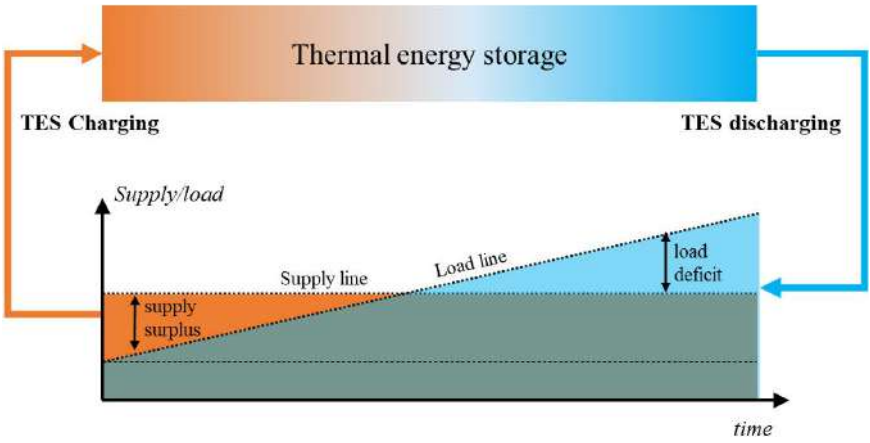

The energy scenario has significantly changed in the last decade for a variety of factors. The first one is the increase in the amount of electrical capacity supplied by variable and non-predictable renewable sources [1-3]. In recent years, the growing awareness at both the public and institutional levels of the "energy issue" has led to a series of initiatives aimed at promoting the use of renewable energy sources (RESs) [4]. Definitely, their use often results in a lower environmental impact in terms of a reduction of both resources consumption and emissions, with special regard to carbon dioxide, which is responsible for the greenhouse effect. The comparison between the installed capacity and energy production allows us to evaluate the load factor of such plants, expressing the ratio between the energy actually produced and that theoretically producible if the plant would run throughout the year at its design power: the value is low and around 22% for wind power and 12% for solar. This is due to the extreme variability of the sun and of the wind over the year and even in a single day, so that the plant can operate

at design load only for a limited number of hours per year. In addition, the low predictability of these variations makes production scheduling more difficult, especially for wind power even in the very short term [2, 3].

A second aspect is due to the progressive deregulation of the energy market carried out in many developed countries aims to separate the activities of generation, transmission and distribution of electricity and where for every hour of the year the price of energy is determined by the intersection between supply and demand curves. The main goal of deregulation is the promotion of fair competition in the production and sale of electricity in order to reduce energy costs and increase the efficiency of the system [4]. The first consequence has been the significant and rapid growth of the installed generation capacity in OECD countries, the power plants had a total installed capacity of 2,680 GW, of which 1,811 GW was from thermal power plants in 2020. But in some countries, this expansion has been even greater [5, 6].

The stability of the power grid depends on various actors working in concert to maintain a balance between electricity supply and demand. Traditionally, electricity assets are categorized based on their function; i.e., generation, transmission, or distribution. Storage systems differ in that they have the ability to balance supply and demand across the segments that comprise the value chain. The new control points offered by storage systems enable operators to selectively respond to fluctuations in grid inputs and outputs. Such functionality is essential to realizing the vision of "smart cities" where producers and consumers are equally informed and equipped to respond to market dynamics in real time. However, many electrical grids were not originally designed to accommodate assets that can both generate and consume electricity. The implications of two-way power flow and the role of energy storage within a modern electricity ecosystem have been studied by many institutions. Potential applications and appropriate storage technologies within each segment of the value chain are illustrated in Figure 2.

Figure 2. End use electricity consumption

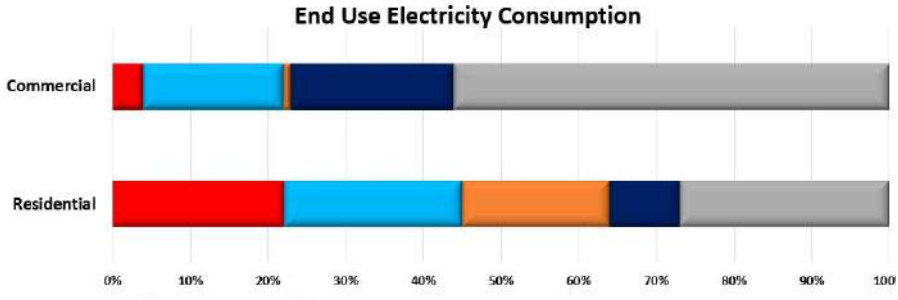

In almost all the developed countries, in a more or less marked way, the combined effects of the aforementioned factors have created a situation where the installed capacity is overabundant with respect to the users' peak demand, and where quite a high fraction of power is made available by variable and difficult to predict renewable sources. This condition definitely implies a significant saving of fossil fuels and the reduction of emissions, but introduces some critical elements into the market [10-15]. In addition, the advent of generators powered by renewable sources has drastically changed the structure of the electricity network with the presence of a large number of small power production facilities spread over the country in the vicinity of the users and of the available sources, instead of a classic structure with "a few" large facilities concentrated in the industrial zones of the country [7-9].

It is important to remember that the power grid is a very complex system that transmits and distributes electricity generated from the production plants to users through a set of power lines, transformer stations, isolation, protection systems, and is subject to very stringent technical constraints, in particular [1-4]:

- An instantaneous and continuous balance between the amount of energy released and that required by the network is necessary, taking into account the losses due to transformers, transport and distribution.
- The frequency and voltage must be kept within a very narrow range of values is essential to protect the safety of the generation and end-user facilities.
- It must always be ensured that the energy flow in each power line does not exceed the maximum permissible load on the power line itself.

The change of any one of the abovementioned parameters, even if minor and/or of very short duration, can rapidly induce a state of crisis into the entire local electrical system and subsequently, because of a "domino" effect, to a possible blackout of the entire network. For example, the sudden drop in power available from wind turbines caused by an unexpected reduction of the wind speed can cause stability problems to the network when the share of energy provided by these systems is significant [2, 3, 5]. Therefore, when thermal plants are called upon to operate, sometimes suddenly, they impose a high price on the market, which partly offsets the higher costs associated with frequent stops and part-load operation. This great variability on the supply side has enhanced the role and the value of the markets for ancillary service and has led to a major diffusion and increased importance of the capacity markets have to ensure supply will be available when it is needed [7, 9, 1]. Figure 3 shows the energy storage density of the phase change materials.

Figure 3. Energy storage density of phase change materials for energy storage material cost ($/kWh)

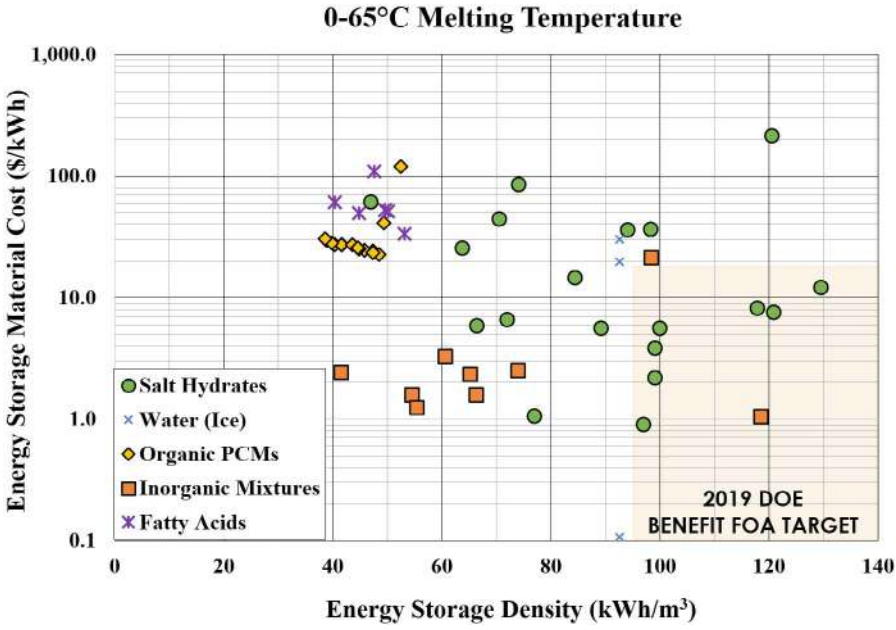

As a final issue, the transport sector is also undergoing many changes. The most important driver is the requirement to reduce pollutants, mainly particulates, in urban areas. This issue demands new transportation solutions: one of the most promising and studied is that of pure electric

and hybrid vehicles, combining a traditional fossil-fueled engine with an electric propulsion system. These vehicles are powered by the energy stored in an onboard battery, which will be recharged at the so-called "charging points" usually connected to the grid. With a proper operation strategy, these charging stations can be managed as users with flexible demand and are able to dampen the peaks and gaps in energy supply [1-3].

The combination of all these elements has led therefore to the need to rethink the arrangements for managing both the electricity network as a whole, as well as individual plants. The main target is to supply energy with high efficiency, low cost, high reliability, and low environmental impact. As a last point, it is important to note that in developing countries or for communities looking for energy self-sufficiency, the exploitation of renewable sources is an opportunity to increase the number of people who have access to electricity with an adequate degree of availability and reliability. In such countries, the number of renewable energy or hybrid power plants is increasing. In this case, the systems are not grid-connected and it is even more important to arrange power units able to meet the demand in spite of the intermittency of variable energy sources. Figure 4 shows the electric vehicle stock target.

Figure 4. Electric vehicle (EV) stock target [8].

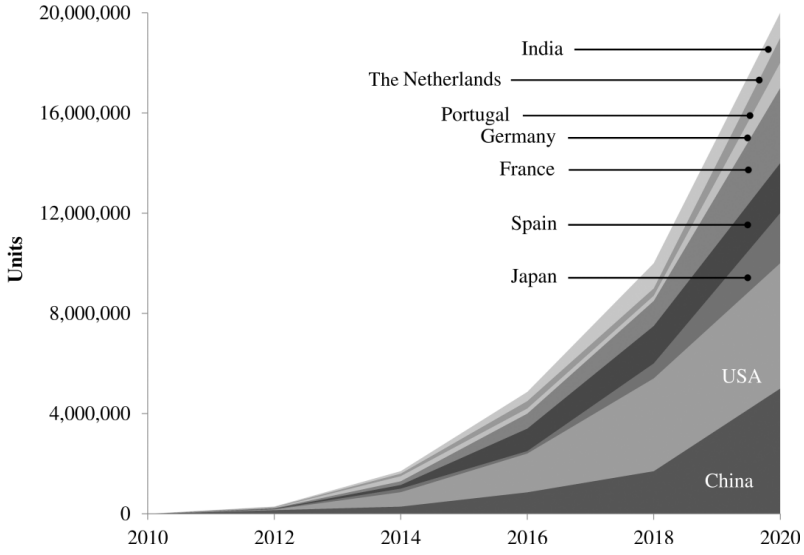

The new situation needs to be addressed with adequate instruments. Possible areas of research and application are manifold and involve very different aspects:

- Thermal plant flexibility, partial load efficiency and start-up and shutdown speed.
- Emission control and removal, including carbon capture and storage technology.
- New technologies for the exploitation of low-quality energy sources with high efficiency.
- Control systems and smart grids.
- Policies that are able to promote the use of renewable sources and energy efficiency without distorting the market.
- Energy storage permits the separation of energy production from its consumption.

2. The Main Characteristics

As mentioned previously, energy storage is a challenge for the electricity system where the optimum efficiency can still be improved. Briefly, the aim is to separate the supply and demand for energy. However, each storage technology has specific features, which make it better suited for some applications than for others.

For this reason, before explaining the role of energy storage in actual and future markets, the most important characteristics of energy storage units are outlined below [9–14]:

- *Storage capacity (C):* This represents the maximum amount of energy that can be stored. For some technologies, due to the presence of a maximum allowable depth of discharge, it differs from the usable energy.
- *Charging and discharging rating power (P):* This is the nominal charge–discharge power, usually that of maximum efficiency. For some systems, the charge and discharge powers have the same value, while in other cases, they differ (for example if different devices are used for the two phases and/or for specific users' needs). Usually, the actual power can differ from the rating value and varies from a maximum to a minimum value.
- *Specific energy and specific power (Es and Ps):* They quantify the density of energy or power, and are defined as E/V and P/V , where V is the volume of the storage. The higher these values, the lower the volume

at constant energy or power. Sometimes, these values are supplied per mass unit.

- *Round trip efficiency (η):* This is the ratio of the discharged to the charged electricity. Its value is related to the losses both during the charge–discharge cycle itself and the self-discharge during the storage period. It usually differs from the cycle efficiency, considering only the charge and discharge phases.
- *Rated discharge time (T):* This represents the duration of the discharge time at the rated discharge power starting from full storage, and can be defined as C/P. Obviously, the actual value of the rated discharge time depends on the actual discharge power and on the energy stored.
- *Response time (tr):* This is the time between the request to change the operation and the system response.
- *Inversion time (ti):* This is the time needed to pass from the charge to the discharge phase or vice versa. Here, tr and ti represent the ability of a system to vary the power and to quickly respond to the grid operation regulation signal.
- *Expected lifetime (L):* This value can be defined in terms of a lifetime or as the number of charge and discharge cycles.
- *Reliability:* This gives an idea about the robustness of the storage units operation.
- *Environmental impact:* This point is very important and public acceptability is closely related to it. The main impact can be during the building phase (for example, due to the use of materials in short supply), during the operation (due to pollutants) or during the decommissioning (if potentially dangerous substances must be disposed of). The location of the storage system and its size influence this aspect.
- *Levelized unit electricity cost (LUEC):* This is the price at which the electricity should be sold in order to cover all the costs related to the building, operation and decommissioning costs and to assure a return on the investment. This value depends on many factors, such as the size, location, charge and discharge history of the storage unit, and also it is related to the market and the incentives policy. In any case, this value is fundamental in order to evaluate the feasibility of a storage solution.

As a last remark, for some technologies, the performance indices (C, P, η, T) are almost constant during the lifetime of the storage system, while for others, they decrease due to different deterioration phenomena. Other aspects can be important for the selection of storage technology, for example, its commercial maturity, the constraints required by the installation site, or the operational constraints (pressure, temperature), plus safety problems.

3. The role of energy storage in the energy scenario

The traditional role of storage systems was to store energy when the demand, and consequently its cost, were low, typically at night, and to make the energy available during the hours of peak demand. In this way, the inflexible thermoelectric plants could work all day at almost constant power and an energy reserve for peak hours was assured. In these systems, the main requirement for energy storage was the ability to exchange power with a rated discharge time of several hours [1-5].

In the new scenario, the energy storage system is also required to provide, in a very short time, power to overcome the intermittence of renewable sources and contribute to the regulation of the mains voltage: in this case, the amount of energy that can be stored is less important, but the response speed is critical. Therefore, depending on the application, different features are required. The most evident application difference is between stationary and automotive storage.

3.1 Stationary Applications

For stationary applications, storage units can either be connected to the grid or work in isolated areas for stand-alone energy systems. In the first case, they can operate as independent units to serve the grid or may be connected to a RES plant or to an end-user to provide the needed support [13-15]. Generally, the so-called "energy performance" storage systems are able to provide power for many operation hours and have a low value of P/C, are suitable for energy management applications that include moving power over long timescales, and generally require continuous discharge ratings of several hours or more. Typically, one or a few cycles/day are required.

The traditional service of this kind to the grid is the time-shift or energy arbitrage. Storage systems are used to decouple synchronization between power generation and consumption. A typical application is load leveling, which implies storing up energy during off-peak hours and using the stored energy during peak hours. This is convenient if the ratio between peak and base load prices is lower than the round-trip efficiency of the system. In this

case, the storage system is required to have high-rated discharge times (from some hours to days) and capacity (from 10 MWh to about 10,000 MWh).

To the time shift service, the peak shaving service is often added, which helps decrease the number of shut-down/start-ups of traditional plants, the operation hours of more expensive/less efficient power plants, and the high line loss rates that occur during peak demand. Another service for the grid is the not-programmable sources integration helps boost the penetration of RES, decreases the energy losses from power plants, compensates for the power fluctuations and provides a more regular and predictable power profile.

Deferral of grid investments and congestion relief is another benefit that energy storage can guarantee. Distribution systems must be sized for peak demand; as demand grows, new systems must be installed, often only to meet the peak demand for a few hours per year. New distribution lines may be difficult or expensive to build, and can be avoided or deferred by deploying distributed storage located near the load. Response in minutes to hours is required plus a rated discharge time of some hours. The power performance of the storage technologies, able to supply high power for relatively short periods are suitable for providing grid ancillary services.

The "fast response" (in seconds to minutes from null to rated power) nature of these energy storage technologies makes them ideally suited to meet grid stability and reliability challenges. Among these services is the contribution to primary frequency control, which also requires a low inversion time to guarantee a high regulation band, and a good round trip efficiency. Some tens of cycles/day are usually required [7, 9]. Similar features are required of energy storage systems to contribute to secondary and tertiary frequency control. Black start is the restart of electricity supply after a major power system disturbance, and requires capacity and energy after a system failure restart and must provide a reference frequency for synchronization. It requires several minutes to over an hour of response time, plus several hours of discharge time. Usually, cycling is very low. For contingency reserve, stored energy is used for seconds to minutes to ensure service continuity when switching from one source of electricity to another. Discharge times in the range of up to about an hour are usually required. Far less cycling is required than for power-quality applications [3-5].

Another benefit that energy storage can provide to the grid is the power quality control: stored energy is only used for a few seconds or less to ensure the quality of power delivered. Power quality applications require rapid

response and include transient stability and frequency and voltage regulation. As with the other applications, the timescales of discharge may vary; but this kind of services typically requires discharge times of up to about 10 min and nearly continuous cycling (hundreds of cycles per day).

The features required for the storage system depend on the size of the RES plant, but usually a continuous discharge of several hours and a response of minutes are required. In conclusion, the presence of energy storage units provides benefits for:

- The traditional production facilities, which can work at nearly constant load, plan their production and limit the number of on/off switches.
- The renewable source plants, whose production can be entirely and profitably used.
- The grid, whose stability and reliability are enhanced.
- The users, who are ensured a safer and more reliable electric service.

3.2 Automotive Applications

The main constraint for energy storage units for EVs and plug-in hybrid electric vehicles (PHEVs) is the necessity to remain on board the vehicle. Therefore, high volume and mass energy densities are paramount. Batteries are the most suitable technology for vehicles. For EVs they need to be designed to optimize their energy storage capacity, while for PHEVs they typically need to have higher power densities. Other important requirements are the rated discharge time, the fast charging, a high life expectancy, plus a low-temperature sensitivity [8]. On the other hand, the charging of EVs can potentially be controlled, and provides a source of planned demand and demand response. Controlled charging can be timed to periods of greatest RES energy production, while charging rates can be controlled to provide contingency reserves or frequency regulation reserves. EVs could potentially provide the grid services discussed previously.

4. Energy Storage Technologies

In this section, only a very brief summary of the main characteristics of each technology will be given. The following sections provide a more complete description of many of these storage technologies [9-15]:

4.1 Pumped-Hydro Energy Storage (PHES)

In brief, water is pumped into an upper reservoir and stored there; when energy is required by the grid or the price of electricity is high, water is released through one (or more) turbines to a lower reservoir and the electricity produced is sold. PHES is a proven technology, suitable for large-scale storage. It is very efficient and flexible in power, has a short response time, can ramp up to full production capacity within minutes providing a quick response for peak-load energy supply and is already used for both primary and secondary regulations. On the other hand, it needs to be located in suitable geological sites, containing a geodetic head and natural upper and lower basins or at least the possibility of building artificial reservoirs. This requires relatively high initial costs. The environmental impact can also be non-negligible, in terms of land occupation and modification, disturbance of the aquatic life, and modification of the natural water flow.

4.2 CAES

In these storage systems, the air is compressed during charging and then stored in an underground cavern or other pressure vessel. When electricity is required, the air is heated to avoid freezing and then expands in a turbine. If the heat generated during compression is stored and then used to preheat the air in order to increase the round-trip efficiency, the process is called adiabatic. If external heat input by means of combustion is used to preheat the air, the process is called diabetic. Despite the large interest of this technology, there are only two plants in operation around the world. CAES is basically suitable for medium and large energy storage for energy applications. Recently, many studies are related to its use in small systems. The use in direct connection to wind farms or other non-programmable RES plants, or for distribution grid support seems to be very promising. At present, the main drawback is the cost.

4.3 Flywheels (FWs)

Flywheels store energy in the form of kinetic energy. The storage unit is composed of FWs driven by an electric motor able to work either as a generator or as a motor and located inside a housing. If the motor provides a positive torque, the FW increases its rotation speed and energy is stored. When energy is needed from the FW, the electrical machine applies a negative torque and the stored energy is released. This technology is already mature and is suitable for high-power applications. In addition, FWs present long cycling expected life and short response and inversion times. On the other

side, mainly due to friction losses, the round-trip efficiency strongly and speedily decreases during the operation. For this reason, the FWs are suitable only for short-term storage and, at present, are mainly used as voltage and frequency control, as support for wind farms or in transportation to increase the efficiency of trains, ferries or large EVs.

4.4 Fuel Cell Hydrogen (FC-HES)

Chemical energy storage is the transformation of electrical energy into chemical energy carriers (the so-called power-to-gas or P2G). At present, the most promising energy vector is hydrogen. Hydrogen is produced by means of water electrolysis which is a process consuming electricity. Then, hydrogen is stored as a liquid at cryogenic temperature, or as a gas at very high pressure or as a solid in hydrides. Finally, the stored hydrogen may be used to produce electricity. The most common solution is by means of fuel cells. There are many different kinds of fuel cells, which mainly differ in the electrolyte used and the operating temperature. Note that the use of hydrogen in fuel cells produces only water and does not emit any pollutants or greenhouse gas. This technology has a high energy density and the possibility of storing very large quantities of hydrogen for a long time. Hydrogen can also be transmitted from one location to another. These features make chemical storage suitable for energy management applications, even for seasonal storage. At the same time, electrolysis has a short response time. The main drawbacks are the excessive costs, the low round trip efficiency and the short lifetime expectancy.

4.5 Electrochemical Batteries (EBES)

Batteries, or accumulators, are based on a single device with the functions of energy storage and discharge of electricity. The basic element is an electrochemical cell having voltages from below 1-4 Volt; many cells can be put in series in order to reach higher voltages. Electricity is produced by an oxidation–reduction reaction where a flow of electrons is created from a chemical species (anode) to another one (cathode) in contact by means of an electrolyte. The reverse process can recharge the battery. Many different batteries are available on the market, and others are under study: they differ for the materials used for the anode, the cathode and the electrolyte, and in the design. Batteries have a high technological maturity, high energy density, good round trip efficiency, and great modularity that permits them to be tailored to users' requirements. Their main inconvenience is their relatively low life for large-amplitude cycling. During their operation they do not emit pollutants or noise. However, their disposal can present a significant

environmental impact due to the materials used for the electrodes and/or the electrolyte.

4.6 Supercapacitors (ECES)

Supercapacitors or electrochemical capacitors (ECs) or also electric double- layer capacitors (EDLCs), store electrical energy in an electric field between two electrodes separated by a dielectric and immersed in a liquid electrolyte. The electrodes are characterized by a very large useful surface and the distance between the electrodes is very small. The process is easily reversible. ECs are suitable for high-power applications since they have a very fast response time, high round trip efficiency, high power density, but low energy density, long expected lifetime and can guarantee a very high number of charge–discharge cycles. They are an interesting solution also for electric transportation both for brake energy recovery and for propulsion over very short stretches of roads without electric connection. Supercapacitors have not yet reached commercial maturity, but they are expected to improve their performances in the near future.

4.7. Magnetic Superconductors (SMES)

In magnetic superconductors, energy is stored in the magnetic field of one or more superconducting coils characterized by very low losses. To reach this condition, they must work at very low temperatures (near absolute zero). At present, they have no commercial market, but are still in the research phase and are considered a promising technology. The main problem is the necessity of a cryogenic temperature with the related prohibitive cost and high energy requirement. This brings a low energy density and low round-trip efficiency. However, they have very interesting characteristics, such as very fast delivery of high power at high cycle efficiency. For this reason, they are suitable for power applications, requiring continuous operation with many charge and discharge cycles.

4.8. Thermal Storage (TES)

Thermal energy storage (TES) includes many technologies where energy is stored in the form of heat. Heat can be stored as:

- Sensible heat: if storage is achieved by increasing or decreasing the temperature of a storage material. In this case, the amount of stored energy is proportional to the temperature difference.
- Latent heat: if storage is connected to a phase transition of the storage material, usually from solid to liquid and vice versa. In this case, the

temperature remains constant and the stored energy depends on the latent heat of fusion of the material.

- Thermochemical heat: if heat is stored as chemical compounds created by an endothermic reaction and it is recovered again by recombining the compounds in an exothermic reaction. The stored energy is equivalent to the heat of the reaction.

These technologies are used for many heating and cooling applications. For example, where heat supply and demand are often not simultaneous, as for solar heating systems, or to utilize peak shaving of heating demand. Energy storage in these applications can be very long-term storage, even seasonal. Nowadays, TES is also used for electric applications as support of renewable energy plants. For concentrated solar power plants, energy from the sun is stored by means of molten salt and then released, when needed, to steam which operates a Rankine steam power plant. Further support to the grid can be given by storing heat from electric boilers working as a fast balancing service, or helping limit the demand for electrical power from electric boilers where the need for heat is not continuous and varies in intensity. As a last remark, recently many researchers are studying the possibility of combining different energy storage technologies in the same system in order to exploit the synergy among their different features: for example, the use of batteries together with FWs can increase the life of the batteries.

The power technologies are those with low discharging time and low rating power that fit well with the power quality applications. Some examples are batteries and FWs. The energy technologies are those with high discharging time and high rating power. These technologies fit well with applications like time shift, peak shaving and capacity reserve. Some examples are Pumped-Hydro Storage and CAES technologies. Figure 5 shows the different maturity levels of the main energy storage Technologies [17]. The present level (left end of each arrow representing a technology) and the expected level in 2030 (right end of the arrow) are reported. Some of them are still in a first research phase, others are already proven technologies. Nevertheless, improvements are expected for all of them. Note that for some of them, the expected development is really important.

Fig. 5. State-of-the-art and forecast development of the most promising energy storage technologies.

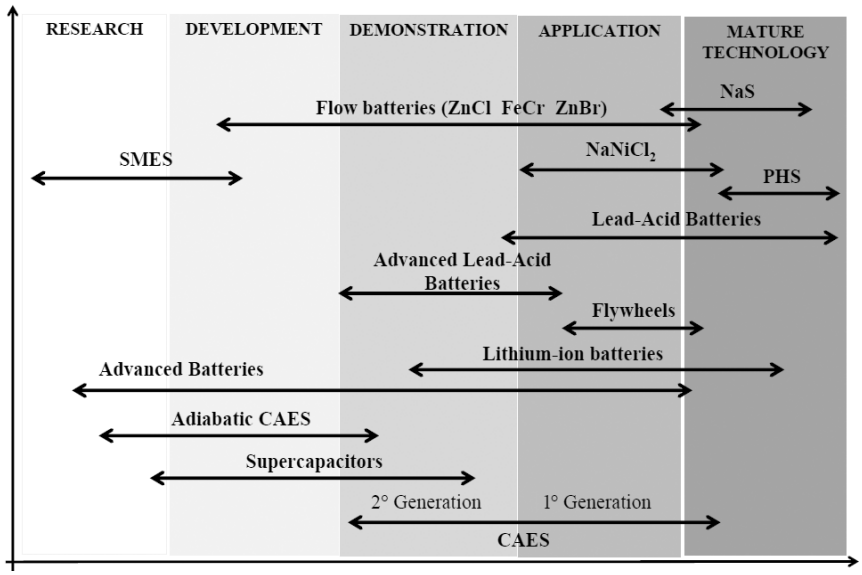

5. State-of-the-Art and Projects

At present (2020), the worldwide capacity of operating storage systems is estimated at nearly 245 GW and is equivalent to about 2% of the overall electric installed capacity. Many of these systems were built between the late 1970s and 1980s when the increasing price of oil and natural gas drove the construction and operation of many coal and nuclear power plants, which need to work at a steady base load and are not very flexible [14, 15]. Starting from the late 1990s, with the development and the large spread of Combined Cycle Gas Turbines, which are very efficient and flexible, the necessity for energy storage decreased until the last ten years, as explained in the Introduction. Batteries are mainly used for stand-alone applications: only two big grid-connected systems are installed, in Japan and Abu Dhabi, respectively. Also, only one CAES plant in the USA and another one in Germany are operating [1-6].

The International Energy Agency (IEA) has estimated that an additional 310 GW of grid-connected electricity capacity would be needed in the United States, Europe, China and India to support electricity sector decarbonization [1-5]. The estimated worldwide installed capacity in 2050 is about 400 GW: the main contribution is expected from countries where there are (or are planned) many solar and wind power plants, or where geodetic heads

available for PHES are present. Regarding this point, mountainous places are the most suitable, but there is an increasing interest, supported by a technological development for seawater pumped-energy storage systems, which exploit the geodetic head connected to high coasts and use the sea as the lower reservoir.

Even if it is possible to find many studies about energy storage all over the world, at present only a few official technology roadmaps are in force. In any case, most of the international and national administrations have put energy storage as a key objective of their respective work programs about energy [12]. On the other hand, Japan, European Union and IEA elaborated the strategy about energy storage together with other energy technology roadmaps. In the United States, a federal map was not published, but some States have done so. California is the main example. In 2050, it is estimated that there will be an installed storage capacity of about 150 GWin the US, primarily achieved by means of the addition of new CAES plants [1-7].

In developing countries, the main contribution to energy storage in the short–medium term is expected to be small-scale stand-alone systems: many projects of renewable energy or hybrid plants integrated with the use of batteries, hydrogen or small PHES have been presented. Often, these systems require a pumping station for access to water. From the studies of many different agencies, it seems that in the short–medium term, batteries will be the winner for small-scale storage plants, while for large scale, probably CAES and Power to gas should be an attractive alternative to PHES, but they still need some improvements. It also calls attention to the importance that there is diversity in energy storage in order to exploit the suitable characteristics of each technology.

6. Barriers to Diffusion

As mentioned earlier, even if energy storage has a long history and much research and many improvements have been recently achieved, further efforts are needed in order to fulfill the new energy market needs [1]. The main challenges for storage concern the technologies, the market regulatory issues, and the strategies [2-4]. With regard to the technological aspects, improvements are required to increase the capacity, efficiency, autonomy, lifetime and reliability of the existing technologies. For proven technologies, the improvements should mainly consist in the upgrading of the existing devices, while for new and developing ones, they will also involve new storage concepts or important modifications of the present design, such as the use of different materials or working pressures and temperatures or

innovative cycles. In any case, the key point for each improvement is the reduction of the LUEC. Since the LUEC is also a function of the operating history of the storage unit, it is essential that the development paths are tailored to the specific applications [5-8].

Improvements are also required to the control and regulation systems of the grids where storage units are connected. Note that when the share of non-programmable RES electricity exceeds 20–25% energy storage could enable bi-directional energy flows in the grid, and this eventuality must be predicted. For batteries used in the EVs, the major challenge is the increase of energy density and the reduction of charging times [4]. This last point also requires development of the devices used in the recharging stations. Great attention must also be paid to the environmental impact of the storage units: for many technologies, such as EBES, FC-HES and ECES, the major targets are the sustainable use of resources, the prevention of dangerous wastes and the possibility of recycling, for PHS the use of existing reservoirs and the minimization of the interference with the natural streams of water and of land use, for FWs, the main issue is noise control. In the analysis of the environmental impact of a storage unit, a life cycle approach must be used and the impact for each useful energy unit supplied must be evaluated [5-8].

Finally, improvements to the safety requirements for people living near the energy storage systems, and also the surrounding devices, have to be carried out: dangerous materials which can lead to explosions, toxic emissions, and corrosion are used in some technologies (EBES, SMES, ECES), failure of the rotating wheel is possible for FW, high pressure (CAES) or temperature (FC-HES) are required by some cycles, electrical hazards must be considered for all the technologies; for EVs also recharging security is a concern to be studied. Note that the perceived environmental impact and safety of storage technologies is an important social barrier to the spread of energy storage, so this point needs particular attention [1-4].

A second important challenge for the diffusion of energy storage is the creation of a market able to incentivize the connection to the grid of storage capacity and the supplying of storage services [22]. Since the value of energy arbitrage alone is not sufficient to justify the building of new plants, the market must recognize and pay for the help that an additional offered capacity gives to the grid in terms of flexibility, service safety and reliability. It should be paramount that the price paid by the final users is not increased. So, a preliminary detailed cost–benefits analysis is very important. To attract investment in fast response energy storage technologies, the market must be

willing to pay for the value of the speed and accuracy that energy storage provides to the grid, reducing the overall need for, and cost of, regulation services. So the payment can be composed of two different terms: the first one based on the speed and amount of energy transferred by the resource in response to a control signal, and the second one based on the capacity that a unit makes available to provide regulation. Another interesting approach can be the employment of a regulation dispatch algorithm that selects fast response resources before slow response resources in order to minimize the total amount of regulation capacity required in the balancing area [8-12].

The difficulty in defining the rules for the proper support of energy storage systems is increased by the complexity due to the different functions that the same energy storage unit can assume in-service to the grid and to the different features that its function requires. When a unit is in the direct service of an RES plant or of final users, the possible presence of different owners and stakeholders makes the regulation more complicated. Another important issue is that the market rules must be clear and well defined in the short–medium term since the costs for a storage unit are often very high and investors need to plan their investments with a certain degree of confidence. This is paramount for Europe where a common balancing market must be built up [1-3].

In the United Stated, there is already a quite favorable environment for energy storage due to the well-developed ancillary services market: energy storage is allowed to participate and provide services that account for both its qualities and shortcomings [6–8]. Finally, it is important to note that the presence of energy storage also involves other markets such as the gas market (P2G), local districting heating markets (TES), and the transportation sector. A common development strategy must be implemented. It is clear that some strategic issues also have to be faced. The development of energy storage systems is linked to the progress of the whole energy system. Therefore, it is important that a systemic approach is employed, where technical, regulatory, market and political aspects are combined.

Some points are particularly related to the spread of energy storage systems:

- The regulatory framework for the reduction of CO2 emissions, which can strongly encourage the growth of RES.
- The penetration of EVs, which is connected to the evolution of the automotive industry and to the motivation for change in the behavior of users.

- The development of smart grids, which support the diffusion of small-scale energy storage and also of EVs as storage units.
- The upgrade of the Transmission and Distribution grids with the construction of new cables, connecting areas where large amounts of RES are available to areas where electricity is needed. This includes both new long cables in large geographic areas and an increase of the number of interconnections between different smart energy grids.

It is clear that strong public engagement is needed, which depends on investment priorities. Public investments are required to develop new projects and to help the construction of large test case facilities to validate the effective features of the storage technologies. It is important, at this development stage, that technology diversity is encouraged and promoted. A mix of all solutions is needed, tailored for each region and system architecture.

7. Conclusions

In this chapter, a general overview of TES systems, their importance to the thermal systems design, and their rising importance was discussed. A brief breakdown of their various manifestations and embodiments was also conducted with an emphasis on recent developments. The core thrusts of TES study, namely, material, design, and system integration, were defined and their research directions were briefly reviewed. The subsequent chapters will provide greater details on different forms of TES, starting from the fundamentals to present-day case studies.

As the energy landscape continues to evolve with higher levels of variability from climate change and renewable energy sources, the progress of TES systems is expected to grow significantly including various approaches to better manage thermal systems. While heat storage was central to the thermal management of the past systems, rising global temperatures have led to the growing need for cold TES systems in places where ambient temperatures continue to appreciate. Accordingly, a certain degree of emphasis will be placed on cold-TES systems in a subsequent chapter.

Acknowledgement: The author acknowledged to Turkish Academy of Sciences for finalcial support of this study.

References

[1] IEA, International Energy Agency. World Energy Outlook 2020. IEA, Paris, 2020.

[2] Stoppato, A., Benato, A. The importance of energy storage. World Scientific, NY, 2012.

[3] Soh, A., Prabakaran, V., Chua, KJE. Thermal Energy Storage-From Fundamentals to

Applications. World Scientific, New York, 2023.

[4] Dinçer, I., Rosen, MA. Thermal Energy Storage Systems and Applications, Third Edition, John Wiley, Hoboken, NJ, USA, 2021.

[5] Shukla, A., Sharma, A., Biwolé, PH (Eds.). Latent Heat-Based Thermal Energy Storage Systems-Materials, Applications, and the Energy Market. CRC Press, New York, 2021.

[6] Guelpa, E., Verda, V. Thermal energy storage in district heating and cooling systems: A review, Applied Energy, 2019; 252: 113474.

[7] IRENA, International Renewable Energy Agency. Innovation Outlook: Thermal Energy Storage, Abu Dhabi, 2020.

[8] Kocak, B., Fernandez, A.I., Paksoy, H. Review on sensible thermal energy storage for industrial solar applications and sustainability aspects. Solar Energy 2020; 209: 135–169.

[9] Agarwala, S., Prabhu, KN. Review of thermal characterization techniques for salt-based phase change materials, Journal of Energy Storage 2022; 46: 103865.

[10] Lei, J., Yang, L., Yang, EH. Energy performance of building envelopes integrated with phase change materials for cooling load reduction in tropical Singapore, Applied Energy, 2016; 162: 207–217.

[11] Rubitherm Technologies GmbH, Macroencapsulation — CSM, Rubitherm Technologies GmbH [Online]. Available: https://www.rubitherm.eu/en/index.php/

[12] Desai, F., Prasad, S., et al. Thermochemical energy storage system for cooling and process heating applications: A review, Energy Convers Mgmt, 2021; 229: 113617.

[13] Li, Y. Hwang, R. Radermacher, R., Chun, HH. Review of cold storage materials for subzero applications, Energy, 2013; 51: 1–17.

[14] Chandra, YP., Matsuka, T. Stratification analysis of domestic hot water storage tanks: A comprehensive review. Energy & Buildings, 2019; 187: 110–131.

[15] Huggins, RA. Energy Storage Fundamentals, Materials and Applications, Second Edition, Springer, London, 2016.

Nomenclature

C = Storage capacity

E_s = Specific energy

L = Expected lifetime

P = Charging/discharging rating power

P_s = Specific power

T = Rated discharge time

V = volume

t_i = Inversion time

t_r = Response time

η = Round trip efficiency

CAES = Compressed air energy storage

EBES = Electrochemical battery energy storage

ECES = Supercapacitors energy storage

EDCL = Electric double layer capacitor

EV = Electric vehicle

FC-HES = Fuel cell hydrogen energy storage

FW = Flywheel

LUEC = Levelized unit electricity cost

PHES = Pumped-hydro energy storage

PHEV = Plug-in hybrid electric vehicle

RES = Renewable energy source

SMES = Superconductors magnetic energy system

TES = Thermal energy storage

Chapter 3

Comparison of Power Performance of Horizontal Axis Wind Turbines with NACA 4412 and NREL S809 Airfoils

Mehmet Bakırcı[1]

Abstract

To investigate the power coefficient values, two different horizontal axis wind turbines were designed with the use of two airfoils; NACA 4412 and NREL S 809. These had three blades with a radius of 40 cm and were produced using a 3D printer. Power coefficients were calculated by measuring the torque values generated in these turbines for different tip speed ratios. The homogeneous wind obtained by a moving vehicle is used to produce artificial wind. The highest power efficiency was achieved with NACA 4412 compared to NREL S809, but the power efficiency value was higher with NREL S809 at values greater than 9 of the tip speed ratios with NACA 4412.

1. Introduction

Our world's need for energy, especially electrical energy, continues to increase day by day. Countries, especially in the last 30 years, have focused on the development of electricity generation technologies using sustainable resources like solar, wind, geothermal, biogas, tidal energy, which do not pollute the atmosphere and are not depleted. Three-blade horizontal axis wind turbines (HAWT), which are among the wind turbine types developedto utilize wind energy, have become the most preferred type due to their high efficiency [1].

The power efficiency of these turbines depends on the airfoil selected as the blade section, how these airfoils are positioned on the blade and the rotor tip speed ratio (TSR) value [2].

Studies on the parameters on which the tip speed ratio (TSR), ratio of the wing tip tangential (linear) velocity and the wind speed, depends and its optimum value are found in the literature. In general, optimum tip

[1] Karabuk University, Mechanical Engineering, mehmetbakirci@karabuk.edu.tr

https://doi.org/10.58830/ozgur.pub130.c540

speed ratio (OTSR) values ranging from 1 to 5 for multi blades, 4-10 for three blades, 9-15 for two blades and 15-20 for one blade are given [3]. For example, Bai [4] stated this value as 5, while Wang [5] stated it as 10 for three bladed ones. In this study, the tip speed ratio value at where the highest power efficiency is obtained is investigated. The second aim of this paper is to compare the power efficiencies of the HAWT designed with NACA 4412 and NREL S809 airfoils. While NACA series airfoils were used more in the past, NREL series airfoils, which were specially developed for wind turbines, were preferred [6].

Blade tip tangential speed and the wind speed in the free region (V_∞) ratio is defined as the tip speed ratio (TSR) and is denoted by λ in this paper. The blade tangential velocity U is equal to the product of the rotational angular velocity ω and the blade length R [7].

$$\lambda = \frac{\omega R}{V_\infty}$$

The power to be obtained from a wind turbine equals to the product of the rotational angular speed and the torque produced by the blades [7]. When it is desired to obtain high torque (moment), low rotational speed is generated, while low torque is generated at high rotational speeds. The product of these two values (torque and angular rotational speed) gives the power value to be obtained. For obtaining the maximum power, calculating the optimum values of the angular rotational speed or torque is important [8]. In other words, the optimum tip speed ratio (OTSR) for obtaining the maximum power coefficient (C_P) value must be determined for a HAWT.

The rotor rotates very slowly, allowing the wind to pass through the openings between the blades, so that some of the wind passing through the rotor cross-section is not utilized. But when the rotor rotates excessively fast, the blades function like a barrier blocking the passage of wind, resulting in an incomplete utilization of wind power. Therefore, a HAWT should be designed to operate at the most favorable TSR for extracting the maximum possible power from this flow of wind. The power efficiency (C_P) value of the HAWT varies according to the TSR value. While the C_P value takes small values at very low TSR values, the C_P value also increases when the TSR value is increased. However, this increase occurs up to a certain TSR value, after this value, the C_P value starts to decrease while the TSR value increases (Figure 1) [9].

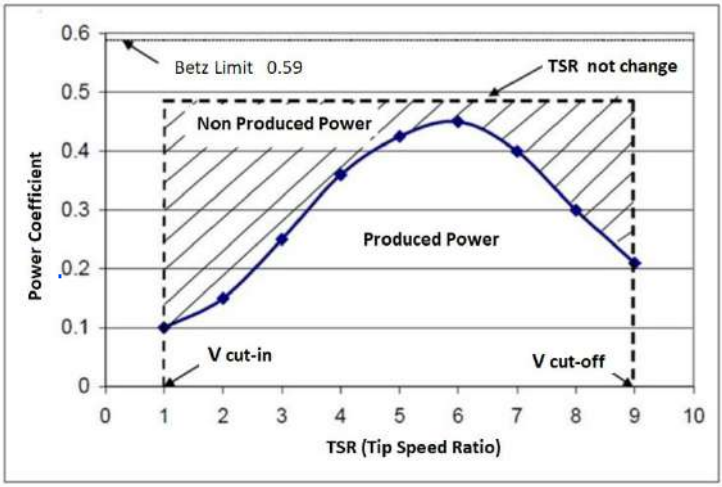

Figure 1. Power coefficient-TSR relationship [9].

M.Ragheb[10] proposed the optimum tip speed ratio's mathematical calculation in this way: For a wind turbine with horizontal axis, the time required for one of its blades to be replaced with its next one is same as the required time for the wind entering inside and being disturbed and restored after hitting it. Where B is indicated as the blade number, time for the next blade to replace it, it is calculated with the following equation;

$$t = \frac{2\pi}{B\omega}$$

The time it takes for the wind hitting the blade to regain its original state after it is disturbed t=S/V; S=the path taken by the wind hitting the blade until it regains its original state, V=wind speed. If these two times are equalized and the angular velocity is written;

$$\omega = \frac{2\pi V}{B.S}$$

The above relation is obtained. Here the value of S is based on the experimental results and is stated by Ragheb [10] to be taken as R/2. If the definition of TSR is used, the optimum tip speed ratio value (OTSR) is equal to $4\pi/B$. We observe that the optimum tip speed ratio (OTSR) value for B=3 blades is $4\pi/3$ and this value is approximately 4.19. It is stated that if the airfoil selection is made correctly, the optimum tip speed ratio value will be 25%-30% higher than this value. That is, it can be expressed as $5.24 < \lambda_{optimum} < 5.45$ [10].

An empirical formula is given in the literature [11] where the power coefficient (C_P) value can be calculated as a function of TSR (λ), blades number(B) and the maximum C_L/C_D ratio of the airfoil used in the wing section:

$$C_p = (\frac{16}{17})\lambda \left[\lambda + \frac{1.32 + \left(\frac{\lambda - 8}{20} \right)^2}{B^{2/3}} \right] - \frac{0.57\lambda^2}{\frac{C_L}{C_D}\left(\lambda + \frac{1}{2B} \right)}$$

In the above formula, C_P (power coefficient) and OTSR ($\lambda_{optimum}$) values found according to the maximum values of C_L/C_D ratio for HAWT having 3 blades are given in Table 1.

Table 1. C_L/C_D - $C_{p(max)}$-OTSR values according to the formula.

$(C_L/C_D)_{(max)}$	$C_{p(max)}$	OTSR
25	0.43	3.5
50	0.47	5
75	0.5	6
100	0.52	8
130	0.3	9

The higher the $(C_L/C_D)_{(max)}$ ratio that demonstrates the airfoil's aerodynamic performance, the higher the C_P value [12]. The OTSR value is also affected in the same way (Table 1). In the mentioned formula, the effects of the number of blades (B) on $C_{P(max)}$ and OTSR can also be calculated. While the effect of C_L/C_D value on $C_{P(max)}$ and OTSR is high when the number of blades is low, it is seen that this feature of the airfoil does not have much effect as the number of blades increases. However, in this formula, the effects of airfoil $(C_L)_{max}$ value, design angle of attack, Design Tip Speed Ratio (DTSR) value and dimensions of the blade geometry on $C_{P(max)}$ and OTSR are not taken into account [13].

Mc. Cosker calculated the effects of the design tip speed ratio value on the blade geometry as well as rotor aerodynamic performance of the

selected airfoil in the design of a R=2.5 m long HAWT with 3 blades using the BEM theorem. As a result of his study, he obtained $C_{p(max)}$=0.53 with NACA 23012 at OTSR=7. While creating this geometry, DTSR=6 value was used. NACA 4412 airfoil obtained $C_{p(max)}$=0.55 value at OTSR=11 value. While creating this geometry, the design used the value TSR=8. Again, using these two airfoils, he calculated the effects of design TSR values on $C_{p(max)}$ and OTSR (using values 6, 7, 8 for DTSR) with the Blade Element momentum (BEM) theorem. In cases where the TSR value is less than 6, the NACA 23012 airfoil is more efficient in contrast with the NACA 4412 airfoil, while for cases where this ratio is greater than 8, the NACA 4412 is more efficient. In general, he stated that NACA 4412 is more optimum. Cosker used the airfoil C_L and C_D values from the literature [22] and Re=6.10^6 [14].

Raşit Ata has developed an optimum design method by calculating how the power multiplier value is affected by which parameters in the HAWTs using artificial neural network. Taking into account the airfoil C_D (drag coefficient), blade tip losses, air reverse flows in the turbine downstream, power losses due to the number of blades, the maximum power multiplier and OTSR values were calculated using the artificial neural network optimization method. For a 3-blade HAWT, $C_{P(max)=}$0.4576 value was found at OTSR=8.5 with NACA 4415 airfoil and $C_{P(max)=}$0.492 value was found at OTSR=10 with LS-1 airfoil. In the study, the effects of the number of blades and airfoil attachment angle on power performance were shown with numerical values [15].

Bai et al. used the NACA 4418 airfoil in the design of a three-winged HAWT with a 0.36 m long wing. At 10 m/s wind speed, they found the maximum $C_{P(max)}$ value to be approximately 0.43 by BEM theorem, approximately 0.42 by Computational Fluid dynamics (CFD) simulation and approximately 0.415 by experiment. These values were obtained at OTSR=4.9. They also used 5 as the design TSR value while creating the geometry. They stated that the Reynolds number affects $(C_L/C_D)_{(max)}$ the value and thus has a significant effect on $C_{P(max)}$ and OTSR values. For this reason, when calculating $C_{P(max)}$ and OTSR values with empirical formulae and BEM Theorem, it is necessary to be very careful at which Reynolds value the $(C_L/C_D)_{(max)}$ value is taken. In a graph given by Bai, it is seen that the $(C_L/C_D)_{(max)}$ value of NACA 4418 airfoil is 13 for Re=40 000, 32 for Re=70 000, 42 for Re=100 000. For very long blades, the value of Reynolds number changes significantly

from the center towards to the tip. However, when the wing width is reduced from the center of the wing to the tip, it is stated that the Reynolds number will not change much since the air's relative velocity while striking airfoil will increase towards the tip while the airfoil chord length will decrease towards the tip. It has been observed in many studies in the literature that the optimum TSR value for HAWTs with a blade length of 10 m and more is above 7, while in the Bai study, the OTSR value for the HAWT with a length of 0.36 m was realized around 5 [16].

Han Cao analyzed the 2D aerodynamic performance of DU 93-W-210 and NREL S 809 airfoils with CFD. The air velocity was taken as 23.8 m/s and Reynolds number as 1 million. Since DU 93-W-210 aerodynamic performance is better than NREL S 809, this airfoil was used in the HAWT design. Using DU 93-W-210, he designed a 4.5 m radius LWT. He performed 3D CFD simulation to calculate the power that this wind turbine can generate. He calculated that the power that can be obtained at a wind speed of 8.8 m/s is 9518 W while the optimum TSR value is 8. In this CFD simulation with Ansys fluent, he calculated that the part of the torque value caused by pressure is 448.7 N.m and the negative torque caused by viscosity is 21.7 N.m and 427 N.m net. Improvements were made in the tip and hub geometries of the wing and CFD simulation showed an 11% improvement in power performance. While at a wind speed of 3.5 m/s as well as the rotational speed of 60 rpm, the torque was 106 N.m and the power coefficient value was 0.42. At a wind speed of 8.8 m/s and the rotational velocity of 150 rpm, the torque value was 812 N.m and the C_P value was 0.49 [17].

Azevedo-Mendoncha, in their study in which they applied the maximum power tracking method, it is seen in the (C_P-TSR) graph that the different sizes of the HAWT have different OTSR and Cp(max) values. It is understood from the graph that $C_{P(max)=}0.2$ and OTSR=2 when R=5 cm, $C_{P(max)}=0.29$ and OTSR=3.7 when R=15 cm, $C_{P(max)}=0.4$ and OTSR=8.2 when R=40 cm. It is seen from the graphs that $C_{P(max)}$ value exceeds 0.45 and OTSR value is around 8 for the larger HAWT. For HAWTs smaller than 1 m diameter, it is understood that $C_{P(max)}$ and OTSR values are highly affected. Since it is known from other studies that these values are also affected by wind speed, it is clear that it would be more accurate to express these two parameters with Reynolds number. Reynolds number due to its determining impact on $(C_L/C_D)_{max}$ value, which is the aerodynamic property of the airfoil. It is understood from

many studies in the literature such as mathematical- empirical formulas, BEM theorem, CFD simulation that $(C_L/C_D)_{max}$ value directly affects OTSR and $C_{P(max)}$ values[18].

Wang calculated the C_P values for a 83 m diameter 3-bladed HAWT with three different methods for different TSR values ($3<TSR<13$). These methods are as follows: 1-FVM (free vortex method), 2-Computational fluid dynamics (CFD), 3-Wind tunnel experiment. While the FVM method found the $C_{P(max)}$ value as 0.53 at OTSR=10, the CFD simulation found the $C_{P(max)}$ value as 0.51 at OTSR=9.5 and the wind tunnel experiment found the $C_{P(max)}$ value as 0.5 at OTSR=10 [19].

Padmanabhan-Saravanan compared the performance of NACA and NREL airfoils with R=2.5 m radius and 3 blades: While $C_{P(max)}$ value of 0.52 was obtained with NACA at TSR=10, $C_{P(max)}$ value of 0.49 was obtained with NREL airfoil at TSR=10. However, while $C_{P(max)}$ values close to each other were obtained with both airfoils at TSR values less than 10, higher C_P values were obtained with NREL at TSR values greater than 12. Although NACA has a higher $C_{P(max)}$ value, they concluded that NREL airfoil is more efficient for a wider range of values of TSR [20].

In this study, the power efficiencies at different angular rotational speeds of two different horizontal-axis wind turbines designed using two airfoils selected from NACA and NREL series were experimentally measured.

2. Materials and Methods

There are different types of experiments to measure the aerodynamic performance of wind turbines [21]; such as experiments in the wind tunnel, long-term open field tests in naturalwind environment, turbine test in the face of artificial wind generating fan, experiment mounted on a pick-up truck. In the wind tunnel, there are difficulties in providing the desired dimensions of the ratio of turbine size and duct cross-section size (for accurate measurements, it should be at most 1/5 [21]. There are difficulties in obtaining homogeneous wind in the study of creating artificial wind with a fan and conducting experiments. In natural wind environment, it is not always possible to obtain constant speed wind [21]. In this study, in order to provide homogeneous and constant speed wind flow, a 40 cm long HAWT experiment with 3 blades mounted on a car was carried out (Figure 2).

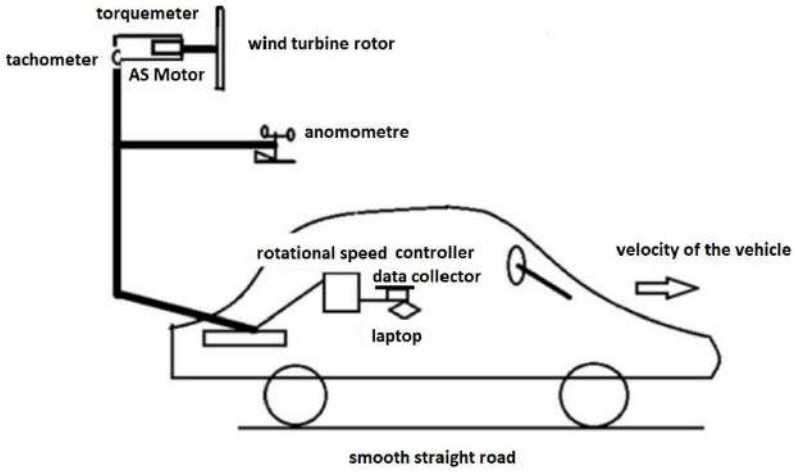

Figure 2. Experimental setup.

A 40 cm blade-length, three-bladed HAWT was designed according to the Schmitz equations with NACA 4412 [23], and NREL S 809 [24]. Schmitz equations;

$$c(r) = \frac{16\pi r}{B(C_L)_T}\sin^2\left(\frac{1}{3}\arctan\left(\frac{R}{r\lambda_T}\right)\right)$$

$$\beta(r) = \frac{2}{3}\arctan\left[\frac{R}{r}\frac{1}{\lambda_T}\right] - \alpha_T$$

c(r): airfoil length.

r: distance from the rotor center.

B: number of blades.

$(C_L)_D$: airfoil design lift coefficient value

R: blade length (rotor radius)

β(r): airfoil pitching angle

α_D : airfoil design angle of attack

λ_D : design tip speed ratio

NACA 4412 and NREL S 809 airfoils are shown in Figure 3 and Figure 4. The designed blades were produced with a three-dimensional printer (Figure 5).

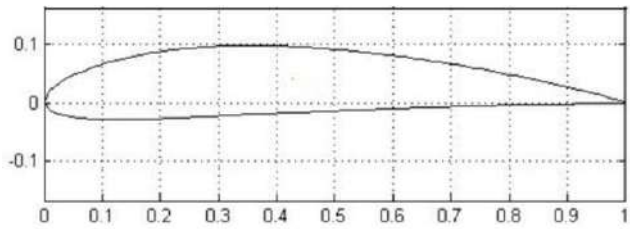

Figure 3. NACA 4412 cross section [23].

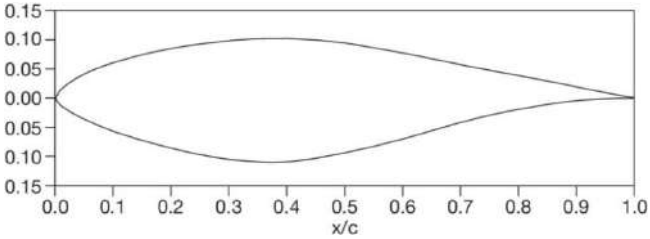

Figure 4. Cross section of NREL S809 [24].

The NACA 4412 airfoil has a maximum lift coefficient of 1.4, whereas the NREL S809 airfoil has a maximum lift coefficient of 1.3. This means that the NACA 4412 airfoil can generate more lift than the NREL S809 airfoil. The NREL S809 airfoil has a lower drag coefficient than the NACA 4412 airfoil at low angles of attack. However, at higher angles of attack, the NACA 4412 airfoil has a lower drag coefficient than the NREL S809 airfoil. The NACA 4412 airfoil has a sharp stall, meaning that it experiences a sudden drop in lift when it reaches its maximum lift coefficient. In contrast, the NREL S809 airfoil has a more gradual stall, which means that it can maintain lift at higher angles of attack before experiencing a drop in lift. both airfoils have different design characteristics that make them suitable for different applications. The NACA 4412 airfoil is better suited for low-speed applications, while the NREL S809 airfoil is designed for higher-speed applications, particularly in wind turbines.

The C_L and C_D values for the NREL S809 airfoil are taken from Sorensen ([24], while these values for the NACA 4412 airfoil are taken from Abbot [23]. When these values are used for NACA 4412; the design

AOA is 6° where the maximum value of C_L /C_D is obtained. The C_L value at this angle of attack (AOA) is 1.04. Similarly, for NREL S809, the design angle of attack (DAOA) is 5° while the design lift coefficient value is 0.76. The design tip speed ratio value was taken as 7, based on the study of Cosker [14].

Figure 5. HAWT picture produced by three-dimensional printer.

The turbine was mounted on the car as shown in Figure 2 and a system was installed to measure wind speed, wind direction, rotational speed and torque 5 times per second to ensure homogeneous airflow. The rotational speed was controlled by an electronic control system that braked the AS motor. The circuit diagram is shown in Figure 6. The vehicle was driven on a flat smooth road at a constant speed between 16 km/h and 54 km/h. The data obtained were analyzed with Microsoft Excel software.

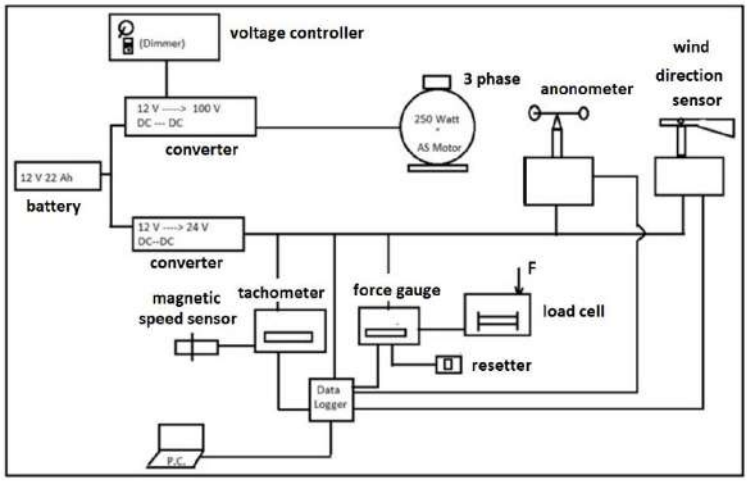

Figure 6. Circuit diagram of the experimental measurement system.

The pictures of the measuring instruments used in the experiment to measure the wind speed, rotor rotational speed (by number of revolutions) and torque (moment) values are shown in Figure 7. The blades rotating at a certain wind speed were braked by the AS motor to rotate at different angular speeds. For the torque values at different rotational speeds, the force values were first measured with a load cell. The measured force values were multiplied by the distance of 0.15 m, which is the length of the force arm in the system, and moment values were obtained.

Figure 7. Experimental measurement devices.

Wind speed was measured with an anemometer, the number of revolutions of the blades with a tachometer and torque values with a force gauge at different rotational speeds. The values found were recorded in the excel program on the computer with a data logger. The values recorded with the data logger were calibrated to convert volt values into numerical data and recorded on a laptop computer. Wind speed, wind direction, rotor speed and torque (momentum) values were recorded 5 times every second. In order to change the number of revolutions, braking was provided with AS motor. Based on the values measured at different times, torque values were measured at different speeds for cases where the wind speed was 6 m/s. TSR values were obtained using these values and angular velocity, speed and wind speed. For each different TSR values, the power was obtained by multiplying the torque value by the angular velocity ω. C_P power multiplier value was obtained by dividing the power values by the maximum power value. C_P-TSR values Table 2 and Table 3 was created for NACA 4412 and NREL S809 HAWT. $C_{P(max)}$ as well as OTSR values have been determined from this table.

3. Results and Discussions

The product of the torque (Nm) measured in the experiment and the angular rotational speed ω (rad/s) gives the power value (Watt). The maximum power of the wind flowing across the rotor section can be calculated by below equation;

$$P = \frac{1}{2}\rho V^3 \pi R^2$$

In this equation, the maximum power value of the air flowing across the turbine rotor section is calculated as 65.1 Watt when the air density ρ = 1.2 kg/m^3, V wind speed 6 m/sand R = 0.4 m. The power value obtained at the rotor is calculated as torque (T) Nm and angular velocity (ω) rad/s. Power obtained is calculated by using following equation;

$$P = T.\omega$$

Two HAWT vehicles with NACA 4412 and NREL S809 sections were measured at different rotational speeds and torque values by providing homogeneous wind. The number of revolutions per second is obtained by dividing the number of revolutions per minute by 60 and the angular velocity ω (rad/s) value is obtained by multiplying this number by 2π, and the wing tip tangential velocity is found by multiplying the ω value with R

= 0.4 m. The TSR (λ) value is calculated by dividing the wing tip tangential speed by the wind velocity V=6 m/s. The results obtained as a result of the measurement values and calculations are given in Table 2 and Table 3.

Table 2. NACA 4412 measured values

Number of revolutions (rpm)	ω (rad/s)	TSR(ƛ)	Torque (N.m)	Power(watt)
573	60.00	4	0.282	16.92
717	75.08	5	0.260	19.52
860	90.06	6	0.253	22.78
1003	105.03	7	0.248	26.05
1147	120.11	8	0.238	28.59
1290	135.09	9	0.173	23.37
1433	150.06	10	0.117	17.56
1576	165.04	11	0.071	11.72
1720	180.12	12	0.0325	5.85
1863	195.09	13	0.0267	5.21
2006	210.07	14	0.0217	4.56

With NACA 4412 HAWT, the maximum power was measured as 28.59 Watt at a rotationalspeed of 1147 rpm (ω=120.11 rad/s). As the TSR values increase from 4 to 8, the power value obtained also increases, but the power value starts to decrease after 8. The OTSR value of the HAWT designed with NACA 4412 and DTSR=7 was 8.

Table 3. NREL S809 measured values

Number of revolutions (rpm)	ω (rad/s)	TSR(λ)	Torque (N.m)	Power (Watt)
573	60.00	4	0.270	16.20
717	75.08	5	0.243	18.25
860	90.06	6	0.224	20.17
1003	105.03	7	0.211	22.16
1147	120.11	8	0.200	24.02
1290	135.09	9	0.188	25.40
1433	150.06	10	0.147	22.06
1576	165.04	11	0.130	21.45
1720	180.12	12	0.112	20.17
1863	195.09	13	0.067	13.07
2006	210.07	14	0.046	9.66

With NREL S809 HAWT, the maximum power was measured as 25.4 Watt at a rotational speed of 1290 rpm (ω=135.09 rad/s). As the TSR values increase from 4 to 9, the power value obtained also increases, but the power value starts to decrease after 9. The OTSR value of the HAWT. When the stance angle of the blade to the rotor is adjusted to facilitatethe first movement, the maximum rotational speed is lower than in the other case.

designed with NREL S809 and DTSR=7 was 9. However, in order to see the different results in the values obtained due to the effect of the road surface, slight differences in vehicle speed and errors in the measurements, measurements were made with 5 different experimental studies for both HAWT. After organizing the obtained data as given in Table 5 and Table 6, the power efficiency (C_P) values were calculated using the below equation. To calculate the rotor power efficiency value, below equation is used.

$$C_P = \frac{P}{\frac{1}{2}\rho A V^3}$$

C_P-TSR values and average values obtained in 5 separate experiments (E1, E2, E3, E4, E5) for the NACA 4412 cross-sectioned HAWT are shown in Table 4 and graphically in Figure 8.

Table 4. NACA 4412 Cp-TSR values

NACA 4412 C_P-TSR EXPERIMENTAL						
TSR	E1	E2	E3	E4	E5	Mean Values
4	0.25	0.24	0.26	0.3	0.27	0.264
5	0.3	0.34	0.32	0.28	0.33	0.314
6	0.32	0.31	0.34	0.37	0.39	0.346
7	0.45	0.41	0.39	0.42	0.4	0.414
8	0.47	0.42	0.43	0.46	0.42	0.44
9	0.39	0.37	0.36	0.42	0.43	0.394
10	0.24	0.29	0.28	0.25	0.32	0.276
11	0.17	0.15	0.17	0.19	0.22	0.18
12	0.13	0.06	0.08	0.1	0.12	0.098
13	0.08	0.06	0.11	0.1	0.07	0.084
14	0.05	0.09	0.06	0.04	0.08	0.064

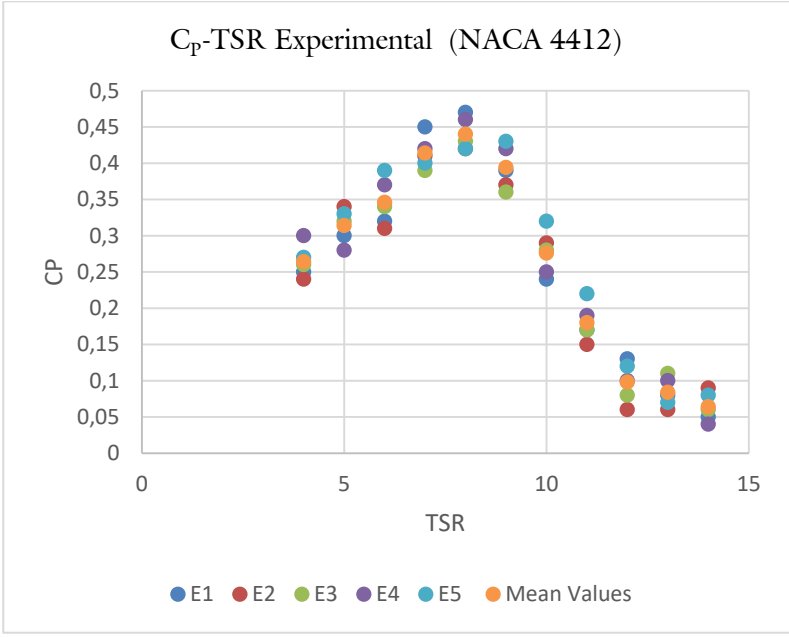

Figure 8. C_P-TSR(λ) values of NACA 4412 sectioned HAWT

Similarly, the C_P-TSR values and average values obtained in 5 separate experiments (E1, E2, E3, E4, E5) for NREL S809 cross-sectioned HAWT are shown in Table 5 and graphically in Figure 9.

Table 5. NREL S809 C_P-TSR(λ) values

NREL S809 C_P-TSR(λ) EXPERIMENTAL						
TSR	E1	E2	E3	E4	E5	Mean Values
4	0.22	0.25	0.24	0.25	0.27	0.246
5	0.29	0.28	0.25	0.28	0.25	0.27
6	0.33	0.29	0.32	0.31	0.33	0.316
7	0.35	0.33	0.34	0.34	0.3	0.332
8	0.34	0.36	0.37	0.36	0.35	0.356
9	0.34	0.39	0.38	0.36	0.35	0.364
10	0.33	0.34	0.34	0.35	0.36	0.344
11	0.34	0.33	0.33	0.3	0.32	0.324
12	0.26	0.25	0.31	0.3	0.33	0.29
13	0.18	0.22	0.2	0.21	0.22	0.206
14	0.17	0.16	0.15	0.15	0.13	0.152

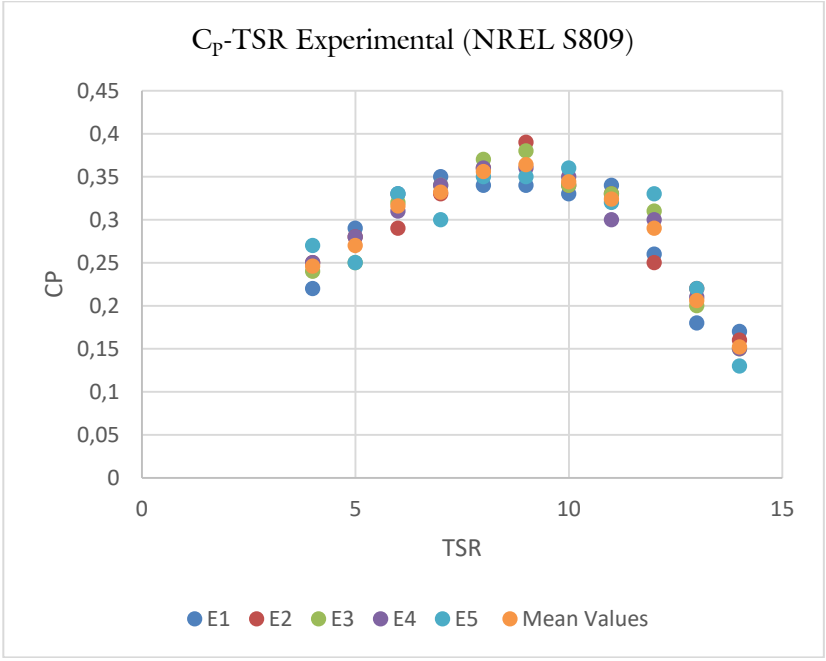

Figure 9. Cp-TSR(λ) values of NREL S809 sectioned HAWT

The graph given in Table 6 and Figure 10 is obtained according to the results obtained by averaging the C_P values of the HAWTs with both cross-sections obtained in experiments E1, E2, E3, E4, E5.

Table 6. NACA 4412 and NREL S809 Cp-TSR(λ) values

C_P-TSR(λ)	NACA	NREL
TSR	Mean Values	
4	0.264	0.246
5	0.314	0.27
6	0.346	0.316
7	0.414	0.332
8	0.44	0.356
9	0.394	0.364
10	0.276	0.344
11	0.18	0.324
12	0.098	0.29
13	0.084	0.206
14	0.064	0.152

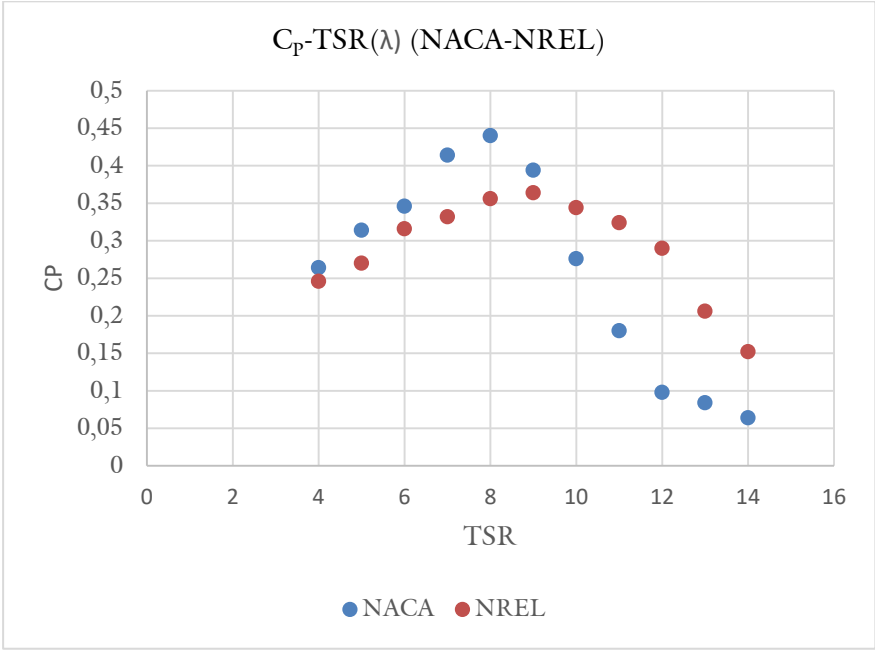

Figure 10. Compare NACA 4412 and NREL S809 HAWT C_P-TSR(λ).

According to the C_P-TSR graph obtained here, it is seen that although the performances of both are close to each other at TSR(λ) values less than 7, higher power efficiency is obtained with NACA 4412. While the highest power efficiency value was 0.44 with NACA 4412, this value was only 0.364 with NREL S809. However, at TSR(λ) values greater than 9, the values obtained with NREL S809 are larger. This situation is more clearly seen in Figure 10. The result obtained in this study may be because of the horizontal axis wind turbine blade root region stall and centrifugal pumping of flow on the blade [3].

Another situation noticed in this experimental study is that when the stance angle of the blade relative to the rotor is adjusted so that the maximum rotational speed is high, the first movement starts later. When the stance angle of the blade to the rotor is adjusted to facilitate the first movement, the maximum rotational speed is lower than in the other case.

4. Conclusion

In the experimental studies, it was observed that when the angle of the blade with the rotor plane was slightly increased, the initial movement

started more easily, but it caused lower values in terms of obtaining maximum torque. A higher maximum power multiplier value was obtained with NACA 4412. However, higher power multiplier values were obtained with NREL S809 at TSR values greater than 9. As a result of the experimental study for NACA 4412 HAWT, the OTSR value was measured as 8. With NREL S809, the OTSR value was obtained as 9.

The experimental method used in this study is not a commonly used method for studying wind turbine performance. In order to obtain more reliable or accurate results, those methods such as field measurements, wind tunnel testing, or numerical simulations using validated models may be used to determine the power performance of horizontal axis wind turbines. We should say here that the method used in this study is very successful in terms of obtaining steady and uniform artificial wind, as well as many weak aspects.

To compare the power performance of two different horizontal axis wind turbines (HAWTs) with different airfoils, an experimental setup can be created in a wind tunnel. The following steps can be followed for this experiment:

1. Design and build two identical HAWTs, with the only difference being the airfoil shape. It is important to ensure that the two turbines have the same blade length, number of blades, pitch angle, and rotor diameter to ensure a fair comparison.

2. Install the two turbines in a wind tunnel, which provides a controlled environment with a steady and uniform wind flow. The wind tunnel should have a velocity range that is appropriate for the size of the turbines and airfoils being tested.

3. Connect each turbine to a power meter or dynamometer that can measure the torque of the turbine. Start the wind tunnel and adjust the wind velocity to the desired level. It is important to ensure that the wind velocity is steady and uniform across the test section of the wind tunnel.

4. Run the experiment for a predetermined amount of time, allowing the turbines to reach a steady-state condition. This will ensure that the power output measurements are accurate and repeatable.

5. Repeat this experiment at the different rotational speed of the rotor. Record the power output measurements for both turbines, and compare the results.

6. The airfoil that produces the higher power output at a given wind velocity or at a given tip speed ratio is considered to have better power performance. Repeat the experiment multiple times to ensure the reliability and repeatability of the results.

References

[1] Spera. D.A. "Wind Turbine Technology second ed.", ASME Press. New York (2009).

[2] Hau. E. "Wind Turbines Fundamentals, Technologies, Application", Economics second ed. Trans: H.Von Renouard. Springer. Hardcover (2005).

[3] Hansen. M. O. L. "Aerodynamics of Wind Turbines", 2nd ed. Earthscan. London. Sterling. VA. USA. 7-78 (2008).

[4] Bai. C. J. Hsiao. F. B. Li. M. H. Huang. G. Y. and Chen. Y. J. "Design of 10 kW horizontal-axis wind turbine (HAWT) blade and aerodynamic investigation using numerical simulation", 7th Asian-Pacific Conference on Aerospace Technology and Science. 7th APCATS (2013).

[5] Wang. T. Wang. L. Zhong. W. Xu. B. and Chen. L. "Large-scale wind turbine bladedesign and aerodynamic analysis", Chinese Science Bulletin (2012).

[6] Tangler. J. L. and Somers. D.M. "NREL airfoil families for HAWT's", Proc. WINDPOWER'95. Washington D.C. 117-123 (1995).

[7] Gundoft. S. "Wind Turbines", University Collage of Aarhus Denmark. Copyright (2009).

[8] Burton. T. Jenkins N. Sharpe D. Bossanyi. E. "Wind Energy Handbook". 2nd ed. John Wiley & Sons. Ltd. England. 41-184 (2011).

[9] Manwell J.F. Mc. Gowan. J.G. Rogers. A.L. "Wind energy explained; theory, design and application" 2nd ed.". John Wiley and Sons Ltd. publication. Chichester. 90-141 (2009).

[10] Ragheb. M. "Optimal Rotor Tip Speed Ratio" USA University of Illinois at Urbana-Champaign (2014).

[11] Diveux. T. Sebastian. P. Bernard. D. and Puiggali. J. R. "Horizontal axis wind turbine systems: Optimization using genetic algorithms." Wind Energy. 4(4): 151-171 (2002). [1]

[12] Anderson John D. "Fundementals of Aerodynamics", Third Edition, McGraw-Hill Book Company. New York. USA. 331-332 (2001).

[13] Gash. R. Twele J. "Wind power plans. Fundamentals, design, construction and operation", James and Janes, (2005).

[14] Cosker. Mc. J.. "Design and optimization of a small wind turbine", Requirements for MSc of mechanical engineering, Master's Thesis. Rensselaer Polytechnic Institute Hartford. Connecticut. USA (2012).

[15] Rashid. A. "An adaptive neuro-fuzzy inference system approach for prediction of power factor in wind turbines", Journal of Electrical & Electronics Engineering. 9(1): 905 -912. (2009).

[16] Bai. C. J. Hsiao. F. B. Li. M. H. Huang. G. Y. and Chen. Y. J. "Design of 10 kW horizontal-axis wind turbine (HAWT) blade and aerodynamic investigation using numerical simulation", 7th Asian-Pacific Conference on Aerospace Technology and Science. 7th APCATS (2013).

[17] Cao. H. "Aerodynamics analysis of small horizontal axis wind turbine blades by using 2D and 3D CFD modelling", Requirements for MSc of The School of Computing, Master's Thesis, Engineering and Physical Sciences, University of Central Lancashire. England (2011).

[18] Azevedo. J. and Mendoncha F. "Small Scale Wind Energy Harvesting with Maximum Power Tracking Funchal", Portugal Centre for Exact Science and Engineering, University of Madeira (2015).

[19] Wang. T. Wang. L. Zhong. W. Xu. B. and Chen. L. "Large-scale wind turbine blade design and aerodynamic analysis", Chinese Science Bulletin (2012).

[20] Padmanabhan. K. K. and Saravanan. R., "Study of the performance and robustness of NREL and NACA blade for wind turbine applications", European Journal of Scientific Research 440-6 (2012).

[21] Boorsma. K. Schepers. J. "Description of experimental setup MEXICO measurements", Technical Report, ECN-X09-0XX; ECN: Petten. The Netherlands (2003).

[22] Burton.T.. Jenkins. N. Sharpe. D. Bossanyi. E. "Wind Energy Handbook", second ed.John Wiley and Sons. Ltd. Chichester (2011).

[23] Abbot. I. H. Von D. A. E. "Theory of wing sections including a summary of airfoildata" New York, Dover publication (1959).

[24] Bertagnolio. F. Sorensen. N. Johansen. J. Fuglsang. P. "Wind turbine airfoil catalogue", Riso National Laboratory, Roskilde (2001).

[25] Internet: UIUC Airfoil Coordinates Database

[26] http:/aerospace.illinois.edu/mselig/ads/coord_database.html (2016).

[27] Pope, A. and Burton, D. "Wind Tunnel Testing for Buildings and Other Structures", John Wiley & Sons, Chichester, (1999).

[28] Burton, T., Sharpe, D., Jenkins, N., and Bossanyi, E., "Wind Energy Handbook", 2nd Edition. Wiley, Chichester, (2011).

[29] Snel, H., Schepers, J.G., and Montgomerie, B. "Wind turbine rotor aerodynamics and aeroelasticity – a simulation approach", Journal of Wind Engineering and Industrial Aerodynamics, 90(8), 923-939. (2002).

[30] Sørensen, N.N. and Mygind, L. "Airfoils for Wind Turbine Applications", Risø National Laboratory, Roskilde, (2001).

Chapter 4

Investigation of Turbulence Models in the Analysis of Two Different Airfoils with Computational Fluid

Mehmet Bakırcı[1]

Abstract

Various standard airfoils are used in aviation, wind turbine blade designs, and for other applications that rely on aerodynamic forces. The rapid evolution of computing methods now allows you to accurately calculate the flow behavior of the airfoil in the short term. In this study, the aerodynamic performance of the NACA 63-215 and NACA 65-421 standard airfoils created by the National Aeronautics Advisory Committee (NACA) was analysed with two-dimensional computational fluid dynamics. These analyses were performed on a 1×10^6 Reynolds number and at different attack angles to discover better aerodynamic performance. Spalart-Allmaras, the standard k-ε and standard k-ω turbulence models are evaluated comparatively based on experimental data. Finally, the results and comparison of various properties i.e., drag and lift coefficients, pressure distribution over the airfoils are presented to help the user choose the right airfoil, and the turbulence model for a wing design or other aerodynamic modelling corresponds.

1. Introduction

Airfoil aerodynamics is a global field of study that has made a significant contribution to the growth of the wing and propeller industries. Airfoils and aerodynamically formed objects are widely utilized in a variety of aerial vehicles, including the aircraft, airplanes, helicopters and even rocket missiles. With regard to fluid machines like turbines, windmills, and pumps, the impeller and propeller shapes are particularly important. All of the critical parameters for representing the characteristics of the airfoils must be precisely regulated. This is due to the importance of flow analysis across an airfoil [1].

The aerodynamic performance of the airfoil is important for many applications. For example, aircraft aerodynamic performance affects factors

[1] Karabuk University Mechanical Engineering mehmetbakirci@karabuk.edu.tr

https://doi.org/10.58830/ozgur.pub130.c541

such as aircraft speed, range, and fuel economy. The aerodynamic performance of wind turbines affects the amount of energy produced by the turbines. The aerodynamic performance of vehicles affects fuel consumption and emissions [1].

Airfoil sections are designed to optimize aerodynamic performance. This helps create less resistance and produce more thrust or lift when moving over air or water. Airfoil sections can be designed at many different scales. This allows them to be used in different applications. For example, large-sized airfoil sections can be used for aircraft wings, while small-sized airfoil sections can be used for aircraft engine turbine blades. They are used in many areas in engineering designs. For instance, airfoil sections are used in the design of aircraft parts such as aircraft wings and horizontal stabilizers and are designed to optimize the airplane's effect on airflow. They are used in the design of wind turbine blades. They are also used in wind turbine blades to generate electrical energy by making more rotational movement under the influence of the wind. Airfoil sections are used in the design of vehicles in the automotive industry. In order to optimize the aerodynamic performance of the vehicles, they are utilized in the design of various vehicle parts such as windshield, rear glass, and rear spoiler. Additionally, airfoil sections are used in ship design. In the structure of the rudders positioned at the stern of the ship and on the sides of the deck. In order to reduce the effect of wind loads, especially for tall buildings, airfoil sections can be used in structural elements of buildings. As can be seen from these examples, airfoil sections are used in many engineering designs. The design and their use help to increase aerodynamic performance and to design more efficient systems. Airfoil sections can be produced from different materials. These materials can be chosen depending on the application's requirements and performance goals. Airfoil sections generally have smooth surfaces. This helps create less resistance and produce more thrust or lift when moving over air or water [1].

The moment coefficient of the airfoil is an important factor that measures the tendency of the flow around the airfoil to produce moment. It complements the aerodynamic properties of the airfoil, along with other coefficients such as torque coefficient, lift coefficient and drag coefficient. It is important as one of the factors affecting the aerodynamic performance of the airfoil, because the moment coefficient of the airfoil determines the aerodynamic moments that affect the balance and control properties of the airfoil. This affects the airfoil's horizontal stability and vertical control ability, roll moment, and other properties. It depends on factors such as

the size and shape of the airfoil, the angle of attack, and the Reynolds number. Moment coefficients help determine the stability and control characteristics of aircraft. Airfoil moment coefficients are also used in ship propeller design and many other applications. The stability performance of the airfoil depends on the aerodynamic moment coefficients of the airfoil and other factors and determines how the airfoil responds to changes in angle of attack or other external influences [2].

Previously, research on airfoil aerodynamics was limited to field testing, theoretical studies, and wind tunnel testing, all of which require significant work and money. Aerodynamic performance of airfoil sections might be evaluated using the finite element technique (FEM) used in computational fluid dynamics (CFD) for fluid flows, which has led to the creation of computer-assisted design programs. Numerical approaches for performance analysis and optimal design of an airfoil save money and time when compared to theoretical and experimental methods [3].

In general, airfoils are designed using one of two methods: First, make some tweaks to the real airfoils and repeat the procedure until improved performance is obtained. Second, identify the pressure coefficient distribution that will provide the desired aerodynamic performance and obtain the geometry that will produce this distribution. The National Advisory Committee on Aeronautics (NACA) performed an extensive variety of studies and tests on airfoil design. As a result, they developed their own standard airfoil section geometry series [2].

The NACA airfoil series, which is being used today, was created for World War II warplanes. The literature continues to investigate airfoils. Many researchers looked at the lift and drag presentation of NACA airfoils. To date, the following studies have been presented. S. Sarada et al. (2010) [4] used the ANSYS Fluent CFD tool to examine the NACA 64618 airfoil in 2D and 3D. They employed the k-epsilon turbulence model. With this model, they captured respectable values for the stall moment in 3D but not the same in 2D. A. Saraf et al. (2013) [5] investigated the aerodynamics of the NACA 4412 section using CFD and conventional k-epsilon and k-omega turbulence models. While they obtained comparable findings with studies at low attack angles by utilizing k-omega, the results at high angles were different with both models. D. Hartwanger and Dr. A. Horvat (2008) [6] used CFD, X-FOIL, and ANSYS CFX computer package tools to study the NREL S809 wind turbine blade section (airfoil). He performed a 2D flow study, employing laminar flow for the first half of the airfoil and turbulence for the rest. He demonstrated that the new model's conclusions were completely consistent with the experiments for the

circumstances prior to the stall. He did, however, state that the data obtained during and after the stall were incompatible with the trials. The lift and drag coefficients of the NACA 4412 airfoil were computed using CFD by H. C. Ravi et al. (2013) [7]. They picked the k-omega SST transition turbulence model to take into account the change of flow over an airfoil from laminar to turbulence and compared the findings produced by this model with the results obtained by the Spalart-Allmaras model and tests. They discovered concordance between both models and experiments at the end of the research. The mesh is the collection of small elements used to represent the fluid domain in the simulation.

E.C. Douvi et al. (2012) [8] evaluated turbulence models for modeling of flow over the NACA 0012 airfoil. J. Johansen (1997) [9] investigated the laminar/turbulent transition in airfoil flows. The numerical calculation of turbulent flows was emphasized by B.E. Launder and D. B. Spalding (1974) [10]. O. Gulzar et al. (2014) [11] used the Spalart-Allmaras turbulence model to simulate the effect of attack angle modification on the NACA 7420 airfoil in transonic compressible flow. NACA 4412 and NREL S 809 airfoils were compared by B.N. Kumar et al. (2016) [12]. The comparison of the NACA 4412 airfoil with the S 809 airfoil revealed that the NACA 4412 had superior aerodynamic performance over the whole spectrum of angles of attack. O. Badran (2008)[13] investigated a two-equation turbulence model that may forecast boundary layer separation on a NACA 4412 airfoil at a position of $\alpha=15°$. The developed turbulence model was proven to be capable of predicting the physics of unstable separated flow. The models provided results that were very close to the experimental data. G.E. Hassan et al. (2014) [14] determined the lift and drag coefficients of the NACA 0018 airfoil for angles of attack (α) between 0^o and 25^o and Reynolds numbers from 300 000 to 1 000 000. When compared to experimental data in the literature for all tested ranges of Re values, the k– ω SST model yields the best correct predictions for lift coefficient (C_L) and drag coefficient (C_D).

The quality of the mesh can have a significant impact on the accuracy and reliability of the simulation results. Therefore, much research is focused on developing new methods to improve mesh quality. There are many different turbulence models, each with its own set of assumptions and limitations. Current studies in airfoil aerodynamics are focused on developing and refining turbulence models to improve their accuracy and reduce the computational cost of simulations. airfoil aerodynamics is a rapidly advancing field, with many exciting new developments and research opportunities [15].

In this work, two different National Advisory Committee on Aeronautics (NACA) airfoils, NACA 63-215 and NACA 65-421, are chosen for modeling of the flow field and the various turbulence models; Spalart-Allmaras, standard k-ε, and standard k-ω are used to obtain the aerodynamic coefficients. The results from the three different turbulence models are compared to reliable experimental results [16].

2. Mathematical Model

2.1. Flow Over an Airfoil

Airfoils are specially designed geometries that extract maximum lift while minimizing drag forces during air intake. These forces are generated by an airfoil due to pressure differences between its upper and lower surfaces. Drag is defined as the force exerted on an object in the flow direction. And the lift force may be expressed as a compound force that is vertical to the flow direction. Figure 1 describes the lift force, drag force and moment that occur around an airfoil section as a function of air speed [2].

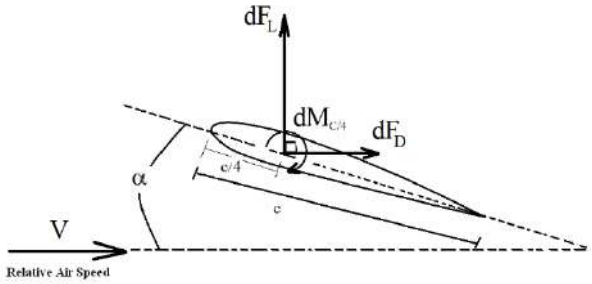

Figure 1. The factors on an airfoil.

When pressure (P) and shear (τ) forces apply on a differential surface area (dA), the differential lift and drag forces acting on dA are as follows:

$$dF_L = PdA\sin\theta - \tau dA\cos\theta \quad (1)$$

$$dF_D = PdA\cos\theta + \tau dA\sin\theta \quad (2)$$

From Eqns. 3 and 4 we can calculate the lift and drag coefficients that occur,

$$C_L = \frac{dF_L}{\frac{1}{2}\rho V^2 cdr} \quad (3)$$

$$C_D = \frac{dF_D}{\frac{1}{2}\rho V^2 c dr} \quad (4)$$

$$C_M = \frac{dM}{\frac{1}{2}\rho V^2 c^2 dr} \quad (5)$$

Where the variables are shown in Table 1.

Table 1. Nomenclatures of Eqns. 3, 4.

Symbol	Name	Unit
C_L	*coefficient of lift*	-
C_D	*coefficient of drag*	-
dF_L	*partial lift force*	N
dF_D	*partial drag force*	N
dM	*partial moment*	Nm
V	*wind speed*	m/sec
c	*chord*	m
dr	*partial width of the blade element*	m

As the airflow passes over an airfoil, the speeds of the air molecules change. Since the upper surface is humped, the speed increases when passing over it and decreases when passing over the lower surface. While the static pressure increases on the lower surface where the velocity decreases, it decreases on the upper surface where the velocity increases. This pressure difference, which occurs on the lower and upper surfaces of the airfoil, causes the lift force [2].

The lifting phenomena may also be described using the Bernoulli equation. Based on Bernoulli's equation, pressure rises as flow velocity falls in an incompressible steady-state flow, and vice versa. So, we can observe that when the air goes over the airfoil, the velocity increases as it flows from the leading edge to the top surface, decreasing the pressure in that region. On the other hand, when air flows through the bottom of the airfoil, pressure rises even while velocity falls. Upward positive pressure is the most important factor in creating lift [2].

When a moving liquid separates from a body, a separated region forms between the object and the air flow. The split region is a low-pressure area behind the body that is subject to re-circulation and back-flows. The size of the separated field determines the drag force. The word "wake" refers to a

flow region trailing the body where the velocity impacts of the body may be sensed. Vortexes in the wake creates drag by creating negative pressure in the area. Wake does not occur with bluff bodies. Wake may arise in an aerodynamic body. This angle of attack is slightly larger than 15 degrees for most airfoils. This is known as a stalling point (Fig 2.)[2].

The stability of the airfoil is calculated by determining the aerodynamic moment coefficients and the aerodynamic center position. Aerodynamic moment coefficients measure the tendency of the flow around the airfoil to produce moment (torque), while the aerodynamic center position is the point where the aerodynamic moment coefficients of the airfoil change according to the lift coefficient change. Stability performance is measured by two types of stability: static stability and dynamic stability. While static stability measures the airfoil's response to changes in angle of attack, dynamic stability measures how the airfoil behaves in a moving environment. The stability performance of the airfoil depends on the aerodynamic moment coefficients, aerodynamic center position and other factors. These factors depend on various parameters such as the size and shape of the airfoil, angle of attack and Reynolds number. The stability performance of the airfoil is important in aircraft design and many other applications because it is an important factor determining the safety and control characteristics of the airfoil [2].

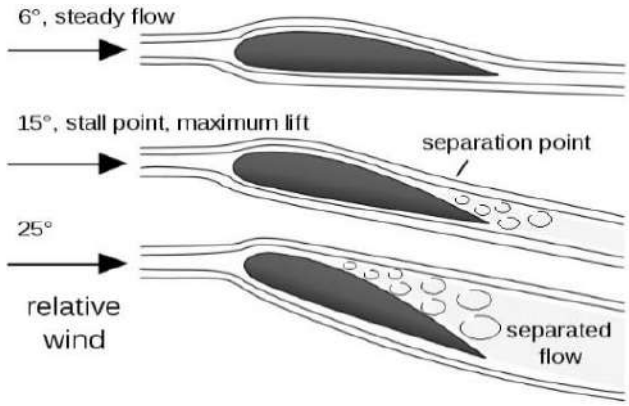

Figure 2. Flow separation on an airfoil.[2]

The curves of the airfoils drawn by the standard coordinates which the study uses, NACA 63-215 and NACA 65-421 are shown in Figures 3 and 4. [16]

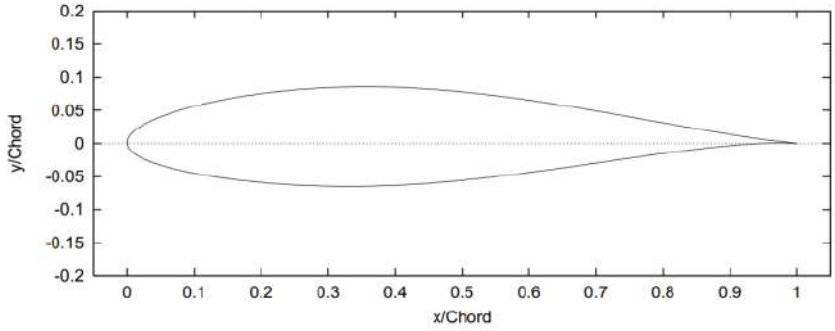

Figure 3. The airfoil section curve of NACA 63-215.

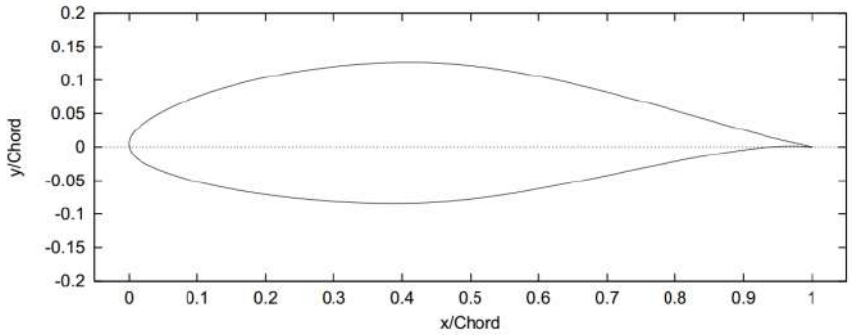

Figure 4. The airfoil section curve of NACA 65-421.

NACA airfoil designation provides information about the key geometric features of the airfoil, including the maximum camber and thickness, which is useful in aerodynamics analysis and design. For the case of NACA, NACA 63-215 and NACA 65-421, the numbers "63" and “65” respectively refer to the location of the maximum camber in percentage of the chord length (63% and 65% from the leading edge) while the numbers "2" and “4” respectively refer to the maximum camber in percentage of the chord length (2% and 4% of the chord length). The numbers “15” and "21" respectively refer to the maximum thickness of the airfoil in percentage of the chord length (15% and 21% of the chord length) [1].

The NACA 63-215 and NACA 65-421 airfoils are primarily designed for subsonic flow applications, which means they are most suitable for vehicles that operate at relatively low speeds, such as general aviation aircraft, drones, and small wind turbines.

2.2. Computational Fluid Dynamics (CFD)

Airfoil (airfoil profile) can be examined with CFD analyses to determine its aerodynamic performance. During the analysis, the following issues can be examined; The flow field around the airfoil can be studied in detail by CFD analysis. This analysis is performed by considering variables such as airflow rate, pressure, temperature and other flow characteristics. The pressure distribution on the airfoil can be calculated in detail by CFD analysis. This provides information on the aerodynamic performance of the airfoil and can be used to optimize it. The frictional forces on the airfoil can be calculated by CFD analysis which is important for understanding the factors that affect the resistance of the airfoil and its aerodynamic performance. The lift coefficient of the airfoil can be calculated by CFD analysis which is crucial for determining the aerodynamic performance of the airfoil and can help optimize the design of the airfoil. The aerodynamic noise around the airfoil can be calculated by CFD analysis. This is important for making design changes to reduce noise on airplanes. CFD analysis of the airfoil is important for understanding and optimizing the aerodynamic performance of the airfoil. These analyses are used in aircraft design, wind turbines, vehicle design and many other applications [3].

Reynolds Averaged Navier-Stokes (RANS), Large Eddy Simulation (LES), Detached Eddy Simulation (DES) and Direct Numerical Simulation (DNS) models used in computational fluid dynamics are designed for simulation of different flow events. RANS approaches model turbulence behavior by averaging over time, providing accurate results on the average flow behavior. However, these models cannot model natural turbulence events and there is a possibility of serious error. Therefore, they are mostly used in industrial applications. LES models accurately capture large-scale turbulent structures and model small-scale structures. Therefore, LES models are used to simulate natural turbulence events. However, these models are generally used in a limited number of research applications due to their high computational cost. DES models are a combination of RANS and LES models. Models employ the LES method to capture large-scle structures and the RANS method to model small-scale structures. Therefore, DES models provide more accurate results for industrial applications. DNS models resolve all scales of the flow. Hence, DNS models provide the most accurate results. However, these models are the most computationally costly and are used only in small-scale research applications. Therefore, the selection of the right turbulence model depends on the nature of the simulated flow event, accuracy and computational cost. Industrial applications often use RANS or DES models, while research applications may use LES or DNS models [17].

Turbulence models used in computational fluid dynamics (CFD) applications are essential to accurately predict fluid motion. Different turbulence models try to model the effect of turbulence using different approaches. Simpler models often come with less computational costs, but are less accurate. More complex models tend to produce more accurate results, but the computational cost may be higher. Some models are only suitable for certain types of flows, while others can be used for a wider range. Whether the models are compatible with experimental data can also be a comparison criterion [18].

Turbulence models used in computational fluid dynamics (CFD) simulations provide solutions by mathematically modelling the turbulent motion of fluids. The k-epsilon, k-omega and Spalart-Allmaras models are three different turbulence models frequently used in CFD. The k-epsilon model is used to calculate the balance between turbulent kinetic energy (k) and dissipated energy (epsilon). This model gives good results in smooth flows and adiabatic walls, but it may not be accurate in pressurized surfaces and high sections. The k-omega model was developed to overcome the disadvantages of the k-epsilon model. This model requires less computation than the k-epsilon model and gives better results at low Reynolds number flows. However, it may not give accurate results on pressurized surfaces. The Spalart-Allmaras model is used to determine the viscosity of turbulent flow. This model gives good results at high Reynolds number flows and pressure surfaces. It also requires fewer iterations than other models. However, it cannot give accurate results in various flow conditions, such as turns in flow. As a result, each turbulence model offers advantages and disadvantages in different flow conditions. To obtain accurate results, the turbulence model to be applied should be chosen according to the characteristics of the flow, the Reynolds number, and the purposes of the analysis [19, 20].

The k-epsilon turbulence model is a turbulence model frequently used in CFD simulations and has various sub-models. The most common sub models are: Standard k-epsilon model: This model is used to calculate the balance between turbulent kinetic energy (k) and dissipated energy (epsilon). It performs well in smooth flow conditions, but may give inaccurate results on pressurized surfaces and high cross sections. Realizable k-epsilon model: This model was developed to overcome the disadvantages of the standard k-epsilon model. The realizable k-epsilon model uses a realistic set of equations to calculate the Reynolds stress tensor. This model gives more accurate results on pressurized surfaces and high sections. RNG k-epsilon model: This model was developed by

Richardson and Nicoud and uses the balance between turbulent kinetic energy (k) and dissipated energy (epsilon) instead of directly calculating the Reynolds stress tensor. This model gives good results for high Reynolds number flows and complex geometries. Nonlinear k-epsilon model: This model uses a nonlinear set of equations to calculate the balance between turbulent kinetic energy (k) and dissipated energy (epsilon). This model gives more accurate results on pressurized surfaces and high sections.

These sub models include different approaches to turbulence kinetics and offer different mathematical solutions to better adapt to different flow conditions [21] .

The k-omega turbulence model is a turbulence model used to calculate the relationship between turbulent kinetics and turbulent viscosity. The most common sub models of this model are: Standard k-omega model: This model uses a transport equation to calculate turbulent viscosity and defines a new variable called omega as a function of turbulent kinetics. It performs well in smooth flow conditions, but may give inaccurate results on pressurized surfaces and high cross sections. SST (Shear Stress Transport) k-omega model: This model was developed to overcome the disadvantages of the standard k-omega model. The SST k-omega model gives better results than the standard k-omega model under smooth flow conditions and gives more accurate results on pressurized surfaces and high sections. BSL (Baldwin-Lomax) k-omega model: This model was developed to perform better at low Reynolds number flows. The BSL k-omega model gives better results than the standard k-omega model on pressurized surfaces and high sections. These sub models use different mathematical equations for the calculation of turbulent viscosity and offer different approaches to better adapt to different flow conditions [22].

The Spalart-Allmaras (SA) turbulence model is a single-equation turbulence model and uses a single variable, turbulent viscosity, rather than turbulence kinetics. There are no sub models of the SA model. However, modifications and updates of the SA model are in progress. For example, the Spalart-Allmaras-DDES (Detached-Eddy Simulation) model is a model developed based on the SA model. This model performs better in simulating high Reynolds number flows and gives more accurate results due to the combination of the turbulence model and the eddy-viscosity model. Similarly, the Spalart-Allmaras-IDDES (Improved Detached-Eddy Simulation) model is an improved version of the SA model and gives more accurate results in simulating high Reynolds number flows [23].

When choosing turbulence models, some factors should be taken into account in order for the calculations to give accurate results and reflect the flow behaviors observed in real life. Pressurized or unpressurized flow, turbulence level and Reynolds number play an important role in turbulence model selection. According to the purpose of the calculations, the choice of turbulence model may vary. For example, RANS models can be used if the flow needs to be examined in detail, while LES or DNS models can be preferred for highly turbulent flows. Sufficient data for the geometry or flow to be calculated is important in turbulence model selection. For example, some turbulence models may require smooth geometry. The accuracy of turbulence models is important so that calculations give accurate results and reflect real-life flow behavior. Therefore, the accuracy of the turbulence model should be compared with the data in the literature and its suitability should be tested. Some turbulence models give more accurate results by increasing the computation time, while others require less computation time but give less accurate results. Considering these factors, turbulence model selection should be made. Also, by comparing the results of different turbulence models, it can be determined which model is the most suitable [24].

Experiments, theoretical formulae, or CFD can be used to compute the occurrence of aerodynamic force coefficient values as they flow across an airfoil. Because of the exceptions based on theoretical calculations, the obtained numbers are only approximations. Experiments can produce more reliable findings; however, the flow separation of stall moments reduces dependability [25].

CFD, on the other hand, provides rapid and consistent results for the force and coefficient values that occur around an airfoil. However, the flow physics, cell formation mechanism, and selection of the appropriate turbulence model all have a direct impact on the accuracy of the results [26, 27].

Many commercial CFD software packages are used in engineering. The primary simulation procedure is the same regardless of the type of CFD software utilized. Setting up governing equations is a prerequisite for CFD modelling; the three fundamental governing equations are mass, momentum and energy conservation equations. Following that, boundary conditions are defined based on various flow circumstances, and a mesh is formed. The meshing model's objective is to discretize equations and boundary conditions into a single cell. A cell is the fundamental building block of both organized and unstructured networks. While tetrahedral and pentahedral cells are often employed in unstructured grids, hexahedral cells

are utilized in organized grids. The mesh quality is necessary for obtaining appropriate physical solutions, and it is up to the engineer's competence. The more nodes in the mesh, the longer it takes to solve the aerodynamic issue, hence, developing an efficient mesh is critical [18].

CFD is a mathematical model based on Euler or Navier-Stocks that provides a consistent and physically accurate simulation of the flow field and may naturally be used to solve the complicated flow over an airfoil. The simulation approach of Reynolds-Averaged Navier-Stokes (RANS) is widely employed [17].

Two dimensional Navier Stokes equations include one continuity (Eqn. 5) and two momentum conservation (Eqns. 6, 7) equations:

$$\frac{\partial u}{\partial x} + \frac{\partial v}{\partial y} = 0 \tag{5}$$

$$\rho u\frac{\partial u}{\partial x} + \rho v\frac{\partial u}{\partial y} = \frac{\partial p}{\partial x} + \frac{\partial}{\partial y}\left[\mu\left(\frac{\partial v}{\partial x} + \frac{\partial u}{\partial y}\right)\right] + \frac{\partial}{\partial x}\left(-\rho\overline{u'v'}\right) \tag{6}$$

$$\rho u\frac{\partial v}{\partial x} + \rho v\frac{\partial v}{\partial y} = \frac{\partial p}{\partial y} + \frac{\partial}{\partial x}\left[\mu\left(\frac{\partial v}{\partial x} + \frac{\partial u}{\partial y}\right)\right] + \frac{\partial}{\partial y}\left(-\rho\overline{u'v'}\right) \tag{7}$$

While the right side of the equation expresses average body force and divergence stress, the left side of the equation explains the change in mean momentum. In these equations, u and v define velocity components in the x and y directions, respectively, p represents pressure, μ dynamic viscosity, ρ fluid density, and u' and v' represent horizontal and vertical turbulence speed deviation. -ρu'v' is turbulent shear stress, denoted as τ_{xy} and derived using the Eqn. 8 formula:

$$\tau_{xy} = -\rho\overline{u'v'} = \eta\left(\frac{\partial u}{\partial y} + \frac{\partial v}{\partial x}\right) \tag{8}$$

Where η is called turbulence viscosity, and many turbulence models have been created to determine it (Anderson J. D., 1995) [3]. Because RANS equations are open owing to the inclusion of a stress factor, a turbulence model is required to generate a closed system of a solvable solution. Many turbulence models are employed today, including algebraic, single-equation, two-equation, and Reynolds stress models. The majority of turbulence models used are Spalart-Allmaras turbulence, k-ε turbulence and k-ω turbulence models. There is no single optimum turbulence model

that applies to all flows. If required, the results acquired using multiple models for the same flow should be compared, especially with low wind speeds (Mach number<<1) at attack angles before stall since found result values are quite near to each other [28].

2.2.1 The Spalart-Allmaras turbulence model

The Spalart-Allmaras turbulence model is a one-equation model that solves a modelled transport equation with kinematic eddy (turbulent) viscosity (1992). It was developed particularly for aerospace applications having especially wall-bounded flows, and it has been demonstrated to provide appropriate results for boundary layers subjected to unfavorable pressure gradients. It's also becoming more popular in turbomachinery. In its original form, it is simply a low-Reynolds number model that necessitates precise resolution of the viscous-affected portion of the boundary layer. The gradients of the conveyed variable in the model are significantly less than those in the k-ε or k-ω models. The transport equation of the Spalart-Allmaras turbulence model can be stated in the operational parameter v~, as shown below [20]:

$$\frac{D\tilde{v}}{Dt} = c_{b1}(1-f_{t2})\tilde{S}\tilde{v} + \frac{1}{\sigma}\left[\nabla.\left((v+\tilde{v})\right)\nabla\tilde{v} + c_{b2}(\nabla\tilde{v})^2\right] - \left(c_{w1}f_w - \frac{c_{b1}}{K^2}f_{t2}\right)\left(\frac{\tilde{v}}{d}\right) + f_{t1}\Delta U^2 \qquad (9)$$

Sutherland's (1893) method is used to compute v, which is the chemical viscosity. The four words on the right-hand side are, in order, production, diffusion, dissipation, and transformation. Individual components of the production term are as follows: (2021):

$$f_w = \frac{\tilde{v}}{\tilde{S}k^2d^2}\left[1 + C_{w2}\left(\left(\frac{\tilde{v}}{\tilde{S}k^2d^2}\right)^5 - 1\right)\right](1 + C_{w3}^6)^{1/6}\left\{\left[1 + C_{w2}\left(\left(\frac{\tilde{v}}{\tilde{S}k^2d^2}\right)^5 - 1\right)\right]^6 + C_{w3}^6\right\}^{-1/6} \qquad (10)$$

$$f_{t1} = C_{t1}g_t \exp\left[-C_{t2}\frac{\omega_t^2}{\Delta U^2}(d^2 + g_t^2 d_t^2)\right], f_{t2} = C_{t3}\exp\left[-C_{t4}\left(\tilde{v}/v\right)^2\right] \qquad (11)$$

In these equations, S is the value of the vorticity, d is the distance to the closest wall, d_t is the distance from the point in the flow field to the trip on

the wall, ω_t is the wall vorticity at the trip, ΔU is the difference between velocity at the field point and that at the trip, $g_t = min\ (0.1,\ \Delta U/\omega_t \Delta x_t)$ where Δx_t is the grid spacing along the wall at the trip.

The empirical constants in the Spalart-Allmaras model are: $C_{b1} = 0.1355$, $\sigma = 2/3$, $C_{b2} = 0.622$, $k = 0.4187$,

$C_{w1} = 3.239$, $C_{w2} = 0.3$, $C_{w3} = 2.0$, $C_{v1} = 7.1$, $C_{t1} = 1$, $C_{t2} = 2$, $C_{t3} = 1.2$ and $C_{t4} = 0.5$.

2.2.2 The standard k-ε turbulence model

The standard k-ε turbulence model equations account for the contribution of the change in average speed and the lift force in creating turbulence kinetic energy and swashes, which are compressible at all spread rates and expandable in the turbulence. The following transport equations, Chan et al., (2002) [29] are used to calculate the turbulent kinetic energy, k, and rate of dissipation, ε:

$$\frac{\partial(\rho k)}{\partial t} + \frac{\partial(\rho k u_j)}{\partial x_j} = \frac{\partial}{\partial x_j}\left[(\mu + \frac{\mu_t}{\sigma_k})\frac{\partial k}{\partial x_j}\right] + G_k + G_b - \rho\varepsilon \quad i,j = 1,3 \qquad (12)$$

$$\frac{\partial(\rho \varepsilon)}{\partial t} + \frac{\partial(\rho \varepsilon u_j)}{\partial x_j} = \frac{\partial}{\partial x_j}\left[(\mu + \frac{\mu_t}{\sigma_\varepsilon})\frac{\partial \varepsilon}{\partial x_j}\right] + C_{1\varepsilon}\frac{\varepsilon}{k}(G_k + C_{3\varepsilon}G_b) - C_{2\varepsilon}\rho\frac{\varepsilon^2}{k} \quad i,j = 1,3 \qquad (13)$$

The turbulent (or eddy) viscosity, μ_t, is computed by combining k and ε as follows:

$$\mu_t = \rho C_\mu \frac{k^2}{\varepsilon} \qquad (14)$$

Where G_k is the turbulence kinetic energy production. It is due to the change in average velocity. G_b indicates the turbulence kinetic energy production caused by the buoyancy force.

In this study, as the experimental data of k-epsilon turbulence model, $C_{1\varepsilon} = 1.44$, $C_{2\varepsilon} = 1.92$, $C_\mu = 0.09$, $\sigma_\varepsilon = 1.3$, $\sigma_k = 1$ values were used [21].

2.2.3 The standard k-ω turbulence model

The standard k-ω turbulence model is an empirical model that is relied on the transport equations related to turbulent kinetic energy (k) and particular dissipation rate (ω). It may alternatively be regarded as the ratio of ε to k. This model is developed on the Wilcox k-ω model, which has been modified to account for low-Reynolds-number effects, compressibility, and shear flow spreading.

The turbulence kinetic energy, k, and the specific dissipation rate, ω, are obtained from the following transport equations [22],

$$\rho\frac{\partial k}{\partial t}+\ \rho u_j\frac{\partial k}{\partial x_j}=\frac{\partial}{\partial x_j}\left[(\mu+\sigma^*\mu_t)\frac{\partial k}{\partial x_j}\right]+G_k-\rho\beta^*k\omega \quad i,j=1,3 \tag{15}$$

$$\rho\frac{\partial \omega}{\partial t}+\ \rho u_j\frac{\partial \omega}{\partial x_j}=\frac{\partial}{\partial x_j}\left[(\mu+\sigma\mu_t)\frac{\partial \omega}{\partial x_j}\right]+\alpha G_k\frac{\omega}{k}-\rho\beta\omega^2 \quad i,j=1,3 \tag{16}$$

In these equations, G_k is the turbulent kinetic energy production. σ, σ^*, α, β, and β^* are constants of values 1/2, 1/2, 5/9, 3/40, and 9/100, respectively. The turbulent viscosity, μ_t, is computed by combining k and ω by following equation [22]:

$$\mu_t=\rho\frac{k}{\omega} \tag{17}$$

3. Methodology

In the software, the CFD package solves three basic equality equations: mass, momentum, and energy conservation. Flow and flow field characteristics define boundary conditions. The flow field is segmented into cells (mesh). In these cells, these three conservation equations are solved along with boundary conditions. Cells in two-dimensional fields can be structured quadratic or unstructured triangular, as seen in Figure 5.

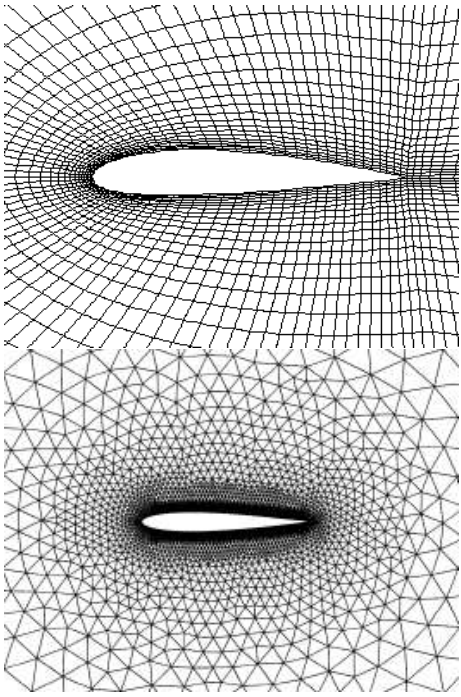

Figure 5. **(a)** Structured quadratic mesh grid; **(b)** Unstructured triangular mesh grid.

Triangular meshes can represent complex geometries more easily than quadrilateral meshes. Triangles can be used to represent curved boundaries and irregular shapes, and they can also be easily refined in regions where higher resolution is required. Triangular meshes may require more computational resources to achieve the same level of accuracy as a quadrilateral mesh. This is because triangular elements have fewer nodes than quadrilateral elements, which can lead to a higher number of elements required to represent a given geometry. Quadrilateral meshes can be more efficient computationally than triangular meshes. This is because quadrilaterals have more nodes than triangles, which means that fewer elements are required to represent a given geometry. Quadrilateral meshes may not be able to represent complex geometries as easily as triangular meshes. Quadrilaterals are generally less flexible than triangles in terms of their ability to represent curved boundaries and irregular shapes.

The precise division of cells is critical for obtaining accurate physical findings. While using fewer cells might result in incorrect findings, using too many cells necessitates high-capacity computers and additional time. Therefore, it is important to determine the optimal cell number.

Aerodynamic evaluations of NACA 63-215 and NACA 65-421 conventional wing section geometries were performed at various attack angles of flow conditions. As angle of attacks, 0 degrees, 10 degrees, and 20 degrees were employed. The length (c) of the wing section beam (chord) has been set at 1m. The velocity and pressure changes occurring about the two airfoils have been investigated and C_L lift C_D drag coefficients were calculated. These operations have been performed in the following order:

1. The airfoil coordinates were entered into a CAD computer, and two-dimensional geometries were generated.

2. The flow field geometry shown in the Figure 5 was created, and the limits of the flow region around the airfoil are depicted in Figure 6. Curve F and line C have been designated as the inlet and outlet, respectively, and the airfoil (curve G) has been designated as the 'wall.' As symmetry, AB and DE edges have also been introduced.

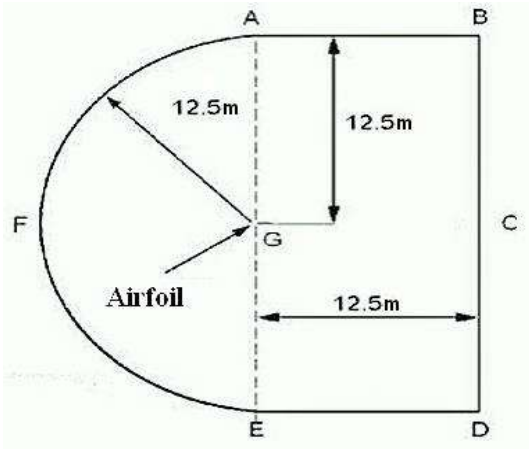

Figure 6. The flow domain, boundaries and dimensions.

3. After entering this geometry, including the wing cross-section (airfoil) and flow area, into the mesh software, the flow area was separated into cells (meshes). As illustrated in Figure 7, smaller cells on the surface of the airfoil and increasing cells by moving away from the geometry were generated. Each cell may be thought of as an infinitely small control volume in which the conservation equations are solved. CFD solution accuracy is determined by the size of the mesh grid. In this investigation, about 10 000, 107 000, and 1 500 000 triangular meshes were employed. However, after

100 000 meshes, it was discovered that the findings did not change much, therefore this mesh count was used throughout the research. Furthermore, it can be shown that the mesh metrics are of high quality.

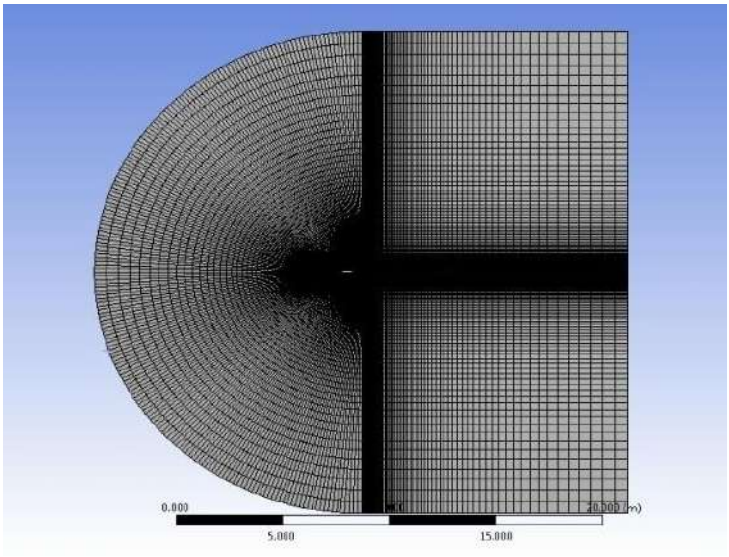

Figure 7. Meshed flow domain.

4. After the meshing procedure was completed, the flow domain geometry was imported into the CFD solution and the boundary conditions were established, as illustrated in Table 2.

Table 2. Boundary conditions

Boundary Conditions	Choices
Simulation Type	Steady Simulation
Fluid	Air
Flow Type	Incompressible flow
Temperature	300 K
Kinematic Viscosity	1.4607×10^{-5} m^2/s
Pressure	101325 pa.
Wind Speed	20 m/s
CFD Algorithm	SIMPLE
Turbulent model	For each simulation respectively; Spalart-Allmaras, k-ε and k-ω

Solution Methods	Pressure-Velocity Coupling Least Squares Cell Based Pressure (Standard) Density Momentum Turbulent Kinetic Energy Specific Dissipation Rate
Solution Controls	Pressure: 0.5 Momentum: 0.5 Density: 1.1 kg/m^3 Turbulent Kinetic Energy: 0.75
Boundary Conditions	Velocity Inlet (20 m/s) and Pressure Outlet (gage pressure: 0)
Mesh Cells	Around 100000

5. The conservation equations and turbulence models are repeatedly solved for all cells starting with initial values. For iterations, the convergence criterion has been set at 10^{-6}.

4. Results and Discussion

The aerodynamic efficiency of the airfoils was evaluated at different angles of attack. The experimental results were compared to the results obtained by using Spalart-Allmaras, k-ε, and standard k-ω turbulence models.

Figures 8 and 9 show the lift coefficient values for these two airfoil sections. The stall angle is the angle at which the coefficient of lift decreases with increasing angle of attack. In Figure 8, for NACA 63-215, while all models yield near results to the experimental data before stall, only Spalart-Allmaras approaches the experimental results after stall. In Figure 9, the k-ε turbulence model nearly matches the experimental data before and after stall for NACA 65-421.

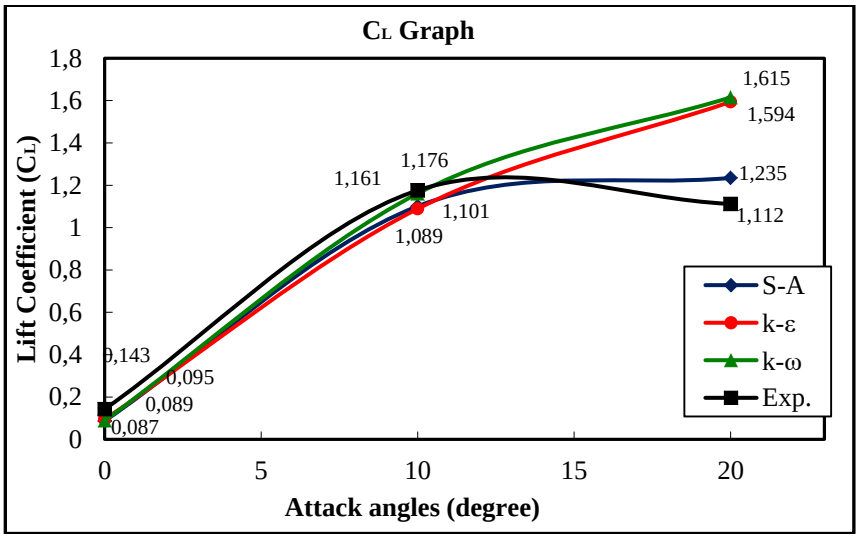

Figure 8. Lift coefficient comparison of NACA 63-215.

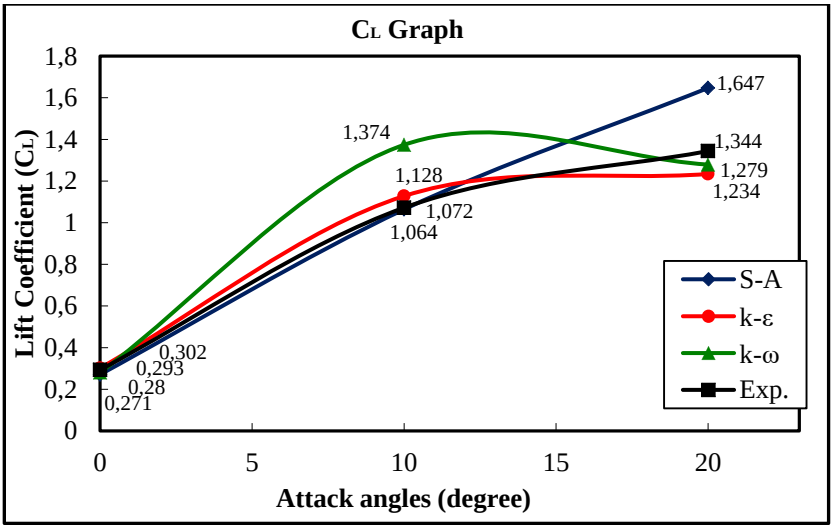

Figure 9. Lift coefficient comparison of NACA 65-421.

Figures 10 and 11 show the drag coefficient values for the various airfoil sections. In Figure 10, the estimated drag force for NACA 63-215 is somewhat greater than the experimental data before stall, but lower after stall. In Figure 11, whereas the other models miss the experimental data for NACA 65-421, the S-A turbulence model almost captures it before and after stall.

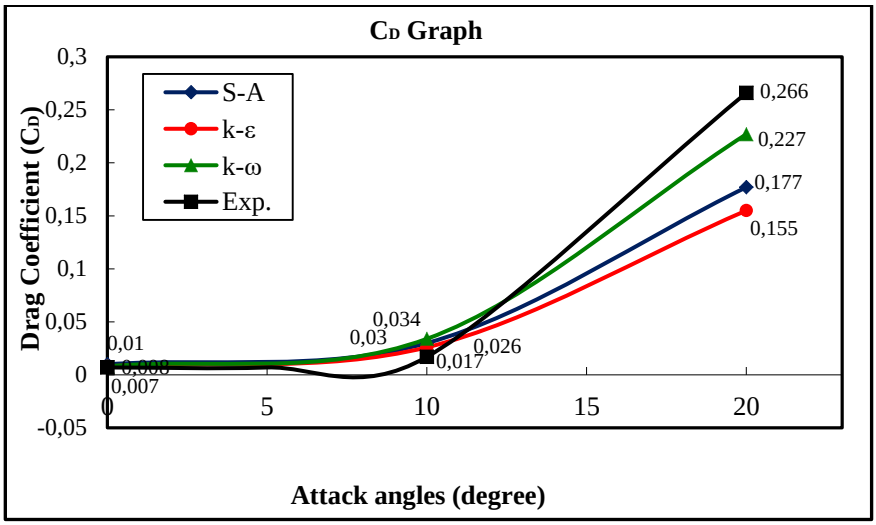

Figure 10. Drag coefficient comparison of NACA 63-215.

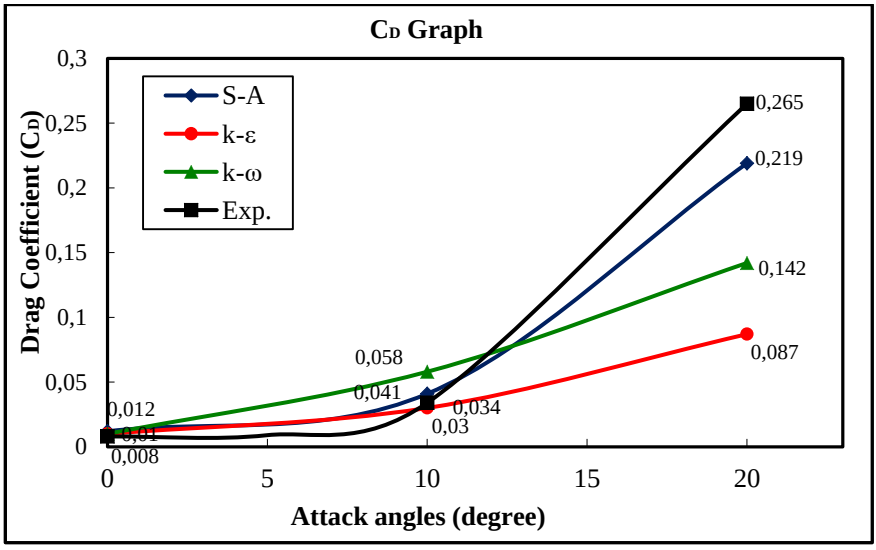

Figure 11. Drag coefficient comparison of NACA 65-421.

If we want to enhance aerodynamic performance, we should increase lift force while decreasing drag force. When the data in Figures 8, 9, 10, and 11 are taken into consideration, the lift/drag ratio is determined, as illustrated in Figures 12 and 13. In Figure 12, for NACA 63-215, while the predicted findings are closer to the experimental results at 0 and 20 attack angles, all models fail with substantially lower data at 10 degrees. In

Figure 13, for NACA 65-421, while all models have far results before stall, the S-A model has a closer result to the experimental data after stall.

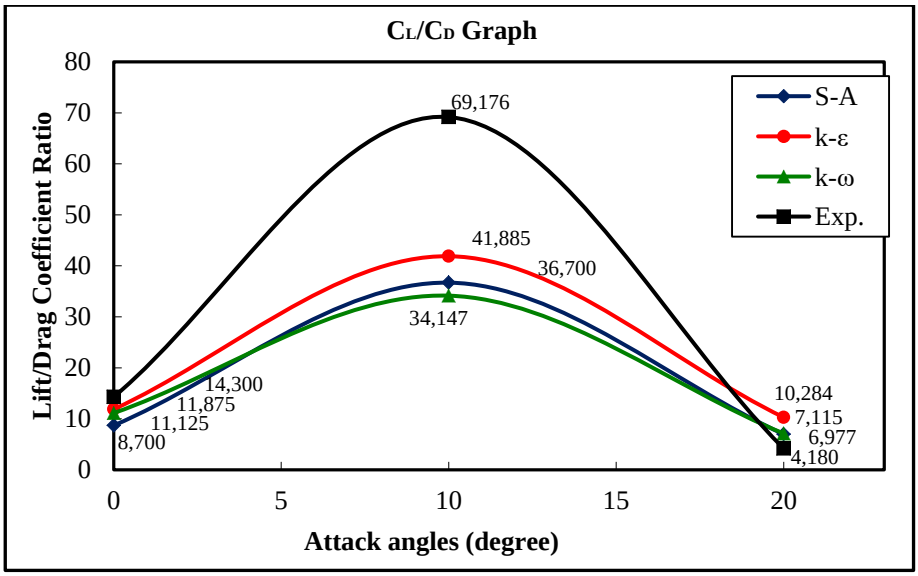

Figure 12. Lift/Drag coefficient ratio comparison of NACA 63-215.

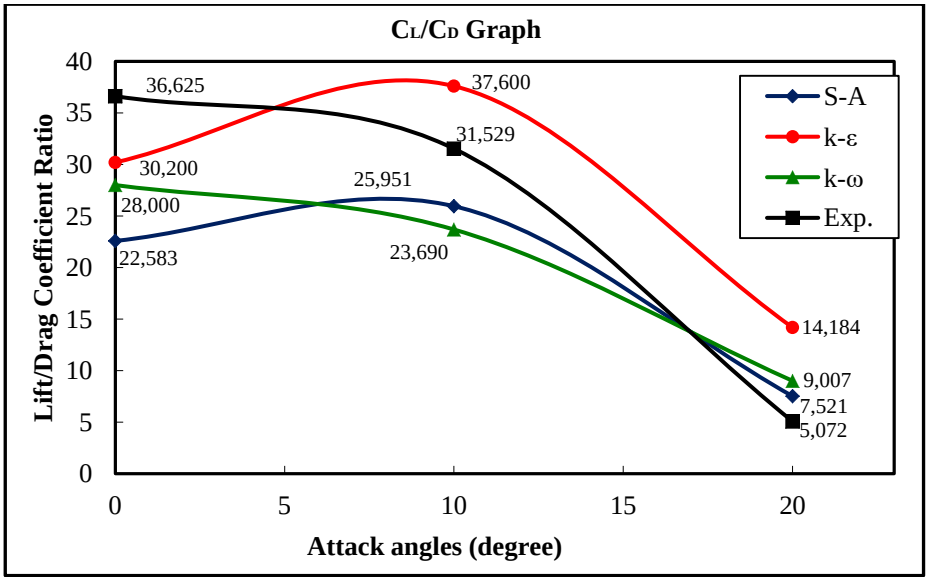

Figure 13. Lift/Drag coefficient ratio comparison of NACA 65-421.

One of the ways to understand the properties of flow around an object is to examine the pressure coefficient graph. The pressure coefficient takes

values that change from every point on the object to every point. This coefficient value is obtained by dividing the pressure value (which is the difference between the static pressure value at a certain point on airfoil surface and the static pressure value in the free region) by the dynamic pressure value in the free region. By looking at the graphs showing the changing values of the static pressure coefficient values according to the position on the upper and lower surfaces of the airfoil, it is possible to analyze the magnitude of the lift force and how it changes on the airfoil. Table 3 shows the pressure coefficient graphs obtained as a result of computational fluid dynamics analysis. The graphs obtained with Spalart Allmaras, k-epsilon and k-omega turbulence models for NACA 63-215 and for NACA 65-421 airfoils at 0, 10 and 20 degrees are shown comparatively in Table 3. The static pressure coefficient has different values at each point on the solid body surface around which there is flow. For this reason, static pressure graphs formed on the airfoil are drawn. These graphs are used to analyse the aerodynamic performance of the airfoil. As the area of the closed region formed in the static pressure coefficient graphs increases, the buoyant force value also increases. The static pressure values at each position at the top of an airfoil section are less than those at the bottom. Thus, lift and drag forces are results of the pressure difference of the pressure and suction sides of a body. There is more lift force where there is less pressure on the top section and more pressure on the bottom part.

Table 3. Pressure coefficient graphs of the airfoils.

Pressure Coefficient	**NACA 63-215**	**NACA 65-421**
0° Spalart-Allmaras	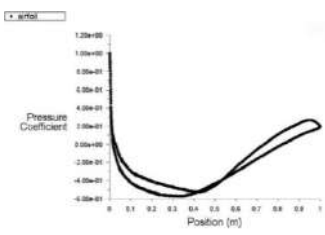	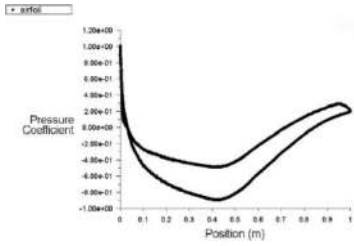

0°
k-ε

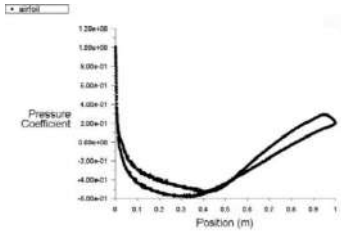

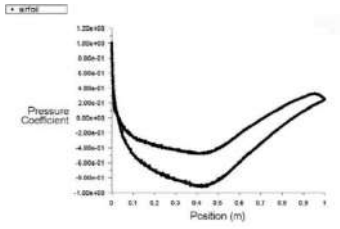

0°
k-ω

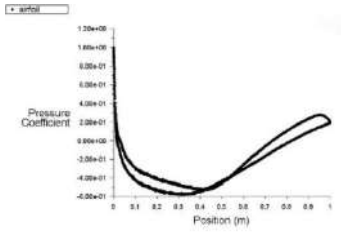

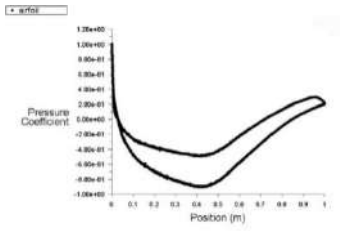

10°
Spalart-
Allmaras

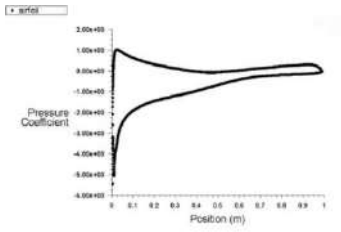

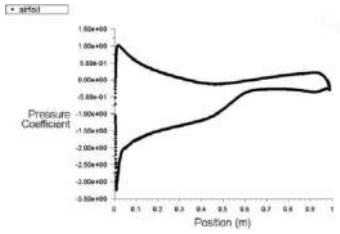

10°
k-ε

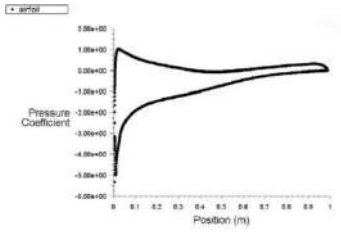

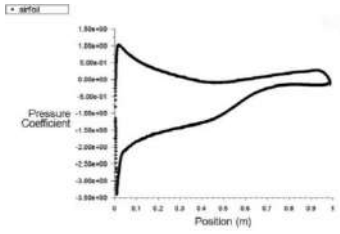

10°
k-ω

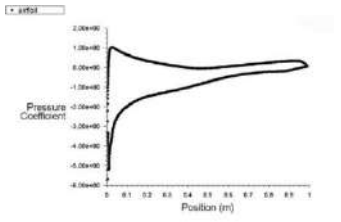

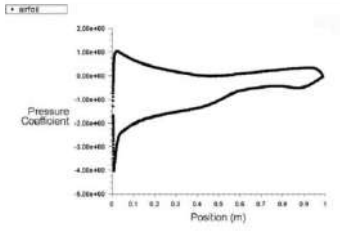

20° Spalart-Allmaras

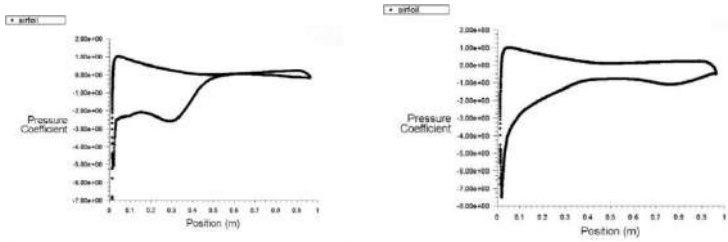

20° k-ε

20° k-ω

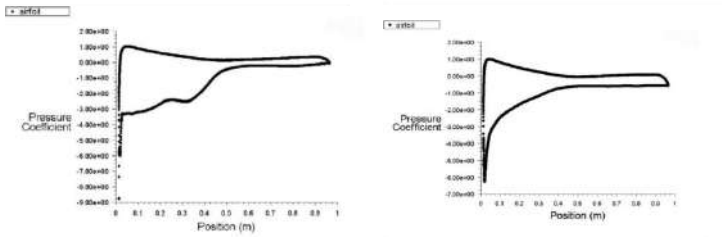

Table 3 compares the pressure coefficient graphs of the airfoils. The size of the closed regions between the upper and lower curves on the table graphs is related to the lift force. This region is greater than NACA 63-215 at NACA 65-421 cross section for all models. As a result, the lift force is greater. The same thing happens when the angle of attack rises: as the angle grows, so does the area.

For NACA 63-215, the position of the minimum static pressure coefficient value on the airfoil is 0.35c, 0.01c and 0.02c from the leading edge at zero degrees, 10 degrees and 20 degrees attack angles, respectively. For NACA 65-421, these values are 0.42c, 0.01c and 0.02c in the same order. These values are the same in all turbulence models. However, the minimum static pressure coefficient values were different for both airfoils and turbulence models. For NACA 63-215, the values found in three different turbulence models (S-A, k-epsilon, k-omega) are -0.6, -0.6, -0.6 at zero degrees of attack, while these values are respectively. -7, -11 and -8.8 at 10 degrees of attack values while at 20 degrees angle of attack, -5.4, -5.8 values were obtained.

For NACA 65-421, the minimum static pressure coefficient values were -0.9, -0.9, -0.8 at zero-degree angle of attack (S-A, k-epsilon, k-omega) and -3.2, -3.5, -4 at 10-degree angle of attack and -7.4, -6.4, -6.4 values

respectively at 20 degrees angle of attack. Although this coefficient is affected by the angle of attack, it can be said that while the airfoil has negative values in almost all of its upper surface, it takes positive values in most of the lower surface.

In relation to the Bernoulli equation, different velocities around the airfoil generate a varied pressure distribution at each position around the body. The area on the upper surface rises as the cross section is bent, increasing the speed of the air traveling through the cross section. In comparison to the Bernoulli equation, as air velocity increases, pressure decreases much more.

The change in velocity in the flow around the airfoil can be represented by the map shown in a different colour. Similarly, the static pressure change can be shown by the colour change. Red colours represent the highest values, while blue colours represent the lowest values. Other colours represent values in this range. Table 4 compares the pressure contours of the airfoils for the three attack angles. The blue areas on the figures in the table show where the static pressure is low, while the green, yellow, and red sections show where the static pressure is higher than the blue zone.

Table 4. Pressure contour figures of the airfoils.

Pressure Contour	**NACA 63-215**	**NACA 65-421**
0° Spalart-Allmaras	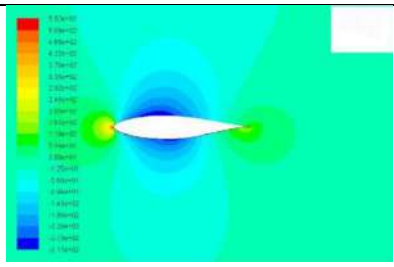	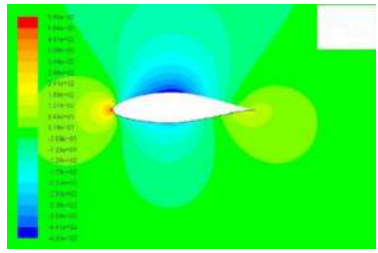
0° k-ε	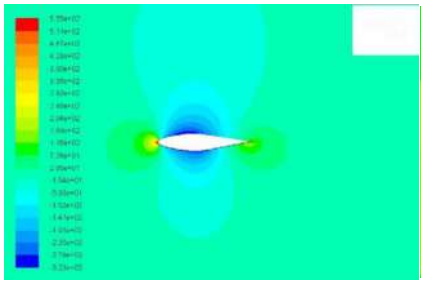	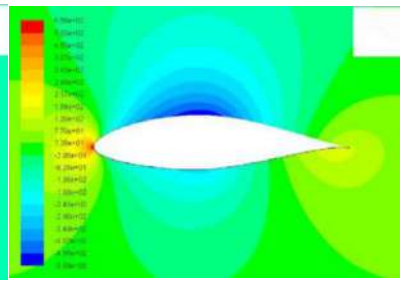

0° k-ω

10° Spalart-Allmaras

10° k-ε

10° k-ω

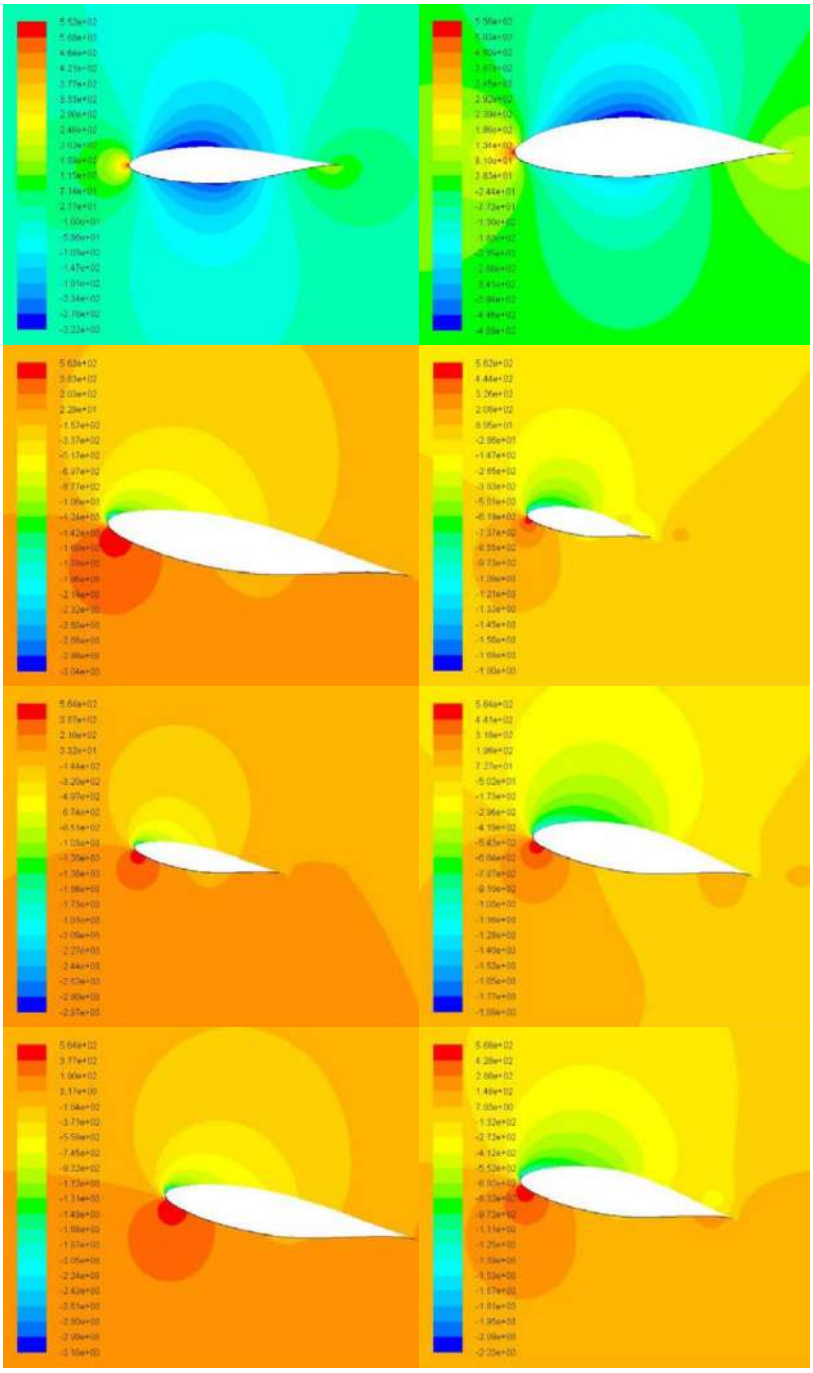

20° Spalart - Allmaras

20° k-ε

20° k-ω

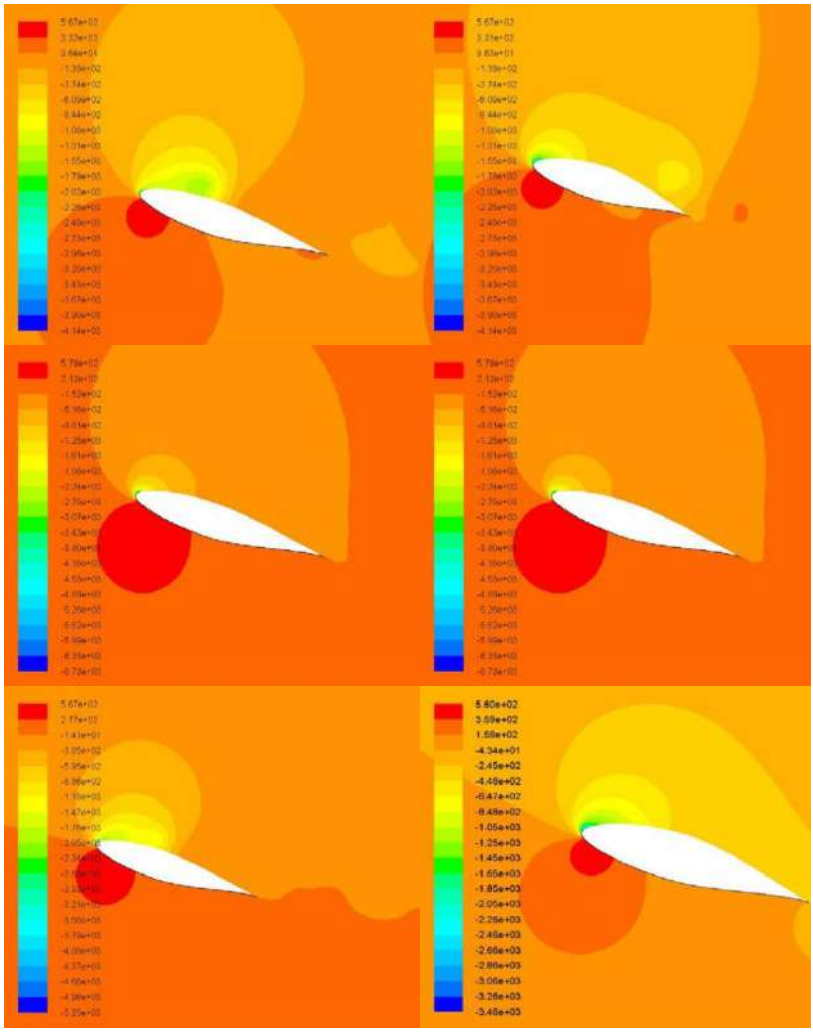

The static pressure is shown in red in Table 4 at the front tip of the airfoil sections because the flow velocity is zero at this location, as shown in Table 5, and the static pressure achieves its maximum value. The color of the region under the airfoil changes from blue to yellow as the attack angle increases. This variation is perceived as a rise in static pressure, and hence an increase in pressure differential and lift force.

When the pressure contours are carefully examined, it can be seen that there are slight differences between the turbulence models and the results. At zero-degree angle of attack, the minimum static effective pressure value obtained on the NACA 63-215 airfoil was calculated as -317 pascals in the Spalart-Allmaras turbulence model, -325 pascals in the k-epsilon

turbulence model and -322 pascals in the k-omega turbulence model. These values were calculated as -493 pascals, -509 pascals and -498 pascals for the Spalart-Allmaras, k-epsilon, k-omega turbulence models for NACA 65-421 airfoil, respectively. Maximum static pressure values were almost the same with all three turbulence models; For NACA 63-215, 555 pascals were obtained with Spalart-Allmaras, while 552 pascal values were obtained with k-epsilon and k-omega. The maximum (positive) effective static pressure value obtained in the NACA 65-421 airfoil was calculated as the same value, 556 pascals, with all three turbulence models.

Considering the pressure contours at 10 degrees angle of attack, the results obtained with the Spalart Allmaras, k-epsilon, k-omega turbulence models were as follows, respectively; Minimum static effective pressure values of -3044 pascal, -2970 pascal and -2430 pascal were obtained in NACA 63-215 airfoil. The maximum static effective pressure values obtained in the same airfoil were 563 pascals, 564 pascals and 564.4 pascals, respectively. Although there is a difference in the minimum values, it is understood that the maximum values are almost the same. Similarly, for the NACA 65-421 airfoil; The minimum pressure values obtained by turbulence models were -1800 pascals, -1834 pascals and -2230 pascals, respectively, while the positive pressure values were 562 pascals, 564 pascals, and 568 pascals, respectively.

While the negative pressure values obtained at 20 degrees angle of attack were obtained in the same turbulence order (SA, k-epsilon, k-omega) in NACA 63-215, -4140 pascals, -6720 pascals, -5250 pascals, in NACA 65-421 airfoil these values were respectively (SA, k-epsilon, k-omega) -4140 pascals, -5270 pascals, -3450 pascals were determined. Positive static pressure values, on the other hand, were the same as 567 pascals with all three turbulence models in NACA 63-215, slightly different values were obtained with three different turbulence models in the NACA 65-421 airfoil; if expressed in the same turbulence order; these values were 567 pascals, 558 pascals and 560 pascals.

In general, it can be said that in the calculation of positive pressure values, very close values are obtained with turbulence models. However, significant differences were observed in obtaining negative static pressure values. When the two airfoils are compared, it can be said that there is not much difference in terms of positive static pressure values, but there are significant differences in negative static pressure values.

At the point where the air approaching the airfoil first contacts the airfoil, the velocity is zero and the static pressure is at its maximum value, this point is called the stagnation point. The location of the stagnation points for the different angle of attacks are shown in Figure14.

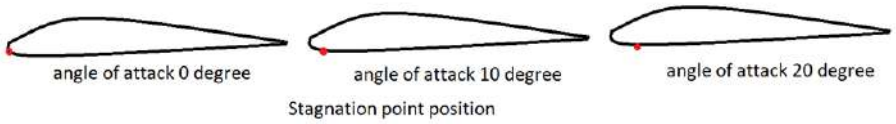

Figure 14. Position of the stagnation point varying with angle of attack

While the stagnation point is on the leading edge of the airfoil at zero degrees of attack, it can be observed from the static pressure contours (dark red zone) that this point is displaced towards the trailing edge at the lower surface of the airfoil by approximately 5% chord at 10 degrees attack angle and approximately 10% chord at 20 degrees attack angle.

Maximum velocity of the air particles moving over the airfoil result in minimum static pressure. The region that has high velocity around the airfoil changes with angle of attack. This is shown in Figure 15.

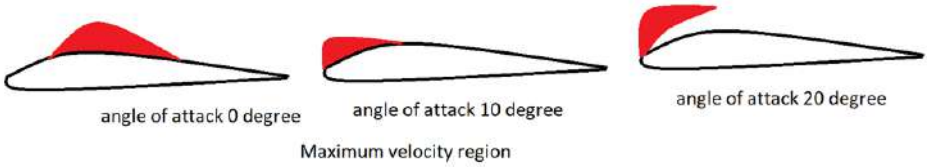

Figure 15. Position of the maximum velocity region varying with angle of attack

Finally, Table 5 compares the velocity contours of the airfoils for each of the three attack angles. The figures show that where flow separation occurs, the region becomes bluer and darker, and the velocity approaches zero.

Table 5. Velocity contour figures of the airfoils.

Velocity Contour	NACA 63-215	NACA 65-421
0° Spalart-Allmaras	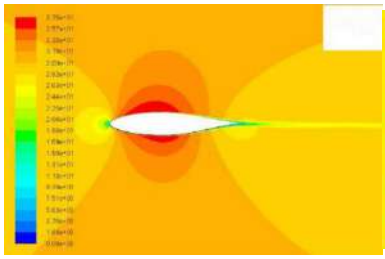	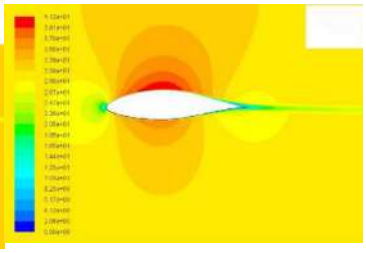
0° k-ε	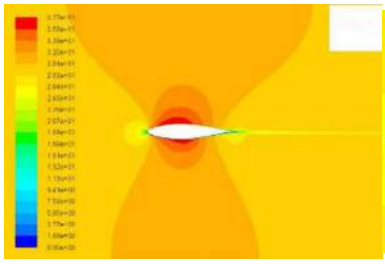	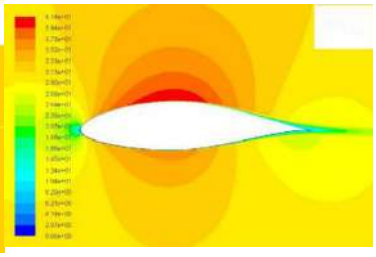
0° k-ω	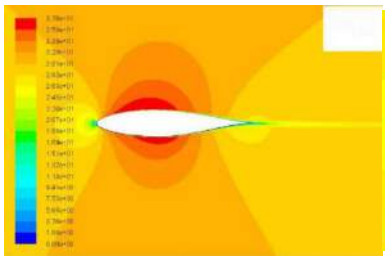	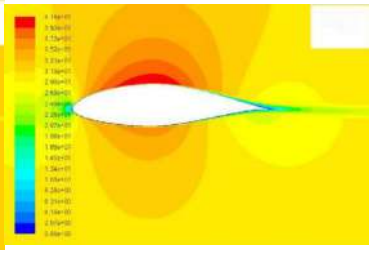
10° Spalart-Allmaras	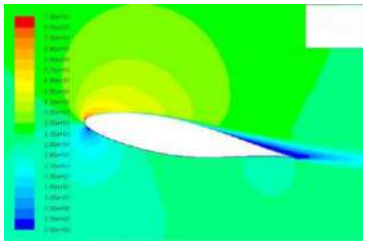	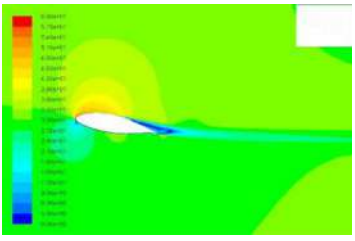

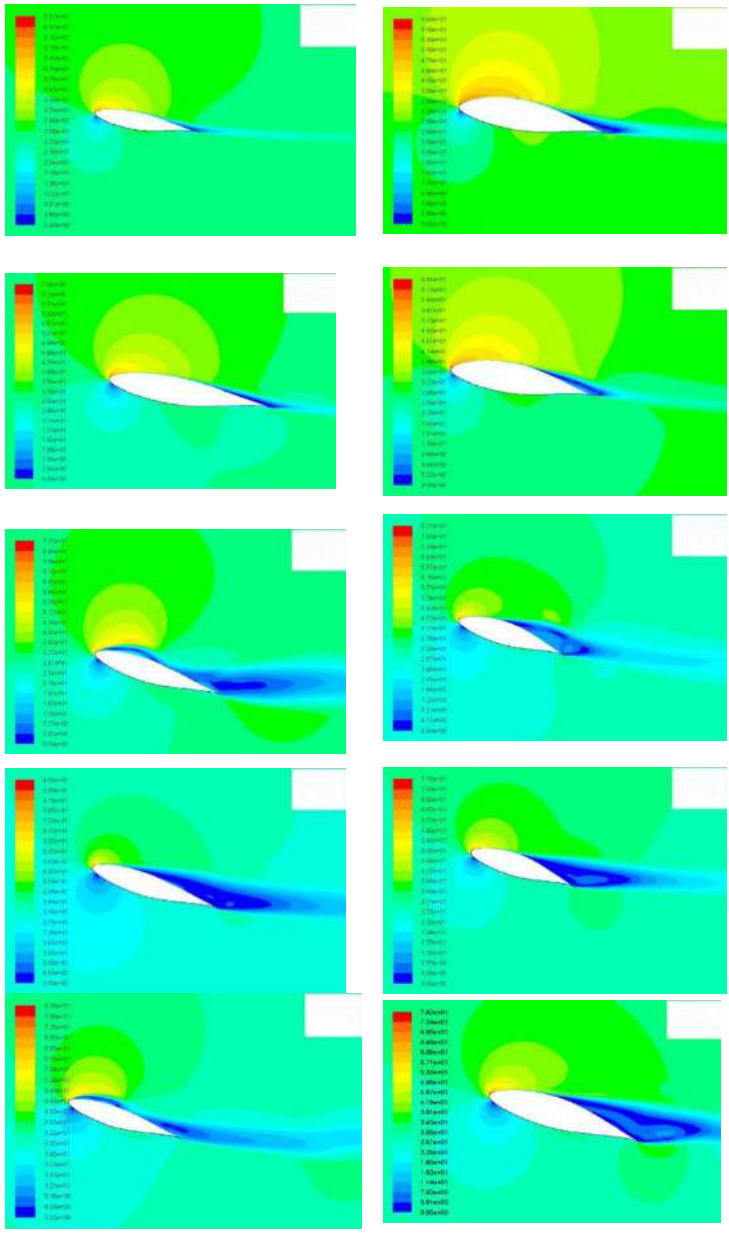

Looking at the velocity contours, it can be easily seen that the velocity of the air increases as it passes over the upper surface of the airfoil (dark red areas). At zero-degree angle of attack, the values of the maximum velocity found by turbulence models (S-A, k-epsilon, k-omega) in NACA 63-215 were obtained as 37.5 m/s, 37.7 m/s, and 37.6 m/s, respectively.

The same values were obtained for the NACA 65-421 airfoil as the maximum velocity values of 45.2 m/s, 41.4 m/s, and 41.3 m/s, respectively. It is seen from the contours that the maximum speed values increase when the angle of attack is increased to 10 degrees. At 10 degrees angle of attack, the maximum velocity values for NACA 63-215 in the order of turbulence models (S-A, k-epsilon, k-omega) are 70 m/s, 68 m/s, 70.8 m/s, while these values for NACA 65-421 are 60 m/s, 56 m/s, 64.4 m/s respectively. While at 20 degrees angle of attack, maximum speed values of 72.2 m/s, 90.5 m/s, 80.6 m/s were obtained in NACA 63-215 in the same order of turbulence, while these values were 82 m/s, 77.6 m/s, 76.2 for NACA 65-421, respectively.

It is understood from the speed contours that maximum speed values occur at NACA 65-421 at low angles of attack, while maximum speed values occur at NACA 63-215 at high angles of attack. In addition, in both airfoils, it can be said by looking at the contours that the maximum speed region shifts from the upper middle region of the airfoil towards the leading edge with the increase in the angle of attack.

The NACA 63-215 airfoil, with its low camber and thickness, is well-suited for aircraft wings that require low drag and good lift characteristics, such as light general aviation aircraft, gliders, and UAVs. NACA 65-421 airfoil, on the other hand, has a higher camber and thickness compared to NACA 63-215 airfoil, which makes it more suitable for aircraft that require higher lift, such as transport aircraft and some military aircraft. This airfoil has also been used in wind turbine blades, where its high lift-to-drag ratio makes it a good choice for low-speed wind energy conversion. While these airfoils are primarily designed for subsonic flow applications, they may still be used in transonic flows with proper design considerations. However, they are not suitable for supersonic flow applications.

5. Conclusion

The experimental results were correlated with the estimated coefficients of lift and drag powers. Both turbulence models before and after the stall angle indicated a considerable discrepancy with the experimental data, with the anticipated drag force being greater than the real data.

The static pressure distribution was illustrated on these two airfoils. At the same angle of attack, it was determined that NACA 63-215 had less negative pressure on the upper surface than NACA 65-421.

The main goal of this simulation was to evaluate the different characteristics of the NACA 63-215 and NACA 65-421 airfoils for the different turbulence models and with experimental data available in the literature to determine which model is the most efficient.

The study used the Spalart-Allmaras, turbulence standard k-ε turbulence, and standard k-ω turbulence models. The basic k-ω model is optimized for boundary layer flows and separation, but it does not reliably estimate coefficients of lift and drag in the far domain free-stream regions beyond the shear layer due to the solution's sensitivity to k values and ω in the free flow regions beyond the shear layer. Aside from that, k-ω; k-ε exhibits a better agreement with experimental data. However, it loses its balance following a stall argument. The Spalart-Allmaras turbulence model is found to produce a more accurate estimation of lift and drag coefficients in both the pre-stall and post-stall areas when compared to the other models.

The suitability of an airfoil for a particular vehicle or application depends on several factors, such as the desired lift and drag characteristics, the operating conditions, and other design considerations. Therefore, the selection of an appropriate airfoil should be made based on a thorough analysis of the specific application requirements. Both airfoils have similar aerodynamic properties, such as a low drag coefficient and a high lift-to-drag ratio. However, the NACA 63-215 airfoil has a higher critical Mach number and is more suitable for high-speed flight, while the NACA 65-421 airfoil has a higher lift coefficient and is more suitable for lower speed flight. As a continuation of this study, the aerodynamic performances of other airfoils can be calculated in a similar way. The lift and drag force coefficient values of symmetrical cambered airfoils can be compared.

In recent years, significant progress has been made in improving the accuracy and reliability of CFD simulations for airfoil aerodynamics. One major area of research is the development of more accurate and computationally efficient turbulence models, particularly in LES (Large Eddy Simulation) and DES (Detached Eddy Simulation). Additionally, advances in high-performance computing and meshing techniques have enabled more complex and detailed simulations, allowing for better understanding of the complex flow physics around airfoils**.**

The future of airfoil aerodynamics by CFD is likely to involve further advances in turbulence modelling, meshing techniques, and high-performance computing. Additionally, researchers are exploring the use of

machine learning and artificial intelligence techniques to improve the accuracy and speed of CFD simulations. These advances are expected to lead to the development of even more efficient and innovative airfoils.

References

[1] Anderson Jr., J.D. (2001). "Fundamentals of Aerodynamics", McGraw-Hill Education, New York.

[2] Abbot, I.H. and Von Doenhoff, A. E. (1959). "Theory of wing sections, Including a summary of airfoil data", Dover Publications Inc., New York, USA.

[3] Anderson J. D. (1995). "Computational Fluid Dynamics", McGraw-Hill, USA.

[4] Sarada, S., Shankar, M. S., Rudresh, G. (2010). "Numerical Simulation of Viscous, In-compressible Flow Around NACA64618 Subsonic Airfoil using Computational Fluid Dynamics", Proceedings of National conference on advances in Mechanical Engineering, India.

[5] Saraf, A., Nazar, F. A., Singh, S. P. (2012). "Analysis of the k-ϵ and k-ω Standard Models for the Simulation of the Flow Over a National Advisory Committee for Aeronautics (NACA) 4412 Airfoil", International Journal of Scientific & Engineering Research, India.

[6] Hartwanger, D., Horvat, A. (2008). "3D modeling of a Wind Turbine using CFD", NAFEMS Conference, United Kingdom.

[7] Ravi, H. C., Madhukeshwara, N., Kumarappa, S. (2013). "Numerical Investigation of Flow Transition for NACA-4412 Airfoil using Computational Fluid Dynamics, International Journal of Innovative Research in Science", Engineering and Technology, India.

[8] Eleni, D. C., Athanasios, T. I., Dionissios, M. P. (2012). "Evaluation of the Turbulence Models for the Simulation of the Flow over an Aerofoil", Journal of Mechanical Engineering Research, Greece.

[9] Johansen J. (1997). "Prediction of Laminar/Turbulent Transition in Airfoil Flows", Journal of Aircraft, Aerospace Research Central, Denmark.

[10] Launder, B. E. & Spalding D. B. (1974). "The Numerical Computation of Turbulent Flows", Computer Methods in Applied Mechanics and Engineering, ScienceDirect, United Kingdom.

[11] Gulzar, O., Gulzar, S., Bhatele, S., Soni, N. (2014). "Impact of Variation in Angle of Attack on NACA7420 Airfoil in Transonic Compressible Flow Using Spalart-Allmaras Turbulence Model", IJRMET, India.

[12] Kumar, B. N., Paramasivam, K. M., Prasanna, M., Karis, M. (2016). "Computational Fluid Dynamics Analysis of Aerodynamic Characteristics of NACA 4412 vs S809 Airfoil for Wind Turbine Applications", International Journal of Advanced Engineering Technology, India.

[13] Badran, O. (2008). "Formulation of Two-Equation Turbulence Models for Turbulent Flow over a NACA 4412 Airfoil at Angle of Attack 15 Degree", Proceedings of 6th International Colloquium on Bluff Bodies Aerodynamics and Applications, Italy.

[14] Hassan, G. E., Hassan, A., Youssef, M. E. (2014). "Numerical Investigation of Medium Range Re Number Aerodynamics Characteristics for NACA0018 Airfoil", CFD letters, Egypt.
[15] Smyth, Thomas AG. "A review of Computational Fluid Dynamics (CFD) airflow modelling over aeolian landforms", Aeolian Research 22 (2016): 153-164.
[16] Hansen, M.O.L. and Sørensen, N.N. (2004). "Aerodynamics of Wind Turbines", 2nd Edition. Earthscan, London.
[17] Wilcox, C. D. (1993). "Turbulence Modelling for CFD, DCW Industries", library copy, USA.
[18] N. K. Anand and C. L. Streett, "A comparative study of turbulence models in predicting flow over a NACA 0012 airfoil", Journal of Aircraft, vol. 48, no. 1, pp. 207-214, January-February 2011.
[19] R. L. Spalart and S. R. Allmaras, "A one-equation turbulence model for aerodynamic flows", AIAA Paper 92-0439, January 1992.
[20] Spalart, P.; Allmaras, S. (1992). "One-equation turbulence model for aerodynamic flows", 30th Aerospace Sciences Meeting and Exhibition, AIAA. doi: 10.2514 / 6.1992-439.
[21] Fluent Inc, (2006). "Standard and SST – k-epsilon Models Theory", FLUENT 6.3 User's Guide,
[22] Menter, FR (1994). "Two-Equation Eddy-Viscosity Turbulence Models for Engineering Applications", AIAA Journal. 32 (8): 1598-1605. doi : 10.2514 / 3.12149
[23] Spalart, P. R., Allmaras S. R. (1992). "A One-Equation Turbulence Model for Aerodynamic Flows", AIAA Paper, USA.
[24] Launder, B.E. and Spalding, D.B. (1972). "Lectures in Mathematical Models of Turbulence", Academic Press, London.
[25] Sahin, I & Acir, A. (2015). "Numerical and Experimental Investigations of Lift and Drag Performances of NACA 0015 Wind Turbine Airfoil", International Journal of Materials, Mechanics and Manufacturing, Turkey.
[26] Hanjalic, K.; Laundering, B. (1972). "A Reynolds stress model applying to turbulent and fine shear flows". Journal of Fluid Mechanics. 52(4): 609–638. doi: 10.1017 / S002211207200268X
[27] Sørensen, N.N. and Mygind, L. (2001). "Airfoils for Wind Turbine Applications", Risø National Laboratory, Roskilde.
[28] Shih, T.H., Liou, W.W., Shabbir, A., Yang, Z., and Zhu, J. (1995). "A new k-epsilon eddy viscosity model for high Reynolds number turbulent flows", Computers & Fluids, 24(3), 227-238.
[29] Chan, T. L., Dong, G., Leung, C. W. Cheung, C. S., Hung, W. T., (2002). "Validation of a two-dimensional pollutant dispersion model in an isolated street canyon", Atmospheric Environment, Hong Kong, China.

Chapter 5

Simulation-Based Investigation of Heat Collection in Various Absorber Plate Materials for Solar Water Heating Systems

Mara Niebling[1]

Coskun Firat[2]

Altin Maraj[3]

A. Talat Inan[4]

Abstract

The main component of a solar water heating system is the collector. The absorber plate is another crucial component of the collector. For a more effective system, the absorber layer should, to the greatest extent possible, be made of materials with good thermal properties. In this study, in addition to copper and aluminum, new materials such as pyrolytic graphite and glass for the absorber plates of solar water heaters are presented. Along with a performance comparison analysis of the collector utilizing various materials, the costs of each material are also reported. It was concluded that pyrolytic graphite provided the best heat transfer. There is different type of pyrolytic graphite with different thermal conductivity. Calculations, however, show that even the PG with the highest thermal conductivity (1800/15 W/mK in plane and in z-direction, respectively) only slightly increases the temperature of the usable energy. In other words, increasing the thermal conductivity above a certain level does not improve the performance of the solar panel. Glass is another material which offers a better performance while maintaining very low thermal conductivity. Despite having different heat transfer mechanisms when used as absorbers, pyrolytic graphite and glass can be offered as a new material for absorber plates because they outperform conventional materials like copper. In comparison to copper, the efficiency of the collector with the pyrolytic graphite absorber was found to be 2% higher.

1 Ms., Johannes Gutenberg University, Mainz, Germany

2 Assoc. Prof. Dr., Istanbul Technical University, Energy Institute, Istanbul, Türkiye, coskun.firat@itu.edu.tr, Orcid: 0000-0002-2853-8940, (corresponding)

3 Assoc. Prof. Dr., Polytechnic University of Tirana, Faculty of Mechanical Engineering, Tirana, Albania, amaraj@fim.edu.al, Orcid: 0000-0003-3976-9303

4 Assoc. Prof. Dr., Marmara University, Faculty of Technology, Istanbul, Türkiye, ainan@marmara.edu.tr, Orcid: 0000-0003-2720-5711

https://doi.org/10.58830/ozgur.pub130.c534

1. Introduction

Sunlight is an almost infinite resource on our planet [1]. Solar water heater (SWH) systems harness the sunlight with a solar thermal collector and convert it into heat. Thus, SWHs are environmentally friendly heat exchangers and run without to minimal operation and maintenance costs. The first solar water heater was patented in 1891 by Kemp and thereafter, the development and improvement of SWHs started [2]. Nowadays, solar water heating is one of the cheapest and resource-efficient applications which supplies domestic hot water [3]. According to Ekramian et al. [4], solar energy is one of the best alternatives to fossil energy sources. Especially, in developing countries, often located in sunny regions, solar energy offers great opportunity. Accordingly, SWHs are gaining increasing importance as a sustainable alternative to conventional energy sources. One of the main components of SWHs is the absorber plate, and its selection plays a significant role in the overall efficiency of the system. This study aims to investigate the performance of different absorber plate materials and to provide insights into the design of more effective solar water heating systems.

Flat-plate thermal collectors (FPTCs) are the most studied and used technology among different SWH systems, because of the simplicity and the working temperature range suitable for domestic solar water heating as well as space heating applications. A common size is 1m×2m×0.15m [5]. They are made with a strong frame, an often-glazed glass front, a solid back and insulation on the sides and the back. The absorber plate is mostly under the glass cover since glass transmits more than 90% of the incident short-wave solar radiation and emits only part of the long-wave radiation emitted by the absorber plate [6]. Traditionally, flat plate collectors have two bigger water tubes, called manifolds, at the top and the bottom as well as several thinner riser tubes that run perpendicular [5]. The tubing allows a heat transfer fluid (HTF), often water, to run through the collector.

The absorption and transmission properties of an absorber plate depend on the material as well as the coating of the plate [6]. Ideally, an absorber should absorb all incoming radiation and emit no heat back to the atmosphere. So, the optical, chemical and structural properties of absorber plates and coatings have been changed to improve the absorption (in the solar spectrum or short-wave) to emission (long-wave) ratio [7]. Most absorber plates are made out of metals like copper, aluminum and steel with relatively high thermal conductivities of about 50 to 400 W/mK showed an increase in absorber efficiency with absorber conductivity [4]. However, this dependence is not linear. Even though the thermal conductivity of copper is almost

twice that of aluminum, the efficiency of the SWH is just slightly better. The use of corrugated absorber plates that both increase the absorber surface area and friction are beneficial for efficiency [8]. Lu et al. improved the absorber plate with a Copper Oxide nano-structure selective coating [8, 9]. Non-metallic materials like engineering [10] and commodity [11] polymers also can be used as solar absorber plates, especially for un-glazed SWHs. It has been shown that the absorption and emission coefficients of a polyethene absorber are about 0.85 and 0.1, respectively, which is quite comparable with selectively coated solar absorbers with absorption and emission coefficients of about 0.95 and 0.05 [12].

Efficiency for solar air heaters is found for adding porous material on top of the absorber plate to create a swirling airflow and avoid thermal boundary layers [16-18]. Likewise, inserting wire coil into the tubes of a water heating collector can lead to an efficiency increase of up to 4.5% since it changes the flow characteristics of the HTF [19]. The effective surface area of a collector highly influences the collector's performance. To increase the surface area, he investigated semi-spherical absorber plates [20]. On top of that, he focused on collecting not only direct, but also diffuse and reflected radiation to maximize collector efficiency [21].

In this study, various materials such as copper, aluminum, pyrolytic graphite, and glass were tested for their efficiency in absorbing and transferring heat. The study found that pyrolytic graphite and glass are new materials that outperform conventional materials such as copper in terms of heat transfer efficiency.

Additionally, the study also reports on the cost-effectiveness of each material, which is a crucial factor for practical implementation. The results showed that pyrolytic graphite is more expensive than copper, while glass is relatively cheaper. However, both materials offer better performance while maintaining low thermal conductivity. This information can help manufacturers and designers to select the most appropriate absorber plate material for their solar water heating systems.

The significance of this study lies in the fact that it provides a better understanding of the performance of different absorber plate materials, which can lead to the development of more efficient and cost-effective solar water heating systems. The use of pyrolytic graphite and glass as absorber plate materials can lead to significant improvements in the overall efficiency of solar water heating systems. The findings of this study can also help policymakers in promoting the use of renewable energy sources by making solar

water heating systems more attractive and cost-effective. In conclusion, this study can contribute significantly to the development and advancement of sustainable energy solutions.

2. Thermal performance principles of SWH

When an increase in heat difference between the inlet and outlet fluid temperature of a solar collector, the system efficiency is increasing. This is reflected in the efficiency (η) as follows:

$$\eta = \frac{Q_u}{G}. \tag{1}$$

The useable energy Q_u that heats the fluid inside the collector is included in the efficiency equation together with the incoming solar radiation I_{rad}, which is connected to the energy arriving ($G=A.\ I_{rad}$) onto the collecting area (A). The discrepancy between G and Q_u results from losses to the environment, such as radiation and convection, or from heating all collector materials. The mechanism for this heat transfer in the collector is shown in Fig. 1.

Figure 1. Heat transfer mechanism in the collector

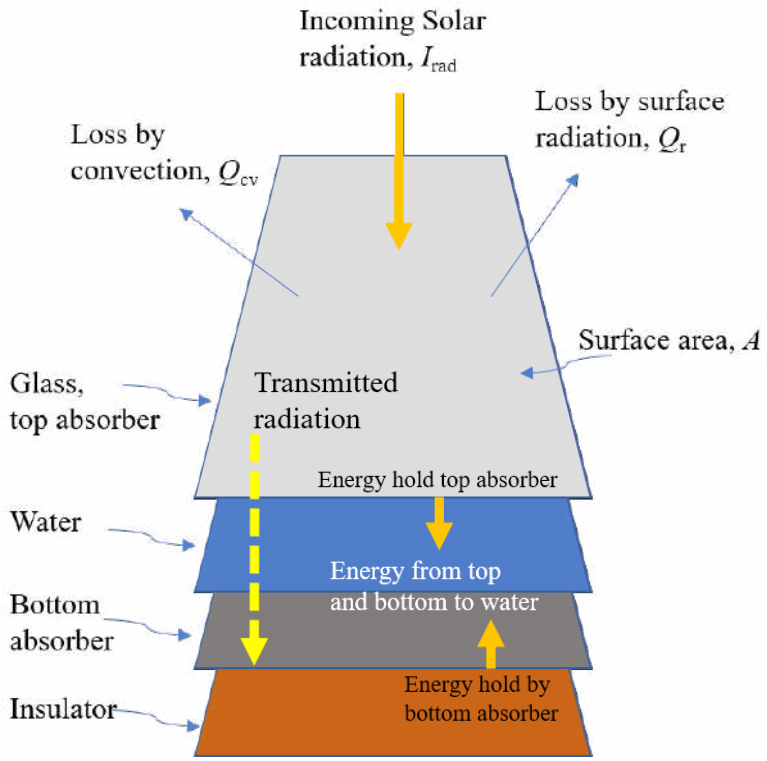

Water is used as an HTF. Thus, the usable heat Q_u is dependent on the specific heat of water c_w and its mass flow rate $\dot{m}_w \dot{m}_w$ as it is shown in Eq.(2) as [24]:

$$Q_u = \dot{m}_w c_w (T_o - T_i). \tag{2}$$

It was assumed that the bottom and sides of the collector had perfect thermal insulation in order to make the analytical calculations easier, namely $\vec{n}.\vec{q} = 0$ with the surface normal $\vec{n}$ and the heat flow $\vec{q}$. It was also assumed that the radiation arriving at the surface strikes perpendicularly. In that case, the full incoming radiation hits the top surface of the flat-plate collector. Given that glass has an emissivity of 0.94, where 1 indicates perfect transmission of incoming radiation, the reflection losses are minimal and can be disregarded.

When the collector surface is hotter than the ambient temperature, energy will be lost through radiation Q_r and convection Q_{cv} if there is an airflow as well. Furthermore, when heat is conducted through different media, additional heat losses occur. They can be imagined as heat resistances *R* of the materials and their boundary layers. The thermal resistance of a solid (Eq.3) depends on the thermal conductivity *k*, the thickness *l* and the surface area *A*, of the materials [26]:

$$R = \frac{l}{kA}. \tag{3}$$

The higher the thermal resistance of a material, the better its insulating properties. The sum of all thermal resistances, including conductive, convective, and radiative losses, yields the total system energy loss, Q_L (Eq.4). Due to energy conservation, these losses are exactly the difference between the incoming energy and the useful energy in a perfectly insulated collector:

$$Q_L = Q_r + Q_{cv} + Q_c = G - Q_u. \tag{4}$$

Since we assumed perfect insulation of the collector, the useful energy Q_u can be calculated by subtracting the losses from the incoming solar radiation energy.

The mathematical model of the thermal heat transfer mechanism must be recorded in order to determine the water output temperature. The incoming solar energy is split into losses to the environment due to convection (Q_{cv}) and surface radiation (Q_r), and some of the remaining energy (Q_g) is stored by conduction in glass (Q_{cg}), and also transmitted to the bottom side of the glass (Q_{gt}) [24]:

$$G = Q_r + Q_{cv} + Q_g. \tag{5}$$

$$Q_r = \sigma \varepsilon_g A\left(T_g^4 - T_a^4\right). \tag{6}$$

$$Q_{cv} = h_v A\left(T_g - T_a\right). \tag{7}$$

$$Q_g = Q_{cg} + Q_{gt} = \frac{k_g A}{l_g}\left(T_g - T_a\right) + \tau_g Q_g, \tag{8}$$

where AA is the surface area, $\sigma\sigma$ is the Stefan-Boltzmann constant, T_a is the ambient temperature, ε_g is the surface emissivity, T_g is the temperature, k_g is the thermal conductivity coefficient, l_g is the thickness and τ_g is the transmittance of glass. The surface convection heat transfer coefficient h_v depends on the wind speed vv as [27]:

$$h_v = 11.4 + 5.7v. \tag{9}$$

Thus, the energy on the glass is rewritten as;

$$Q_g = \frac{k_g A}{l_g(1-\tau_g)}\left(T_g - T_a\right), \tag{10}$$

by considering Eqns. (5–10), the glass temperature (T_g) can be determined from the energy balance.

$$G = \frac{k_g A}{l_g(1-\tau_g)}\left(T_g - T_a\right) + \sigma \varepsilon_g A\left(T_g^4 - T_a^4\right) + h_v A\left(T_g - T_a\right). \tag{11}$$

A portion ($\tau_g \tau_w Q_g$) of the remaining energy ($\tau_g Q_g$)is subsequently transmitted onto the absorber layer while the other portion of it (Q_w) is transferred to water. Writing the energy balance will yield the mean water temperature (T_{mw}).

$$\tau_g Q_g = Q_w + \tau_g \tau_w Q_g. \tag{12}$$

$$\tau_g \frac{k_g A}{l_g(1-\tau_g)}\left(T_g - T_a\right) = h_w A\left(T_{mw} - T_g\right)$$

$$+ \tau_g \tau_w \frac{k_g A}{l_g(1-\tau_g)}\left(T_g - T_a\right) \tag{13}$$

where h_w is the convection heat transfer coefficient and τ_w is the transmittance of water. The energy transmitted onto the absorber layer will be stored there by conduction heat transfer. The absorber temperature (T_m) can be obtained by using this energy balance;

$$\tau_g \tau_w \frac{k_g A}{l_g(1-\tau_g)}\left(T_g - T_a\right) = \frac{k_m A}{l_m}\left(T_m - T_{mw}\right). \tag{14}$$

The output water temperature (T_{out}) can then be determined by considering the energy balance between usable energy and the energy transferred to the water from the top and bottom layers as well as by convection;

$$\frac{k_m A}{l_m}(T_m - T_{mw}) + \frac{k_g A}{l_g}(T_g - T_a) = \dot{m}_w c_w (T_o - T_i)$$

$$+ h_w A(T_{mw} - T_g). \quad (15)$$

3. Material selection and simulation design

Similar values and assumptions as in the analytical study (Sect-2) were used in the simulation. It is based on the finite element method (FEM) which divides the collector model into multiple small grid elements to solve separately. The collector model (Fig. 2) is scaled to 0.33 m × 1.00 m to prevent using more computing power than necessary.

Figure 2. Sketch of the model flat-plate collector

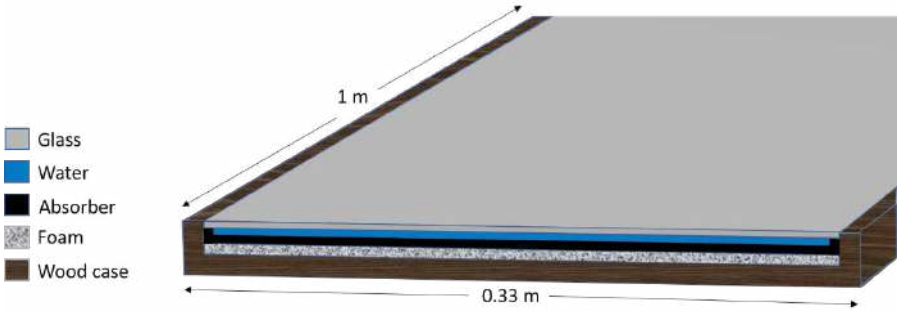

If the absorber plate is allowed to be placed loosely inside the collector, it can change in size as a function of temperature without restrictions or increased pressure [7]. The current study differs from that since it was determined that water flows through an envelope-like channel between the glass and the absorber.

The insulation layer of solar water heaters is often made of insulating wool or foam [13]. In the present study, polyurethane foam is selected as insulator that is suited to insulate the collector from +130 °C to -40 °C [28]. The top layer of the model collector is made of glass, which is widely used for solar collectors due to its favorable transmission to emission ratio [8]. The simulations assume that the solar radiation impinges normal to the surface with an irradiance of I_{rad} = 1000 W/m², as in the ASTM standard [29].

In a study, Shariah et al. found that the thermal conductivity and characteristic factor of a collector from a negatively curved hyperbole that is asymptotic to 1. Thus, increasing the thermal conductivity up to 100 W/mK improves the collector's performance significantly. Whereas, for higher

conductivities the asymptotic behavior of the function dominates and higher thermal conductivity only raises the efficiency slightly [30]. Still, we introduce annealed pyrolytic graphite [31] as an absorber material as it could still increase the efficiency slightly. Additionally, glass was tested as an absorber plate material even though its thermal conductivity is low. Currently, the most popular materials for the absorber plate of solar water heaters are made of copper and aluminum [4].

Pyrolytic graphite (PG) sheets (also commonly referred to as thermal interface graphite pads or graphite film) is created from a high temperature sintering process, heating a polymer film to its decomposition temperature in a vacuum and allowing it to carbonize then graphitize until ultimately left with a highly oriented graphite material. Graphite's sheet-like crystals known as graphene are stacked on top of each other, allowing for extremely high in-plane thermal conductivity (x-y direction/a-b plane) compared to its through-plane thermal conductivity (z direction/c plane) [32]. A summary on comparing the absorber materials used in previous studies in the literature on solar water heating systems is given in Table 1.

Table 1. Used materials and their properties at 21 °C [8, 23, 33-36].

Material	Thermal conductivity [W/(mK)]	Density [kg/m^3]	Cost [$/kg]
Pyrolytic graphite (PG)	1050 (in plane x-y) 20 (in z-direction)	1500	3.68
Pyrolytic graphite (PG)	1800 (in plane x-y) 15 (in z-direction)	2170	3.68
Copper sheet (Cu)	386	8930	7.35
Aluminum sheet (Al)	238	2700	2.45
Silica glass	1.38	2203	6.12 $/m^2
Polyurethane foam	0.03	30-80	3.68
Water (HTF)	0.58	1000	0.80 $/m^3

The PG sheets offer up to five times the thermal conductivity of copper, at only a fraction of the weight. There are numerous advantages of PG sheets, especially when compared to their metallic counterparts [32]:

- High in-plane thermal conductivity up to 1950 W/mK.

- Lightweight when compared to its metallic counterparts such as aluminum or copper.
- Highly anisotropic structure allows for high thermal conductivity only in the x-y plane.
- Can be die-cut into customizable shapes.
- Offered with adhesives for fast installation (peel-and-stick attachment).
- Can be laminated with plastics, metals, or foam to improve performance.

There are many applications of PG in thermal management as heat sinks, as thermal interface material and as thermal energy storage material due to its high thermal stability. PG has been used as a heat sink material due to its high thermal conductivity. In a study by Wen et al. (37), PGs was used for the thermal management of a fuel cell system. They found that PGS reduces the maximum cell temperature and improves cell performance at high cathode flow rates. The temperature distribution is also more uniform in the cell with PGS than in the one without PGS.

4. Results

In this study, in the analytical and the numerical calculations, copper, aluminum, glass, and aPG sheet are taken into consideration as the absorber materials to perform the collector with various absorbers. The Table 2 lists the materials' thermal characteristics as well as the weather conditions for the calculations.

Table 2. The weather conditions and the thermal properties of the materials used in the collector.

Solar radiation	1000 W/m^2
Aperture area of the collector	0.33 m^2 (1 x 0.33)
Emissivity of glass	0.94
Stefan-Boltzmann constant	5.67×10^{-8} W/m^2K^4
Ambient temperature	20 ^oC
Transmittance of the glass	0.97

Transmittance of water	0.83
Thickness of glass	0.003 m
Wind speed	2 m/s
Heat transfer coefficient of water	3000 W/m^{2}K
Water inlet temperature	15 ^{o}C
Mass flow of water	0.002 kg/s
Specific heat capacity of water	4186 J/kgK
Thickness of absorber	0.005 m

As an example, Figure 3 shows the temperature distribution inside the panel using a PG (1050/20) absorber.

Figure 3. Temperature distribution in the panel with an absorber made of PG.

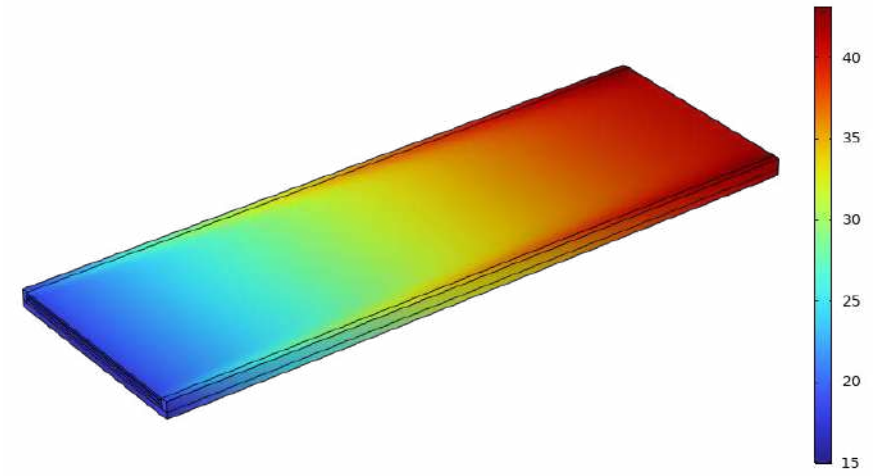

Table 3 shows the outcomes of stationary analytical and numerical calculations. Analytical calculations are performed assuming perfect isolation, but no assumption was made in the numerical calculations. In other words, one can see the heat transfer in numerical calculations for the collector's case and insulator layer (foam) as well.

Table 3. Stationary analytical and numerical results for the output water.

Absorber material	Analytical result, T_o (°C)	Numerical result, T_o (°C)
Copper	38.54	38.73
Aluminum	38.87	39.04
Glass	39.40	39.50
PG (1050/20)	39.44	39,51
PG (1800/15)	39,46	39,53

Pyrolytic graphite provides the best heat transfer according to time-dependent numerical simulations shown in Figure 4. Moreover, PG (1800/15) gives slightly higher results to those expected for highly conductive materials in [30]. In other words, increasing the thermal conductivity beyond a certain level will not improve the performance of the solar panel dramatically.

Figure 4. Material performance comparison. The legend shows used absorbers.

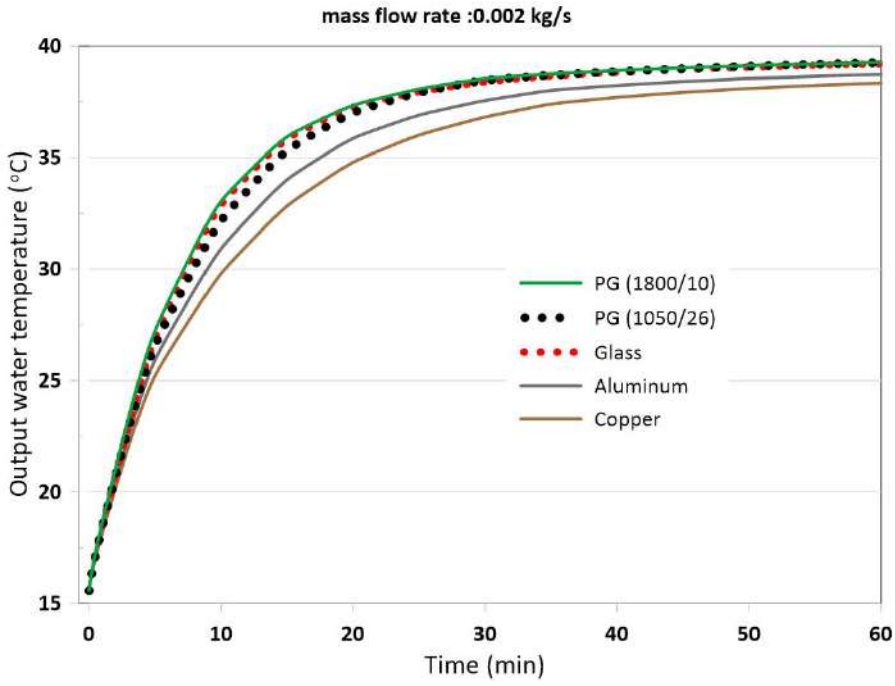

According to the stationary heat transfer calculations, the collector efficiency related to absorber material is given in the Table 4.

Table 4. The stationary collector efficiency related to absorber material.

Absorber material	Inlet water temperature (°C)	Outlet water temperature (°C)	Collector efficiency (%)
Copper	15	38.73	64.09
Aluminum	15	39.04	64.92
Glass	15	39.50	66.17
PG 1050/20	15	39.51	66.19
PG 1800/10	15	39.53	66.25

*Efficiency is based on the specific study and may vary depending on the design and operating conditions of the solar water heating system.

5. Conclusion

In this study, new materials such as pyrolytic graphite, glass for absorber plate of a solar water heater were introduced. A comparative performance analyze of the collector is done with different materials as well as the costs of each material is also presented.

The results make the model presented in this study remarkable with respect to absorber plates currently made of copper. Absorber plate made of pyrolytic graphite rise the water temperature faster and make the collector efficiency better than conventional materials such as copper and aluminum. Glass also offers better performance while maintaining a very low thermal conductivity. This is because longer wavelengths are produced when photons pass through glass and/or water and lose energy. As a result, long wavelength photons are trapped between the layers and their energy is transferred to the water. It is observed that the system's efficiency is 66% and the water temperature rises more quickly when both glass and pyrolytic graphite are used as absorbers.

Another reason that the model may give different results than expected may be due to the more complex computation of the flow properties and the unusually shaped channels that vary spatially.

It was seen that there is a potential in improving the efficiency of solar water heaters by further material studies. To verify the results from the analytical calculations and the numerical simulations, a collector prototype should be built and tested.

References

[1] C´edric Philibert. "The present and future use of solar thermal energy as a primary source of energy", *International Energy Agency,* Paris, 2005.

[2] R. Shukla, K. Sumathy, P. Erickson, and J. Gong, "Recent advances in the solar water heating systems: A review", *Renewable and Sustainable Energy Reviews*, 19:173–190, 2013.

[3] I. Sarbu and C. Sebarchievici, "Chapter 5 - solar water and space-heating systems", Eds. I. Sarbu and C. Sebarchievici, *Solar Heating and Cooling Systems*, pages 139–206. Academic Press, 2017.

[4] E. Ekramian, S. G. Etemad, and M. Haghshenasfard, "Numerical analysis of heat transfer performance of flat plate solar collectors", *Journal of Fluid Flow, Heat and Mass Transfer*, 1, 2014.

[5] B. Ramlow and B. Nusz, Solar *Water Heating*. 2nd edition, New Society Publishers, 2006.

[6] I. Sarbu and C. Sebarchievici, "Chapter 3 - solar collectors", Ed.s: I. Sarbu and C. Sebarchievici, *Solar Heating and Cooling Systems*, Academic Press, London, 2017.

[7] A. Amri, Z. T. Jiang, T. Pryor, C. Y. Yin, and S. Djordjevic, "Developments in the synthesis of flat plate solar selective absorber materials via sol-gel methods: A review", *Renewable and Sustainable Energy Reviews*, 36, 316–328, 2014.

[8] E. Vengadesan and R. Senthil, "A review on recent development of thermal performance enhancement methods of flat plate solar water heater", *Solar Energy*, 206: 8, 935–961, 2020.

[9] Y. Lu and Z. Chen, "Experimental study on thermal performance of solar absorber with CuO nano structure selective coating", *Energy Procedia*, 158, 1303–1310, 2019.

[10] S. Kahlen, G. M. Wallner, and R. W. Lang, "Aging behavior of polymeric solar absorber materials–Part 1: Engineering plastics", *Solar Energy* 84:9, 1567-1576, 2010.

[11] S. Kahlen, G. M. Wallner, and R. W. Lang, "Aging behavior of polymeric solar absorber materials–Part 2: Commodity plastics", Solar Energy 84:9, 1577-1586, 2010.

[12] Y. Selikhov, J.J. Klemeš, P. Kapustenko, O. Arsenyeva, "The study of flat plate solar collector with absorbing elements from a polymer material", Energy 256, 124677, 2022.

[13] S. A. Sakhaei and M. S. Valipour, "Performance enhancement analysis of the flat plate collectors: A comprehensive review", *Renewable and Sustainable Energy Reviews*, 102:3, 186–204, 2019.

[14] H. Pandya and A. K. Behura, "Experimental study of v-through solar water heater for tilt angle and glass transmissivity", *Energy Procedia*, 109, 377 – 384, 2017.

[15] R. P. Garcia, S. del Rio Oliveira, and V. L. Scalon, "Thermal efficiency experimental evaluation of solar flat plate collectors when introducing convective barriers", Solar *Energy*, 182, 278–285, 2019.

[16] Z. F. Huang, A. Nakayama, K. Yang, C. Yang, and W. Liu, "Enhancing heat transfer in the core flow by using porous medium insert in a tube", *International Journal of Heat and Mass Transfer*, 53:2, 1164–1174, 2010.

[17] P. Waramit, P. Chanmak, R. Peamsuwan, and B. Krittacom, "Forced convection enhancement of air flowing inside circular pipe with varying the pitch (p) of wire-mesh porous media", *Energy Reports*, 7:11, 70–82, 2021.

[18] B. Krittacom, S. Bunchan, and R. Luampon, "Heat transfer enhancement of solar collector by placing wire mesh stainless porous material on the solar absorber plate of indirect forced convection solar dryer", *Thermal Science and Engineering Progress*, 32:7, 2022.

[19] R. H. Martin, J. Perez-Garcia, A. Garcia, F. J. Garcia-Soto, and E. Lopez-Galiana, "Simulation of an enhanced flat plate solar liquid collector with wire-coil insert devices", *Solar Energy*, 85:3, 455–469, 2011.

[20] C. Armenta-Deu, "Performance test in semispherical solar collectors with discontinuous absorber", *Renewable Energy*, 143, 950–957, 2019.

[21] C. Armenta-D´eu. "Effective Absorber Area in Semispherical Solar Collectors with Spiral Cylindrical Absorber", *Journal of Solar Energy Engineering*, 141:6, 2019.

[22] W. M.K. Van Niekerk and T. B. Scheffler, "Measured performance of a solar water heater with a parallel tube polymer absorber", *Solar Energy*, 51: 1, 339–347, 1993.

[23] S. Gupta, S. Rajale, F. Raval, M. Sojitra, A. Kumar Tiwari, A. Joshi, and R. Singh, "Comparative performance analysis of flat plate solar collectors with and without aluminum oxide-based nano-fluid", *Materials Today: Proceedings*, 46, 5378–5383, 2020.

[24] A.A.M. Sayigh, Solar Energy Engineering, Academic Press Inc., London, 1997.

[25] J. Carvill, *Mechanical Engineer's Data Handbook*, Butterworth - Heinemann, oxford, UK, 2009.

[26] F. P. Incropera, D. P. Dewitt, T. L. Bergman, A. S. Lavine, Fundamentals of Heat and Mass Transfer: With Introduction to Mass and Heat Transfer, 6.th Ed., John Wiley & Sons Incorporated, MA, USA, 2007.

[27] R. J. Cole, N. S. Sturrock, "The convective heat exchange at the external surface of buildings". Building and Environment, 12:4, 207–214, 1977.

[28] A. Demharter, "Polyurethane rigid foam, a proven thermal insulating material", *Cryogenics*, 38, 113–117, 1998.

[29] Standard tables for reference solar spectral irradiance at air mass 1.5: Direct normal and hemispherical for a 37-degree tilted surface, https://www.astm.org/g0173-03r20.html, accessed 10.01.2023.

[30] A. M. Shariah, A. Rousan, Kh. K. Rousan, and A. A. Ahmad, Effect of thermal conductivity of absorber plate on the performance of a solar water heater", *Applied Thermal Engineering*, 19:7, 1999.

[31] <URL> https://www.schukat.com/, accessed on 27/01/2023

[32] <URL> https://hpmsgraphite.com/pyrolyticgraphitesheet, accessed on 27/01/2023.

[33] <URL> https://www.indiamart.com/, accessed on 27/01/2023.

[34] <URL> Panasonic Industry," pgs" graphite sheet, https://www.digikey.com/en/product-highlight/p/panasonic/ pyrolytic-graphite-sheets, accessed on 27/01/2023.

[35] <URL> Su Birim Fiyatları, https://www.iski.gov.tr/web/tr-TR/musteri-hizmetleri/su-birim-fiyatlari1, accessed on 27/01/2023.

[36] <URL> Cam fiyatları - 1 m2 cam ne kadar? https://birimfiyatim.com / cam-fiyatlari-1-metrekare-cam-ne-kadar/, accessed on 27/01/2023.

[37] Chih-Yung Wen, Guo-Wei Huang, Application of a thermally conductive pyrolytic graphite sheet to thermal management of a PEM fuel cell, Journal of Power Sources, 178:1, 2008, 132-140.

Chapter 6

Using of Electric Scooters in the Individual Electric Vehicle Category to Improve the Life Quality of Physically Disabled Person: A New Electric Wheelchair Design with Brushless DC Motor and Li-Ion Battery

Taner Çarkıt[1]

Anıl İbrahim Topçular[2]

Mehmet Yılmaz[3]

Türkan Ağır[4]

Gökhan Cumali[5]

Abstract

According to the information obtained from the World Health Organization, more than 1 billion individuals, which corresponds to approximately 15% of the world's population, have various disabilities. Dysfunction is seen in approximately 720 million people in this rate. Similarly, approximately 12.5% of Türkiye's population has various disabilities. Approximately 2.5 million people in this population have a physical disability that requires the use of manual and electric wheelchairs. In this study, it is aimed to realize a new engineering-based design for individuals who need the use of manual or battery powered chairs with motivation supported by technological development and change. The mobility of the prototype product is provided by the Li-Ion battery energy transferred to the brushless DC motor. SolidWorks computer program has been used during the design phase. As a result of research, development, modification and design studies on electric scooters and wheelchairs, which are in the category of individual electric vehicles, a new prototype product has been obtained. The advantages, disadvantages

1 Dr., Kırklareli University, tanercarkit@klu.edu.tr, 0000-0002-5511-8773

2 BSc., WattEnergy Ltd., Co., anilibrahimeem@gmail.com

3 BSc., Mert Döküm Inc., mehmetyilmaz092@gmail.com

4 BSc., turkanagir8@gmail.com

5 BSc., Teklas-Bulgaria EAD Inc., gokhancumali9@gmail.com

https://doi.org/10.58830/ozgur.pub130.c578

and mobility features are emphasized by making comparisons with existing products.

1. Introduction

Depending on the changing disability definition and classification systems in the world, data collection criteria regarding the profile of the disabled in Turkey are also transforming. Questions and information on disability have been prepared by the "General Directorate of Services for the Disabled and Elderly" [1]. In the creation of these data, the disability question set, which has been created by considering the regional studies as well as the studies, censuses, researches and "Washington Group" recommendations made within the United Nations (UN) in related fields, has been useful. The question set in question has been also developed in accordance with the "International Classification of Functioning, Disability and Health (ICF)" developed by the World Health Organization (WHO).

The last current research that estimates the distribution of disabled people on a provincial basis throughout Turkey is the "2011 Population and Housing Survey" [2]. With the new approaches in the definition and classification of disability, in the research conducted in 2011, disability has been defined as follows: It focuses on limitations in functions rather than medical approach (organ loss, dysfunctions). In the research, disability is visual, hearing, speaking, learning for peers/performing simple four operations, remembering/concentration and mobility (walking, carrying, holding and going up and down stairs).

According to the information obtained from the WHO in 2021, more than 1 billion individuals, which corresponds to approximately 15% of the world's population, have various disabilities [3]. Dysfunction is seen in approximately 720 million people in this rate [4]. Similarly, approximately 12.5% of Türkiye's population has various disabilities. Approximately 2.5 million people in this population have a physical disability that requires the use of manual and power wheelchairs [5]. In addition, approximately 2500 people suffer from spinal cord paralysis every year in Turkey [6]. Almost all of these individuals who have had a stroke lose their ability to walk.

In the literature, the wheelchairs shown in Figure-1 have been developed to partially meet the living standards and expectations, ability and transportation needs of individuals with physical disabilities. There are two types of wheelchairs, which are seen as a tool and used to partially meet the needs of people who cannot walk or move easily due to a physical disorder

or disability, such as providing mobility and transportation, increasing their living standards and meeting their expectations [7]:

- Manual wheelchair,
- Powered (battery) wheelchair.

Figure-1: Wheelchair

Manual wheelchairs, which are based on mechanical mobility and developed as the first product, are based on human power. Transportation in the city is very difficult with manual wheelchairs. Manual wheelchairs are tools that give people the ability to move with muscle power. To look at the development of the manual wheelchair in the literature, although its history dates back to 4000 BC [8], it was turned into a product by the English inventor James Heath in 1750 AC. In 1933, Jennings & Everest added the foldable feature and turned it into a wheelchair. Choosing a wheelchair suitable for their physical condition and living standards is seen as a useful tool to improve the health, social and economic conditions of people with walking difficulties. The average weight of manual wheelchairs varies between 9 and 20 kg. The benefits of using a wheelchair for physically disabled people can be listed as follows:

- It increases the mobility of people to realize the things they cannot do freely and want to do,
- Users are provided access to social life by providing access to places such as schools, shopping, markets and homes,

- It can provide freedom in limited capacity by keeping their own lives under control with the mobility gained by the users' muscle power [9].

Developed as an alternative to manual wheelchairs, battery-powered wheelchairs are a technological product. Battery-powered chairs are produced with a mechanical-electrical-electronic design for the use of people who have walking difficulties, who cannot walk completely or partially, and who cannot turn the wheels with arm strength. Considering the development of battery-powered chairs in the literature, although the prototype product creation studies could date back to 1916 AC, it was turned into a commercial product by George Klein after the 2nd World War [10]. In the 2010s, R&D studies have been carried out on commercial products and battery-powered chairs that could be controlled by brain signals have been developed [11]. The weight of the electric chairs can start from 35 kg and go up to 85 kg. The load capacities they can carry vary between 100 kg and 200 kg. Battery-powered wheelchairs also have some disadvantages such as:

- Difficulty moving on uneven (rough) floors,
- Unable to fold,
- Covering a large area in the usage area,
- Difficult to transfer with one person due to their weight,
- Some models cannot brake on slopes due to low engine power, forcing the user to open the handbrake,
- Possible control lock failure,
- Difficulty in transportation with vehicles in daily use.

In this study, one of the basic building blocks of the prototype product designed by making technological contribution and difference is the electric scooter. Looking at the development of the electric scooter in the literature, a product that can be steered with an arm and a pedal was developed by Honda in 1974. In 1996, foldable scooters became available worldwide. After the 2000s, the use of electric scooters has spread more and more. They are mobility solutions in individual electric vehicles that are becoming more and more widespread in the transportation sector such as electric scooters and electric bicycles. It is foreseen that it will come to the fore in the formation of new mobility business models such as scooter rental, pick up from wherever you want / drop off wherever you want. Electric scooters are among the most popular transportation vehicles of recent times

in providing short distance transfers within the city. Especially in cities with a large population and in smart city works, the means of transportation offered by technology companies to reduce traffic are electric scooters. It is predicted that the market share of electric scooters will reach 38.6 billion USD by 2025 [12]. It is predicted that the market share will reach 42 billion USD by 2030 [13]. According to Mc Kinsey's global research report, it is predicted that worldwide "Micro Mobility (micro mobility)" companies will generate revenues between 150 billion USD and 500 billion USD by 2030. According to McKinsey's research report in 2019, 40% of car journeys are made for distances below 5 kilometers, while electric scooter technology, which provides short-distance transportation service, has achieved good success in a short time and reduced car usage [14-16].

It is thought that the advantageous features of the prototype product, which is expected to be obtained from the research, analysis and test stages in the study, such as being light, being easily foldable, and being easily portable, will be effective in the preference of the users. The aim of this study has been to obtain a multifunctional technological wheelchair by eliminating the disadvantages of manual and battery powered wheelchairs.

2. Method and Materials

Table-1 shows the number of individuals with at least one disability in the general population in Turkey by age group and gender. Similarly, the detailed version of the data in Table-1 according to the nature of the disability is presented in Table-2. In Table-2, the detailed distribution of the proportion of the disabled population in the general population is given [2]. Considering the walking disability category in the table that is directly related to this study, it seems essential to carry out such a study in this paper.

Table-1: Distribution of the population with at least one disability in the general population by age group and gender

Disabled Human	Population Ratio (%)	Male (%)	Female (%)
All Age Groups	**6.9**	**5.9**	**7.9**
3-9	2.3	2.5	2.1
10-14	2.1	2.4	1.8
15-19	2.3	2.6	2.0
20-24	2.7	3.4	2.0
25-29	2.6	3.0	2.3

Disabled Human	Population Ratio (%)	Male (%)	Female (%)
30-34	3.2	3.4	3.0
35-39	4.0	4.0	4.1
40-44	5.1	4.7	5.6
45-49	6.9	5.9	7.8
50-54	8.8	7.1	10.7
55-59	12.1	9.2	15.0
60-64	16.5	12.3	20.4
65-69	23.0	18.3	27.2
70-74	31.9	26.3	36.3
75 +	46.5	40.9	50.3

Table-2: Distribution of the disabled population in the general population by disability group

Disability Group	Total Population Ratio (%)	Male (%)	Female (%)	Total (Number of Persons)	Male (Number of Persons)	Female (Number of Persons)
Seeing	1.4	1.3	1.5	1 039 000	478 000	561 000
Hearing	1.1	1.1	1.2	836 000	406 000	429 000
Speaking	0.7	0.8	0.6	507 000	278 000	229 000
Walking	3.3	2.4	4.1	2 313 000	861 000	1 452 000
Holding, Carrying	4.1	3.2	5.1	2 923 000	1 136 000	1 787 000
Learning, Remembering	2.0	1.6	2.4	1 412 000	565 000	847 000

The mobility of the product, which is planned to be designed within the study, is provided by the DC (Hub) brushless motor in Figure-2, whose power can vary in the range of 250-350W [17, 18]. It is planned to use a ready-made intermediate product as a motor protection and driving circuit.

The advantages of the engine preferred in the design in this study can be stated as follows:

- Having high efficiency,
- Requiring less maintenance than other engines,
- Having a long service life,
- Low electrical noise ratio,
- Existence of mobile motor capability. In this study, the motor is placed in the front wheel (Alternatively, the engine can be placed in the rear wheel).

In addition to the advantages that affect its preference in the market, the engine also has some disadvantages:

- High installation cost,
- Confuse controls,
- High price,
- Requiring external power electronics circuit.

Figure-2: DC HUB motor

It is planned to use 18650 cylindrical type Li-Ion battery cells in 6-8 serial connection configuration during the transfer of energy to the electric motor [19]. The speed and range level of the motor in the product varies according to the connection configurations of the electrochemical Li-Ion battery cells used in the battery block. To give the product a multi-functional mobility feature, it is foreseen that the battery block should be in the front of the metal frame that forms the prototype skeleton in Figure-3. The importance of R&D activities in secondary electrochemical Li-Ion battery cells, called rechargeable cells, is increasing day by day. In addition to the

increasing demand for portable electronic devices, the increasing importance of individual/collective electric vehicles in the transportation sector increases the importance of Li-Ion batteries day by day [20, 21]. Some of the reasons why Li-Ion batteries are preferred as a power and energy unit in technological developments are as follows:

- Long life,
- No memory effect,
- Not require maintenance,
- Some types enable fast charging,
- Having high energy efficiency (≥ 90%),
- Having energy conversion efficiency,
- High energy-power density (270Wh/lt, 220 Wh/kg),
- Wide operating temperature range (-20, +60 C),
- High safety rates of some species by making different additives.

In addition to the advantages of Li-Ion batteries, there are naturally disadvantages that should be considered:

- Medium-high price ratio (Despite its high price, production costs are decreasing day by day),
- Requiring a protective electronic control circuit in order to take security measures (Battery management system (BMS) and charge control based protective electronic circuits).
- Loss of capacity that occurs normally due to long-term use,
- Loss of capacity as a result of overcharge-discharge.

Figure-3: Battery layout

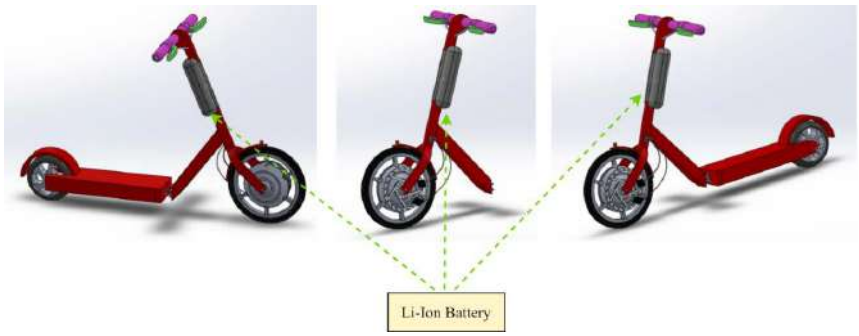

The prototype product in Figure-4, designed in the study, can be put into the service of disabled individuals in the form of a wheelchair. Moreover, it can be offered to individuals without disabilities due to its ability to transform into an electric scooter and use it while standing. Another advantage of the design is that it can be used easily on uneven and sloping floors. The design is more convenient and practical for physically disabled individuals using wheelchairs compared to battery powered chairs. It also meets the expectations of individuals better by raising their living standards. While the design can be turned into an electric scooter by easily attaching to the wheelchair with mechanisms such as hooks or grippers, it can also be transformed into an electric scooter that can be used by a normal person without disabilities by attaching the other standing part of the scooter. On the other hand, optionally, a seat mechanism with plug-in feature can be added to use the scooter in a sitting position. It is planned to gradually control the speed parameter of the prototype in the design and increase it up to approximately 20-25 km/h. The weight of the power and steering part of the product is aimed to be approximately 12-14 kg. The carrying capacity of the product is expected to be in the range of 100-150 kg. It is foreseen that this weight will provide comfort and convenience in transportation and in case of being taken to desired places.

Figure-4: Designed product

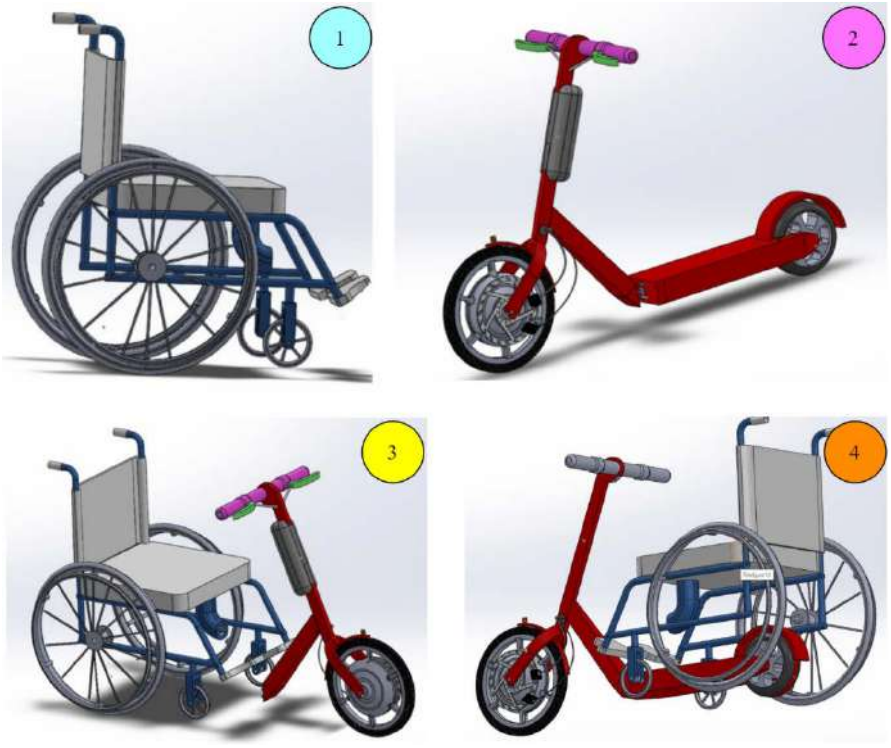

3. Conclusion and Discussion

The design, which is seen as a single product, can transform into two different products and fulfill two different functions as both an electric scooter and a battery powered wheelchair. On the other hand, it can be used as four different products. As a result of the design, it is aimed to obtain a product for the physically handicapped and their families who use medical devices and apparatus such as wheelchairs, battery powered chairs and walking sticks. In the battery part, which is the power source of the product planned to be designed, it was deemed appropriate to use Li-Ion batteries, one of the components of clean energy and current technology.

An output that is more useful, practical, more efficient, more environmentally friendly and more suitable for the consumer, raising the living standards and meeting the expectations of the individuals better has been achieved for the physically disabled individuals using wheelchairs with the help of the designed product. While the design can be turned into an electric scooter by easily attaching to the wheelchair with mechanisms such as hooks or grippers, it can also be transformed into an electric scooter that

can be used by a normal person without disabilities by attaching the other standing part of the scooter. A prototype that is ready for the use of the user and their family at any time, which offers the opportunity to be transported by being folded in the trunks of cars in daily use, has been obtained. In the prototype, which is the subject of the study focused on R&D and innovation, the opportunity to offer two products (with four different usage options) to a wide market share has arisen as the biggest innovation element.

As a result, it is aimed to improve the mobility of physically disabled individuals and to present a common product prototype that can be used by their families and themselves.

Acknowledgement

Thanks to TÜBİTAK for providing project support to the work at the focal point of this study, Erdoğanlar Alimünyum Inc. and Kırklareli University for their material and moral support of the project.

References

[1] Ministry of Family and Social Services, General Directorate of Disabled and Elderly Services, "Publication/Source", (Web: https://www.aile.gov.tr/eyhgm/yayin-kaynak/), (Access Date: 2023).

[2] Ministry of Family and Social Services, "Disabled and Elderly Statistics Bulletin", 2022.

[3] Anatolian Agency, (Web: https://www.aa.com.tr/tr/turkiye/turkiyede-yaklasik-2-5-milyon-ortopedik-engelli-var/1143665), (Access Date: 2023).

[4] World Health Organization, "World Disability Report", 2011.

[5] Öztabak, M. Ü., "Investigation of Life Expectations of Disabled Persons", FSM Scholarly Studies Journal of Humanities and Social Sciences, No. 9, pp. 355-375, 2017.

[6] Ekenci, M. T., "Analyze of Turkey Health Survey 2012 in terms of Measurement of Disability Prevalence", Journal of Social Policy Studies, Vol. 35, No. 2, pp. 95-112, 2015.

[7] Vikipedia, (Web: https://tr.wikipedia.org/wiki/Tekerlekli_sandalye), (Access Date: 2023).

[8] Disabled Platform, (Web: https://engelliler.gen.tr/f19/tekerlekli-sandalyenin-tarihcesi-8319/), (Access Date: 2020).

[9]] World Health Organization, "Wheelchair Service Training Package", 2012.

[10] Bellis, M., "History of the Wheelchair", (Web: https://tr.eferrit.com/tekerlekli-sandalyenin-tarihcesi/), (Access Date: 2020).

[11] India Today, (Web: https://www.indiatoday.in/lifestyle/wellness/story/no-buttons-no-joystick-please-welcome-the-worlds-first-mind-controlled-wheelchair-created-by-diwakar-vaish-313689-2016-03-17), (Access Date: 2020).

[12] Haber Türk, (Web: https://www.haberturk.com/elektrikli-scooter-isine-girdiler-2510990-ekonomi), (Access Date: 2020).

[13] Haber Türk, (Web: https://www.haberturk.com/turkiye-ye-geliyor-2507069-ekonomi), (Access Date: 2020).

[14] McKinsey & Company, "Micromobility's 15000 Mile Checkup", 2019.

[15] Anatolian Agency, (Web: https://www.aa.com.tr/tr/dunya/sehir-ici-kisa-mesafede-yeni-trend-elektrikli-scooter/1416602), (Access Date: 2020).

[16] Time Turk, (Web: https://m.timeturk.com/sehir-ici-kisa-mesafede-yeni-trend-elektrikli-scooter/haber-1055294), (Access Date: 2020).

[17] Hüner, E., Ekren, N., Akıncı, T. Ç., "An Overview Wheel Motor and Using in Electrical Vehicles", e-Journal of New World Sciences Academy Natural and Applied Sciences, Vol. 3, No. 2, pp. 298-309, 2008.

[18] Adams, W., "Electric Motor, Specification forming part of Letters Patent No. 300,827. Patented June 24, 1884. Application filed March 27, 1883.

[19] Uysal, M., Gül, H., "Characterization and Electrochemical Properties of the Sn-Cu/Rgo (Reduced Graphene Oxide) Anode Materials for Lithium Ion Batteries", Academic Platform Journal of Engineering and Science, Vol. 5, Issue 3, pp. 19-25, 2017.

[20] Moralı, U., Erol, S., "Electrochemical Impedance Analysis of 18650 Lithium-Ion and 6HR61 Nickel-Metal Hydride Rechargeable Batteries", Journal of the Faculty of Engineering and Architecture of Gazi University, Vol. 35, No. 1, pp. 297-309, 2020.

[21] Polat, B. D., Keleş, Ö., "Lithium Ion Battery Technology", Union of Chambers of Turkish Engineers and Architects (UCTEA) Journal of UCTEA Chamber of Metallurgical and Materials Engineers, Technical Writing, pp. 42-48, 2012.

Chapter 7

GIS-Based Evaluation of Disaster and Emergency Assembly Areas with AHP in Local Scale

Deniz Arca[1]

Hülya Keskin Çıtıroğlu[2]

Abstract

In an area that is tectonically active and has various fault zones, earthquakes of varying magnitudes have occurred in our country both in the past and today. Like in the rest of the world, various analyses and research are being conducted in our country to eliminate or minimize the loss of life and property caused by earthquakes. In this study, the locations of existing disaster and emergency assembly areas in the Ovacık district were determined and visualized on Google Earth. Furthermore, using Geographic Information Systems (GIS)-based analysis and weighted overlay method, a risk classification was conducted. To this end, basic inputs in the GIS environment, including slope, geology, distance to rivers, distance to roads, distance to settlements, elevation, distance to fault lines, land use, and population data layers, were used. Existing collection areas were digitized and incorporated into this framework as vector layers. The disaster and emergency assembly area sensitivity map of the study area is divided into 3 sensitivity classes. According to this map; regions of high, middle and low sensitivity were obtained as 8.35%, 76.23% and 15.42%, respectively. It is observed that both existing assembly areas are within the high sensitivity zone. The two existing assembly areas are geologically located within the Karabük formation (Teka). Because it contains coal levels, assembly areas on the Karabük formation require more detailed field studies and taking field measures. Apart from this, it has been observed that the existing assembly areas comply with the other parameters used.

1 Department of Architecture and Urban Planning, Izmir Vocational School, Dokuz Eylul University, Izmir, Türkiye, deniz.arca@deu.edu.tr Orcid: 0000-0002-0439-4938

2 Directorate of Investment Monitoring and Coordination, YIKOB, Aydın, Türkiye keskinhc@yahoo.com Orcid: 0000-0002-2999-9570

https://doi.org/10.58830/ozgur.pub130.c603

1. Introduction

Disasters, which are natural or human-induced events that cause various losses affecting the whole or a specific part of society, disrupt normal life and activities. One of the most destructive natural disasters is earthquakes, which are prevalent worldwide and also affect Türkiye due to its geographical location. Earthquakes occur when vibrations generated by fractures in the Earth's crust propagate as waves, causing shaking (Özkılıç, 2020). Earthquakes lead to people becoming homeless due to the collapse or damage of structures, and shelter becomes one of the primary needs for affected individuals after an earthquake. The diminishing open and green spaces that individuals use for gathering and shelter day by day pose a significant problem. The absence of a well-established open and green space system resulting from unregulated urbanization nationwide poses a significant risk, especially during earthquakes and other disasters. Therefore, this issue has started to be addressed within the scope of disaster management (Aman, 2019). The fact that the issue of determining the post-disaster assembly and emergency shelter (tent-city) areas cannot be resolved and that this issue is always left to the post-disaster period prevents being prepared for disasters. Disaster and emergency assembly areas are pre-determined easily accessible, adequately sized, and capacity-equipped safe areas for individuals to feel secure after a disaster.

The determination of disaster and emergency assembly areas, evaluation of their capacities, and establishment of routes are carried out using Geographic Information Systems (GIS) in many studies conducted within the framework of disaster management. GIS allows data integration, querying, spatial analysis, and network analysis. Timely and effective post-disaster response is important in reducing losses. GIS plays an effective role in minimizing the potential losses caused by potential disasters (Turoğlu et al., 2010). Geographic Information Systems (GIS) capture spatial data obtained from various sources such as maps, digital images, and tabular data, extract specific features from the data, and combine them to produce new derived maps that are useful for decision-making and understanding spatial relationships (Carter, 1994). When multiple data need to be evaluated simultaneously in GIS-based analysis and their impact factors are not equal, the weighted overlay method can be used. Therefore, not evaluating all criteria equally will enable more realistic synthesis.

In this study, basic inputs in the GIS environment, including slope, geology, distance to rivers, distance to roads, distance to settlements, elevation, distance to fault lines, land use, and population data layers, were used. Existing collection areas were digitized and incorporated into this framework as vector layers.

Numerous studies have been conducted both in Türkiye and worldwide to determine disaster and emergency assembly areas, and it has been observed that different criteria are taken into account in each study. This indicates the lack of universal standards and criteria for determining disaster and emergency assembly areas. In the creation of assembly areas, issues such as population, accessibility, suitability for disabled and elderly transportation, unevenness of the land, proximity to structures where basic needs can be met, secondary hazards, distance from sea, river, liquefaction and fault lines have been put forward by the Disaster and Emergency Management Presidency (AFAD) (AFAD, 2023a; Şirin and Ocak, 2020). Despite the existence of studies aimed at establishing criteria and standards for determining assembly areas in Türkiye, the preferences for these areas are ultimately determined by the discretion of local authorities. Therefore, this study will contribute to the establishment of criteria and standards for determining collection areas specifically in the Ovacık district and the systematic approach to addressing collection areas through the academic work conducted in the Ovacık district.

2. Study Area

The district of Ovacık in the province of Karabük located in the region of Western Black Sea in Türkiye. The study area covers an area of 13,165 ha. The study area is sided by the provinces of Çankırı in the south, Kastamonu in the east and Karabük in the west and the district of Safranbolu in the north (Fig. 1).

Figure 1. Site position map (URL-1, 2020, Keskin Citiroglu and Arca, 2022).

Ovacık has a mountainous, forested and rough land structure. Although there are many small-scale streams that flow in winter and dry up in summer, the largest stream in the district is Soğanlı (Melan) river (Ovacık District Governorship, 2023). There are no industrial facilities in the district consisting of 42 villages and 1 central neighborhood. There are an electricity-operated flourmill and small-scale workshops (Ovacık Municipality, 2023).

According to the census based on address records system data of recent year, the population of the district of Ovacık was 3731 (Turkish Statistical Institute, 2023). When compared with the population figures of previous years, it has been observed that there is a continuous decrease in the population of the district. There are migrations out of the district towards mainly Karabük, Istanbul and Ankara in addition to other provinces, and thus, the population decreases in comparison to previous years (Ovacık Municipality, 2023). There are two disaster and emergency assembly areas in the Ovacık district, which is the study area (Karabük AFAD, 2023).

3. Importance of Assembly Areas after Earthquake

During an earthquake or in the first minutes of an earthquake, due to the panic among people, there is a need for publicly owned and easily accessible areas where people can easily notice and move from indoor spaces to open areas. These areas are defined as assembly areas (Kırçın et al., 2017). Assembly areas are the first stage of the evacuation process and serve multiple purposes in the context of disasters. Squares, open and green spaces, sports halls, marketplaces, school or public institution gardens are potential use areas during disasters. Assembly areas are important as they serve as short-term accommodation areas before transitioning to temporary shelter areas (Çelik et al., 2018).

After a disaster, the first 12 to 24 hours are crucial for disaster victims to access accurate information. In this environment of panic and chaos, it is essential not only to provide accurate information but also to ensure the evacuation and management of people towards safe areas without physical hazards, timely arrival of response teams at the scene, and prevention of chaos in the environment. Therefore, it is of utmost importance to determine safe assembly areas within the city, announce these areas to the public, especially on a neighborhood basis, assign trained personnel who are familiar with the community and direct citizens to these areas according to pre-prepared programs, and ensure the safe transportation of those who have survived the disaster to secure environments (Çiçekdağı and Kırış, 2012). When creating assembly area criteria, five factors are taken into consideration: accessibility,

usability and multifunctionality, connection with road axes, property, and spatial size (JICA and IMM, 2002).

4. Establishment of Decision Criteria

The primary purpose of assembly areas is to reduce or eliminate risks in order to ensure the safety of individuals during emergencies. The factors influencing the determination of assembly areas in the Ovacık district center have been identified through national and international studies. These factors include slope, geology, distance to rivers, distance to roads, distance to settlements, elevation, distance to fault lines, land use, and population.

4.1. Slope

The criterion of slope is a factor that affects the accessibility of the assembly areas during the site selection process. It can contribute to drainage issues that may cause water accumulation or secondary hazards such as earthquake-induced landslides and soil erosion. Suitable slopes facilitate pedestrian access and provide convenience for the establishment of temporary shelters such as tents and container-like shelters. For pedestrian access, the preferred areas should have an average slope of 5% and a maximum slope of 8% (NZ Transport Agency, 2009). According to the Turkish Red Crescent, the maximum slope for potential assembly and shelter areas is determined as 7%, with a preference for slopes ranging from 2% to 4% (Kılcı et al., 2015). Areas with slopes steeper than 25% pose a high risk of mass movement and landslide hazards and are not suitable for pedestrian access. On the other hand, areas with slopes ranging from 2% to 8% are considered stable and safe (Soltani et al., 2014; Soltani et al., 2015). The slope map of the study area was derived from a 12.5m resolution DEM dataset specific to the region, using GIS (Fig. 2a).

4.2. Geology

From the bottom to the top, the study area stratigraphically includes the Ulus formation (Ku), Kışlaköy formation (Tek), Safranbolu formation (Tes), Karabük formation (Teka) and the Çerçen member of this formation (Tekaç), Soğanlı formation (Teso), Akçapınar formation (Tea), Yunuslar formation (Teyu) and alluvium (Qal). Ulus formation (Ku) consisting of alternations of claystone, shale, marl, sandstone, limestone, sandy limestone and conglomerate. The Kışlaköy formation (Tek) has alternations of marl, sandstone, conglomerate, limestone, siltstone and claystone. The Safranbolu formation (Tes) starts with a thin conglomerate-sandstone

layer at the bottom and transitions to layers of carbonate sandstone, sandy limestone and limestone upwards. The Karabük formation (Teka) consists of marl at the bottom layers and alternations of claystone, sandstone and also thin coal levels upward. The Çerçen Member (Tekaç) of the Karabük formation consists of sandstone, conglomerate, claystone, siltstone and mudstone. The Soğanlı formation (Teso) consists of limestones and also marl layers among limestone layers. Limestones have joints and deep karst structures in the Soğanlı formation. The Akçapınar formation (Tea) has an alternations of dolomitic limestone, mudstone, claystone, marl, but mainly argillaceous limestone. The Yunuslar formation (Teyu) has an alternations of conglomerate, marl, mudstone, sandstone and shale. Alluvium (Qal) aged Quaternary consists of sand, gravel and mud sediments developing on riverbeds, old concavities and flat areas (Timur and Aksay, 2002). As alluvium has an uncemented and discretely grained unit structure, it is not suitable for assembly areas. As it contains deep karstic structures, assembly areas on the Soğanlı formation, and it contains coal levels, assembly areas on the Karabük formation require more detailed field studies. The other formations in the study area are to varying degrees suitable for assembly areas provided that detailed research. The geology map of the study area is given in Fig. 2b (Timur and Aksay, 2002).

4.3. Distance to River

Seasonal changes experienced in streams (floods and increased flow rates at certain points during the year) and long-term location changes experienced in the course of streams are among important factors that affect the locations of disaster and emergency assembly areas. For these reasons, for disaster and emergency assembly areas to not be affected by floods and for easy transportation to the assembly areas to be achieved, assembly areas need not to be too close to rivers (Fig. 2c). The largest stream in the district is Soğanlı (Melan) river in the study area.

4.4. Distance to Road

Accessibility has been the most repeated criterion in the determination of assembly areas location selection criteria. In the event of a disaster, people must be able to reach assembly or shelter areas safely. It is necessary to plan as evacuation routes and to be designed according to the rules determined by the laws and regulations so that the roads are not closed in case of emergency and allow people to remove. During a disaster, while people flee from closed areas, chaos occurs in traffic due to the simultaneous movement of pedestrians and vehicles (ECPFE and OASP, 2002). The distance from

the building blocks to the assembly areas should be maximum 500 m or less, and the connection of the assembly areas with the main arteries should be established and their continuity with the other assembly areas should be ensured (Çınar et al., 2018). Buffer zones were created to investigate the effect of the road factor on the assembly areas (Fig. 2 d)

4.5. Distance to Settlement Areas

Another important point to be considered in the selection of assembly areas is that these areas are far enough away from the buildings to protect them from the dangers of falling debris, glass, etc. The larger the potential area, the less likely it is to be affected by the building collapse hazard. As it gets closer to the center of the assembly area, the rate of being affected by the danger of collapse of the building decreases. At the same time, it should be close enough to allow people to reach the assembly areas on foot. Buffer zones were created to investigate the effect of the residential areas factor on the assembly areas (Fig. 2e).

4.6. Elevation

When determining assembly areas, it is preferable to choose locations that are elevated above sea level in order to protect against tsunami and flood hazards. In order to utilize elevation data in the analyses, continuous data representing elevation values as surfaces are required, rather than discrete data that exhibits discontinuity (Demir, 2018). The elevation data for the study area has a resolution of 12.5 meters. The elevation map of the study area is shown in Figure 2f.

4.7. Distance to Fault Lines

Distance to fault lines is another determining parameter in assembly area assessment. In the neighborhoods established on the active fault, the emergency assembly areas on the faults will not be safe in case of an earthquake and will also receive the greatest damage (Aşıkkutlu et al., 2021). Moreover, there are no active faults in the study area, and the area is approximately 20 km far from the Northern Anatolia Fault Zone (NAFZ) (MTA, 2023; AFAD, 2023b; Timur and Aksay, 2002) (Fig. 2g).

4.8. Land Use

Land use is an important factor in determining the most suitable locations for disaster and emergency assembly areas. It is essential to consider factors such as the gathering areas not being far from settlements and not being

established on lands used for agriculture or forestry (Şirin and Ocak, 2020). In this study, land use was examined under 5 classes as pasture, forest, irrigated farming, dry farming and residential (MEUT, 2020) (Fig. 2h).

4.9. Population

The size of the assembly area is an important factor for the safety of the people staying. Evacuation areas should be planned to accommodate a large number of people after the disaster, so the location should be chosen to allow faster and more convenient transportation to areas with high population density in order to take into account the number of people served by the area (Chu and Su, 2011) According to the census based on address records system data of recent year, the population of the district of Ovacık was 3731 (Turkish Statistical Institute, 2023). The population map of the study area has been generated in a GIS environment using the interpolation method (Fig 2i)

Figure 2. Parameters. (a slope, b geology, c distance to rivers, d distance to roads, e distance to settlements, f elevation, g distance to fault lines, h land use, i population)

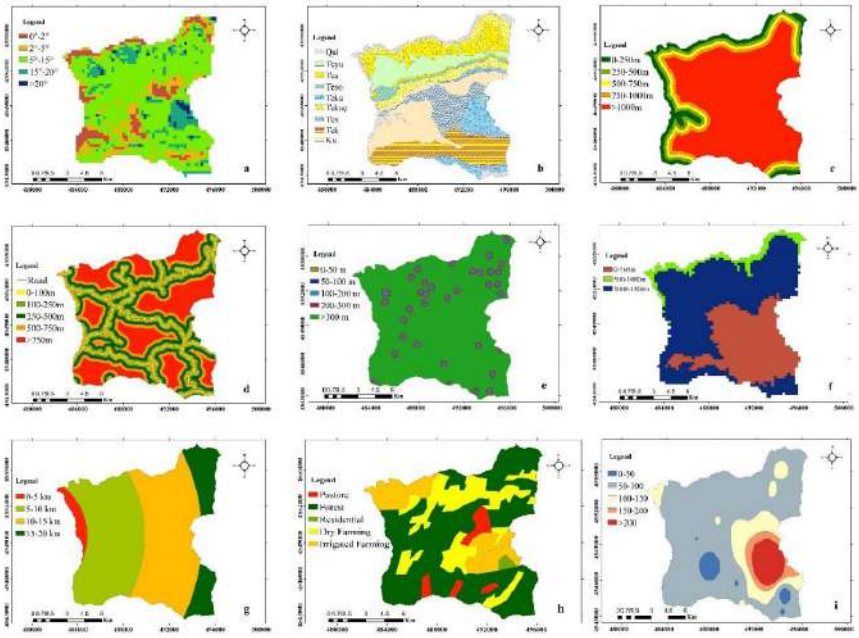

5. Method

The study utilized Geographic Information System (GIS) technology. Geographic Information Systems (GIS) is one of the effective methods used in disaster management and planning studies due to its capabilities in spatial data management, spatial analysis, and graphical visualization, enabling query and analysis. The reasons for the effective use of GIS in disaster management are its role as an efficient data sharing tool, the ability to collect and share data in the same format from different institutions that collect data in different formats, the ability to keep the data up-to-date, quick data analysis and providing easy solutions, and the versatility in visualizing data in the form of maps, graphs, and tables (Arca, 2012).

The Analytic Hierarchy Process (AHP) was used in determining the relative importance of criteria and scoring the identified potential areas according to the criteria in the process of creating the decision matrix for this study. Developed by Thomas Lorie Saaty in the 1970s, the Analytic Hierarchy Process (AHP) is fundamentally based on pairwise comparisons and seeks to answer the question "Which one?" (Ünal, 2011). AHP is a widely preferred method in comparing, evaluating, ranking, and selecting alternatives by expressing the relationship between objectives, criteria, sub-criteria, and alternatives in a complex problem faced by a decision-maker (Chandran et al., 2005). The most significant advantage of AHP compared to other multi-criteria decision-making methods is its ease of use and its ability to successfully handle complex decision problems that encompass both objective and subjective judgments (Yıldırım and Önder, 2015).

In his study, Turgut (2015) mentioned the reasons why AHP is chosen by many researchers. These reasons include:

a. Not requiring extensive technical knowledge to apply AHP.

b. Some data being created based on individuals' discretion.

c. Evaluating criteria individually and comparing them pairwise.

d. Having a simple process that allows different individuals with different opinions to reach a consensus.

e. Applicability to both qualitative and quantitative data.

The pairwise comparison method in AHP involves three main steps:

1. Developing the pairwise comparison matrix: This crucial step in AHP involves ranking the identified decision criteria. The pairwise comparison matrix uses a 1-9 scale developed by Saaty (1990).

Here, a score of 1 indicates equal importance between the two factors, while a score of 9 signifies that one row factor is much more important than the column factor it is compared to (Domakinis et al., 2008). Regarding the other scores, a score of 3 is assigned to weak importance, a score of 5 represents moderate preference, and a score of 7 is used for strong importance. Even numbers 2, 4, 6, and 8 are employed when a compromise is needed between odd-numbered scores (Mai Dang et al., 2011). Additionally, fractional values are used to indicate that one factor is less important than the matched factor. The determination of relative importance between two factors is often established by sending surveys to different experts, requesting them to compare the relative importance between the two factors concerning a specific objective (Mai Dang et al., 2011; Hayati et al., 2013; Lai et al., 2013). In rare cases, this comparison may be defined arbitrarily (Rozos, 2011).

2. Calculation of Weights: The calculation of weights is done in three stages. In the first stage, the values in each column of the matrix are summed. Then, each element in the matrix should be divided by the sum of its respective column. The resulting matrix represents the normalized pairwise comparison matrix. The calculation involves finding the average of the elements in each column of the normalized matrix. The obtained matrix involves summing the normalized scores for each element multiplied by the number of criteria considered. These averages enable the estimation of the relative weight value for each considered criterion.

3. Calculation of Consistency: One of the significant features of AHP is determining the consistency in comparisons (Yaralıoğlu, 2001). To ensure the consistency of subjective judgments and the accuracy of relative weights, two coefficients are used: Consistency Index (CI) and Consistency Ratio (CR). The CI value is calculated using the fundamental eigenvalue λ of the pairwise comparison matrix (Yıldırım and Önder, 2015). Therefore, when calculating the λ value, the pairwise comparison matrix is multiplied by the weight matrix W, and each element in each row is summed to obtain the column vector D. By taking the ratio of the corresponding elements in the obtained D column vector and the W weight matrix, the fundamental value matrix E for each evaluation criterion is obtained (Equation 1). The arithmetic average of these E values is taken

to find the fundamental value λ (Equation 2), and then the CI is calculated (Equation 3).

$$E_i = \frac{d_i}{w_i} \ (i = 1,2,3, \dots, n) \qquad \text{Eq (1)}$$

$$\lambda = \frac{\sum_{i=1}^{n} E_1}{n} \qquad \text{Eq (2)}$$

$$CI = \frac{\lambda - n}{n-1} \qquad \text{Eq (3)}$$

The consistency ratio (CR) can be determined using the following formula.

$$CR = \frac{CI}{RI}$$

Here, RI refers to the random index and is dependent on the number of elements being compared. In the study, since 9 criteria were used, RI was assumed to be 1.45 (Saaty, 1980).If CR<0.10, it can be stated that the consistency in pairwise comparisons is at an acceptable level. However, if CR>0.10, the ratio values indicate inconsistent judgments being made.

6. Findings

The data set components for generating the sensitivity map of collection areas using AHP include slope, geology, distance to rivers, distance to roads, distance to settlements, elevation, distance to fault lines, land use, and population. Firstly, using the AHP algorithm and mathematical formulas expressed by Saaty (1980) and Mai Dang et al. (2011), weights were calculated for all factors, and the results are shown in the Table 1.

After calculating the weights of the factors, the rasterized data sets were combined using the widely used Weighted Linear Combination (WLC) analysis within the framework of MCDA. WLC is based on the theory of a true utility function defined by the decision maker's desired set of possible solutions (Fishburn, 1967; Triantaphyllou and Mann, 1989). In WLC, all attribute values of an option are considered, and regular arithmetic operations such as addition and multiplication are used. In this method, attribute values and weights need to be numerical and comparable (Triantaphyllou and Mann, 1989).

Table1. Pairwise comparison matrix and weights of parameters (a slope, b geology, c distance to rivers, d distance to roads, e distance to settlements, f elevation, g distance to fault lines, h land use, i population)

Parameters	a	b	c	d	e	f	g	h	i	Weights
a	1	3	5	2	5	9	7	4	2	0.27
b		1	3	1/2	3	7	5	3	1/3	0.13
c			1	1/3	1	3	2	1/2	1/5	0.05
d				1	3	5	4	3	1/2	0.15
e					1	3	2	1/2	1/4	0.05
f						1	1	1/3	1/5	0.02
g							1	1/3	1/4	0.03
h								1	1/3	0.09
i									1	0.21

The application of AHP indicates that the most important parameter in determining disaster and emergency assembly areas has a weight of 0.27, which is assigned to slope. The second significant parameter is the population with a weight of 0.21. The less important parameters, in descending order, are the distance to road (weight: 0.15), geology (weight: 0.13), land use (weight: 0.09), distance to river and distance to settlement (weight: 0.05), and distance to fault lines (weight: 0.03). Additionally, the Consistency Ratio (CR) value is calculated as 0.05. Since the CR value is significantly smaller than 0.1, it indicates that the weights of the factors influencing the determination of disaster and emergency gathering areas have been assessed well. After calculating the weights of the factors, the obtained weights are applied to the maps, and by combining the maps, suitable areas for disaster and emergency assembly areas is generated.

The disaster and emergency assembly area sensitivity map of the study area is divided into 3 sensitivity classes and the spatial distribution of this map is shown in Figure 3. According to this map; regions of high, middle and low sensitivity were obtained as 8.35%, 76.23% and 15.42%, respectively.

Figure 3. Disaster and emergency assembly area suitability map obtained by AHP method

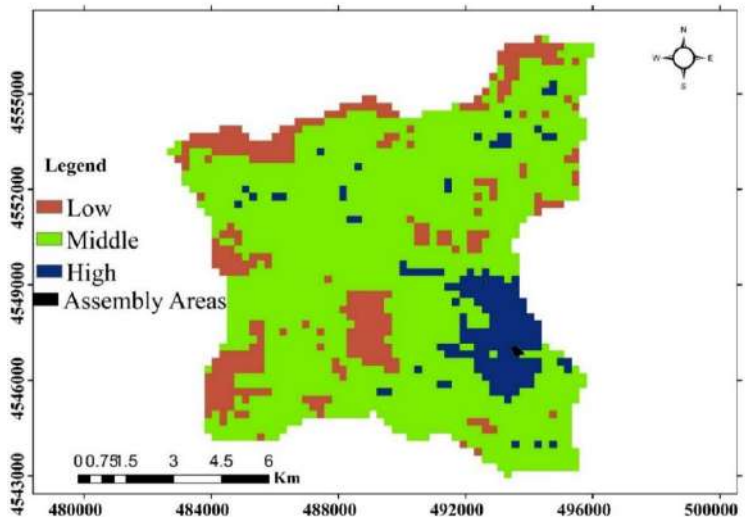

The disaster and emergency assembly area of the study area was calculated as 1.10 ha in areas with high sensitivity and as 10.03 ha in areas with medium sensitivity. 2.03 ha of the study area has low sensitivity for the assembly area. When evaluated considering the location of the existing two disaster and emergency assembly areas in the study area (Karabük AFAD, 2023), it is determined that the assembly areas are located approximately 15 km away from the faults and about 20 km away from the KAFZ (Seismic Risk Zone), as well as being 300 m away from the settlement center and located in areas with a higher population. In terms of disaster and emergency assembly area sensitivity, it is observed that both existing assembly areas are within the high sensitivity zone.

7. Conclusions

Due to the sudden occurrence of earthquakes and their potential for causing significant loss of life, property, and socio-economic impacts, taking precautionary measures and actions before, during, and after earthquakes is of vital importance. Among these measures, the identification of pre-disaster assembly areas and temporary shelter locations is a crucial step in the preparation phase, considering their adequacy in terms of population at the provincial, district, and neighborhood levels, as well as their accessibility.

In this study, Geographic Information Systems (GIS) technology was employed to examine the existing two disaster and emergency assembly areas

in Karabük Ovacık district and generate a sensitivity map for new assembly areas in the future. A comprehensive suitability analysis was conducted, considering spatial features such as slope, geology, distance to watercourses, distance to roads, distance to settlements, elevation, distance to fault lines, land use, and population parameters.

Urban open and green spaces are used as assembly and evacuation areas during and after earthquakes. Selecting the locations of these areas based on specific criteria is necessary to ensure the safety of individuals in these spaces. However, the decreasing availability of open and green spaces used by individuals for assembly and sheltering purposes after earthquakes poses a significant problem.

The two existing assembly areas are geologically located within the Karabük formation (Teka). Because it contains coal levels, assembly areas on the Karabük formation require more detailed field studies and taking field measures. Apart from this, it has been observed that the existing assembly areas comply with the other parameters used.

References

AFAD. (2023a). Afet ve Acil Durum Toplanma Alanları, https://www.afad.gov.tr/ kurumlar/afad.gov.tr/39521/xfiles/toplanma_alanlari.pdf (Visited on 25.04.2023).

AFAD. (2023b). Deprem Verileri, Afet ve Acil Durum Yönetim Başkanlığı, Deprem Dairesi Başkanlığı http://www.deprem.gov.tr/sarbis/Shared/Default.aspx (Visited on 23.04.2023).

Aman, D.D. (2019). Site location criteria of refuge areas for possible Marmara earthquake: case study of İstanbul Bağcilar. PhD thesis, Istanbul Technical University, Institute of Science, Landscape Architecture Department, Landscape Architecture Program.

Arca, D. (2012). Geographic Information System and Remote Sensing in Disaster Management, *Karaelmas Journal of Science and Engineering*, 2 (2), pp.53-61.

Aşıkkutlu, H.S., Aşık, Y., Yücedağ, C. and Kaya, L.G. (2021). Olası deprem durumunda mahalle ölçeğinde Burdur kenti acil toplanma alanlarının yeterliliğinin saptanması, *Mehmet Akif Ersoy İktisadi ve İdari Bilimler Fakültesi Dergisi*, 8(1):442-456.

Carter, G.F.B. (1994). Geographic Information Systems for Geoscientists: Modelling with GIS. *Computer Methods in the Geosciences*, 13, London, United Kingdom.

Chandran, B., Golden, B. and Wasil, E. (2005). Linear programming models for estimating weights in the analytic hierarchy process. *Computers & Operations Research*, 32(9), 2235-2254.

Chu, J. and Su, Y. (2011). Comprehensive Evaluation İndex System in the Application for Earthquake Emergency Shelter Site. *Advanced Materials Research*, (156-157), pp.79-83.

Çelik, H.Z., Aydın, B.S., Partigöç, N.S. and Erdin, H.E. (2018). Deprem Riskleri Bağlamında Toplanma Alanlarının Güvenlik Kriterleri Temelinde Değerlendirilmesi Bayraklı (izmir) Örneği. *International Symposium on Natural Hazards and Disaster Management*. Sakarya.

Çiçekdağı, H.İ. and Kırış, S. (2012). Site Selection for Disaster Station and Assembly Center and an Application, Dumlupınar University, *Journal of Science Institute*, Issue 28, August 2012 ISSN -1302-3055, Kütahya.

Çinar, A.K., Akgün, Y. and Maral, H. (2018). Investigation of Factors in Planning Post-Disaster Emergency Assembly and Temporary Shelter Areas: The Example of İzmir-Karşıyaka, *Journal of Planning*, 28(2):179-200, doi: 10.14744/planlama.2018.07088.

Demir G. (2018). Landslide susceptibility analysis by using GIS for Suşehri (Sivas), *GÜFBED/GUSTIJ*, 8 (1):96-112, https://doi.org/10.17714/gumusfenbil.299987

Domakinis, C., Oikonomidis, D. and Astaras,T. (2008). Landslide mapping in the coastal area between the Strymonic Gulf and Kavala (Macedonia, Greece) with the aid of remote sensing and geographical information systems, *Int J Remote Sens*, 29(23):6893–6915.

ECPFE (European Centre on Prevention and Forecasting of Earthquakes), OASP (Earthquake Planning And Protection Organization). (2002). Emergency Evacuation of the Population in Case of an Earthquake, Athens. http://Ecpfe.Oasp.Gr/Sites/Default/ Files/Eee_0.Pdf

Fishburn, P.C. (1967). Additive Utilities with Incomplete Product Set: Applications to Priorities and Assignments, *Operations Research Society of America (ORSA) Publication*, 15(3): 537-542. Baltimore, MD

Hayati, E., Majnounian, B., Abdi, E., Sessions, J. and Makhdoum, M. (2013). An expert-based approach to forest road network planning by combining Delphi and spatial multi-criteria evaluation, *Environ Monit Assess*, 185:1767–1776.

JICA (Japanese International Cooperation Agency) and IMM (Istanbul Metropolitan Municipality). (2002). Republic of Turkey Istanbul Province Disaster Prevention/Mitigation Basic Plan Study, Including Seismic Microzonation Final Report Volume V, Istanbul, Turkey. Access address http://www.ibb.gov.tr/tr-TR/SubSites/DepremSite/PublishingImages/JICA-TUR.pdf

Karabük AFAD. (2023). Karabük Toplanma Alanları, Karabük Valiliği, İl Afet ve Acil Durum Müdürlüğü. https://karabuk.afad.gov.tr/karabuk-toplanma-alanlari (Visited on 15.05.2023)

Keskin Citiroglu, H. and Arca, D. (2022). GIS-Based Determination of Solar Power Plant (SPP) Sites by the MCDA Method: Ovacık District, Karabük-Türkiye. *Environmental Engineering and Management Journal,* 21:1899-1910.

Kılcı, F., Yetiş Kara, B. and Bozkaya, B. (2015). Locating Temporary Shelter Areas after an Earthquake: A Case For Turkey, *European Journal of Operational Research*, 243:323–332.

Kırçın, P.N., Çabuk, S.N., Aksoy, K. and Çabuk, A. (2017). A Research on Increasing the Possibilities of Using Green Areas as Post-Disaster Gathering Areas in Our Country. *4th International Conference on Earthquake Engineering and Seismology*. Eskisehir: Anadolu University

Lai, T., Dragic´evic´. S. and Schmidt, M, (2013). Integration of multicriteria evaluation and cellular automata methods for landslide simulation modelling", *Geomat Nat Hazards Risk*, 4(4):355–375.

Mai Dang, N., Babel, M. and Luong, H. (2011). Evaluation of food risk parameters in the Day River Flood Diversion Area, Red River Delta, Vietnam, *Nat Hazards*, 56:169–194.

MEUT. (2020). Karabük Zonguldak Bartın Provinces Environmental Status Assessment. 264 p. Ministry of Environment and Urbanization of Turkey, Environment and Urban Library, http://www.cevresehirkutuphanesi.com/basili-yayinlar/detay/karabuk-zonguldak-bartin-illeri-cevresel-durum-degerlendirmesi (Visited on 02.11.2020).

MTA. (2023). Yer Bilimleri Harita Görüntüleyici ve Çizim Editörü, MTA Genel Müdürlüğü, http://yerbilimleri.mta.gov.tr/anasayfa.aspx (Visited on 23.04.2023).

NZ Transport Agency. (2009). Pedestrian Planning and Design Guide, October 2009 NZ Transport Agency, ISBN 978-0-478-35228-3.

Ovacık District Governorship. (2023). Geographical structure, Online at: http://www.ovacik.gov.tr/ilcemizin-cografi-yapisi (Visited on 28.05.2023).

Ovacık Municipality. (2023). General introduction of the district, Online at: http://www.ovacik.bel.tr/?pnum=12&pt=Ovac%C4%B1k+Tarih%C3%A7e (Visited on 28.05.2023).

Özkılıç, E.N. (2020). Analysis and evaluation of capacity and accessibility of after earthquake assembly areas in Istanbul by GIS. Master's thesis, Istanbul technical university, institute of sciences, Geomatics Engineering Department, Geomatics Engineering Program

Rozos, D., Bathrellos, G.D. and Skillodimou, H.D. (2011). Comparison of the implementation of rock engineering system and analytic hierarchy process methods, upon landslide susceptibility mapping, using GIS: a case study from the Eastern Achaia County of Peloponnesus, Greece, *Environ Earth Sci*, 63:49–63.

Saaty, T.L. (1980). *The analytical hierarchy process*. New York: Mc Grow-Hill Company.

Saaty, T.L. (1990). How to make a decision: the analytic hierarchy process. *European Journal of Operational Research*, 48(1): 9-26.

Soltani, A., Ardalan, A., Darvishi Boloorani, A., Haghdoost, A., Hosseinzadeh-Attar, M.J. (2014). Site Selection Criteria for Sheltering after Earthquakes: A Systematic Review. *PLOS Currents Disasters*, Edition 1. doi:10.1371/currents.dis.17ad1f98fb85be80785d0a81ced6a7a6.

Soltani, A., Ardalan, A., Darvishi Boloorani, A., Haghdoost, A., Hosseinzadeh-Attar, M.J. (2015). Criteria for Site Selection of Temporary Shelters after Earthquakes: a Delphi Panel. *PLOS Currents Disaster*s, Edition 1. doi:10.1371/currents.dis.07ae4415115b4b3d71f99ba8b304b807

Şirin, M., Ocak, F. (2020). Evaluation of Disaster and Emergency Meeting Areas in the City of Gümüşhane in the Geographical Information Systems Environment. *Eastern Geographical Rewiew*, 25(44):85-106.

Timur, E. and Aksay, A. (2002). 1:100 000 scale geological map of Turkey No:30 Zonguldak F–29 section, Geological Studies Office, General Directorate of Mineral Research and Exploration MTA, Ankara, Turkey, pp. 23.

Triantaphyllou, E. and Mann, S.H. (1989). An examination of the effectiveness of multi-dimensional decision-making methods: A decision-making paradox, *International Journal of Decision Support Systems*, 5:303-312.

Turgut, E.C. (2015). Measuring the performance of suppliers using AHP and fuzzy AHP methods in supply chain management, new method suggestions and applications. Unpublished Master's Thesis, Dokuz Eylul University Institute of Social Sciences, Izmir.

Turkish Statistical Institute. (2023). Address based population registration system results, Turkish Statistical Institute, Online at: https://biruni.tuik.gov.tr/medas/?kn=95&locale=tr (Visited on 26.05.2023).

Turoğlu, H., Döker, F. and Bayrakdar, C. (2010). Importance of UZAL and GIS Technologies for Istanbul in Post-Disaster Response. *Istanbul Disaster Vulnerability Symposium*, p.293-297, Istanbul.

URL-1. (2020). Civil administration maps of Turkey, CografyaHarita, Online at: http://cografyaharita.com/turkiye_mulki_idare_haritalari.html (Visited on 06.09.2020).

Ünal, O.F. (2011). Analytical hierarchy process and its applications in personnel selection. *Akdeniz University Journal of International Alanya Business Faculty*, 3(2):18-38.

Yaralıoğlu, K. (2001). Analytical hierarchy process in performance evaluation. *Journal of D.E.U.İ.İ.B.F*, 16(1):129-142.

Yıldırım, B.F. and Önder, E. (2015). *Multi-criteria decision making methods*. Bursa: Dora Publishing and Distribution.

Chapter 8

Investigation of the Behavior of Steel-Concrete Composite Structure with Different Design Properties Under Far-Fault and Near Fault Earthquake Records

Serkan Etli[1]

Melek Akgül[2]

Abstract

Calculations of earthquake effects can be handled in different ways in current national or international regulations. It is of great importance to consider the second-order effects of properties. After the structural modeling, the designs are completed by using the forces obtained in the section calculations made by considering the earthquake effects. Deformations due to second-order effects can cause greater damage in sections. Within the scope of this study, steel-concrete composite systems, which are produced in Eurocode norms and have remarkable features among structural systems, have been examined. The effects of considering the sensitivity coefficient in the Eurocode in the examinations on the system were evaluated separately in internal and external frames. Especially in elastic design and force-based designs, the effect of this coefficient has been evaluated in buildings with different coefficients in this study. As an example, the number of floors of the studied buildings were modeled as 8, 10, 13 and 15-storey composite moment-resisting frames. During the modeling, the sensitivity coefficient was evaluated to be $0<\theta\leq0.1$ and $0.1<\theta\leq0.2$ in two different intervals. In the evaluations, Nonlinear Time History analyzes, and nonlinear element and material models were used to evaluate the nonlinear behavior. To evaluate the behavior of the systems, the average and maximum values of the interstory drift ratios were carried out. In systems consisting of exemplary composite moment-resisting frames, it has been theoretically evaluated that there were important effects of the use of this coefficient, especially in outer frames.

1 Dr. Ögr. Üyesi, Munzur University, Dep. of Emergency Aid and Disaster Management, serkanetli@munzur.edu.tr, Orcid: 0000-0003-3093-4106

2 Ögr. Gör. Dr. Munzur University, Tunceli Vocational Schools, melekakgul@munzur.edu.tr, Orcid: 0000-0001-8815-3762

https://doi.org/10.58830/ozgur.pub130.c604

1. Introduction

Composite structures designed by combining the superior properties of steel and concrete together provide effective solutions to the designer during the design stage. CMRFs can be characterized as one of the most economical designs in terms of structural behavior and strength characteristics, when system features and element capacities are considered. The economy required in this manner is especially important in buildings with a service life in areas that are likely to be affected by severe earthquakes. During the engineering design of composite structures for earthquake effects, the high ductility that steel and concrete will show as expected on the basis of working together on demand increases the theoretical and practical applicability of the structure in the face of high energy formation that will result from repeated earthquake loads. For these structures, which are suitable to be designed as moment-bearing frames (MRF), the lateral dynamic loads that constitute the main effect in earthquake forces are mainly met by the flexural strength capacities of beam and column elements. In this case, the biggest challenge during the design of such structures is the design of the column elements as composite elements. When the methods of capacity design principles are applied under earthquake effects, ductility should be the first determining factor for the designer in terms of engineering (Elghazouli et al., 2008). When the previous studies in the literature related to the composite structures are examined, several studies have been done to examine the parameters related to the connection points (Hawkins & Mitchell, 1984; Leon et al., 1998), shear interaction (Caldara, 1998), floor effect (Plumier, 2000) and seismic performance (Miranda, 2012; Thermou et al., 2004). Moreover, in the previous studies by Denavit et al., the behavior of CFST elements was examined in detail and the behavior of the structures of CMRFs systems consisting of these elements was evaluated. Especially after this condition, which is an important parameter in the calculation of design loads, is met, ductility, which is the design criterion of the structures planned to be designed, is provided by the composite columns designed in relation to the behavior of CMRFs according to the design requirements. Achieving the goal of proper building design is not always sufficient with simple techniques used in calculations involving traditional design methods. On the other hand, it is very important to detail the behavior of the building elements closest to reality, which will occur with the effect of the forces they will be exposed to during an earthquake, in the design. The behavior of the building elements against these dynamic effects is addressed to the building systems in accordance with the behavior factors specified by the design codes. These factors, which are included in force-based designs, which is

one of the traditional design styles, are the values used to reduce the lateral loads that will occur in the structure (under the effect of earthquake) with mathematical expressions during the calculation. The "q" behavior factors specified in European codes are used for this purpose. In addition, to reach the most sufficient or most accurate validity from these factors in designs, it is very related to the system features to be designed and the accuracy of the basic assumptions of the elements in the system. More importantly, considering the region where the structure will be built, it should not be forgotten that the structural behavior of the structure under the influence of different dynamic loads can be quite transitory in the design of the structure, which also originates from the fundamental properties of the earthquake loads. (Broderick & Elnashai, 1996; Elghazouli et al., 2008). In many studies of the structures produced in this type and the structures produced in the relevant national standards, similar properties are evaluated in the relevant designs (Etli, 2021, 2022; Etli & Güneyisi, 2020, 2021, 2022b, 2022a; Güneyisi & Etli, 2020).

In this study, CMRFs were analyzed using nonlinear dynamic analysis (NDA) technique with time-history records (TH) in different properties. CMRFs were designed as 8-,10-,13- and 15-story according to the Eurocode seismic design specifications. Moreover, in the seismic design stage, only θ parameter properties were selected in different range as $0<\theta\leq0.1$ and $0.1<\theta\leq0.2$. Therefore, in the seismic design situation there are two cases, the first one is for $0<\theta\leq0.1$ and second one is $0.1<\theta\leq0.2$. Then, the CMRFs were divided in two frames according to the position, the frames were selected as inner and outer frames. Finally, in the study there were four case and they classified as Case-I is inner frame for $0<\theta<0.1$, Case-II is inner frame for $0.1<\theta\leq0.2$, Case-III is outer frame for $0<\theta\leq0.1$ and Case-IV is outer frame for $0.1<\theta\leq0.2$.

In seismic design stage of all CMRFs, the CMRF were modelled as elastic elements according to the Eurocode. Then, in the NDA stage of CMRFs, the CMRFs members were remodeled using distributed plasticity force-based elements. The NDAs were performed with TH and TH records were selected in 3 different groups. The groups were created using FEMA earthquake record classification. Moreover, the earthquake acceleration was selected based on the seismic design stage spectra parameters. The parameters of elastic design spectra were selected as Ground-C class and the earthquake magnitude is greater than 6.5. Then, the TH records groups and specifications are selected as far-field (FF), near-field without-pulse (NF-NP) and near field with pulse (NF-P) from FEMA guidelines. Each TH record

groups contained 10 TH records. After selection of TH records according to the given above specifications, TH record were scaled for seismic design elastic spectra using the Seismomatch software. After that point, the CMRFs were analyzed using NDA method with FF, NF-NP, and NF-P type TH records. The results of NDAs were evaluated in terms of interstory drift ratio (IDR), roof drift ratio (RDR), base-shear coefficient, base moment, roof accelerations. The results are presented at the next session.

2. Structural Configuration and Design Procedures

8, 10, 13 and 15-story CMRFs were used for the comparison of the seismic behavior. Regarding the designs of the structures in the study, earthquake resistant structures were designed with Eurocode-8 (EN 1998-1, 2004) by using the earthquake spectra obtained with 0.2g peak ground acceleration (PGA) in these structures whose specific parameters were examined after design. In the CMRF multi-storey structures designed, the designs were carried out with multiple compartments and the plan geometries of all structures were ensured to be the same. The selected plan and the system facade views of the designed buildings are presented in Figure 1. The CFST columns were placed every 7 m in the x-direction and y-direction to maintain the system symmetry. Considering the rigid diaphragm formation in the floors, the deformations under vertical loads and the ductility capacity of the beams, the floor thicknesses were dimensioned by considering the design features given in the relevant design codes. Hollow square section steel box profiles (SHS) selected from the catalogs published by European steel manufacturers in composite column elements planned to be used in CFSTs due to earthquake resistant design, and sections of steel beams to be used in composite beams were selected. The analyzes continued with the assumption that there is a complete shear interaction between the steel beam and the concrete slab at the design stage in the design and strength properties of the composite beams within the system. During the earthquake resistant design of the building, a value of 2 kN/m^2 was chosen for the dead load in the pavement and spatial partitions in addition to the dead load and slab weight transferred from the floors. The live load on the floor is used as 3 kN/m^2 in the calculations. As a result of the analyzes made on the system under the gravitational loads, the structural elements with sufficient strength in section properties were selected, and the CMRFs were evaluated in terms of earthquake resistant designs.

Fig. 1. Structural arrangement for the 5, 10, 15 and 20 story modelled structures: (a) Plan configuration and (b) Elevation of moment-resisting frame

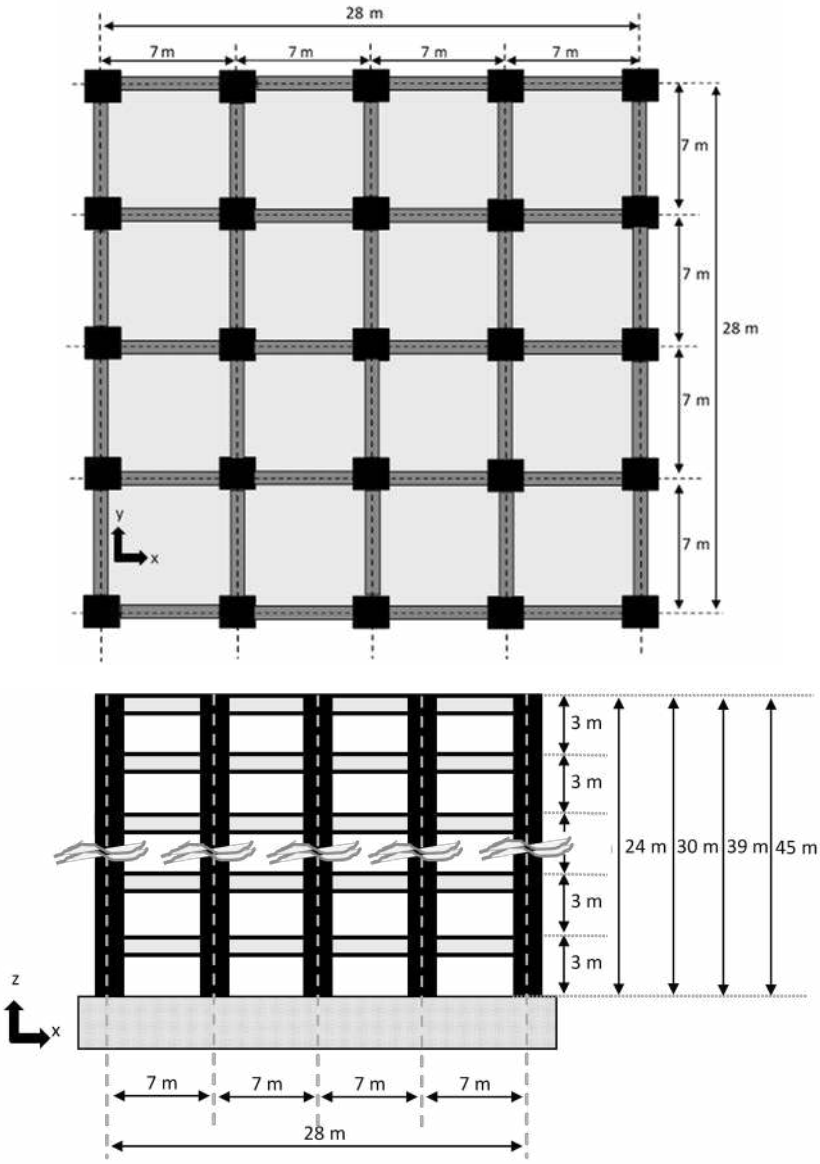

Considering the Eurocode-8 (EN 1998-1, 2004) conditions in the design of the structures, high ductility (DCH) systems were selected. Response spectra are used to calculate the forces transmitted from the ground to the structure due to the earthquake effect. There are some data needs in

the formulas included in the recommendations of the standards for these response spectra. In addition to the PGA values selected in the design of the structures that are subject to evaluation in the study, the C class soil was evaluated as the soil type characteristic of the place where the structure will be built. On the other hand, Eurocode-8 (EN 1998-1, 2004) is also included in a classification of seismicity, that is, the magnitude f-value of the earthquake. By paying attention to these situations, type-1 spectrum calculations were used, considering the seismicity of the location where the construction activities will be carried out. When the system properties are evaluated in earthquake resistant structural design for Eurocode-8 (EN 1998-1, 2004), it is considered appropriate to use the modal analysis method in these structures. In addition, as is known, the section designs that are not made in accordance with the selected structural behavior coefficient may cause the structures not to reach the selected ductility value. Therefore, the guidelines for the relevant ductility conditions for Eurocode-8 (EN 1998-1, 2004) have been considered, and attention has been paid to the suitability of element sections and behaviors. For multi-span and multi-storey buildings, 5□u/□1 formula is used in the calculation of the proposed behavior factor in Eurocode-8 (EN 1998-1, 2004). As a result, the behavior factor is obtained with the mentioned values as 6.5. On the other hand, it has been reported in previous studies that wind pressure does not have a significant effect during element sizing in such structural elements (Acun, 2012).

During the earthquake resistant design of the building, the necessary features for the strength capacities of the elements as well as the drift ratio between the floors and thus the limit values for the stability of the structure were taken into consideration. After calculating the earthquake forces, the sensitivity coefficient defined in Eurocode-8 (EN 1998-1, 2004) was used to reflect the second-order effects and the effects of these effects on the elements in the design. Economic designs were tried to be used by converging to the minimum cross-section capacities by using two different group designs, with the value of the coefficient taken as the basis in the CMRFs designs between 0-0.1 and 0-0.2. The calculation method required for the aforementioned sensitivity coefficient "θ" is as follows:

$$\theta = \frac{P_{tot} \times d_r}{V_{tot} \times h} \quad (1)$$

Among the parameters in the equation, the cumulative gravity load for P_{tot} and the total earthquake shear force acting on the ground level to the building foundation for V_{tot} are included in the calculations. The story heights and the values of the offsets of the floors calculated during the design

are symbolized as h and d_r, respectively. The design shift value, which is considered as the limit value during design, is obtained by multiplying the elastic relative drift and the behavior factor. Another inequality in Eurocode-8 (EN 1998-1, 2004) is given as follows for the evaluation of the story drifts of the building after calculating the lateral seismic forces:

$$d_r \times \nu \leq \psi \times h \tag{2}$$

It is stated that the definition made in the standard for the ψ value in the inequality given above is used to reflect the behavior of the non-structural elements of the building design. Regarding this value, the values given in Eurocode-8 (EN 1998-1, 2004) are 0.5%, 0.75% and 1.0%. While choosing these values, it is stated that they are used in structural systems designed with brittle, ductile and non-structural or insulated elements, respectively. The integration of the characteristic properties determined in the service properties and the inter-floor drift properties to this limit state is given as the value of ν, this value is between 0.4 and 0.5. While the ψ value was used as 0.75% for the design of the structures designed within the scope of this article, the ν value was chosen as 0.5.

It has been stated that the second-order effects, which are controlled by the definition of the sensitivity coefficient and symbolized by θ, reach up to 0.2 within the scope of the study for some case studies. Therefore, after the θ value exceeds 0.1, it should be considered during the seismic design with the help of a simplified formula given in Eurocode-8 (EN 1998-1, 2004). This simple formula is considered by multiplying the calculated seismic effects at the floor level by the factor calculated by 1/(1-θ) to be included in the calculations for the second order effects.

For a design constructed with weak beam/strong column behavior, the special rule used during the design of composite columns in moment-transmitting frames after the ductile behavior of beams is provided by section designs is given below:

$$M_{Ed} = M_{Ed,G} + 1.1 \times \gamma_{ov} \times \Omega \times M_{Ed,E} \tag{3}$$

In the given formula, the moment values for $M_{Ed,G}$ and $M_{Ed,E}$ are given as calculated after gravity and seismic analysis, respectively. In addition, γ_{ov} value was defined to reflect the material properties and this value was included in the calculations as 1.25 within the scope of the study. Another term Ω value in the expression is calculated as the beam overload factor, which is calculated with the ratio $M_{pl,Rd,i}/M_{Ed,i}$ and selected to be the smallest

of the values. The values in the ratio are considered in the calculations as the plastic moment capacity and the design moment value of the "ith" beam, respectively.

Moment frame systems are since the bearing capacities of the vertical carrier columns are stronger than the beams. Reaching the shear capacities of concrete beams after bending capacities and trying to provide buckling formation in steel braces before the columns are basically three important examples of capacity design. Another general rule used in all frame structure types in Eurocode-8 (EN 1998-1, 2004) is that the moment strengths of all columns on a certain joint point must be at least 1.3 percent of the moment strengths of the beams. This requirement is formulated as follows:

$$\sum M_{Rc} \geq 1.3 \times \sum M_{Rb} \quad (4)$$

$\sum M_{Rc}$ and $\sum M_{Rb}$ in the given formula are expressed as the total moment capacity of columns and beams at the same joint, respectively.

For all designed CMRFs, the design analysis is two-step. The first is the design under gravity loads for the availability limit state (SLS), which is defined as preliminary analysis. In all designed CMRFs, the maximum bearing capacity (ULS) design criteria for the seismic ultimate limit state given in Eurocode-8 (EN 1998-1, 2004) were checked after the SLS design for an earthquake effect of 0.2g. Ensuring ULS and SLS status is essential. To obtain the desired and modeled behavior during earthquake resistant design in CMRF models, CFST columns are welded and rigidly connected with steel beams at the nodal (Elghazouli et al., 2008).

Table 1. Modal periods and mass ratios of the analyzed frames

	T_1 (s)	T_2 (s)	T_3 (s)	U_1 (%)	U_2 (%)	U_3 (%)	T (s)
8stry-I	1.081	0.336	0.179	79.258	10.400	4.394	1.146
10stry-I	1.181	0.372	0.202	78.911	10.134	4.186	1.254
13stry-I	1.364	0.436	0.241	78.762	9.970	3.910	1.452
15stry-I	1.467	0.467	0.258	78.171	10.030	3.909	1.561
8stry-II	1.344	0.404	0.206	77.749	10.917	4.811	1.419
10stry-II	1.650	0.500	0.257	77.036	10.690	4.699	1.744
13stry-II	1.886	0.583	0.309	77.140	10.276	4.341	1.998
15stry-II	2.118	0.649	0.340	76.347	10.372	4.421	2.242

Table 2. Member properties of the structure

	Beam	Column	Concrete	Steel
8stry-I	IPE 500	550X40	C30	S275
10stry-I	IPE 550	600X50		
13stry-I	IPE 600	650X60		
15stry-I	HEA 550	750X60		
8stry-II	IPE 400	550X40		
10stry-II	IPE 400	600X45		
13stry-II	IPE 450	650X60		
15stry-II	IPE 450	750X60		

Modal periods and mass ratios of the analyzed frames were presented in Table 1. In the seismic design of CMRFs, natural vibration periods of CMRFs were change according to the selected θ values in the seismic design stage. According to the θ value range, CMRFs structures names were given with 8stry-I, 10stry-I, 13stry-I and 15stry-I for $0<\theta\leq0.1$ and 8stry-II, 10stry-II, 13stry-II and 15stry-II for $0.1<\theta\leq0.2$. Modal periods of 8stry-I, 10stry-I, 13stry-I and 15stry-I structures are greater than the modal periods of 8stry-II, 10stry-II, 13stry-II and 15stry-II, respectively. CMRFs structures has greater member section for the $0<\theta\leq0.1$ case than in the case of $0.1<\theta\leq0.2$ situation whereas composite members section smaller in the case of $0.1<\theta\leq0.2$ (Table 2). Therefore, CMRFs stiffness decreases in the case of $0.1<\theta\leq0.2$ situation against the $0<\theta\leq0.1$ case, so that the periods of the $0.1<\theta\leq0.2$ case CMRFs are higher periods.

Table 3. Design properties of the analyzed frames

	W_{FRAME} (kN)	V_{tot}	d_r	θ	α
8stry-I	17561.3	974.71	0.0184	0.0920	5.2231
10stry-I	22374.2	1337.03	0.0192	0.0912	6.3596
13stry-I	29765.9	1551.90	0.0173	0.0962	7.1942
15stry-I	35633.8	1729.22	0.0162	0.0957	8.6876
8stry-II	17488.8	922.08	0.0267	0.1400	7.4944
10stry-II	22150.3	966.50	0.0265	0.1726	9.9061
13stry-II	29534.2	1144.14	0.0239	0.1766	11.8225
15stry-II	35307.1	1203.10	0.0228	0.1929	16.6806

Some parameters were calculated at the design stage is presented in Table 3. These parameters were given with W_{FRAME}, V_{tot}, d_r, θ and α, these parameters defined as structure weight, earthquake shear force acting on the floor level, design drifts, sensitivity coefficient and the over-strength of column against the beams. It can be clearly seen from Table 3 that V_{tot} values of CMRFs for in the case of $0<\theta\leq0.1$ greater than in the case of $0.1<\theta\leq0.2$ ones. Similarly, 8stry-I, 10stry-I, 13stry-I and 15stry-I structures d_r and α values are greater than the 8stry-II, 10stry-II, 13stry-II and 15stry-II structures, respectively. This is mainly provided the CMRFs stiffness. Moreover, the section size of beams is greater size in the 8stry-II, 10stry-II, 13stry-II and 15stry-II structures, while the column size was similar.

3. Details of numerical modelling

In this section, the properties related to the steel and concrete models selected in order to obtain a realistic behavior in non-linear analyzes of the composite beams in which the steel beams working with the column and slab obtained by using CFST sections are explained. While the structures designed to be earthquake resistant and inspected by the provisions of Eurocode-8 (EN 1998-1, 2004) are examined under earthquake forces, the behavior of concrete in structural elements due to earthquakes in the model is evaluated by using the model developed by Martinez-Rueda and Elnashai (Martínez-Rueda & Elnashai, 1997) as the concrete model. considered. Regarding this concrete material model, it was defined as "con_ma" in the Seismostruct software and the sample image of the model taken from the software is presented in Figure 2(a). In the "con_ma" model included in the software, while the effects of the confinement effect occurring around the concrete or reinforced concrete were determined, the related effect was used in the "con_ma" model thanks to the coefficient obtained by simulating the circular spiral reinforcement. Moreover, in the studies, it is seen that the data obtained in the experimental and theoretical studies with concrete filled tubes are higher than the concrete elements surrounded by circular reinforcements (Choi & Xiao, 2010; Uy, 2001; Xiao & Wu, 2000). Since the structures were not examined under the influence of earthquake records after the earthquake resistant structural design, the confinement effect that will occur in the concrete in the CFST columns is provided by the steel SHS section used in the outermost part of the element section. The evaluation of the winding effect is defined using the kc value in the selected concrete model of the Seismostruct (Seismosoft, 2016) software. The confinement factor value kc is defined by the ratio between the compressive strength of the coiled concrete model and the concrete strength obtained by the

confinement effect. Susantha et al. (Susantha et al., 2001) created some theoretical calculation methods for determining the load capacities of such cross-section members, namely CFST members. When the data obtained from the calculations and models produced using theoretical calculations and the data obtained from the experimental models are compared, it has been shown that the necessary convergence has occurred. Susantha et al. (Susantha et al., 2001) used experimental work on a large number of CFST elements (with different geometry and other mechanical parameters) and theorized calculations. The physical and mechanical properties of the CFST composite column used in the design models obtained are similar or close to the cross-section properties of the element used in previous studies in the literature (Etli, 2021, 2022; Etli & Güneyisi, 2020, 2021, 2022b, 2022a; Güneyisi & Etli, 2020).

For the material behavior of the sections consisting of steel profiles in composite beams, information on material models operating under the effect of elasto-plastic cyclic loads is used in material modeling. This model is defined as "stl_mn" in Seismostruct software and the software image of the model is given in Figure 2(b). It is frequently used in the literature as a material behavior model of steel developed by researchers by examining experimentally and theoretically by various researchers (Antoniou et al., 2008; Filippou et al., 1983; G. Monti, C. Nuti, 1996; Menegotto & Pinto, 1973; Shahrooz et al., 1993). On the other hand, there is a need for element modeling including material models. In the definitions of element behavior, many force and displacement-based models are mentioned in the literature. Some modeling techniques are given as defined in the Seismostruct (Seismosoft, 2016) software, it is known that in these element modeling techniques, the models of the elements created using steel and concrete models, show sufficient convergence to the previous experimental results in the literature when the sections are modeled with fiber elements (Xu et al., 2018). Experimental data of test samples used in the literature for CFST (Baba et al., 1995; Huang et al., 2018; Srinivasan & Schneider, 1999; Tomii et al., 1977), and material models described above, and many modeled elements using fiber were examined by researchers (Etli, 2021, 2022; Etli & Güneyisi, 2020, 2021, 2022b, 2022a; Güneyisi & Etli, 2020). It is stated that the results of these models, which are examined with the section model in the Seismostruct (Seismosoft, 2016) software, are obtained converging to the experimental test results (Boukhalkhal et al., 2019; Bruneau et al., 2008; Li et al., 2018; Xu et al., 2018; Zhang & Gao, 2019).

Fig. 2. a) Concrete model and b) steel model schematic view from Seismostrucrt software (Seismosoft, 2016)

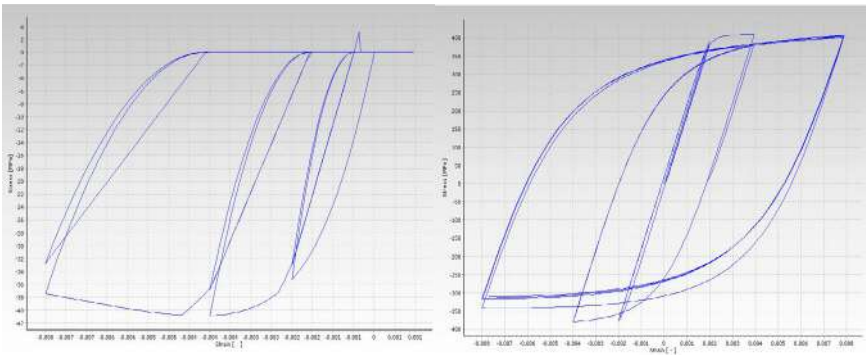

(a) (b)

The models developed for the region, which is defined as the junction region, have been previously investigated experimentally and theoretically by researchers in the literature for the junction points of structural steel elements (e.g., (Kim & Engelhardt, 2002)), reinforced concrete joints (e.g. (Altoontash, 2004)) and junction points of composite elements (e.g., (Fukumoto & Morita, 2005; Kanatani et al., 1987; Muhummud, 2003)). The port properties of the modified Richard-Abbott Model are included to simulate the behavior by defining parameters within the Seismostruct software. The behavior related to this joint point has been programmed by Nogueiro et al. (Nogueiro et al., 2005) and it is possible to simulate any possible steel and composite connection in practice (e.g. welded-flange bolted-web connection, extended end-plate connection, flush end-plate connection, angle connection, etc.). In the study, CFST elements and composite beams are modeled using the Modified Richard-Abbott Model to consider the joints in the behavior.

Seismostruct (Seismosoft, 2016) software was used for nonlinear analysis of CMRFs consisting of composite columns and beam sections modeled using fiber section elements. During the analysis, models were used for composite beams as a complete shear connection between the steel beam body and the concrete slab (Castro, 2006). Another parameter used in beams, 1.225 m, is reflected in the calculations as the effective floor width for inner frame and also 0.6125 m were used at outer frames. In a study in the literature, Miguel, and Castro (Castro, 2006), Eurocode-4 (EN 1994-1-1, 2004) and Eurocode-8 (EN 1998-1, 2004) calculated the effective slab width calculation models. compared. They reported that the models

of the obtained theoretical data helped to obtain the experimental behavior with sufficient accuracy. In another study, Castro et al. (Castro et al., 2007) produced test samples related to the effective slab widths used in composite beams and presented that their experimental results converged with those suggested in such codes.

Steel elasticity modulus (E), poisson ratio (υ) and hardening coefficient (μ) values of the materials used in element models were taken as 210 × 10^3 N/mm^2, 0.3 and 0.5%, respectively. The cross-sectional properties of the elements used in the design and the classes of materials used in these elements are given in Table 2. To summarize these properties, the yield strength of the structural steels used is S275 and the concrete class used in all these buildings is considered as C30 (Etli, 2021, 2022; Etli & Güneyisi, 2020, 2021, 2022b, 2022a; Güneyisi & Etli, 2020).

A schematic representation of the modeling of the cross sections of the composite elements of CMRF structures with the fiber elements in the Seismostruct (Seismosoft, 2016) software is given in Figure 3. In addition, these elements are modeled by the "infrmFB", which is defined as the inelastic force-based frame element in the Seismostruct software. Columns and beams designed as composite members are divided into 5 elements.

Fig. 3. Fiberized sections view for (a) CFST columns' sections, (b) composite beam section.

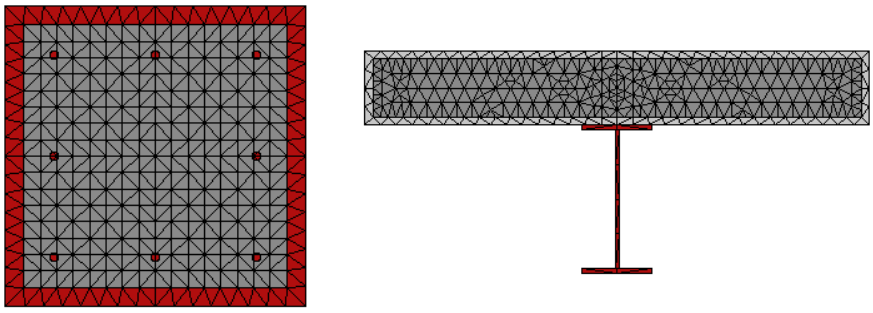

(a) (b)

Fig. 4. Model views from SeismoStruct software.

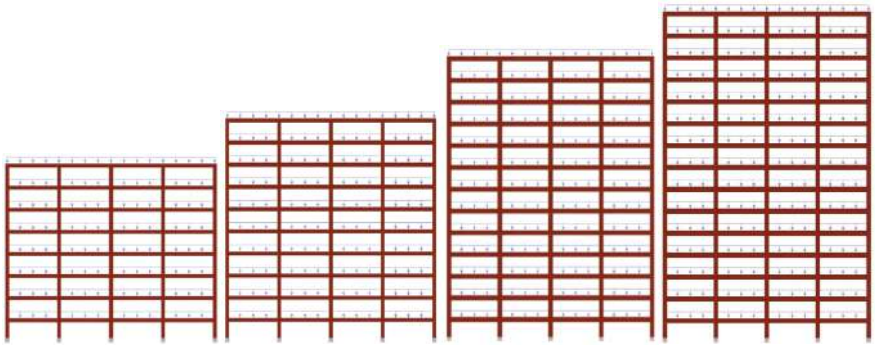

TH records properties given for NDAs of CMRs were given in Table 4. It can be clearly seen that the records properties were properly selected according to the elastic seismic design spectra. The parameters of V_{s30} and M are the preliminary determination properties for selection and these parameters of V_{s30} were defined as the average seismic shear-wave velocity from the surface to a depth of 30 meters while the M is the magnitude of TH record.

Table 4. Details of earthquake records

No.	Record Seq. No.	Component	M	Year	Name	Vs_{30} (m/sec)	Source (Fault Type)	Rjb (km)	Rrup (km)	PGA max (g)	PGV max (cm/s.)
Far-Field Earthquake Record Set											
TH-1	125	0	6.5	1976	Friuli, Italy	425	Thrust	14.97	15.82	0.357	22.8
TH-2		270								0.315	30.5
TH-3	1111	0	6.9	1995	Kobe, Japan	609	Strike-slip	7.08	7.08	0.483	46.8
TH-4		90								0.464	38.3
TH-5	1148	0	7.5	1999	Kocaeli, Turkey	523	Strike-slip	10.56	13.49	0.210	14.0
TH-6		90								0.134	40.1
TH-7	1485	E	7.6	1999	Chi-Chi, Taiwan	705	Thrust	26.00	26.00	0.473	50.1
TH-8		N								0.507	46.4

Table 4. Details of earthquake records (continued)

No.	Record Seq. No.	Component	M	Year	Name	Vs_{30} (m/sec)	Source (Fault Type)	Rjb (km)	Rrup (km)	PGA max (g)	PGV max (cm/s.)
TH-9	1633	L	7.4	1990	Manjil, Iran	724	Strike-slip	12.55	12.55	0.515	42.5
TH-10		T								0.497	50.6
Near-Field Earthquake Record Set											
Pulse Records Subset											
TH-11	802	0	6.9	1989	Loma Prieta	371	Strike-slip	7.58	8.50	0.514	41.6
TH-12		90								0.326	46.0
TH-13	828	0	7	1992	Cape Mendocino	713	Thrust	0.00	8.18	0.591	49.3
TH-14		90								0.662	88.5
TH-15	879	260	7.3	1992	Landers	685	Strike-slip	2.19	2.19	0.725	133.4
TH-16		345								0.789	28.1
TH-17	1086	90	6.7	1994	Northridge-01	441	Thrust	1.74	5.30	0.605	77.5
TH-18		360								0.843	129.4
TH-19	1529	E	7.6	1999	Chi-Chi, Taiwan	714	Thrust	1.49	1.49	0.304	91.7
TH-20		N								0.172	66.4
No Pulse Records Subset											
TH-21	126	0	6.8	1976	Gazli, USSR	660	Thrust	3.92	5.46	0.702	66.2
TH-22		90								0.864	67.7
TH-23	825	0	7	1992	Cape Mendocino	514	Thrust	3.85	10.72	1.494	122.3
TH-24		90								1.039	42.4
TH-25	1004	270	6.7	1994	Northridge-01	380	Thrust	0.16	3.85	0.753	77.7
TH-26		360								0.932	76.3
TH-27	741	0	6.9	1989	Loma Prieta	376	Strike-slip	0.00	6.96	0.645	56.0
TH-28		90								0.483	47.6
TH-29	753	0	6.9	1989	Loma Prieta	462	Strike-slip	0.00	8.44	0.456	51.4
TH-30		90								0.502	44.5

Table 5. Details of earthquake records after scaling

No.	PGA_{max} (g)	PGV_{max} (cm/s.)	PGA/PGV	Arias Intensity: (m/sec)
Far-Field Earthquake Record Set				
TH-1	0.273	33.8	0.0081	0.757
TH-2	0.246	29.7	0.0083	0.772
TH-3	0.229	22.5	0.0102	1.339
TH-4	0.240	20.8	0.0115	1.056
TH-5	0.257	27.5	0.0093	1.034
TH-6	0.281	57.4	0.0049	1.104
TH-7	0.323	33.3	0.0097	0.973
TH-8	0.374	33.2	0.0112	0.732
TH-9	0.255	33.0	0.0077	1.160
TH-10	0.232	26.3	0.0088	1.332
Near-Field Earthquake Record Set				
No Pulse Records Subset				
TH-11	0.222	25.9	0.0086	0.654
TH-12	0.224	30.7	0.0073	0.741
TH-13	0.211	27.2	0.0078	1.104
TH-14	0.232	29.1	0.0080	1.239
TH-15	0.304	25.7	0.0118	0.858
TH-16	0.232	23.2	0.0100	0.928
TH-17	0.360	39.3	0.0092	0.484
TH-18	0.358	33.3	0.0108	0.559
TH-19	0.343	30.4	0.0113	0.637
TH-20	0.303	19.2	0.0157	0.946
Pulse Records Subset				
TH-21	0.305	31.7	0.0096	0.635
TH-22	0.252	40.9	0.0062	0.842
TH-23	0.268	21.6	0.0124	1.148
TH-24	0.271	35.6	0.0076	0.753
TH-25	0.278	41.1	0.0068	0.963
TH-26	0.227	29.1	0.0078	0.858
TH-27	0.289	31.2	0.0093	0.966
TH-28	0.235	39.5	0.0059	0.548
TH-29	0.238	52.7	0.0045	1.329
TH-30	0.260	49.9	0.0052	1.630

4. Behavior of example structures

The structural behaviors were compared with the IDR (inter-story drift ratio). IDR were accepted as a critical design and performance factor in the literature. The comparation of structures were presented below.

4.1. Behavior of example structures inner frames

For each record in Figure 5 and Figure 6, IDR_{max} and IDR_{ave} values of the analyzes performed in Case-I and Case-II CMRFs are given. In Figure 4, IDR_{max} values obtained because of NDAs made using the FF, NF-NP, and NF-P type THs of Case-I and Case-II buildings are presented comparatively. In this stage of this work, the IDR_{max} value of structure were investigated under three different type of TH record as FF, NF-NP and NF-P type of strong ground motion as mentioned above. In this part, the same CMRFs were divided in three sections in terms TH records used in NDAs, firstly the IDR_{max} values were examined with FF type TH, then it's examined with NF-NP type TH record and finally it's investigated with NF-P type TH records. At the first stage of NDAs, the IDR_{max} values of Case-I structures with 8-, 10-, 13- and 15-story CMRFs were 21.74% (TH-8, Chi-Chi, Taiwan), 30.77% (TH-9, Manjil, Iran), 18.81% (TH-6, Kocaeli, Turkey), and 6.41% (TH-5, Kocaeli, Turkey) smaller than the IDR_{max} values of Case-II structure, respectively. In second stage of NDAs, the IDR_{max} values of Case-I structures with 8-, 10-, 13- and 15-story CMRFs were 25.68% (TH-18, Loma Prieta), 28.9% (TH-12, Gazli, USSR), 33.2% (TH-19, Loma Prieta), and 23.53% (TH-14, Cape Mendocino) smaller than the IDR_{max} values of Case-II structure, respectively. Finally, the last stage for NDAs, the IDR_{max} values of Case-I structures with 8-, 10-, 13- and 15-story CMRFs were 24.68% (TH-22, Loma Prieta), 53.57% (TH-28, Northridge-01), 11.01% (TH-29, Chi-Chi, Taiwan), and 7.2% (TH-29, Chi-Chi, Taiwan) smaller than the IDR_{max} values of Case-II structure, respectively. The maximum desired level of damage to a structure under specific earthquake design level is expressed as performance level. Based on FEMA-273 (FEMA 273, 1997) (1997) and Vision 2000 ("Vision 2000, Conceptual Framework for Performance Based Seismic Engineering of Buildings.," 1995) (1995), the performance level can be divided into seven performance stages which include fully operational, operational, immediate occupancy, damage control, life safety, collapse prevention and near collapse. The drifts proposed for these performance levels are 0.2% for fully operational (FO), 0.5% for operational (OP), 1% for immediate occupancy (IO), 1.5% for damage control (DC), 2% for life safety (LS), and 2.5% for collapse prevention (CP), and 3% for near

collapse (NC). In this way, when the Case-I and Case-II structures were examined in three group type of TH records, the 8-story CMRFs inside both group structure were reached the IO performance level in the first and final NDAs stage were examined. Moreover, according to the IDR_{max} value of the 15-story CMRFs structures, it is the only structure stayed under the IO performance level between the Case-II structures for FF and NF-P type TH records. On the other hand, only the 10-story CMRF reached to the IO performance level for NF-NP type records, and it is the only structure between the Case-I CMRFs structure reached only this performance level.

Variation of IDR_{ave} with the story for each earthquake group is given in the Figure 6. When the IDR_{ave} values of Case-I structures are examined for NDAs with FF type records, the IDR_{ave} values remain between 0.0075 and 0.0093. In NF-NP type NDAs records results, the IDR_{ave} values of Case-I structures are examined, IDR_{ave} values remain between 0.0075 and 0.0093 as same as FF type records NDAs results. Final part of records NF-P types of NDAs results, the IDR_{ave} values of Case-I structures are examined, the IDR_{ave} values remain between 0.0075 and 0.0098. The IDR_{ave} values of the Case-II structures are examined, the IDR_{ave} values remain between 0.0086 and 0.012 for FF type TH records of NDAs, and between 0.0086 and 0.011 for NF-NP type TH records of NDAs. Moreover, for NF-P type TH records of NDAs, the IDR_{ave} values stay between 0.0088 and 0.012 (Figure 6).

Fig. 5 Variation of IDR_{ave} with the story for each earthquake group according to sensitivity coefficient (θ) change in inner frames

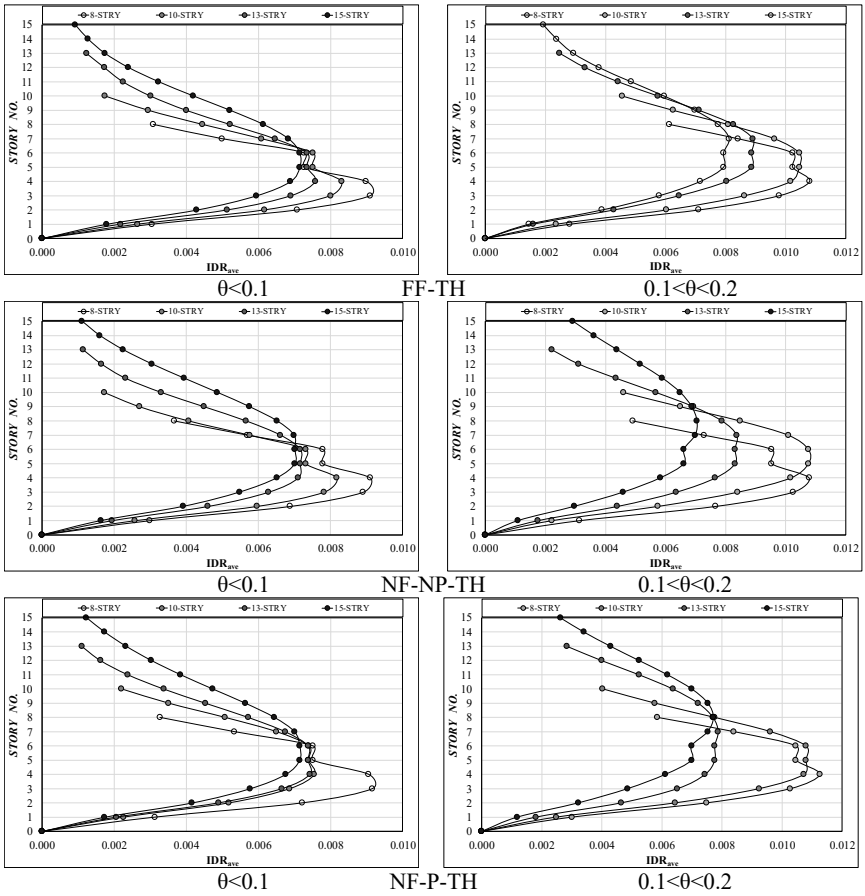

Fig. 6 Variation of the IDR_{max} for each earthquake group according to sensitivity coefficient (θ) change in inner frames

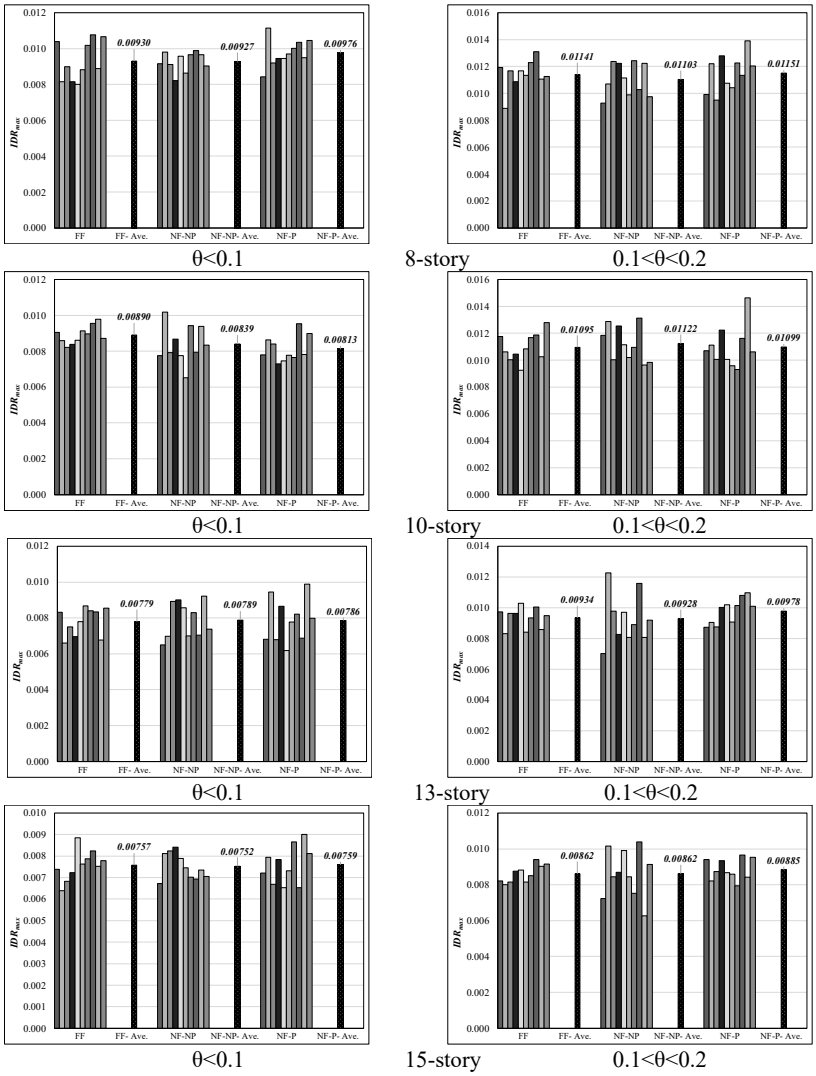

4.2. Behavior of example structures outer frames

In Figure 7 and Figure 8, the IDR_{max} and IDR_{ave} values of Case-III and Case-IV CMRFs were given for each record and also each groups average. When the Case-III structures NDAs were evaluated for FF type TH records, the IDR_{max} values were obtained as 0.00879 (TH-4, Kobe (Japan)), 0.00803 (TH-6, Kocaeli (Turkey)), 0.00710 (TH-3, Kobe (Japan)) and 0.00758 (TH-9, Manjil, (Iran)) for 8-,10-,13- and 15-story CMRFs, respectively.

Moreover, these IDR_{max} values were obtained smaller than the IDR_{max} values of Case-I structures NDAs evaluated for FF type TH records. These TH records were observed differently for each 8-, 10-, 13- and 15-story structure in Case-I and Case-III structures. On the other hand, when the Case-IV structures NDAs were evaluated for FF type TH records, the IDR_{max} values were obtained as 0.01079 (TH-3, Kobe, (Japan)), 0.01120 (TH-8 (Chi-Chi, Taiwan), 0.01062 (TH-10, (Manjil, Iran)), and 0.00958 (TH-10, (Manjil, Iran)) for 8-,10-,13- and 15-story CMRFs, respectively. Case-III structure IDR_{max} values smaller than Case-IV structure IDR_{max} values for NDAs made with FF type TH records, the difference is 22.8%, 39.6%, 49.5%, and 26.3% for 8, 10, 13 and 15-story CMRFs, respectively. TH-10 (Manjil, Iran) record were caused IDR_{max} values for 13- and 15-story CMRF both of the Case-IV structures. Moreover, Case-III and Case-IV structures IDR_{max} values shows different trends. Case-III structures shows decrease until 15-story structures but Case-IV structures IDR_{max} values increase at 10-story structure than it decreases continuously. The effective main earthquake record is similarly the effective component of earthquake records were changing with the structural seismic design parameters. Therefore, the component properties of earthquake records were investigated, and it was observed that the earthquake components where PGA/PGV (peak ground velocity) greater shows mostly biggest IDR_{max} values for 10-,13- and 15-story Case-III structures against the Case-IV structures (Table 5). For the NF-NP type TH records, the IDR_{max} values were obtained as 0.00898 (TH-20, Loma Prieta), 0.00880 (TH-11, Gazli, (USSR)), 0.00783 (TH-15, Northridge-01), and 0.00761 (TH-12, Gazli, USSR) for Case-III structures. For the fourth group with same TH records, Case-IV structures NDAs were evaluated, the IDR_{max} values were obtained as 0.01084 (TH-12, Gazli, USSR), 0.01182 (TH-13, Cape Mendocino), 0.00987 (TH-13, Cape Mendocino) and 0.00999 (TH-12, Gazli, USSR). Case-III structure has smaller IDR_{max} values than Case-IV structure for NDAs made with NF-NP type TH records, the difference is 20.8%, 34.3%, 26.1%, and 31.3% for 8, 10, 13 and 15-story CMRFs, respectively. In Case-III structures, the IDR_{max} results calculated for NF-NP type TH records shows almost a similar trend against the IDR_{max} results calculated for FF type TH records. In Case-IV structures, the IDR_{max} results calculated for NF-NP type TH records shows a different trend against the IDR_{max} results calculated for FF type TH records. The IDR_{max} results calculated for NF-NP type TH records were fluctuating and it reach the max value with 10-story structure then it decreases and then again it increase 15-story CMRFs in Case-IV structures. Like the results of the NF-NP group of IDR_{max}, the component properties

of the earthquake records were investigated, and it was observed that the earthquake components where PGA/PGV was higher showed the largest IDR_{max} values for each Case-III structure against the Case-IV structures (Table 5).

The last group of TH records is NF-P and the IDR_{max} values were obtained as 0.00878 (TH-30, Chi-Chi, Taiwan), 0.00836 (TH-27, Northridge-01), 0.00723 (TH-30, Chi-Chi, Taiwan), and 0.00736 (TH-22, Loma Prieta) for Case-III structures. On the other hand, when the Case-IV structures NDAs were evaluated for NF-P type TH records, 0.01092 (TH-30, Chi-Chi, (Taiwan)), 0.01202 (TH-29, Chi-Chi, (Taiwan)), 0.01088 (TH-29, Chi-Chi, (Taiwan)) and 0.01018 (TH-30, Chi-Chi, (Taiwan)). Case-III structure IDR_{max} values smaller than Case-IV structure IDR_{max} values for NDAs made with NF-P type TH records, the difference is 24.4%, 43.9%, 50.5%, and 38.4% for 8, 10, 13 and 15-story CMRFs, respectively. Moreover, when NDAs were evaluated for NF-P type TH records, it can be clearly seen that the dominant TH record is TH-29 and TH-30 (Chi-Chi, (Taiwan)) for both case and it has the lowest in terms of PGA/PGV values (Table 5).

When the Case-III and Case-IV structures were examined in three group type of TH records, the Case-III CMRFs inside group structure were stay under the IO performance level in all type TH records of NDAs. Moreover, Case-IV structures according to the IDR_{max} value of the NF-P type TH record of NDAs, all structures reached IO performance limit. However, Case-IV structures according to the IDR_{max} value of the FF type TH record of NDAs, all structures reached IO performance limit except 15-story CMRF. Case-IV structures according to the IDR_{max} value of the NF-NP type TH record of NDAs, almost all structures reached IO performance limit (just 13- and 15-story CMRF values 0.0099) (Figure 7).

IDR_{ave} variation with the story for each earthquake group is given in the Figure 8. When the IDR_{ave} values of Case-III structures are examined for NDAs with FF type records, the IDR_{ave} values remain between 0.0065 and 0.0081. In NF-NP type NDAs records results, the IDR_{ave} values of Case-III structures are examined, IDR_{ave} values remain between 0.0063 and 0.0080. Final part of records NF-P types of NDAs results, the IDR_{ave} values of Case-III structures are examined, the IDR_{ave} values remain between 0.0065 and 0.0079. The IDR_{ave} values of the Case-IV structures are examined, the IDR_{ave} values remain between 0.0086 and 0.010 for FF type TH records of NDAs, and between 0.0083 and 0.098 for NF-NP type TH records of NDAs. Moreover, for NF-P type TH records of NDAs, the IDR_{ave} values stay between 0.0085 and 0.0099 (Figure 8).

Fig. 7 Variation of IDR average along the story for each earthquake group according to sensitivity coefficient (θ) change in outer frames

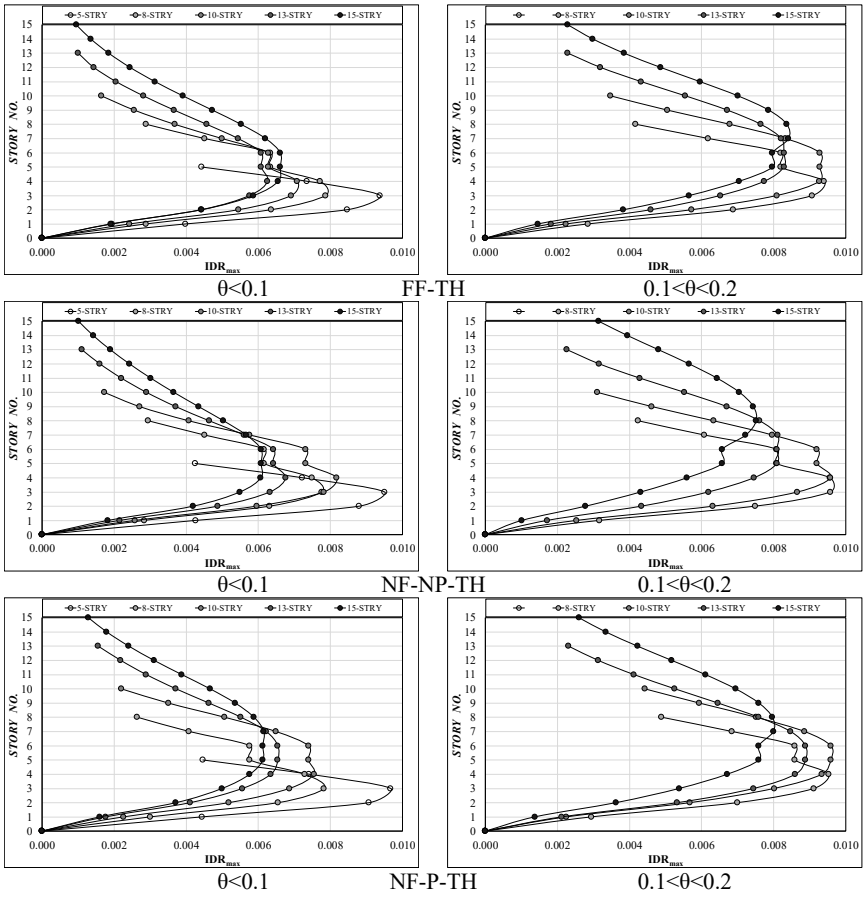

Fig. 8 Variation of the maximum IDR for each earthquake group according to sensitivity coefficient (θ) change in outer frames

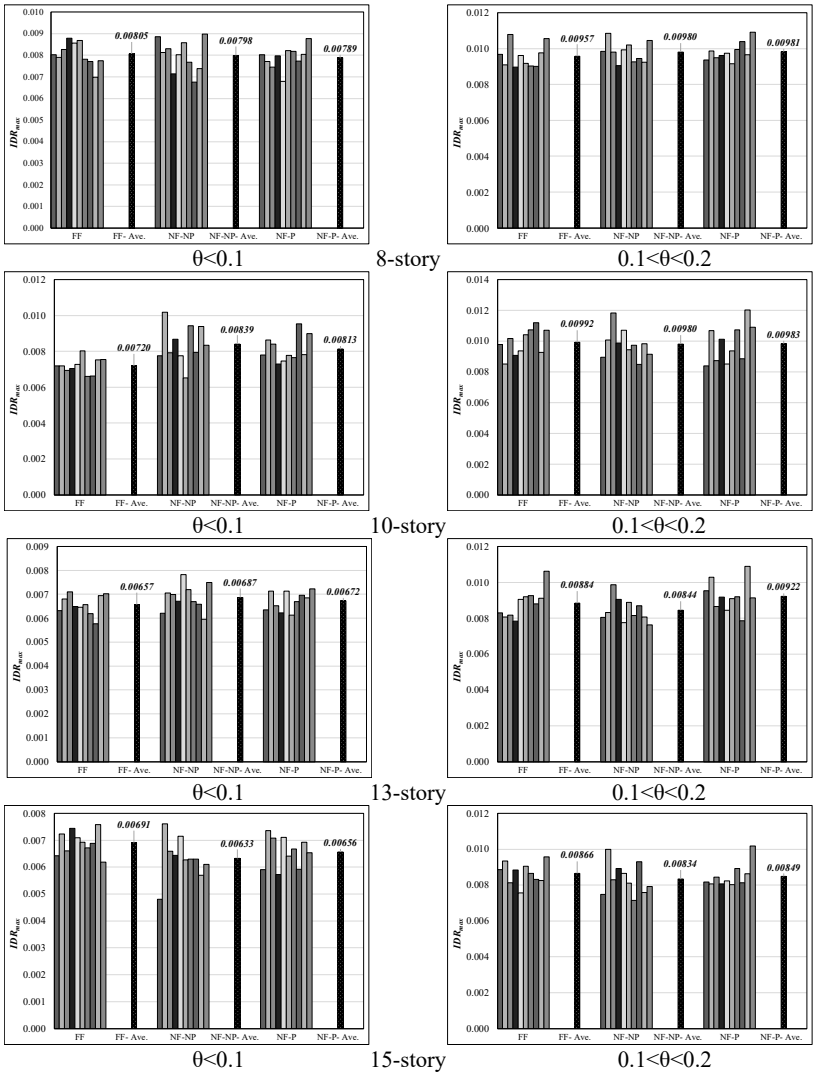

The main variable parameter in the sample structures examined in the study was the change in sensitivity "θ" coefficient. After the structural models were modeled in 3D (all structures are symmetrical), an inner frame in the middle of the structures and a frame from the outside were selected and their behavior was evaluated by NDAs analysis. For NDAs, the series consisting of FF, NF-NP and NF-P type earthquake rockers and with 10 records for each group earthquake were used. The related earthquakes were

matched according to the design spectrum and used in the analysis. As a result, the behavior of the structures was evaluated using IDR coefficients using 4 different frames and 30 earthquake records. According to the data obtained;

- If this coefficient is used in the range of $0<\theta<0.1$, CMRF systems do not reach the IO limit for all earthquake recording types except 8-story CMRF inner frames.
- If this coefficient is in the range of $0.1<\theta\leq0.2$, if this coefficient is used in the relevant range, CMRF systems reach the IO limit for IDR_{max} for all earthquake recording types except 15-story CMRF inner frames.
- In outer frames, if this coefficient is used in the range of $0<\theta<0.1$, all CMRF systems for all earthquake recording types fall below the IO limit for IDR_{max}.
- In outer frames, if it is in the range of $0.1<\theta\leq0.2$, this coefficient exceeds the IO limit for all CMRF systems IDR_{max} in NF-P earthquake records. In other recordings, 8- and 10-story CMRFs reach the IO damage point for IDR_{max}, while the remaining 13- and 15-story CMRF systems reach values very close to the IO limit for IDR_{max}
- In summary, leaving the θ coefficient in this range of $0<\theta<0.1$ creates more reliable results for the IO safety level in earthquakes.

References

Acun, B. (2012). *Eurocode 8: Seismic Design of Buildings, Worked Examples*. Publications Office of the European Union.

Altoontash, A. (2004). Simulation and damage models for performance assessment of reinforced concrete beam-column joints. *PhD Thesis*, *August*, 232.

Antoniou, S., Fragiadakis, M., & Pinho, R. (2008). *Modelling inelastic buckling of reinforcing bars under earthquake loading*. *December*, 347–361. https://doi.org/10.1201/9780203881637.ch22

Baba T, Inai E, Kai M, Noguchi T, M. A. (1995). Structural behaviour of concrete filled steel tubular columns under axial compressive load, part 2: test results on rectangular columns. *Abstracts of the Annual Convention of the Architectural Institute of Japan*, 737–8.

Boukhalkhal, S. H., Ihaddoudène, A. N. T., Da Costa Neves, L. F., & Madi, W. (2019). Dynamic behavior of concrete filled steel tubular columns. *International Journal of Structural Integrity*, *10*(2), 244–264. https://doi.org/10.1108/IJSI-07-2018-0040

Broderick, B. M., & Elnashai, A. S. (1996). Seismic response of composite frames - I. Response criteria and input motion. *Engineering Structures*, *18*(9), 696–706. https://doi.org/10.1016/0141-0296(95)00211-1

Bruneau, M., Uang, C., & Sabelli, R. (2008). Ductile Design of Steel Structures. *Animal Genetics*, *39*(5), 561–563.

Caldara, R. (1998). Composite substructures with partial shear connection: low cycle fatigue behaviour and analysis issues. *Mechanical Engineering*, 1–8.

Castro, J. M. de F. (2006). *Seismic Behaviour of Composite Moment-Resisting Frames*. *April*.

Castro, J. M., Elghazouli, A. Y., & Izzuddin, B. A. (2007). Assessment of effective slab widths in composite beams. *Journal of Constructional Steel Research*, *63*(10), 1317–1327. https://doi.org/10.1016/j.jcsr.2006.11.018

Choi, K. K., & Xiao, Y. (2010). Analytical Studies of Concrete-Filled Circular Steel Tubes under Axial Compression. *Journal of Structural Engineering*, *136*(5), 565–573. https://doi.org/10.1061/(ASCE)ST.1943-541X.0000156

Elghazouli, A. Y., Castro, J. M., & Izzuddin, B. A. (2008). Seismic performance of composite moment-resisting frames. *Engineering Structures*, *30*(7), 1802–1819. https://doi.org/10.1016/j.engstruct.2007.12.004

EN 1994-1-1. (2004). Eurocode 4: Design of composite steel and concrete structures – Part 1-1: General rules and rules for buildings. *European Committee for Standardization*, *3*(February), 33–38. https://doi.org/10.1002/14651858.CD009305.pub2

EN 1998-1. (2004). Eurocode 8: Design of structures for earthquake resistance—Part 1: General rules, seismic actions and rules for buildings. *European Committee for Normalization, Brussels*, *2005*. https://doi.org/[Authority: The European Union per Regulation 305/2011, Directive 98/34/EC, Directive 2004/18/EC]

Etli, S. (2021). *Performance Assessment of Steel-Concrete Composite Buildings* (Issue April) [Ph.D. Thesis]. Gaziantep University.

Etli, S. (2022). Parametric Analysis of the Performance of Steel-Concrete Composite Structures Designed with TBDY 2018. *International Journal of Innovative Engineering Applications*, *6*(1). https://doi.org/10.46460/ijiea.1029942

Etli, S., & Güneyisi, E. M. (2020). Seismic performance evaluation of regular and irregular composite moment resisting frames. *Latin American Journal of Solids and Structures*, *17*(7), 1–22. https://doi.org/10.1590/1679-78255969

Etli, S., & Güneyisi, E. M. (2021). Assessment of Seismic Behavior Factor of Code-Designed Steel–Concrete Composite Buildings. *Arabian Journal for Science and Engineering*, *46*(5), 4271–4292. https://doi.org/10.1007/s13369-020-04913-9

Etli, S., & Güneyisi, E. M. (2022a). Effect of nonlinear modeling approaches used for composite elements on seismic behavior of composite framed buildings. *Sadhana - Academy Proceedings in Engineering Sciences*, *47*(2). https://doi.org/10.1007/s12046-022-01871-w

Etli, S., & Güneyisi, E. M. (2022b). Effect of Using Eccentric Braces with Different Link Lengths on the Seismic Demand of CFST Column-Composite Beam Frames Subjected to Near-Field and Far-Field Earthquakes. In *Iranian Journal of Science and Technology - Transactions of Civil Engineering*. https://doi.org/10.1007/s40996-022-00994-8

FEMA 273, N. (1997). *Guidelines for the seismic rehabilitation of buildings*. Federal Emergency Management Agency Washington, DC.

Filippou, F. C., Popov, E. P., & Bertero, V. V. (1983). Effects of Bond Deterioration on Hysteretic Behaviour of Reinforced Concrete Joints. Report to the National Science Foundation. *Earthquake Engineering Research Center*, *August*, 1–212.

Fukumoto, T., & Morita, K. (2005). Elastoplastic behavior of panel zone in steel beam-to-concrete filled steel tube column moment connections. *Journal of Structural Engineering*, *131*(12), 1841–1853. https://doi.org/10.1061/(ASCE)0733-9445(2005)131:12(1841)

G. Monti, C. Nuti, S. S. (1996). *CYRUS: CYclic Response of Upgraded Sections. A program for the analysis of retrofitted or repaired sections under biaxial cyclic loading including buckling of rebars*.

Güneyisi, E. M., & Etli, S. (2020). Response of steel buildings under near and far field earthquakes. *Civil Engineering Beyond Limits*, *1*(2), 24–30. https://doi.org/10.36937/cebel.2020.002.004

Hawkins, N. M., & Mitchell, D. (1984). Seismic Response of Composite Shear Connections. *Journal of Structural Engineering*, *110*(9), 2120–2136. https://doi.org/10.1061/(ASCE)0733-9445(1984)110:9(2120)

Huang, Z., Huang, X., Li, W., Zhou, Y., Sui, L., & Liew, J. Y. R. (2018). *Experimental behaviour of very high-strength concrete-encased steel composite column subjected to axial compression and end moment*. *Asccs*, 323–329.

Kanatani, H., Tabuchi, M., Kamba, T., Hsiaolien, J., & Ishikawa, M. (1987). A study on concrete filled RHS column to H-beam connections fabricated with HT bolts in rigid frames. *Composite Construction in Steel and Concrete*, 614–635.

Kim, K. D., & Engelhardt, M. D. (2002). Monotonic and cyclic loading models for panel zones in steel moment frames. *Journal of Constructional Steel Research*, *58*(5–8), 605–635. https://doi.org/10.1016/S0143-974X(01)00079-7

Leon, R. T., Hajjar, J. F., Gustafson, M. A., & Shield, C. (1998). Seismic Response of Composite Moment-Resisting Connections. II: Behavior. *Journal of Structural Engineering*, *124*(August), 868–876.

Li, J. T., Chen, Z. P., Xu, J. J., Jing, C. G., & Xue, J. Y. (2018). Cyclic behavior of concrete-filled steel tubular column–reinforced concrete beam frames incorporating 100% recycled concrete aggregates. *Advances in Structural Engineering*, *21*(12), 1802–1814. https://doi.org/10.1177/1369433218755521

Martínez-Rueda, J. E., & Elnashai, A. S. (1997). Confined concrete model under cyclic load. *Materials and Structures*, *30*(3), 139–147. https://doi.org/10.1007/BF02486385

Menegotto, M., & Pinto, P. E. (1973). Method of Analysis for Cyclically Loaded R. C. Plane Frames Including Changes in Geometry and Non-Elastic Behavior of Elements under Combined Normal Force and Bending. *Proceedings of IABSE Symposium on Resistance and Ultimate Deformability of Structures Acted on by Well Defined Loads*, 15–22. https://doi.org/http://dx.doi.org/10.5169/seals-13741

Miranda, B. E. (2012). Strength Reduction Factors in Performance-Based Design. *Ingeniería, Investigación y Tecnología*, 35–39. https://doi.org/10.4156/ijact.vol5.issue9.136

Muhummud, T. (2003). *Seismic behavior and design of composite SMRFs with concrete filled steel tubular columns and steel wide flange beams.* 551.

Nogueiro, P., Simoesdasilva, L., Bento, R., & Simoes, R. (2005). Numerical implementation and calibration of a hysteretic model with pinching for

the cyclic response of steel and composite joints. *Fourth International Conference on Advances in Steel Structures*, 767–774. https://doi.org/10.1016/b978-008044637-0/50112-8

Plumier, A. (2000). European research and code developments on seismic design of composite steel concrete structures. *12 World Conference on Earthquake Engineering--Conference Proceeding*, 1–8.

Seismosoft. (2016). *SeismoStruct A computer program for static and dynamic nonlinear analysis of framed structures V 7.0*.

Shahrooz, B. M., Pantazopoulou, S. J., & Chern, S. P. (1993). Modeling slab contribution in frame connections. *Journal of Structural Engineering*, *118*(9), 2475–2494. https://doi.org/10.1061/(ASCE)0733-9445(1992)118

Srinivasan, C. N., & Schneider, S. P. (1999). Axially Loaded Concrete-Filled Steel Tubes. *Journal of Structural Engineering*, *125*(10), 1202–1206. https://doi.org/10.1061/(ASCE)0733-9445(1999)125:10(1202)

Susantha, K. A. S., Ge, H., & Usami, T. (2001). Uniaxial stress-strain relationship of concrete confined by various shaped steel tubes. *Engineering Structures*, *23*(10), 1331–1347. https://doi.org/10.1016/S0141-0296(01)00020-7

Thermou, G. E., Elnashai, A. S., Plumier, A., & Done, C. (2004). Seismic design and performance of composite frames. *Journal of Constructional Steel Research*, *60*(1), 31–57. https://doi.org/10.1016/j.jcsr.2003.08.006

Tomii, M., Yoshimura, K., & Morishita, Y. (1977). Experimental Studies on Concrete-Filled Steel Tubular Stub Columns Under Concentric Loading. *International Colloquium on Stability of Structures Under Static and Dynamic Loads*, 718–741.

Uy, B. (2001). Strength of short concrete filled high strength steel box columns. *Journal of Constructional Steel Research*, *57*(2), 113–134. https://doi.org/10.1016/S0143-974X(00)00014-6

Vision 2000, Conceptual Framework for Performance Based Seismic Engineering of Buildings. (1995). *Structural Engineers Association of California*, *2*.

Xiao, Y., & Wu, H. (2000). Compressive behavior of concrete confined by carbon fiber composite jackets. *Journal of Materials in Civil Engineering*, *12*(2), 139–146.

Xu, J. J., Chen, Z. P., Ozbakkaloglu, T., Zhao, X. Y., & Demartino, C. (2018). A critical assessment of the compressive behavior of reinforced recycled aggregate concrete columns. *Engineering Structures*, *161*(January), 161–175. https://doi.org/10.1016/j.engstruct.2018.02.003

Zhang, X., & Gao, X. (2019). The hysteretic behavior of recycled aggregate concrete-filled square steel tube columns. *Engineering Structures*, *198*(April), 109523. https://doi.org/10.1016/j.engstruct.2019.109523

Chapter 9

Reflection of Industry 4.0 on Logistics Activities: Logistics 4.0

Beste Desticioğlu Taşdemir[1]

Abstract

The idea of "Industry 4.0" was developed as a result of the industrial industry's transition to digital manufacturing. The term refers to a new industrial era characterized by the combination of automation of production processes, data exchange, artificial intelligence and the internet. The key goals of Industry 4.0 are to make production processes more efficient, to offer flexibility, and to develop a smarter manufacturing environment. The advancements brought about by Industry 4.0 have had an impact on the logistics sector, along with many other industries, highlighting the transition to Logistics 4.0. Logistics 4.0 refers to the digital transformation in supply chain management. This concept aims to make the processes from production to consumer more efficient, flexible and connected. Logistics 4.0 encompasses a number of developments involving the use of technological innovations and digital platforms. In this study, the historical development of Industry 4.0 and Industry 4.0 are discussed and the components of Industry 4.0 are examined in detail. In addition, in the study, information about Logistics 4.0, which has developed with the effect of Industry 4.0, is given. In the study, sample applications made in logistics activities within the scope of Logistics 4.0 are presented.

1. Introduction

In order to compete with other firms, boost efficiency and profitability, and cut costs, organizations are attempting to provide better service by enhancing their business processes with emerging technology. Technological developments in the field of industry have been effective in experiencing 4 industrial revolutions until today. The utilization of steam power in machines brought to the first Industrial Revolution, and the availability of cheap raw materials and the use of electricity and oil in manufacturing led to the second. The third industrial revolution has taken place as a result of advancements in

1 Asst. Prof., National Defence University Alparslan Defence Sciences and National Security Institute, Department of Operations Research, Orcid: 0000-0001-8321-4554

https://doi.org/10.58830/ozgur.pub130.c601

communication and technology as well as machine automation. The fourth industrial revolution, also referred to as "Industry 4.0," has already occurred.

Industry 4.0 refers to human-oriented technologies that integrate with developing technologies where knowledge is at the forefront. At the German Hannover Industry Fair, the phrase "Industry 4.0" was first used. Industry 4.0 can be defined as technologies that enable the integration of physical and digital processes, and the production of products in smart factories with smart processes and their distribution with smart logistics. With the technologies brought by Industry 4.0, production will be realized in a safer and faster way, since information in the processes can be accessed simultaneously, an immediate intervention can be made in case of any error during the processes, faulty production will be reduced with the use of robots and machines, and all processes will be more agile and flexible. With Industry 4.0, new technologies such as the internet of things, big data analysis, cloud computing technology, smart factories, 3D printers have begun to enter our lives.

The logistics sector, along with many other sectors, has been impacted by the innovations brought about by Industry 4.0, which has highlighted the metamorphosis of Logistics 4.0. Logistics 4.0 transformation includes the use of sensors, 3D printers and advanced robots in logistics activities, and the use of software based on information technologies in the entire supply chain. Communication, cooperation and coordination between the stakeholders in the supply chain can be achieved with the digitalization and process automation brought by Logistics 4.0. Today, companies using Logistics 4.0 technologies have an advantage over rival companies. In the coming years, the technologies brought by Industry 4.0 will be used more widely in logistics activities. This will reduce costs and increase efficiency in logistics processes.

Logistics 4.0 enables companies to create new networks, automate the supply chain and be faster in transport activities. This network created by companies includes containers, warehouse management systems, smart pallets, ERP software, driverless transportation systems. Logistics 4.0 consists of the internet of things (IoT), cloud computing technologies, cyber-physical systems (CPS), big data analysis, autonomous robots, 3D printers, smart factories, augmented reality, wearable technologies, etc. In this study, the historical development of Industry 4.0 and the innovations brought by Industry 4.0 are mentioned. In the next stage of the study, the definition of Logistics 4.0 and its historical development are discussed. The

Logistics 4.0 components are covered in the study's last section, which also includes examples of Logistics 4.0 applications in the logistics industry.

2. Industry 4.0

Two important changes that changed the economic history and ensured economic development are the agricultural and industrial revolutions. The change in science and technology over time has greatly affected the industry and industrial revolutions have occurred. With the industrial revolution that emerged in England after 1750, machines began to be used in production instead of hand and body power. Between 1760 and 1840, the introduction of steam power increased industrial productivity in the iron and textile industries. The first industrial revolution, known as Industry 1.0, is defined as the use of steam-powered machinery in manufacturing. After the industrial revolution that emerged in England, it spread to the USA and all over Europe, and the welfare level of the countries began to rise with the increasing production [1].

The technology revolution, also known as Industry 2.0, was the second industrial revolution, beginning in the second part of the 19th century and lasting until the middle of the 20th. The expansion of railway networks and eased access to raw materials were key factors in the 2nd Industrial Revolution's birth. Additionally, the second industrial revolution was made possible by the advancement of technology and the utilization of new energy sources in industry. In the 2nd Industrial Revolution, steel began to be used instead of iron, and it was also among the raw materials used in the production of chemicals. Additionally, the use of oil and electricity as energy sources in place of steam and coal has begun. These technological developments have triggered the emergence of mass production. Henry Ford started using assembly lines around this time to produce the T model car, which provided the groundwork for mass production [2]. As a result of these industrial advancements, urbanization and the establishment of economically robust states both increased. The 2nd Industrial Revolution first started in America and then spread all over the world, especially in Germany and Japan.

After the 1970s, the use of automation in production started to become widespread with the developments in technology. With the end of the cold war, the whole world has become a common market in the globalization process. With the effect of this situation, there has been a great change in traditional production, marketing and sales techniques. With the developments in communication and technology and the use of automation in production,

Industry 3.0, which is the 3rd Industrial Revolution, has emerged. In the 3rd Industrial Revolution, significant developments were experienced especially in the synthetic products, nuclear energy, telecommunications, agriculture, informatics, electronics and fiberoptic sectors [3].

In recent years, the phrase "Industry 4.0," which alludes to the fourth industrial revolution, has gained popularity. At the Hannover Industry Fair in 2011, the idea of "Industry 4.0" was applied for the first time to advance the German economy [4]. Industry 4.0 is a technology-based production method that aims to meet the needs of the sectors in a fast, innovative and reliable way with the developing technology. Industry 4.0 is an industrial revolution that integrates the real and virtual worlds, smart production methods, and the replacement of embedded systems with cyber-physical systems [5]. Industry 4.0 is based on the production process in which smart systems, smart factories and other applications emerging with the development of technology are taken into account. It is thought that efficiency and production capacity will increase with the implementation of Industry 4.0.

New technologies have started to emerge as a result of Industry 4.0. Industry 4.0 consists of internet of things, cloud computing, big data, 3D printers, smart factories, autonomous robots, augmented reality, simulation, and cyber security components.

3. Logistics 4.0

In the globalizing world, companies have to develop new strategies to increase their sales and enter new markets. Today, logistics practices for quickly identifying and meeting customer needs are among the most critical activities for companies. Unlike earlier times when the name "logistics" exclusively applied to transportation-related operations, today's definition of logistics includes all actions taken during the manufacturing and delivery of goods to clients. Logistics covers the activities of allocating, planning and controlling the necessary resources for the realization of production, distribution and supply activities. As can be seen, logistics encompasses all operations from the creation of the product through its delivery to the client. It is not just concerned with distribution activities. On the other hand, logistics management offers the management and control of all required actions, from the creation of the items through the delivery to the consumer [6].

In the logistics sector, it should be fast, flexible and in a structure that will increase efficiency in order to meet customer expectations. It is only

possible for businesses to meet these expectations with the successful use of technology. This transformation, which occurs by using new technologies in the logistics sector, is called "Logistics 4.0" or "Smart Logistics". Advanced information technologies are used in the supply chain, along with cutting-edge robots and sensors, as part of Logistics 4.0 [7]. It is seen that companies that have implemented the Logistics 4.0 transformation in their logistics activities in recent years have gained a great advantage over their competitors. Therefore, companies attach importance to the Logistics 4.0 transformation.

Figure 1: Evolution of Logistics 4.0 [8]

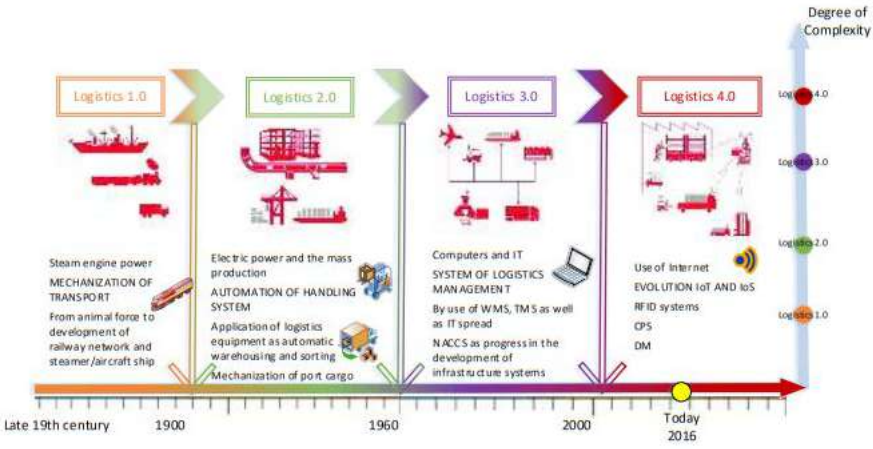

Transformations in logistics and supply chain have also been made possible by changes in information and communication technologies. All systems are affected by industrial revolutions, technological developments and changing concepts. As industrial revolutions have progressed over time, so have the processes utilized in logistics [9]. Logistics 4.0 is a result of the innovations brought on by Industry 4.0. Industry 4.0 and Logistics 4.0 have similarities as well as differences.

As with the development of the industry, there were four phases in the development of logistics. The transformation known as Logistics 1.0 started at the end of the 18th century with the adoption of water and steam power in production and transportation vehicles as well as the modernisation of systems. The carrying capacities have risen and transportation mechanization has begun thanks to the use of water and steam power on ships and trains as well as the construction of railway networks [10]. With the use of steam power in transportation vehicles, rail and sea transportation started to be

carried out besides the highway [3]. During this period, finished products are stored in warehouses and the placement of these products is handled manually. Wheelbarrows are used to transport products to vehicles [11].

As a result of the employment of electricity and oil in transportation and communication equipment, logistics 2.0, the second logistics revolution, was born. During this time, the chemical industry saw significant advancements as well as the beginning of the use of materials like steel, aluminum, and copper in the manufacturing of machines. In addition to road transport, important developments were also experienced in steam ship transport and railway transport in this period. One of the most significant inventions of this era is the use of steam container ships for shipping. In this process, logistics equipment working with electrical energy has also been developed. Forklifts operating with electrical energy have started to be used for placing the products on the shelves and transporting them inside the warehouse [12]. With the advancement of freight handling automation, tools for automatic sorting and warehouses came into use.

Automated production technologies are the foundation of the third industrial revolution. The most significant technology advancements in this industrial revolution are industrial robots and numerically controlled machines (Milling, Turning CNC, etc.) that enable flexible output. With the development of software like the Warehouse Management System (WMS) and Transport Management System (TMS) their usage in logistics operations, the idea of Logistics 3.0 has evolved. These softwares used in logistics management ensure that the orders of the suppliers can be supplied in a short time. In addition, with the help of these software, the planning, routing and scheduling of fleet vehicles can be done beforehand. In the Logistics 3.0 period, automatic machines and industrial robots started to be used in logistics activities [13]. In in-production transportation, the use of automatic moving bands, forklifts and automatic robots with predetermined routes have become widespread.

Industry 4.0, often known as the fourth industrial revolution, is a result of the logistics industry's acceptance of new applications offered by cyber-physical systems. In technology-based logistics processes, the use of software-based applications with Industry 4.0 has facilitated the calculation and communication processes and brought the opportunity to reach all stakeholders quickly [9]. Logistics 4.0, which makes use of advanced internet usage and integrates smart products and smart services, is also known as "smart logistics". Logistics 4.0 can be defined as a structure that provides digital management between logistics processes and targets, customers and

stakeholders in the supply chain [14]. With the transformation brought about by Logistics 4.0, traditional tools and devices with fixed functions have started to be replaced by software-based machines that will adapt to the needs of the user, have a flexible structure and can easily add new functions. In hardware-based devices, the technology is used until the device wears out without being renewed, while in software-based machines, the machine is developed by integrating the developing technology with the software, increasing the performance and life of the machine.

It is feasible to improve customer happiness, lower production costs, optimize production, and boost storage and transportation process efficiency by utilizing the transition brought about by Logistics 4.0. In Logistics 4.0, hardware-oriented logistics systems have started to be replaced by software-oriented smart logistics systems [9].

The innovations and technologies used by Logistics 4.0 and Industry 4.0 are similar. Logistics 4.0, as in Industry 4.0 transformation, consists of IoT, digital transformation, autonomous robots, big data analytics, CPS, cloud computing systems, augmented reality, smart factories, 3D printers, wearable technologies, etc.

4. Technologies Affecting Logistics 4.0

With the effect of developing technology, the logistics industry is also in a great change. Innovation and technology have significantly affected the future of logistics. Innovations such as the internet of things, big data analytics, cyber-physical systems, autonomous robots, 3D printers, and wearable technologies that Industry 4.0 has added to our lives have also contributed to the development of logistics activities by being adapted to the logistics industry. The applications of various technologies that have an impact on the logistics sector are covered in this section.

4.1. Internet of Things (IoT)

The Internet of Things is one of the brightest technologies that has entered our lives with Industry 4.0 and can be applied in many areas with the developing technology. It is a technology that makes it possible for network-connected things to communicate with one another and be controlled remotely. Internet of Things technology is briefly shown as "The IoT". Technically speaking, the IoT is a grouping of physical objects that link with the software of mechanical, electronic, computer, and communication systems to enable data transfer over the internet. This technology, which provides machine-to-machine communication, is being applied in many

areas today and continues to develop. It is thought that the following advantages will be achieved with the more widespread and active use of IoT technology in production and logistics:

- Managers at every stage of production will be able to intervene immediately in case of any problem by using smart communication tools.
- It will be possible to follow the supply chain with the labels or sensors placed on the products or objects.
- With the increase in the use of machines and robots, there will be less need for human resources in production.
- When smart devices are used in the internet of things, there will be a decrease in infrastructure and energy costs.
- The income and profits of the companies will be increased.

The IoT technology ensures that not only objects, but also people, data and processes are in continuous communication without interruption [15]. With the RFID tags, barcodes and sensors placed on the products, all transportation and distribution activities from the starting point of the products until they reach the customer can be monitored IoT-based distribution systems make the supply chain more productive and efficient while also empowering managers to make decisions more quickly and accurately. [16].

With the development of international trade, the logistics sector has become more complex and new technologies have been needed in the logistics sector. Utilizing IoT technology in the logistics industry allows for more effective and efficient management of tasks including inventory and warehouse management, resource management, fleet management, and order management [16]. In addition, the IoT can be used in the logistics sector in the tracking and control of vehicles, communication and information management in subjects such as fleet management, road condition, smart parking and road safety. Activities like storage, transportation, and stock management will be transformed throughout the process from the stage of production to the delivery of the product to the client with the application of IoT in the logistics industry. It will be ensured that all activities in these processes can be monitored and controlled [17].

4.2. Big Data Analytics

Today, it is possible to access a lot of data over the internet. However, among these data obtained, there are data that create information pollution and it is thought that it is difficult to extract the desired information from these data. Big data is a term used for databases that are growing and becoming difficult to manage. The difficulty of managing this data is due to the variety, volume and speed of the data [12]. Since the data that can be accessed over the Internet is very diverse and abundant, various software and applications are used to obtain the desired data. Big data is defined as data that can be collected, stored, analyzed, and managed beyond the capability of database management systems and software tools. Big data records every single action that each user makes on the internet. Big data analytics continuously evaluates organizational strategies and activities carried out in production, and examines technologies, skills and practices that will be effective in creating business planning [18].

Big data is applications that reach and combine many different data and make it possible to make decisions with this data. Big data brings together many different data and is effective in decision making, as well as providing advantages in reducing costs and improving product and service flows. It is intended to boost efficiency, lower mistake rates, and increase flexibility through the analysis of big data [19]. Big data applications in the logistics sector have gained great importance in recent years. RFID readers, sensors, logistics software, transportation management systems, etc. generate large amounts of data. In addition, social media data has also affected logistics activities in recent years. Big data is used in determining the routes of the vehicles, in shift planning, in the selection of warehouses, etc., in address verification. In addition, customer preferences are positively affected by creating personalized opportunities with the analysis of customer habits with big data analysis [20].

4.3. Cloud Computing

Cloud computing systems are the provision of data related to information systems from third parties. Cloud computing services refer to the computer model that provides access to the desired data over the internet at any time by using storage devices, cloud centers and applications shared over the cloud [21]. With cloud computing systems, applications in the cloud can be run over the internet with a remote drive or the user's data can be accessed from a remote drive at any time. Cloud computing systems provide the

opportunity to access the data previously stored on the cloud at the desired place and time.

Today, many companies serving on a global basis store their data in cloud computing systems that allow access from different places. Thus, it is possible to quickly access the desired data at many different points. Cloud computing systems can be thought of as a transformation rather than an innovation.

Cloud computing applications are also used in the logistics sector. There are numerous supply chain participants in the logistics sector. Cloud computing platforms make it possible for supply chain participants to collaborate for the least amount of money. With cloud computing systems, it enables them to create logistics collaborations without incurring any cost to software, hardware and data warehouses with information technology resources. With cloud computing systems, any problem experienced in activities such as logistics, transportation and storage can be solved quickly [16]. With the application of cloud computing systems in the logistics sector, previously manual operations have become possible with automation systems, and with the use of automation systems, costs have decreased and productivity has increased [22].

It is feasible to receive, store, and safeguard logistical data using cloud computing technologies. In order to support logistics operations, it also offers the processing and analysis of logistics data. Thus, cloud computing benefits from logistics software exchange for planning logistics operations, determining the routes of vehicles [21].

4.4. Cyber-Physical Systems (CPS)

Cyber physical systems (CPS) are one of the indispensable elements of smart systems. CPS are all the devices and systems that enable communication and cooperation between the virtual and physical worlds. CPS provides bidirectional flow between decision and production systems in production engineering [9]. CPS are systems that enable the interaction of both people and objects by integrating new methods and software and physical capabilities. CPS also provides the opportunity to carry out activities to make calculations, monitor and control transactions by connecting with the physical world and adapting to developing technologies. CPS uses sensors and actuators to link the real world to the digital one. [3]. CPS consists of five key stages:

1. To ensure the integration of the virtual world and the physical world.
2. Creating a system of easily adaptable systems in a dynamic structure.

3. To create systems that can easily adapt to change.
4. Working together with distributed control systems.
5. Establish comprehensive human-system cooperation.

CPS consists of two components, a network consisting of an object or systems connected to each other over the internet, and a virtual environment with computer-generated simulation of behaviors. The most important feature of CPS systems is that they can be activated in a short time by using technology for events that can hardly be noticed with human skills. Since CPSs are connected to the internet, they can access the data very quickly and process and use this data quickly. CPS forms the basis of Industry 4.0 with IoT technology.

CPS ensures that the value chain, production and logistics activities are carried out simultaneously, ensuring the coordination between them, increasing the performance and quickly finding solutions to variable dynamic situations. CPS is widely used in enterprise resource planning [23].

4.5. Autonomous Robots

The internet of things, smart sensors, technological developments in integrated systems have been influential in the development of autonomous robots that are completely computer-controlled. Autonomous robots can perform their functions automatically without the need for human intervention by using technologies such as sensors, remote sensing, and the internet of things. For a device to be considered a robot, it must first be autonomously controlled. Today, robots can perform their movements by sensing physical quantities such as sensors, light, heat, current, magnetism, speed, which can operate under different conditions.

Autonomous robots provide flexibility in production and support the transition to smart manufacturing. With the increase in the use of robots in the industry, it is expected that the robots will adapt to flexible working, the use and calibration of robots will become easier, the development of robots that will adapt to production activities, the prices of robots will decrease [10]. Autonomous robots select, package, test, manufacture and install faster and more efficiently than human power. With the increase in the use of robots in production, automation will increase and there will be a decrease in human error rates.

Autonomous robots are frequently used in logistics activities such as transportation, storage, labeling, packaging and handling. In logistics

processes, autonomous robots are mostly used in warehousing activities. In addition, with the use of automatic racking, RFID and sensor technologies in warehouses, the use of autonomous robots in warehousing activities has become widespread [14].

4.6. 3D Printings

3D printers are devices that can take computer-generated data and turn it into manipulable, three-dimensional things. 3D printers are a technology that creates 3D objects with a layer-by-layer material arrangement designed by using computer aided drawing software. In this method, various materials are printed in sequential layers on top of one another. After any tool, object is designed, the concrete version of this design can be made in three dimensions with the help of 3D printers. The prototype of the product designed with 3D printers can be produced quickly. Thus, it is ensured that the products are brought to the market more quickly [24].

3D printers play an active role in logistics and supply chain. 3D printers can be decisive in choosing a production center or warehouse location. 3D printers allow production centers to be located close to strategic markets, reducing overall costs and transportation costs [25]. In addition, 3D printers are also used in the production of spare parts. By producing the spare part with 3D printers when needed, it provides savings in both storage and investment costs. With the development of e-commerce, companies have started to switch to the same time delivery approach instead of same day delivery. With 3D printers, the product requested by the customer will be produced and delivered quickly. Thus, superiority will be achieved over rival companies and there will be a decrease in transportation and storage costs [10].

4.7. Smart Factories

New production innovations have been used to launch each industrial revolution. Industry 4.0, on the other hand, has been realized with the widespread use of machines with automation in production. In smart factories where production is carried out using automated machines, sensors and robots, there is a decrease in the workforce needed. In addition, less faulty production is made in the production carried out with machines with automation. In order for smart factories to work effectively, it is possible to use the internet of things technology and sensors without any errors. Smart factories increase efficiency and adapt to flexible production.

In Logistics 4.0, logistics activities will be carried out using autonomous vehicles. Ordering the needed product with autonomous robots will increase efficiency in warehousing and logistics activities. Future production will utilize smart factories, which will result in smart logistics applications [14].

4.8. Wearable Technologies

All types of clothing and accessories with built-in computers and cutting-edge technology are considered wearable technologies. Wearable technologies provide control of machines/devices by taking dynamic, instant interaction with employees and operators. This technology provides the interaction between the virtual world and the real world. Smart watches, RFID readers, sensor gloves, glasses, headphones, belts, pens, shoes are used as wearable technologies. These objects are not only light and easy to use, but also do not hinder the movements of the operator [26]. Wearable technologies do not hinder the ability of the staff to use both hands, allowing them to work efficiently.

Wearable technologies, which are especially used in packaging, storage and transportation activities in the logistics sector, are integrated into business processes, increasing efficiency and being effective in reducing costs. For example, the staff working in the warehouse can access all information from the barcode on the product, pallet or equipment with the barcode reader glasses they wear, or the inventory can be processed by determining the location of the product while the vehicle is being loaded. As you can see, wearable technologies increase productivity by speeding up work.

4.9. Augmented Reality

Augmented reality is the images projected from computers in detail with image, sound, graphics, video and GPS data to our environment. This technology enables the simultaneous merging of the physical world and the digital world by using virtual images, graphics, wearable technologies, cameras on computers and smartphones. Augmented reality applications are encountered in many sectors today.

Augmented reality technology is frequently used in the logistics sector. In the field of logistics, where the shelves will be placed in the warehouse setup, which equipment will be placed where, and the routes of the vehicles can be determined with augmented reality technology. Augmented reality applications ensure that the risks and dangers that the personnel may encounter can be determined in advance, and also prevent occupational

accidents [10]. In addition, the use of this technology provides the reduction of errors, flexibility in production, and an increase in working speed.

5. Conclusions

Nowadays, it is getting harder and harder to compete with the productions made using traditional methods. Therefore, the developing technology in every field should also be effective in the industry. With the use of new applications and automation that emerged with the developing technology in the industry, Industry 4.0, which is the 4th Industrial Revolution, took place. With Industry 4.0, IoT, big data analytics, CPS, cloud computing autonomous robots, augmented reality Technologies, 3D printers have started to be used.

Supply chain management and logistics management have both been impacted by developments in information and communication technology with Industry 4.0. The concept of Logistics 4.0 has evolved as a result of the application of new technologies introduced into our lives with Automation and Industry 4.0 in the logistics industry. Like Industry 4.0, Logistics 4.0 creates integrated solutions that enable the integration of new information technologies with logistics processes. Logistics 4.0, which consists of similar technologies used by Industry 4.0, consists of technological components such as big data analytics, IoT, CPS, RFID technology, cloud computing, autonomous robots, augmented reality, 3D printers.

When Logistics 4.0 is successfully implemented, the logistics process of the product takes place fluently. The success of the companies in the logistics processes provides a more efficient working environment between the customer and the supplier, the manufacturer and the wholesaler. In addition, the use of these technologies reduces costs and is effective in reducing errors in processes. With Logistics 4.0 applications, oil consumption is also reduced, thereby reducing the carbon footprint.

In this study, the industrial revolutions that occur with the reflection of technological developments on the industry are mentioned and Industry 4.0, which is the 4th Industrial Revolution, is discussed in detail. The technologies that came into our lives with Industry 4.0 have had an impact on numerous industries, including the logistics industry, and they have also revealed applications for Logistics 4.0. In this study, the components of Logistics 4.0, which started to be implemented with Logistics 4.0, are explained and information is given about the technological developments in the logistics sector and the new applications that have emerged. However, with the developing technology, new applications, software and technologies

are applied in the logistics sector. In future studies, it is thought that it would be appropriate to develop the literature by considering new applications in the logistics sector in detail.

References

1. Jänicke, M., & Jacob, K. (2009). A Third Industrial Revolution? Solutions to the crisis of resource-intensive growth. *Solutions to the Crisis of Resource-Intensive Growth*.
2. Alizon, F., Shooter, S. B., & Simpson, T. W. (2008, January). Henry Ford and the Model T: lessons for product platforming and mass customization. In *International Design Engineering Technical Conferences and Computers and Information in Engineering Conference* (Vol. 43291, pp. 59-66).
3. Şekkeli, Z. H., & Bakan, İ. (2018). Endüstri 4.0'ın Etkisiyle Lojistik 4.0. *Journal of Life Economics*, *5*(2), 17-36.
4. Kang, H. S., Lee, J. Y., Choi, S., Kim, H., Park, J. H., Son, J. Y., ... & Noh, S. D. (2016). Smart manufacturing: Past research, present findings, and future directions. *International journal of precision engineering and manufacturing-green technology*, *3*, 111-128.
5. Hofmann, E., & Rüsch, M. (2017). Industry 4.0 and the current status as well as future prospects on logistics. *Computers in industry*, *89*, 23-34.
6. Desticioğlu, B. (2021). Green Supply Chain Management and Sample Applications . Journal of Naval Sciences and Engineering , 17 (2) , 283-308 .
7. Jahn, C., Kersten, W., & Ringle, C. M. (2018). *Logistics 4.0 and sustainable supply chain management: innovative solutions for logistics and sustainable supply chain management in the context of industry 4.0*. Berlin: epubli GmbH.
8. Wang, K. (2016, November). Logistics 4.0 solution-new challenges and opportunities. In *6th international workshop of advanced manufacturing and automation* (pp. 68-74). Atlantis Press.
9. Timm, I. J., & Lorig, F. (2015, December). Logistics 4.0-A challenge for simulattion. In *2015 Winter Simulation Conference (WSC)* (pp. 3118-3119). IEEE.
10. Demiral, D. G. (2021). Endüstri 4.0'ın lojistik boyutu: Lojistik 4.0. *IBAD Sosyal Bilimler Dergisi*, (9), 231-251.
11. Alkış, G., Piritini, S., & Ertemel, A. V. (2020). Lojistik Sektöründe Endüstri 4.0 Uygulamalarinin Operasyonel Verimliliğe Etkisi. *Business & Management Studies: An International Journal*, *8*(1), 371-395.
12. Domingo Galindo, L. (2016). *The challenges of logistics 4.0 for the supply chain management and the information technology* (Master's thesis, NTNU).
13. Pamuk, N. S., & Soysal, M. (2018). Yeni sanayi devrimi endüstri 4.0 üzerine bir inceleme. *Verimlilik Dergisi*, (1), 41-66.
14. Taş, A., & Alagöz, S. B. (2021). Lojistik sektörü özelinde endüstri 4.0 farkındalık düzeyleri üzerine bir araştırma. *Karamanoğlu Mehmetbey Üniversitesi Sosyal Ve Ekonomik Araştırmalar Dergisi*, *23*(41), 404-417.

15. Witkowski, K. (2017). Internet of things, big data, industry 4.0–innovative solutions in logistics and supply chains management. *Procedia engineering*, *182*, 763-769.
16. Barreto, L., Amaral, A., & Pereira, T. (2017). Industry 4.0 implications in logistics: an overview. *Procedia manufacturing*, *13*, 1245-1252.
17. Güngör Tanç, Ş., & Öz, A. Ö. (2020). Endüstri 4.0 kapsamında lojistik 4.0'ın incelenmesine yönelik teorik bir çalışma.
18. Kache, F., & Seuring, S. (2017). Challenges and opportunities of digital information at the intersection of Big Data Analytics and supply chain management. *International journal of operations & production management*.
19. Davenport, T. (2014). *Big data at work: dispelling the myths, uncovering the opportunities*. Harvard Business Review Press.
20. Büyüközkan, G., & Güler, M. (2019). Lojistik 4.0 teknolojilerinin analizi için metodolojik yaklaşım. *Journal of Entrepreneurship and Innovation Management*, *8*(1), 21-47.
21. Xu, Z., He, J., & Chen, Z. (2012, December). Design and actualization of IoT-based intelligent logistics system. In *2012 IEEE International Conference on Industrial Engineering and Engineering Management* (pp. 2245-2248). IEEE.
22. Niharika, G., & Ritu, V. (2015). Cloud architecture for the logistics business. *Procedia Computer Science*, *50*, 414-420.
23. Baheti, R., & Gill, H. (2011). Cyber-physical systems. *The impact of control technology*, *12*(1), 161-166.
24. Durach, C. F., Kurpjuweit, S., & Wagner, S. M. (2017). The impact of additive manufacturing on supply chains. *International Journal of Physical Distribution & Logistics Management*, *47*(10), 954-971.
25. Pagano, A. M., & Liotine, M. (2019). *Technology in supply chain management and logistics: Current practice and future applications*. Elsevier.
26. Kong, X. T., Luo, H., Huang, G. Q., & Yang, X. (2019). Industrial wearable system: the human-centric empowering technology in Industry 4.0. *Journal of Intelligent Manufacturing*, *30*, 2853-2869.

Chapter 10

Increasing the Efficiency of Composite Materials Manufacturing Productivity by Using Artificial Intelligent Methods

Mehmet Emin Demir[1]

Onur Denizhan[2]

Abstract

The manufacturing of composite materials plays a vital role in various industries due to their exceptional properties, performance and lightweight characteristics. However, the manufacturing process of composite materials involves numerous complex and time-consuming tasks, resulting in reduced productivity and increased costs. Additionally, there is a continuous need to improve the efficiency and productivity of composite materials manufacturing processes to meet the growing demands and ensure cost-effective production. Artificial intelligence (AI) has the potential to greatly impact the development, design, and use of composite materials. In particular, it can play crucial role in enhancing efficiency and productivity within the manufacturing process. Artificial intelligence offers various techniques and algorithms that can optimize different aspects of the manufacturing process, including predictive maintenance, real time monitoring and control, process parameter optimization, quality control, material characterization, and design and development. By leveraging artificial intelligence, manufacturers can achieve improved productivity, enhanced product quality, reduced waste, and decreased downtime. The utilization of artificial intelligence methods in composite materials manufacturing holds great potential for positioning companies at the forefront of innovation and competitiveness in the industry. This chapter explores the application of artificial intelligence methods to increase the efficiency of composite materials manufacturing productivity.

1 Assistant Professor, Besiri Vocational School, Batman University, memin.demir@batman.edu.tr, Orcid: 0000-0001-9630-6378

2 Ph.D., Department of Electronics and Automation, Batman University, onur.denizhan@batman.edu.tr, Orcid: 0000-0001-8380-9507

https://doi.org/10.58830/ozgur.pub130.c602

1. Introduction

Composite materials have gained significant importance in various industries due to their exceptional properties such as high strength, lightweight, corrosion resistance, and design flexibility. However, with the increasing demand for composite materials, there is a growing need to improve manufacturing productivity and efficiency to meet market requirements and maintain a competitive edge. In recent years, artificial intelligence (AI) methods have emerged as powerful tools to optimize and enhance the manufacturing processes of composite materials.

Artificial intelligence, a branch of computer science, focuses on developing intelligent systems capable of performing tasks that typically require human intelligence. By leveraging AI algorithms and techniques, manufacturers can harness the power of data analytics, predictive modeling, real-time monitoring, and optimization to significantly improve productivity in composite materials manufacturing. Following the most recent articles are some examples of the AI algorithms with the composite materials manufacturing: Denizhan [1] provides valuable insights into the integration of artificial intelligence (AI) with engineering design, highlighting the collaboration between computer science and other engineering fields. Okafor et al. [2] present a comprehensive review focusing on machine learning-aided design of hybrid and reinforced polymer composites, covering AI applications in material and process selection. Fahem et al. [3] conduct experimental and numerical studies on Glass fiber Reinforced Polymer using the artificial neural network-enhanced Jaya algorithm, exploring material prediction and finite element methods. Saleh et al. [4] compare response surface methodology and artificial neural networks for optimizing the mechanical properties of magnesium matrix composites. Stergiou et al. [5] provide a literature review on the utilization of AI methods for property prediction and process optimization in material science. Singhal et al. [6] simulate the mechanical properties of stir cast aluminum matrix composites using artificial neural networks, comparing the results with experimental data. Natrayan et al. [7] investigate the optimization of filler content and size in various composite materials by combining Taguchi methods with AI techniques. Doddashamachar et al. [8] propose a novel artificial neural network method for predicting polypropylene composite properties, demonstrating the accuracy of AI-based predictions. Jazbi et al. [9] provide a comprehensive literature review on AI applications for various materials, focusing on the mechanical properties. Tapeh and Nazer [10] present a review of recent trends an practices in AI applications for structural

engineering, including a discussion on materials. Additionality, Cetkin and Demir [11,12] present two examples of composite materials studies that do not utilize AI methods.

The traditional approaches to manufacturing productivity improvement often involve trial-and-error methods or rely on human expertise, which may be time-consuming, resource-intensive, and prone to errors. In contrast, AI methods offer the potential to revolutionize composite materials manufacturing by providing data-driven insights and automated decision-making processes. This chapter examines the various ways in which AI can be employed to enhance the productivity of composite materials.

2. Ways to Increase Composite Materials Manufacturing Productivity Using AI

There are some ways AI can be used to increase manufacturing productivity: Material design and development, manufacturing process optimization, quality control and defect detection, material characterization, multiscale predictive maintenance and simulation, intelligent robotics and automation, real-time monitoring and control, data analytics and decision-making and structural analysis and optimization.

2.1. Material Design and Development

Artificial intelligence algorithms can assist in the design and development of composite materials. By leveraging AI in composite material design and development, engineers can accelerate the discovery of new materials, optimize designs, reduce development cycles, and ultimately improve the performance and efficiency composite materials in various applications. By analyzing vast amounts of data on material properties, performance requirements, and manufacturing constraints, AI can help identify optimal material compositions, predict material behavior, and accelerate the discovery of new composite formulations with desired properties.

2.1.1. Knowledge Discovery and Innovation:

AI can uncover hidden patterns and relations within vast amounts of data, facilitating knowledge discovery and driving innovation in composite material design. By identifying new material combinations, processing methods, or performance-enhancing factors, AI can contribute to the development of advanced composite materials with improved properties and performance.

2.1.2. Material Property Prediction

AI algorithms can learn from existing datasets of composite materials to predict their mechanical, thermal, or electrical properties. By training on a wide range of data, including material compositions, processing parameters, and test results, AI model can estimate material properties for new compositions without the need for extensive testing. this enables efficient material selection and design optimization.

2.1.3. Material Composition and Formulation

AI algorithms can analyze data on material properties, compatibility, and performance requirements to suggest the most suitable combinations of reinforcing fibers, matrix materials, additives, and processing techniques. By considering various factors such as strengths, weight, cost, and environmental impact. AI can guide the formulation of composite materials that meet specific design goals

2.1.4. Generative Design

AI-powered generative design techniques can explore a vast design space for composite materials. By inputting design constraints and objectives, AI algorithms can autonomously generate and evaluate numerous design alternatives. This approach can lead to the discovery of unconventional and optimized material compositions, fiber orientations, and geometric configurations that maximize performance and meet specific application requirements.

2.2. Manufacturing Process Optimization

Artificial intelligence algorithms can analyze data from sensors, manufacturing parameters, and historical records to optimize the composite manufacturing process. By analyzing sensor data, process parameters, and historical records, AI algorithms can identify process inefficiencies, optimize process conditions, and reduce defects. By identifying optimal process parameters, such as temperature, pressure, and curing time, AI can help manufacturers achieve consistent and high-quality composite products, reducing waste and improving efficiency.

2.2.1. Process Parameter Optimization

AI algorithms can analyze large datasets of process parameters, material properties, and desired outcomes to optimize manufacturing processes. By using machine learning and optimization techniques, AI can identify the

optimal combination of process variables (e.g., temperature, pressure, curing time) to achieve desired material properties, improve production efficiency, and reduce waste.

2.2.2. Energy Efficiency and Resource Optimization

AI algorithms can analyze process data to identify opportunities for energy saving and resource optimization. By optimizing process parameters, equipment utilization, and material usage, AI can help reduce energy consumption, minimize waste generation, and improve sustainability in composite materials manufacturing.

2.2.3. Supply Chain Optimization

AI can optimize the supply chain of composite materials manufacturing by analyzing data on material availability, supplier performance, and demand fluctuations. By using predictive algorithms, AI can forecast material needs, optimize inventory levels, and identify alternative suppliers or materials to minimize disruptions and reduce costs.

2.3. Quality Control and Defect Detection

AI-powered computer vision systems can be used to detect defects in composite materials during manufacturing or inspection processes. By analyzing images or sensor data, AI algorithms can identify defects such as voids, delamination, or fiber misalignment. Early detection of defects allows for timely corrective actions, reducing crap and improving productivity.

2.3.1. Root Cause Analysis

AI can assist in identifying the root cause of defects in composite materials. By analyzing historical data and process parameters, AI algorithms can uncover correlations and patterns that contribute to defect occurrence. This information can guide process optimization efforts and preventive measures to reduce the likelihood of similar defects in the future.

2.3.2. Statistical Process Control

AI algorithms can perform statistical analysis on process data to identify trends, variations, or out-of-control conditions that may affect composite material quality. By monitoring key process parameters, AI can detect deviations from expected values and alert operators to take corrective actions. This helps ensure consistent and high-quality production.

2.3.3. Computer Vision Inspection

AI-powered computer vision systems can analyze images or sensor data to detect defects in composite materials. By training AI models on a dataset of labeled images that represent different types of defects (such as voids, delamination, or fiber misalignment), the algorithms can automatically identify and classify defects in real-time. This allows for efficient and accurate inspection of composite materials

2.3.4. Automated Defect Detection

AI algorithms can analyze sensor data, such as ultrasound or thermal imaging, to identify defects in composite materials. By detecting anomalies or patterns indicative of defects, AI can alert operators or trigger automated actions to address the issues. This proactive approach to defect detection reduces the likelihood of faulty products reaching the market

2.4. Material Characterization

Artificial intelligence can play crucial role in the characterization of composite materials. AI algorithms can exact patterns and correlations to accurately characterize composite materials by analyzing data from various sources, such as material properties, manufacturing parameters, and testing results. AI algorithms can extract patterns and correlations to predict material behavior and guide the selection of optimal material compositions, leading to improved manufacturing efficiency and product performance. This includes identifying key material properties, such as stiffness, strength, and durability, and understanding the relationship between these properties and different manufacturing factors. AI can also assist in identifying optimal material compositions for specific applications by analyzing large datasets. By leveraging AI for material characterization, manufacturers can make informed decisions regarding material selection, process optimization, and product design, ultimately improving the efficiency and effectiveness of composite material manufacturing. This can lead to more efficient and accurate material testing, reducing the need for extensive physical testing and accelerating material development cycles.

2.4.1. Image Analysis

AI algorithms can analyze images of composite materials to extract valuable information about their microstructure, such as fiber orientation, porosity, and fiber-matrix interface quality. By automatically processing and

interpreting images, AI can provide quantitative data on these characteristics, enabling efficient and accurate characterization.

2.4.2. Machine Learning-Based Material Property Prediction

AI algorithms can learn from existing datasets of composite materials to predict their mechanical, thermal or electrical properties. By training on a wide range of data, including material compositions, processing parameters, and test results, AI models can estimate material properties for new compositions without the need for extensive testing.

2.4.3. Material Behavior Modeling

AI can assist in modeling the behavior of composite materials under different loading conditions. By incorporating data from material testing and simulations, AI algorithms can develop predictive models that capture complex material responses, such as stress-strain behavior, fatigue life, or failure modes. These models enable accurate characterization of material behavior and inform design decisions.

2.4.4. Data Fusion

AI can integrate data from various sources, including material testing, manufacturing parameters, and environmental conditions, to provide a comprehensive characterization of composite materials. By combining and analyzing these datasets, AI algorithms can identify correlations and patterns that enhance the understanding of material behavior and performance.

2.4.5. Process-Structure-Property Relationships

AI can establish relations between manufacturing processes, resulting material structures, and their properties. By analyzing data from process parameters, microstructural features, and material properties, AI can uncover the dependencies and interactions between these factors. This knowledge aids in the optimization of manufacturing processes to achieve desired material properties.

2.5. Predictive Maintenance

Artificial intelligence can analyze sensor data from manufacturing equipment used in composite material production to predict maintenance needs. By identifying potential equipment failures or performance degradation in advance, manufacturers can schedule maintenance activities proactively, minimize unplanned downtime, and optimize equipment

utilization. As a result, the productivity of the manufacturing process can be significantly improved, leading to higher efficiency and reduced production disruptions

2.5.1. Data Integration and Analysis

AI can integrate data from various sources, including equipment sensors, maintenance records, and environmental conditions. By analyzing this combined data, AI algorithms can identify correlations and patterns that help understand the root causes of equipment failures. This knowledge enables targeted maintenance actions and process improvements to prevent future failures.

2.5.2. Maintenance Scheduling and Optimization

AI algorithms can optimize maintenance schedules based on equipment health, production demand, and other constraints. By considering factors such as equipment criticality, availability of spare parts, and production downtime windows, AI can generate optimized maintenance plans. This minimizes the impact on production while ensuring timely maintenance to prevent failures

2.5.3. Equipment Health Monitoring

AI can monitor the health of equipment used in composite materials manufacturing by analyzing sensor data over time. By establishing baseline behavior and tracking deviations, AI algorithms can assess the degradation or wear of equipment components. This information helps schedule maintenance activities based on the actual health status of the equipment, maximizing its operational lifespan.

2.5.4. Failure Prediction

AI can predict equipment failures by analyzing historical maintenance records, sensor data, and environmental factors. By employing machine learning algorithms, AI can identify patterns and indicators that precede equipment failures. This enables timely maintenance or replacement of components, minimizing disruptions in the manufacturing process and preventing quality issues.

2.5.5. Condition Monitoring

AI algorithms can analyze sensor data from equipment used in composite materials manufacturing, such as curing ovens, presses, or cutting machines.

By continuously monitoring various parameters, including temperature, vibration, pressure, or power consumption, AI can detect anomalies or patterns indicative of equipment degradation or impending failures.

2.5.6. Fault Detection and Diagnostics

AI can analyze historical data and patterns to identify early signs of equipment faults or anomalies. By comparing real-time sensor data with historical patterns, AI algorithms can detect deviations and trigger alerts or maintenance actions. This enables proactive maintenance, preventing unexpected equipment failures and reducing downtime.

2.6. Predictive Modeling and Simulation

Artificial intelligence can be used to develop advanced simulation models for composite material manufacturing processes. These models can incorporate various parameters, such as material properties, manufacturing parameters, environmental conditions, process conditions, and equipment settings. AI algorithms can optimize the simulation models, enabling manufacturers to predict and optimize manufacturing outcomes, reducing the ne for physical trial-and-error iterations and enhancing productivity

2.6.1. Hierarchical Modeling

AI can enable the development of multiscale models for composite materials. By integrating data from various length scales, AI algorithms can create models that capture the behavior of composite materials at different levels, from the macroscopic to the microscopic. This allows for more accurate predictions of material properties, performance and failure mechanics.

2.6.2. Virtual Testing and Optimization

AI-powered simulations can replace or supplement physical testing by virtually testing composite materials under various conditions. By combining multiscale modeling and AI algorithms, simulations can predict the mechanical, thermal, and electrical properties of composite materials. This allows for virtual testing of different material designs, optimizing material properties, and reducing the need for extensive physical prototyping.

2.6.3. Constitutive Modeling

AI can assist in developing constitutive models for composite materials by learning the relationships between material properties, microstructure,

and loading conditions. AI algorithms can analyze experimental data and computational simulations to identify the constitutive equations that govern the material behavior. This enables accurate predictions of material response under different loading scenarios.

2.6.4. Data-Driven Model Development

AI algorithms can analyze large volumes of data from experimental testing, material characterization, and manufacturing processes to develop data-driven models for composite materials. These models can capture complex relationships and non-linear behaviors, enabling more accurate predictions and simulations of material response under different loading conditions.

2.7. Intelligent Robotics and Automation

AI-powered robots and automation systems can be used in composite material manufacturing to automate repetitive tasks, such as material handling, cutting, or assembly. This increases efficiency and productivity while reducing the risk of errors or injuries. By leveraging AL-powered robots and automation systems, manufacturers can improve productivity, reduce labor costs, enhance quality control, and accelerate the production of composite materials. However, it is important to ensure proper integration, programming, and safety measures to effectively harness the benefits of AI in composite material manufacturing.

2.7.1. Material Handling

AI-powered robots can handle composite materials efficiently and precisely. They can accurately position and transport materials, reducing the risk of damage and ensuring consistent quality. AI algorithms can enable robots to adapt to different material types, and sizes, making them versatile for various manufacturing processes.

2.7.2. Assembly and Manufacturing

AI-powered robots can automate the assembly of composite components, they can perform tasks such as laying up layers of composite materials, placing reinforcements. and applying adhesives or resins. With AI algorithms, robots can optimize the assembly proves, ensuring proper alignment, minimizing waste, and increasing manufacturing speed and accuracy.

2.7.3. Machining and Trimming

AI-powered robots can be programmed to perform precise machining and trimming operations on composite components. With the ability to interpret CAD models and real-time feedback, they can optimize tool paths and adjust cutting parameters for efficient and accurate material removal, reducing manual labor and increasing productivity.

2.7.4. Robotic Composite Manufacturing Cells

AI can integrate multiple robots and automation systems into a cohesive manufacturing cell for composite materials. These cells can be programmed to perform various tasks in a synchronized and efficient manner, reducing cycle times, improving process consistency, and maximizing productivity.

2.7.5. Adaptive Manufacturing

AI algorithms can enable robots to adapt to changes in material properties, process conditions, and design requirements. They can adjust their actions in real-time based on sensor feedback, optimizing the manufacturing process for the specific conditions encountered. This adaptability enhances the efficiency and flexibility of composite materials manufacturing.

2.8. Real-Time Monitoring and Control

Artificial intelligence algorithms can analyze real-time sensor data from the manufacturing process to monitor critical parameters and control process variables. By continuously adjusting process conditions based on real-time feedback, AI can optimize manufacturing efficiency, improve product quality, and reduce waste.

2.8.1. Sensor Data Analysis

AI algorithms can analyze real-time sensor data from composite material manufacturing processes. By monitoring parameters such as temperature, pressure, humidity, and curing time, AI can identify deviations or anomalies that may affect the quality of the final product. This enables timely innervations and adjustments to maintain optimal process conditions.

2.8.2. Automated Decision-Making

AI can automate decision-making processes in real-time based on predefined rules and optimization algorithms. For example, AI can automatically adjust process parameters, trigger material selection choices, or initiate quality control actions based on sensor feedback. This reduces human

intervention and decision-making time, streamlining the manufacturing process and improving efficiency.

2.8.3. Adaptive Control

AI-powered control systems can adapt to changing process conditions and optimize material production accordingly. By continuously monitoring sensor data and applying machine learning algorithms, AI can make real-time adjustments to process variables such as temperature, pressure, or feed rate. This ensures that the manufacturing process remains optimized and delivers consistent quality despite variations in raw materials or environmental conditions.

2.8.4. Fault Detection

AI can detect and predict equipment faults or failures in real-time by analyzing sensor data. By detecting anomalies or patterns indicative of impending equipment issues, AI algorithms can trigger maintenance alerts or automatically adjust process parameters to prevent production disruptions. This proactive approach to maintenance improves equipment reliability, reduces downtime, and increases overall productivity.

2.9. Data Analytics and Decision-Making

Artificial intelligence can analyze large volumes of data collected from composite material manufacturing processes to uncover insights and patterns. These insights can support data-driven decision-making, enabling manufacturers to optimize production planning, resource allocation, and process improvements, leading to increased efficiency and productivity. In other words, AI can provide decision support systems for composite material selection, design, and manufacturing. AI enables data-driven decision-making, proactive monitoring, and continuous process optimization, leading to improved manufacturing outcomes.

2.9.1. Data Integration and Management

AI algorithms can integrate data from various sources, including material properties, process parameters, equipment sensor data, and quality control information. By consolidating and managing this data, AI enables comprehensive analysis and decision-making based on a holistic view of the manufacturing process.

2.9.2. Descriptive Analytics

AI can analyze historical data to provide insights into past performance, trends, and patterns. By applying descriptive analytics techniques, AL algorithms can summarize and visualize data, allowing engineers and decision-maker to understand the current state of the manufacturing process and identify areas for improvement.

2.9.3. Predictive Analytics

AI algorithms can leverage historical data to forecast future outcomes and trends in composite materials manufacturing. By employing predictive analytics techniques, AI can anticipate material properties, process performance, equipment failures, and product quality. This enables proactive decision-making and the ability to optimize processes in advance.

2.9.4. Prescriptive Analytics

AI can utilize optimization algorithms to recommend the best course of action based on defined objectives, constraints, and real-time data. By considering multiple factors such as material properties, process parameters, equipment availability, and production goals, AI algorithms can suggest optimized process settings, production schedules, or material compositions. This facilities data-driven decision-making and improves overall manufacturing efficiency.

2.9.5. Decision Support Systems

AI can assist decision-makers by providing real-time insights, recommendations, and scenario analysis. By utilizing machine learning and optimization algorithms, AI can help optimize process parameters, material selections, production schedules, and quality control measures. This empowers decision-makers to make informed decisions that maximize efficiency, quality, and profitability in composite materials manufacturing.

2.10. Structural Analysis and Optimization

Artificial intelligence can assist in structural analysis and optimization of composite materials. By analyzing complex data sets and using machine learning algorithms, AI can optimize the structural design of composite components, improve load-bearing capacity, and reduce wright while maintaining strength and durability. AI can explore a wide range of design possibilities and identify optimal material compositions, fiber orientations,

or structural configurations. This can lead to the development of lightweight, durable, and high-performance composite products.

2.10.1. Generative Design

AI-powered generative design techniques can explore and generate innovative composite structural designs. By inputting design constrains and objectives, AI algorithms can autonomously generate and evaluate numerous design alternativities. This approach can lead to the discovery of unconventional and optimized structural configurations that maximize performance while minimizing material usage and weight.

2.10.2. Multi-Objective Optimization

AI can handle multi-objective optimization problems in composite material structures. By considering multiple performance criteria, such as weight reduction, stiffness, strength, and cost, AI algorithms can find the best compromise solutions. This allows engineers to explore trade-offs and make informed decisions regarding material selection, structural design and manufacturing processes.

2.10.3. Material Selection

AI can assist in selecting most suitable composite materials for specific applications. by considering factors such as material properties, cos, weight, and manufacturing considerations, AI algorithms can analyze vast amounts of data to identify the best composite materials for structural applications. this ensures that the selected materials meet that desired performance Criteria while minimizing costs and production time.

2.10.4. Finite Element Analysis (FEA) and Simulation

AI algorithms can assist in performing advanced FEA and simulations for composite materials. By incorporating material properties, geometry, loading conditions, and environmental factors, AI can generate accurate simulations of composite structures. This enables engineers to predict structural behavior, stress distribution, and failure modes, leading to more efficient and optimized designs.

2.10.5. Design Optimization

AI algorithms can be employed to optimize the design of composite structures. By integrating FEA with optimization algorithms, AI can explore a wide range of design parameters, such as laminate stacking sequences, ply

orientations, and thicknesses. The al-driven optimization process can identify the most optimal configurations that meet performance requirements, weight reduction targets, and manufacturing constraints.

3. Summary

The manufacturing industry is constantly seeking ways to enhance productivity and efficiency in order to stay competitive in the global market. Composite materials, known for their superior strength-to weight ratio, are increasingly being used in various industries, including aerospace, automotive, and construction. In this context, harnessing power of artificial intelligence (AI) methods has emerged as a promising approach to improving the manufacturing processes of composite materials. This chapter focuses on the application of AI methods in composite materials manufacturing to increase productivity. AI techniques such as machine learning, computer vision, and robotics offer innovative solutions that can streamline and optimize various stages of the manufacturing process.

One area where AI can be leveraged is in materials selection and design. By analyzing vast amounts of data on composite materials, AL algorithms can identify optimal material combinations and configurations for specific applications. This not only saves time and resources but also improve s the overall performance and reliability of the end product.

Another aspect where AL proves valuable is process optimization. AL algorithms can monitor and analyze real-time data from sensors and actuators within the manufacturing environment. This enables proactive identification of potential defects or anomalies, allowing for immediate adjustments to maintain quality standards and prevent costly errors. Furthermore, AI can assist in predictive maintenance, anticipating machine failures and optimizing maintenance schedules to minimize downtime.

Moreover, AI-powered robotic systems can automate repetitive and labor-intensive tasks in composite materials manufacturing. These systems can perform tasks such as cutting, drilling, and assembly with precision and speed, reducing human error and increasing production rates. Collaborative robots, known as cobots, can work alongside human operators, enhancing safety and efficiency in the manufacturing environment.

Implementing AI methods in composite material manufacturing requires data collection and integration from various sources, careful validation and calibration of AI models, and collaboration between engineers, data scientists, and production teams. Therefore, implementing AI methods in composite

materials manufacturing does come with challenges. Issues such as data quality, model interpretability, and integration with existing manufacturing systems need to be addressed. It is important to consider data security, model interpretability, and regulatory compliance while leveraging AI technologies in composite material manufacturing processes. Additionally, ensuring the ethical and responsive use of AI id crucial, considering the potential impact on the workforce and data privacy.

In conclusion, the integration of artificial intelligence methods, into composite materials manufacturing holds great promise for increasing productivity and efficiency. By leveraging AI algorithms, manufacturers can optimize material selection, enhance process control, and automate tasks, leading to improved product quality, reduced costs, and accelerated production rates. Continued research and development in this field will undoubtedly drive advancements and shape the future of composite materials manufacturing.

References

[1] Denizhan, O. (2023). The design of mechanisms via artificial intelligence. In: Kaygusuz, K. (ed.), *Interdisciplinary Studies on Contemporary Research Practices in Engineering in the 21st Century II* (pp. 17-25). Özgür Publications. https://doi.org/10.58830/ozgur.pub95.c437

[2] Okafor, C. E., Iweriolor, S., Ani, O. I. et al. (2023). Advances in machine learning-aided design of reinforced polymer composite and hybrid material systems. *Hybrid Advances*, 2, 100026. https://doi.org/10.1016/j.hybadv.2023.100026.

[3] Fahem, N., Belaidi, I., Brahim, A. O. et al. (2023). Prediction of resisting force and tensile load reduction in GFRP composite materials using artificial neural network-enhanced jaya algorithm, *Composite Structures*, 304(1), 116326. https://doi.org/10.1016/j.compstruct.2022.116326.

[4] Saleh, B., Ma, A., Fathi, R. et. al. (2023). Optimized mechanical properties of magnesium matrix composites using RSM and ANN, *Materials Science and Engineering: B*, 290, 116303. https://doi.org/10.1016/j.mseb.2023.116303.

[5] Stergiou, K., Ntakolia, C., Varytis, P., et al. (2023). Enhancing property prediction and process optimization in building materials through machine learning: A review, *Computational Materials Science,* 220, 112031. https://doi.org/10.1016/j.commatsci.2023.112031.

[6] Singhal, S., Khan, S. A., Muaz, M. et al. (2023) Simulation of mechanical properties of stir cast aluminum matrix composites through Artificial Neural Networks (ANN), *Materials Today: Proceedings,* 72(3), 1102-1109. https://doi.org/10.1016/j.matpr.2022.09.174.

[7] Natrayan, L, Bhaskar, A., Patil, P. P. (2023). Optimization of filler content and size on mechanical performance of graphene/hemp/epoxy-based hybrid composites using Taguchi with ANN technique, *Journal of Nanomaterials*, 2023, 8235077. https://doi.org/10.1155/2023/8235077

[8] Doddashamachar, M., Sen, S., & Setty, R. N. V. (2023) A novel Artificial Neural Network-based model for predicting dielectric properties of banana fiber filled with polypropylene composites. *Journal of Thermoplastic Composite Materials*. 0(0). doi:10.1177/08927057221148455

[9] Jazbi, M., Aghazadeh, A. B. and Mirvalad, S. (2023). A comprehensive review on the artificial intelligence (AI) approaches used for examining the mechanical properties of concrete incorporating various materials. *Int. J. Optim. Civil Eng.,* 13(1), 93-110.

[10] Tapeh, A. T. G., and Naser, M. Z. (2023). Artificial intelligence, machine learning, and deep learning in structural engineering: a scientometrics review of trends and best practices. *Arch Computat. Methods Eng* 30, 115–159. https://doi.org/10.1007/s11831-022-09793-w

[11] Çetkin, E, Demir, M. E, and Ergün, R. K. (2023) The effect of different fillers, loads, and sliding distance on adhesive wear in woven e-glass fabric composites. *Proceedings of the Institution of Mechanical Engineers, Part E: Journal of Process Mechanical Engineering*. 237(2), 418-429. doi:10.1177/09544089221136808

[12] Demir, M. E, Çelik, Y.H., Kilickap, E. et al. (2022). The effect of B4C reinforcements on the microstructure, mechanical properties, and wear behavior of AA7075 alloy matrix produced by squeeze casting. *Proceedings of the Institution of Mechanical Engineers, Part E: Journal of Process Mechanical Engineering*, 0(0). doi:10.1177/09544089221139095

Chapter 11

Solar Irradiance Prediction and Methods Used in Prediction Studies

Erşan Ömer Yüzer[1]

Altuğ Bozkurt[2]

Abstract

Solar energy is considered one of the most important renewable energy sources and is recognized as the fastest-growing energy source worldwide. The power generated in solar energy facilities primarily depends on the amount of radiation reaching the surface of photovoltaic (PV) panels. Prior knowledge of solar radiation is crucial for reliable planning and efficient design of solar energy systems. Therefore, solar radiation forecasting is a highly significant topic. Various techniques can be employed for solar radiation prediction, including fundamental physical and statistical methods, as well as ensemble methods obtained by combining different approaches. However, the remarkable success of artificial neural networks, a form of artificial intelligence application that enhances learning algorithms, in various applications has attracted researchers to this field. The promising potential of this field is evident in the richness of proposed methods and the increasing number of publications. The main objective of this study is to review artificial intelligence-based techniques found in the literature for solar radiation prediction and to identify research gaps by examining radiation predictions using machine learning-based methods and hybrid models created by their combination with other techniques, which have gained popularity recently. Additionally, the aim is to provide an analysis that guides future improvements and understanding of recent advancements in this field. To facilitate and enhance research in this area, a comprehensive review of various artificial intelligence-based prediction methods employed in solar radiation prediction studies, particularly focusing on the most commonly used artificial intelligence-based approach published recently, is presented. Furthermore, information on the required data parameters in solar radiation prediction studies is provided. All research details, fundamental features, and specifics are summarized in tabular and shape formats for a comprehensive overview.

1 Lect. PhD; Hakkâri University, Çölemerik Vocational School, Department of Electricity and Energy. ersanomeryuzer@hakkari.edu.tr, Orcid: 0000-0002-9089-1358

2 Asst. Prof.; Yildiz Technical University, Faculty of Electrical and Electronics, Department of Electrical Engineering. abozkurt@yildiz.edu.tr, Orcid: 0000-0001-6458-1260

https://doi.org/10.58830/ozgur.pub130.c672

1. Introduction

One of the major challenges for global energy supply in the near future is the large integration of renewable energy sources, particularly unpredictable ones such as wind and solar, into the existing or future energy infrastructure. The variability of renewable energy sources poses even greater challenges. Therefore, it is crucial to effectively predict these sources, especially in order to harness a high proportion of renewable energy.

Solar energy is the most abundant and easily accessible energy source among renewable energy sources. However, due to its dependence on weather conditions, solar energy, being a variable energy source, is not reliable without accurate production forecasting. Each year, the latest techniques and approaches emerge worldwide to improve the accuracy of models and reduce uncertainty in predictions. In particular, solar irradiance prediction is a significant component in solar energy production. Providing forecasts to PV plant managers and grid operators assists in better planning of solar energy storage and utilization of other energy sources. This facilitates the integration and optimization of PV systems with the grid. Additionally, the ability to forecast solar irradiance is valuable for the planning and distribution of electricity generated by different units [1]-[4].

Solar irradiance prediction studies require data from the region for which the forecast is to be made. These data can be obtained through on-site measurements, meteorological stations, or remote sensing via meteorological satellites. The most commonly used data sources are ground measurements, satellite data, and sky imagery. Ground measurement data, typically obtained from meteorological stations, include solar characteristics as well as meteorological and physical parameters. The most widely used measurement devices are pyranometers and pyrheliometers, which measure global horizontal irradiance (GHI) and direct normal irradiance (DNI), respectively. While ground measurements provide accurate and high temporal resolution data, the cost of establishing and maintaining a meteorological network limits its installation in every region. Moreover, the need for continuous operation of measurement devices may lead to calibration issues and maintenance requirements, causing interruptions in data collection [5,6]. Figure 1 illustrates the dataset parameters used in solar irradiance prediction studies.

Figure 1. Dataset parameters used in solar irradiance prediction [7]

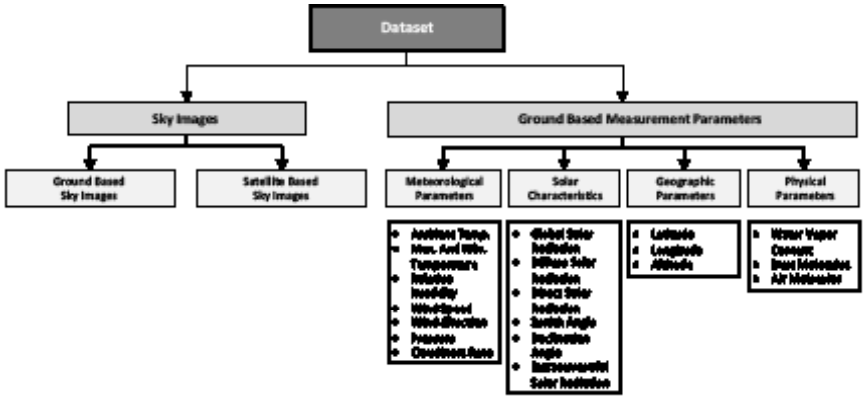

Prediction studies in the field of renewable energy are crucial for both accurately determining the areas for investment and addressing problems that arise during the operational phase based on preliminary forecasts. Artificial intelligence methods, which exhibit superior characteristics compared to traditional prediction methods and are now being utilized in various fields, are among the most important approaches in prediction studies. Performance analyses indicate that these methods outperform conventional methods. Furthermore, in recent years, researchers have developed ensemble methods to uncover the unique features of individual models and enhance the performance of prediction methods. These combinations provide more accurate results compared to individual models [8].

The selection of the prediction method primarily depends on the forecast horizon. However, not all models used have the same accuracy in terms of input parameters and forecast horizon. Predictions are generally classified into long-term (one year to ten years), medium-term (one month to one year), short-term (one day or one week), and very short-term (seconds to minutes). For the development and planning phase of a solar power plant, long-term forecasts are required, while medium-term, short-term, and very short-term predictions are needed for its operation [9]-[11]. Many studies in this field have developed different methodologies for solar irradiance prediction proposed in the last decade. The prediction methods based on forecast horizons and time scales are shown in Figure 2.

Figure 2. Prediction methods based on forecast horizons and time scales **[10,11]**

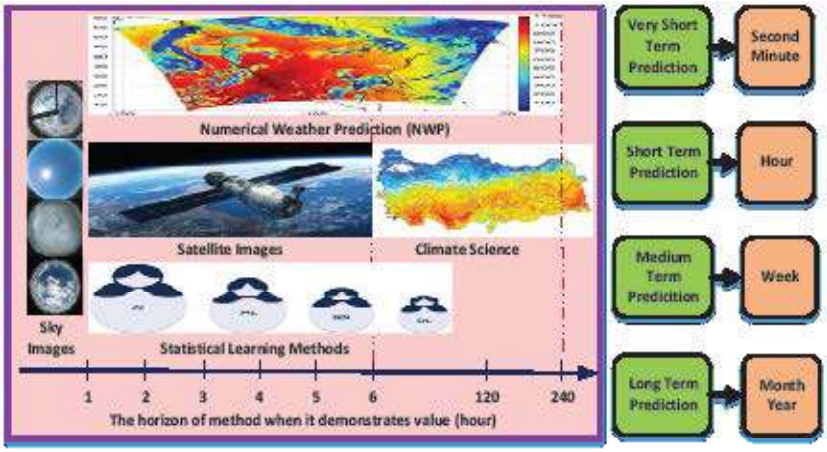

Solar irradiance prediction performance and accuracy are important considerations for all researchers. Therefore, it is necessary to interpret the resulting outcomes. Prediction performance is influenced by various factors such as forecast horizon, weather events, and variability in solar energy. The methods used for solar irradiance prediction can be categorized as shown in Figure 3. Essentially, these methods are commonly classified into physical methods, statistical methods, and ensemble methods, which are the most widely used approaches in this field.

Figure 3. Solar irradiance prediction methods **[12,13]**

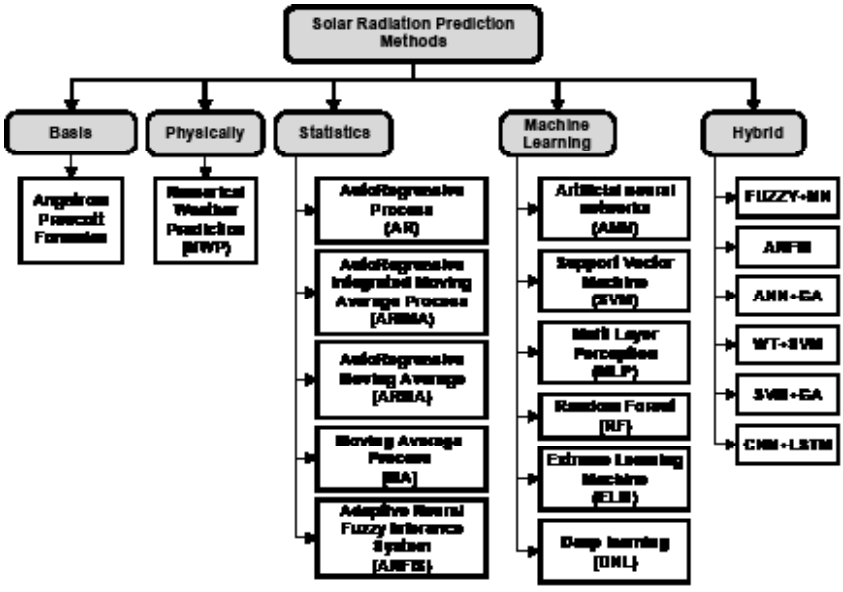

2. Solar Irradiance Prediction Methods

2.1. Physical Methods

Physical methods are primarily based on mathematical equations and aim to determine the physical state of solar irradiance and other meteorological conditions [14]. Since the solutions are obtained using numerical methods, they involve numerical weather prediction (NWP), sky imagery, and satellite data. Satellite imagery data is often used for solar irradiance or cloud index predictions and relies on numerical calculations using meteorological data such as atmospheric conditions and ground-based observations to estimate solar irradiance. Cloud movement can be detected using meteorological satellite imagery. As solar irradiance is significantly influenced by cloud structures, determining cloud movement leads to the prediction of cloud positions, which are subsequently used for solar irradiance prediction [15]. Therefore, by applying image processing technologies, solar irradiance at the ground level can be forecasted.

2.1.1. Numerical Weather Prediction (NWP)

NWP systems have long been the foundation of forecasting applications and are powerful tools for predicting solar irradiance. They forecast the likelihood of local cloud formation and indirectly perform predictions by utilizing a dynamic atmospheric model [16]. These models are designed to pre-determine variables such as temperature, humidity, precipitation probability, and wind, and have recently been optimized for predicting surface solar irradiance. NWP models are also used in weather and aviation forecasting. However, they are now preferred models in renewable energy prediction. Satellite information is frequently utilized in NWP models, and predictions can be made up to two days in advance or six days into the future [17,18].

2.1.2. Prediction Model Using Sky Imagers

Sky imagery can provide detailed information about clouds, which is crucial for accurately estimating surface irradiance. Clouds are the most significant factor affecting surface irradiance, making accurate recognition of cloud pixels a prerequisite for surface irradiance calculation. Sky imagers are automatic, full-color imaging systems that use hemispherical lenses to capture and process real-time images of the entire sky from the ground [19]. By processing the images obtained through sky imagers, cloud motion vectors can be derived. These methods can provide solar irradiance predictions with

very high spatial resolution (at the meter scale) and temporal resolution (at the minute scale) [20]. For time horizons of less than an hour, techniques based on sky imagery offer excellent prediction capabilities [21]. However, the processes involved in deriving the predictions introduce various uncertainties, leading to relatively low reliability [22]. Accurately calculating solar irradiance using sky imagery can effectively enhance the performance and accuracy of sky image-based FV power prediction models [23].

Recent studies have shown an increase in research efforts towards solar irradiance prediction. In one such study, Ref. [6], a cloud detection method was proposed using multi-level local image patches with different dimensions that incorporate local structures and high-resolution information. The proposed system predicts solar irradiance by utilizing information from all-sky images to complement the limited temporal and spatial resolution of satellite imagery and improve prediction accuracy. Sky images can be obtained using a Total Sky Imager (TSI). In Ref. [24], the authors used this method to track and predict clouds in sky images and estimate irradiance. An optimization model was proposed to determine the cloud motion process. Similarly, in Ref. [25], a solar prediction system was suggested that can detect cloud movements from TSI images and subsequently forecast the future cloud positions on solar panels and the resulting fluctuations in solar irradiance for short-term prediction. Ref. [26] developed a framework for predicting Direct Normal Irradiance (DNI) for a 10-minute time horizon, considering atmospheric variables, including relative humidity, wind speed and direction, DNI, and clouds, directly from historical measurements provided through 24-bit color sky images taken every 30 seconds. In Ref. [27], a new model was created for solar irradiance prediction by matching a total of 7000 images captured with a sky camera at a size of 512*512 pixels with measured Global Horizontal Irradiance (GHI) data from a pyranometer. Ref. [28] introduced a deep Convolutional Neural Network (CNN) model called SolarNet, which was developed to predict operational 1-hour ahead GHI using only sky images without numerical measurements or additional feature engineering. Table 1 provides a detailed overview of application studies using sky imagers for solar irradiance prediction.

Table 1. Methods used for solar irradiance prediction with sky imagers

Method	Prediction Time	Prediction Method
ANN	One hour	BP, CNN, LSTM, CNN+LSTM, SVR
ANN	Ten minutes	AR, MLP, SVR, CNN
Deep Learning	Ten minutes	CNN, LSTM
Deep Learning	Up to four hours	KNN, RF
ANN	Ultra short	BPN
Deep Learning	5-20 minutes	CNN

2.1.3. The Prediction Model Using Satellite Images

Ground-based measurements are limited in terms of geographical coverage, and measurements in these areas may require statistical interpolation, which can lead to large errors for increasing geographical distances [29]. Alternatively, satellite images capture a top-down perspective of the atmosphere and local environment, enabling the monitoring of climate change and solar radiation. Therefore, satellite-based methods have demonstrated the ability to produce more accurate solar radiation predictions compared to traditional interpolation methods [30,31]. Meteorological satellites provide continuous image data of environmental information, such as temperature, wind direction and speed, cloud cover, and radiation, covering a wide range of temporal and spatial scales. Solar radiation models convert satellite images captured by geostationary meteorological satellites into surface radiation by employing methods that combine radiative transfer theory and observations. However, satellite predictions are limited by the spatial resolution of the available databases. Therefore, the spatial resolution of existing fixed meteorological satellites may not be sufficient to conduct a detailed study of solar radiation behavior at a specific geographic location [20,32].

Satellite images have been widely used in recent years to study the atmosphere. Clouds, which significantly attenuate solar radiation, have been investigated by many researchers [33,34]. Since cloud cover is a major factor affecting solar radiation, cloud detection and classification are crucial for predicting solar radiation [35]. Satellite-based solar radiation prediction is useful for short-term intra-day time horizons and outperforms numerical

weather predictions with a spatial resolution of 1-5 km and a temporal resolution of up to 4-5 hours [36,37]. The main techniques for satellite prediction are based on advanced cloud motion predictions derived from geospatial satellite images [20]. Satellite images provide information about current and future cloud cover and have the potential to be useful in understanding solar radiation [38]. Sequential satellite images are combined to generate cloud motion vector fields that can be used to predict future cloud positions. It has been shown that this technique is effective in predicting solar radiation intensity from one minute up to six hours ahead.

Satellite images contain all the meteorological parameters at the measurement point simultaneously, depending on the atmospheric conditions. Therefore, the development of solar radiation prediction models using sky imagers and satellite image-based data has become increasingly important. Solar radiation prediction based on satellite data relies on advanced cloud motion predictions derived from geospatial satellite images. Cloud cover-based models can achieve high accuracy in solar radiation prediction since cloud index and sunshine duration are closely related to solar radiation [32]. Table 2 illustrates the satellites and prediction methods used in solar radiation prediction using satellite images.

Table 2. Satellites and prediction methods used in solar radiation prediction with satellite images

Satellite Name	**Country**	**Prediction Models**
Spinning Enhanced Visible and Infrared Imager (Seviri)	EU Countries	Cloud motion vector (CMV) Cloud index methodology (CSD-SI) CLAVR-x Heliosat ANN, CNN, SVM, CNN-LSTM
Geostationary Operational Environmental Satellites (GOES)	USA	
Communication, Ocean, and Meteorological Satellite (COMS)	Korea	
Fengyun	China	
Himawari	Japan	

Cloud Motion Vector (CMV), Cloud Index Methodology (CSD-SI), and CLAVR-x models calculate the speed and direction values determined based on cloud movements observed from satellite images. These values

can be used to determine the solar radiation reaching the Earth's surface. Heliosat, on the other hand, is a method that converts observations made by stationary meteorological satellites into global irradiance predictions at the surface level. Hourly and daily irradiance data obtained from satellites are compared with measurements taken at ground-level meteorological stations using pyranometers. The other prediction methods mentioned in Table 2 are explained below under their respective headings.

2.2. Statistical Methods

These methods are artificial intelligence methods, namely machine learning algorithms. They utilize historical data to build a predictive model. Generally, they match input data to output data using statistical techniques to generate predictions. They rely on establishing relationships between past observations and future values [39]. To employ these prediction methods, historical records of solar radiation in the measurement area are utilized, while real-time measurements determine the current conditions on which the predictions are based. They cover a range of applications from short-term to long-term with shorter time steps [40,41]. The prediction methods within this approach yield the best results for intra-hour time horizons but can have values of two to three hours or more when used in conjunction with other methods. They are limited to solving more complex prediction problems when longer forecast horizons are considered [42]. Statistical learning methods are often used to correct errors in NWP model outputs and to blend outputs from multiple models in a process called model output statistics. Current approaches for solar energy prediction focus on a range of supervised and unsupervised learning techniques such as Support Vector Machines (SVM), decision trees, k-nearest neighbors, or Gaussian processes [43]. Methods such as Artificial Neural Networks (ANN) and SVM, which are statistical methods, provide more reliable solutions for predicting global and horizontal solar radiation and power generation [44]. These methods have been previously used for solar radiation prediction and achieved satisfactory performance. Their usage has been validated through studies conducted for different locations and types of solar radiation, solar energy, and wind speed, proving these machine learning methods to be reliable and versatile [45]-[47]. Statistical methods are widely used for prediction in renewable energy systems, encompassing various approaches ranging from classical regression methods to deep learning methods [48]. Table 3 provides commonly used statistical methods for prediction in renewable energy systems.

Table 3. Some statistical methods used for solar radiation prediction

S/N	Statistical Methods	Abbreviation
1	AutoRegressive Process	ARp
2	Moving Average Process	MAp
3	AutoRegressive Moving Average	ARMA
4	AutoRegressive Integrated Moving Average Process	ARIMA
5	Fuzzy Logic	FUZZY
6	Artificial Neural Networks	ANN
7	Support Vector Machine	SVM
8	Deep Learning	DL

2.2.1. Artificial Neural Networks (ANN)

ANN is an effective and flexible technique widely used in various fields and considered one of the most popular and commonly used networks in the literature [49]. It evaluates the data based on the relationships within the network structure and ensures the inclusion of all factors in the processing. Therefore, the outputs are obtained by considering the weighted evaluation of all factors, rather than using specific formulas. When historical data containing both input and output variables are provided, ANNs can be trained using supervised learning to predict future radiation. The variables used can vary and include on-site radiation measurements, meteorological data, radiation predictions provided by other models, or features obtained from sky or satellite images [50].

ANNs learn patterns from historical data that enable complex mapping between input and output. The training or learning process involves optimizing the model parameters to improve predictions on a training set consisting of input-output pairs [51]. An ANN structure generally consists of input, hidden, and output layers. Additionally, within this structure, there are connection weights, activation functions, and a summation node that combines them. The elements in the input layer, where the inputs are included, can be multiple, and in programs like Matlab, Python, etc., they can only be processed numerically [52]. Relationships are established within the network through the connections using the numerical data taken as input va-

lues. Between the two groups of layers, results are generated as many as the number of neurons in each layer. The obtained results can be transferred to the output layer or new layers can be created between the output and computed values to form new connections. This modeling logic can be shaped according to the needs of the study. In the human brain, this process occurs as the destruction of unnecessary connections in cells. In situations where these connections are needed again, they can be reestablished. The brain prevents the storage of unnecessary information in this way, thus saving energy. The smallest unit known as a perceptron in an ANN is expressed by a function as shown in Equation (1) and modeled as shown in Figure 4 [53].

$$y = W * x + b \quad (1)$$

Figure 4. Mathematical model of a neuron.

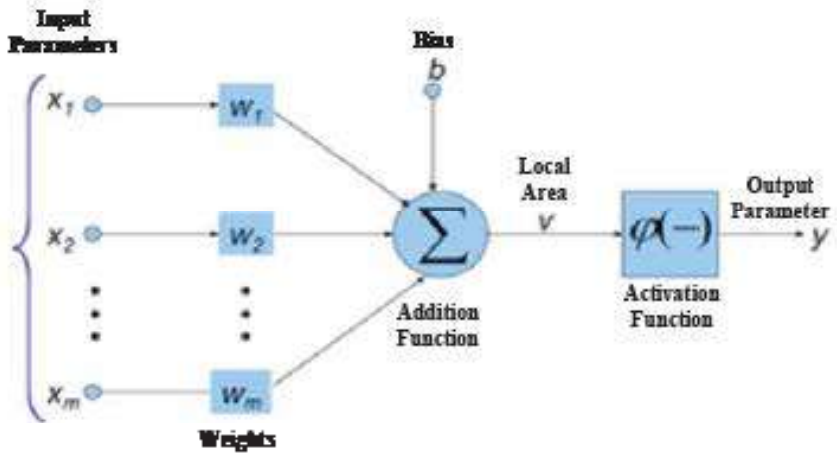

Here, x represents the input values in the input layer, w denotes the weights associated with the processing neuron, b represents the bias value associated with the neuron, and y represents the output in the output layer.

Solar radiation has been analyzed over long periods of time, and it has been predicted using ANNs in different locations [54]. ANNs are more successful than other experimental regression models in predicting solar radiation, and they can be used for both modeling and forecasting solar radiation data [55]. This helps in managing the power generated from a PV system. The performance of ANNs depends on how well they are trained and the quality of the data used. For example, more accurate predictions are generated during clear sky hours compared to cloudy hours. The more accurate the weather forecast parameters used, the more accurate the solar energy predictions can be made.

2.2.2. Support Vector Machines (SVM)

Support Vector Machines (SVM) is a kernel-based machine learning technique that was introduced by Vapnik in 1995, although its foundations date back to the 1960s. It is used for classification tasks and regression problems, and it is a supervised learning algorithm that analyzes training data to generate an inferential function [56,57]. SVM is designed not only to minimize errors but also to maximize the margin of separation between different classes. In terms of prediction, SVM yields similar results to Artificial Neural Networks (ANN), but SVM is considered to be easier to use compared to ANN. It is widely used in energy prediction tasks and exhibits excellent generalization capabilities with high prediction accuracy [58].

2.2.3. Deep Learning (DL)

Deep Learning is a machine learning method that utilizes multi-layered deep artificial neural network architectures. Although the initial works date back to the 1940s, the first scientific research incorporating the concept of DL was conducted by Ivakhnenko and Lapa in 1965. While the concept of DL emerged in the 1960s, its prominence has gained momentum in recent times. This is primarily due to the lack of computational power to train deep architectures and the scarcity of sufficient amounts of data during that time. Nowadays, the increase in computational power and the generation of massive amounts of data through digitization have provided the necessary infrastructure for DL. These advancements have facilitated the widespread utilization of DL in various domains such as computer vision, natural language processing, translation, and time series forecasting [59]. Figure 5 depicts the ANN and DL models commonly used in the literature in the field of renewable energy.

Figure 5. ANN and DL models used in the field of renewable energy

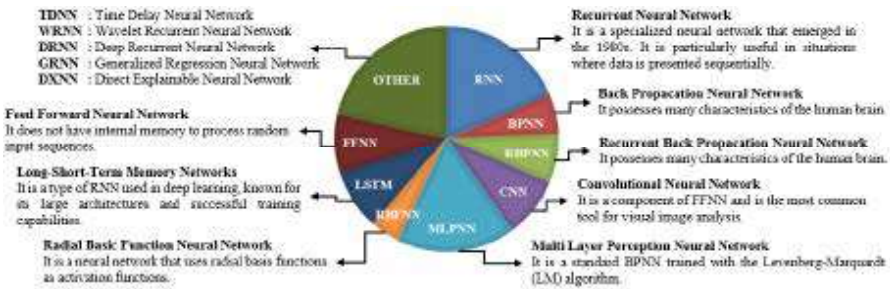

The deep architecture of DL provides support for modeling nonlinear complexities in data, enabling more accurate learning of patterns [60]. As a subfield of machine learning, DL has gained popularity in recent years due to its applicability in various domains [51]. In the field of renewable energy research, DL models, particularly CNN, have been proven to be reliable tools for solar irradiance prediction, wind speed prediction, and PV power output prediction [61,62]. Especially due to its intermittent nature and dependence on various factors such as wind speed, temperature, pressure, and relative humidity, solar data exhibits high-level and nonlinear complex characteristics. These characteristics of solar data are captured by DL models through the extraction of spatial and temporal information. Ongoing research indicates that DL models may outperform ML models in time series, classification, and regression-based prediction problems [63].

When selecting a prediction algorithm, there is a set of criteria that needs to be considered, such as the number of layers, types of layers, activation functions, and so on. These criteria are determined by assessing the performance obtained with certain error metrics when considering different model alternatives. In the field of renewable energy research, DL models, especially CNNs, have been proven to be reliable tools for solar irradiance and PV power output prediction [64]-[66].

2.2.4. Time Series Technique

Time series, which Yule made significant contributions to in 1927, refers to sequentially measured data at specific intervals according to any operation. It represents a chronological sequence of observations related to a specific variable. Time series forecasting can be defined as predicting the future based on past time series data. To determine the prediction model, the fundamental components of a time series, such as trend, cycle, seasonal variations, and irregular fluctuations, need to be identified. Time series data is used to build models using different methods. The process of formulating data appropriately to create a model is called time series analysis. Prediction is carried out through these models, which are primarily based on probability estimates that may not always provide a good generalization for unseen data. Autoregressive Model (AR), Moving Average Model (MA), Seasonal Autoregressive (SAR), Naive Method, Autoregressive Moving Average Model (ARMA), and Autoregressive Integrated Moving Average Model (ARIMA) are approaches based on time series techniques [67,68]. These models show low prediction results when there is weak correlation between meteorological parameters and radiation, and when there are missing or incomp-

lete datasets. Due to the non-stationary behavior of solar radiation data over time, these models cannot accurately capture the non-linearity in the data and therefore exhibit low prediction performance [69,70]. Approaches and features based on time series techniques are illustrated in Figure 6.

Figure 6. Time series techniques and features

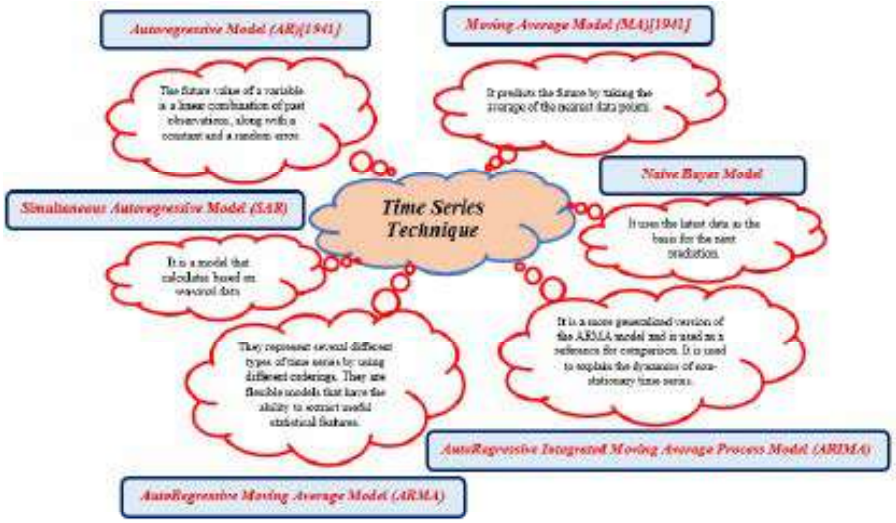

2.3. Community (Hybrid) Methods

Hybrid methods are referred to as techniques that combine different methods to leverage their strong points and overcome the weaknesses of each method. In the literature, several community methods have been proposed by combining physical and mathematical methods with optimization algorithms or machine learning algorithms. This method is essentially a combination of statistical methods or physical methods. In terms of prediction accuracy, it outperforms individual methods. However, it has high computational complexity and therefore takes a long time to reach a result. Additionally, their performance is highly dependent on carefully selected historical inputs [71].

A community consists of a collection of predictions and is an important method to cope with uncertainties, especially in solar energy forecasting. It can identify both linear and nonlinear components in solar time series and overcome any shortcomings of individual models. One of the advantages of the hybrid system is a faster convergence rate [13]. Hybrid models can be modified by adding a deep learning layer, such as Long Short-Term Memory (LSTM), which is a type of recurrent memory, to improve the accuracy

of deep learning algorithms. This approach has been shown to enhance the results of solar radiation prediction and photovoltaic power output prediction [72,73]. In general, the CNN+LSTM hybrid model, which combines the CNN structure with the LSTM algorithm, is widely used in solar radiation prediction studies. In this model, the CNN layers are used to extract features of the changes in the input layer related to solar radiation. The LSTM layer, on the other hand, stores the information transferred from the CNN layer in a control unit and provides a new state unit. Figure 7 illustrates the topological structure of the CNN+LSTM hybrid model used in solar radiation prediction studies.

Figure 7. Illustrates the topological structure of the hybrid CNN+LSTM model **[74]**

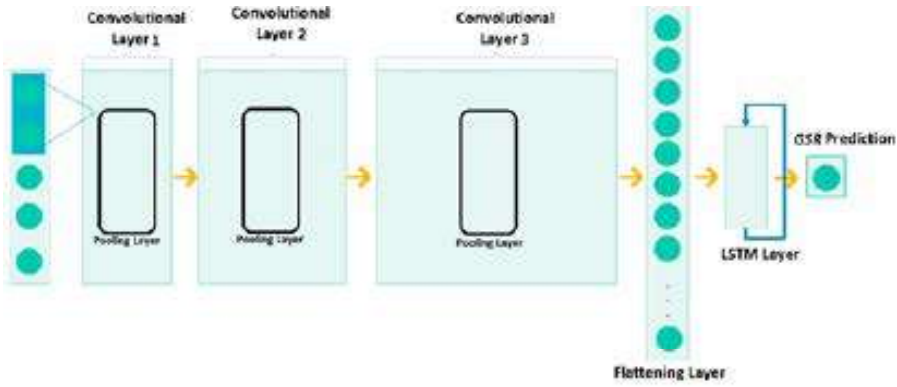

Conclusion

Predicting solar radiation is a challenging task as it varies based on the geographical location and meteorological conditions of the specific area under consideration. Therefore, effective modeling of solar radiation prediction methods has garnered significant interest in controlling and operating solar energy generation. This allows for the identification of the most suitable regions for the installation of PV plants, reducing plant costs, maximizing energy production, and ensuring the secure and stable integration of these plants into the grid.

The accuracy of solar radiation prediction models is often influenced by the prediction horizon and climate conditions. While some models perform well under clear sky conditions, their accuracy significantly decreases in fast-changing and variable weather conditions. Additionally, due to the highly complex nature of the solar radiation phenomenon and its crucial importance for solar power plants, simplistic approaches to modeling

solar radiation prediction may not yield satisfactory results. Therefore, to improve prediction models and achieve higher accuracy, it is essential to incorporate meteorological data obtained through measurements in specific areas where solar radiation needs to be predicted, capturing the entirety of atmospheric dynamics. By considering these data and accounting for variations in meteorological conditions, more accurate predictions can be made. Furthermore, prediction models constructed using such data will help account for more complex structures and rapid changes in weather conditions, leading to higher accuracy. As a result, the management and planning of solar energy resources, such as solar power plants, can be made more efficient.

References

[1] Senapati, Rajendra Narayan; SAHOO, Nirod Chandra; MISHRA, Sukumar. Convolution integral based multivariable grey prediction model for solar energy generation forecasting. In: 2016 IEEE International Conference on Power and Energy (PECon). IEEE, 2016. p. 663-667.

[2] Del Campo-Ávila, J., Takilalte, A., Bifet, A., & Mora-Lopez, L. (2021). Binding data mining and expert knowledge for one-day-ahead prediction of hourly global solar radiation. Expert Systems with Applications, 167, 114147.

[3] Ayala-Gilardón, A., Sidrach-de-Cardona, M., & Mora-López, L. (2018). Influence of time resolution in the estimation of self-consumption and self-sufficiency of photovoltaic facilities. Applied Energy, 229, 990-997.

[4] Cheng, Hsu-Yung; YU, Chih-Chang. Solar irradiance now-casting with ramp-down event prediction via enhanced cloud detection and tracking. In: 2016 IEEE International Conference on Multimedia and Expo (ICME). IEEE, 2016. p. 1-6.

[5] Voyant, C., Motte, F., Notton, G., Fouilloy, A., Nivet, M. L., & Duchaud, J. L. (2018). Prediction intervals for global solar irradiation forecasting using regression trees methods. Renewable energy, 126, 332-340.

[6] Vignola, F., Derocher, Z., Peterson, J., Vuilleumier, L., Félix, C., Gröbner, J., & Kouremeti, N. (2016). Effects of changing spectral radiation distribution on the performance of photodiode pyranometers. Solar energy, 129, 224-235.

[7] El-Amarty, N., Marzouq, M., El Fadili, H., Bennani, S. D., & Ruano, A. (2022). A comprehensive review of solar irradiation estimation and forecasting using artificial neural networks: data, models and trends. Environmental Science and Pollution Research, 1-33.

[8] Sobri, S., Koohi-Kamali, S., & Rahim, N. A. (2018). Solar photovoltaic generation forecasting methods: A review. Energy Conversion and Management, 156, 459-497.

[9] Raza, M. Q., Nadarajah, M., & Ekanayake, C. (2016). On recent advances in PV output power forecast. Solar Energy, 136, 125-144.

[10] Kumari, P., & Toshniwal, D. (2021). Deep learning models for solar irradiance forecasting: A comprehensive review. Journal of Cleaner Production, 318, 128566.

[11] Das, S. (2021). Short term forecasting of solar radiation and power output of 89.6 kWp solar PV power plant. Materials Today: Proceedings, 39, 1959-1969.

[12] Das, Utpal Kumar, et al. "Forecasting of photovoltaic power generation and model optimization: A review." Renewable and Sustainable Energy Reviews 81 (2018): 912-928.

[13] Bhatt, A., Ongsakul, W., & Singh, J. G. (2022). Sliding window approach with first-order differencing for very short-term solar irradiance forecasting using deep learning models. Sustainable Energy Technologies and Assessments, 50, 101864.

[14] Ramadhan, R. A., Heatubun, Y. R., Tan, S. F., & Lee, H. J. (2021). Comparison of physical and machine learning models for estimating solar irradiance and photovoltaic power. Renewable Energy, 178, 1006-1019.

[15] Kamadinata, J. O., Ken, T. L., & Suwa, T. (2019). Sky image-based solar irradiance prediction methodologies using artificial neural networks. Renewable Energy, 134, 837-845.

[16] Perez, R., Lorenz, E., Pelland, S., Beauharnois, M., Van Knowe, G., Hemker Jr, K., ... & Pomares, L. M. (2013). Comparison of numerical weather prediction solar irradiance forecasts in the US, Canada and Europe. Solar Energy, 94, 305-326.

[17] Marquez, R., & Coimbra, C. F. (2013). Proposed metric for evaluation of solar forecasting models. Journal of solar energy engineering, 135(1).

[18] Lara-Fanego, V., Ruiz-Arias, J. A., Pozo-Vázquez, D., Santos-Alamillos, F. J., & Tovar-Pescador, J. (2012). Evaluation of the WRF model solar irradiance forecasts in Andalusia (southern Spain). Solar Energy, 86(8), 2200-2217.

[19] Wang, F., Ge, X., Zhen, Z., Ren, H., Gao, Y., Ma, D., ... & Catalão, J. P. (2018, September). Neural network based irradiance mapping model of solar PV power forecasting using sky image. In 2018 IEEE Industry Applications Society Annual Meeting (IAS) (pp. 1-7). IEEE.

[20] Narvaez, G., Giraldo, L. F., Bressan, M., & Pantoja, A. (2021). Machine learning for site-adaptation and solar radiation forecasting. Renewable Energy, 167, 333-342.

[21] Caldas, M., & Alonso-Suárez, R. (2019). Very short-term solar irradiance forecast using all-sky imaging and real-time irradiance measurements. Renewable energy, 143, 1643-1658.

[22] Dambreville, R., Blanc, P., Chanussot, J., & Boldo, D. (2014). Very short term forecasting of the global horizontal irradiance using a spatio-temporal autoregressive model. Renewable Energy, 72, 291-300.

[23] Tzoumanikas, P., Nikitidou, E., Bais, A. F., & Kazantzidis, A. (2016). The effect of clouds on surface solar irradiance, based on data from an all-sky imaging system. Renewable Energy, 95, 314-322.

[24] Zhen, Z., Wang, F., Mi, Z., Sun, Y., & Sun, H. (2015, September). Cloud tracking and forecasting method based on optimization model for PV power forecasting. In 2015 Australasian Universities Power Engineering Conference (AUPEC) (pp. 1-4). IEEE.

[25] Huang, H., Xu, J., Peng, Z., Yoo, S., Yu, D., Huang, D., & Qin, H. (2013, October). Cloud motion estimation for short term solar irradiation prediction. In 2013 IEEE International Conference on Smart Grid Communications (SmartGridComm) (pp. 696-701). IEEE.

[26] Zhu, T., Zhou, H., Wei, H., Zhao, X., Zhang, K., & Zhang, J. (2019). Inter-hour direct normal irradiance forecast with multiple data types and time-series. Journal of Modern Power Systems and Clean Energy, 7(5), 1319-1327.

[27] Aakroum, M., Ahogho, A., Aaqir, A., & Ahajjam, A. A. (2017, December). Deep learning for inferring the surface solar irradiance from sky imagery. In 2017 International Renewable and Sustainable Energy Conference (IRSEC) (pp. 1-4). IEEE.

[28] Feng, C., & Zhang, J. (2020). SolarNet: A sky image-based deep convolutional neural network for intra-hour solar forecasting. Solar Energy, 204, 71-78.

[29] Jiang, H., Lu, N., Qin, J., Tang, W., & Yao, L. (2019). A deep learning algorithm to estimate hourly global solar radiation from geostationary satellite data. Renewable and Sustainable Energy Reviews, 114, 109327.

[30] Bilionis, I., Constantinescu, E. M., & Anitescu, M. (2014). Data-driven model for solar irradiation based on satellite observations. Solar energy, 110, 22-38.

[31] Linares-Rodriguez, A., Ruiz-Arias, J. A., Pozo-Vazquez, D., & Tovar-Pescador, J. (2013). An artificial neural network ensemble model for estimating global solar radiation from Meteosat satellite images. Energy, 61, 636-645.

[32] Aguiar, L. M., Polo, J., Vindel, J. M., & Oliver, A. (2019). Analysis of satellite derived solar irradiance in islands with site adaptation techniques for improving the uncertainty. Renewable Energy, 135, 98-107.

[33] Janjai, S., Pankaew, P., & Laksanaboonsong, J. (2009). A model for calculating hourly global solar radiation from satellite data in the tropics. Applied energy, 86(9), 1450-1457.

[34] Dazhi, Y., Walsh, W. M., Zibo, D., Jirutitijaroen, P., & Reindl, T. G. (2013). Block matching algorithms: Their applications and limitations in solar irradiance forecasting. Energy Procedia, 33, 335-342.

[35] Dong, Z., Yang, D., Reindl, T., & Walsh, W. M. (2014). Satellite image analysis and a hybrid ESSS/ANN model to forecast solar irradiance in the tropics. Energy Conversion and Management, 79, 66-73.

[36] Aicardi, D., Musé, P., & Alonso-Suárez, R. (2022). A comparison of satellite cloud motion vectors techniques to forecast intra-day hourly solar global horizontal irradiation. Solar Energy, 233, 46-60.

[37] Miller, S. D., Rogers, M. A., Haynes, J. M., Sengupta, M., & Heidinger, A. K. (2018). Short-term solar irradiance forecasting via satellite/model coupling. Solar Energy, 168, 102-117.

[38] Ayet, A., & Tandeo, P. (2018). Nowcasting solar irradiance using an analog method and geostationary satellite images. Solar Energy, 164, 301-315.

[39] Alzahrani, A., Shamsi, P., Ferdowsi, M., & Dagli, C. (2017, November). Solar irradiance forecasting using deep recurrent neural networks. In 2017 IEEE 6th international conference on renewable energy research and applications (ICRERA) (pp. 988-994). IEEE.

[40] Xie, T., Zhang, G., Liu, H., Liu, F., & Du, P. (2018). A hybrid forecasting method for solar output power based on variational mode decomposition, deep belief networks and auto-regressive moving average. Applied Sciences, 8(10), 1901.

[41] Wang, K., Li, K., Zhou, L., Hu, Y., Cheng, Z., Liu, J., & Chen, C. (2019). Multiple convolutional neural networks for multivariate time series prediction. Neurocomputing, 360, 107-119.

[42] Diagne, M., David, M., Lauret, P., Boland, J., & Schmutz, N. (2013). Review of solar irradiance forecasting methods and a proposition for small-scale insular grids. Renewable and Sustainable Energy Reviews, 27, 65-76.

[43] Voyant, C., Notton, G., Kalogirou, S., Nivet, M. L., Paoli, C., Motte, F., & Fouilloy, A. (2017). Machine learning methods for solar radiation forecasting: A review. Renewable Energy, 105, 569-582.

[44] Jurj, D. I., Micu, D. D., & Muresan, A. (2018, October). Overview of electrical energy forecasting methods and models in renewable energy. In 2018 International Conference and Exposition on Electrical And Power Engineering (EPE) (pp. 0087-0090). IEEE.

[45] Jebli, I., Belouadha, F. Z., Kabbaj, M. I., & Tilioua, A. (2021). Prediction of solar energy guided by pearson correlation using machine learning. Energy, 224, 120109.

[46] Chen, J., Zhu, W., & Yu, Q. (2021). Estimating half-hourly solar radiation over the Continental United States using GOES-16 data with iterative random forest. Renewable Energy, 178, 916-929.

[47] Fogno Fotso, H. R., Aloyem Kazé, C. V., & Djuidje Kenmoé, G. (2022). A novel hybrid model based on weather variables relationships improving applied for wind speed forecasting. International Journal of Energy and Environmental Engineering, 13(1), 43-56.

[48] Mosavi, A., Salimi, M., Faizollahzadeh Ardabili, S., Rabczuk, T., Shamshirband, S., & Varkonyi-Koczy, A. R. (2019). State of the art of machine learning models in energy systems, a systematic review. Energies, 12(7), 1301.

[49] Alsina, E. F., Bortolini, M., Gamberi, M., & Regattieri, A. (2016). Artificial neural network optimisation for monthly average daily global solar radiation prediction. Energy conversion and management, 120, 320-329.

[50] Chu, Y., Pedro, H. T., & Coimbra, C. F. (2013). Hybrid intra-hour DNI forecasts with sky image processing enhanced by stochastic learning. Solar Energy, 98, 592-603.

[51] Paletta, Q., Arbod, G., & Lasenby, J. (2021). Benchmarking of deep learning irradiance forecasting models from sky images–An in-depth analysis. Solar Energy, 224, 855-867.

[52] Kılıç, F., Yılmaz, İ. H., & Kaya, Ö. (2021). Adaptive co-optimization of artificial neural networks using evolutionary algorithm for global radiation forecasting. Renewable Energy, 171, 176-190.

[53] Qazi, A., Fayaz, H., Wadi, A., Raj, R. G., Rahim, N. A., & Khan, W. A. (2015). The artificial neural network for solar radiation prediction and designing solar systems: a systematic literature review. Journal of cleaner production, 104, 1-12.

[54] Evseev, E. G., & Kudish, A. I. (2015). Analysis of solar irradiation measurements at Beer Sheva, Israel from 1985 through 2013. Energy Conversion and Management, 97, 307-314.

[55] Elminir, H. K., Azzam, Y. A., & Younes, F. I. (2007). Prediction of hourly and daily diffuse fraction using neural network, as compared to linear regression models. Energy, 32(8), 1513-1523.

[56] Vapnik, V. (1999). The nature of statistical learning theory. Springer science & business media.

[57] Melzi, F. N., Touati, T., Same, A., & Oukhellou, L. (2016, December). Hourly solar irradiance forecasting based on machine learning models. In 2016 15th IEEE International Conference on Machine Learning and Applications (ICMLA) (pp. 441-446). IEEE.

[58] Al-Hajj, R., Assi, A., & Fouad, M. M. (2018, October). Forecasting solar radiation strength using machine learning ensemble. In 2018 7th International Conference on Renewable Energy Research and Applications (ICRERA) (pp. 184-188). IEEE.

[59] Sorkun, M. C., Paoli, C., & Incel, Ö. D. (2017, November). Time series forecasting on solar irradiation using deep learning. In 2017 10th international conference on electrical and electronics engineering (ELECO) (pp. 151-155). IEEE.

[60] Kumari, P., & Toshniwal, D. (2021). Extreme gradient boosting and deep neural network based ensemble learning approach to forecast hourly solar irradiance. Journal of Cleaner Production, 279, 123285.

[61] Feng, C., Zhang, J., Zhang, W., & Hodge, B. M. (2022). Convolutional neural networks for intra-hour solar forecasting based on sky image sequences. Applied Energy, 310, 118438.

[62] Rodríguez, F., Azcárate, I., Vadillo, J., & Galarza, A. (2022). Forecasting intra-hour solar photovoltaic energy by assembling wavelet based time-frequency analysis with deep learning neural networks. International Journal of Electrical Power & Energy Systems, 137, 107777.

[63] Wang, L., Kisi, O., Zounemat-Kermani, M., Salazar, G. A., Zhu, Z., & Gong, W. (2016). Solar radiation prediction using different techniques: model evaluation and comparison. Renewable and Sustainable Energy Reviews, 61, 384-397.

[64] Huertas-Tato, J., Galván, I. M., Aler, R., Rodríguez-Benítez, F. J., & Pozo-Vázquez, D. (2021). Using a Multi-view Convolutional Neural Network to monitor solar irradiance. Neural Computing and Applications, 1-13.

[65] Ghimire, S., Nguyen-Huy, T., Deo, R. C., Casillas-Perez, D., & Salcedo-Sanz, S. (2022). Efficient daily solar radiation prediction with deep learning 4-phase convolutional neural network, dual stage stacked regression and support vector machine CNN-REGST hybrid model. Sustainable Materials and Technologies, 32, e00429.

[66] Haider, S. A., Sajid, M., Sajid, H., Uddin, E., & Ayaz, Y. (2022). Deep learning and statistical methods for short-and long-term solar irradiance forecasting for Islamabad. Renewable Energy, 198, 51-60.

[67] Ji, W., & Chee, K. C. (2011). Prediction of hourly solar radiation using a novel hybrid model of ARMA and TDNN. Solar energy, 85(5), 808-817.

[68] Layanun, V., Suksamosorn, S., & Songsiri, J. (2017, September). Missing-data imputation for solar irradiance forecasting in Thailand. In 2017 56th Annual Conference of the Society of Instrument and Control Engineers of Japan (SICE) (pp. 1234-1239). IEEE.

[69] Huang, X., Shi, J., Gao, B., Tai, Y., Chen, Z., & Zhang, J. (2019). Forecasting hourly solar irradiance using hybrid wavelet transformation and Elman model in smart grid. IEEE Access, 7, 139909-139923.

[70] Sharma, V., Yang, D., Walsh, W., & Reindl, T. (2016). Short term solar irradiance forecasting using a mixed wavelet neural network. Renewable Energy, 90, 481-492.

[71] Ali-Ou-Salah, H., Oukarfi, B., Bahani, K., & Moujabbir, M. (2021). A new hybrid model for hourly solar radiation forecasting using daily classification technique and machine learning algorithms. Mathematical Problems in Engineering, 2021.

[72] Zang, H., Liu, L., Sun, L., Cheng, L., Wei, Z., & Sun, G. (2020). Short-term global horizontal irradiance forecasting based on a hybrid CNN-LSTM model with spatiotemporal correlations. Renewable Energy, 160, 26-41.

[73] Akhter, M. N., Mekhilef, S., Mokhlis, H., Ali, R., Usama, M., Muhammad, M. A., & Khairuddin, A. S. M. (2022). A hybrid deep learning method for an hour ahead power output forecasting of three different photovoltaic systems. Applied Energy, 307, 118185.

[74] Ghimire, S., Deo, R. C., Raj, N., & Mi, J. (2019). Deep solar radiation forecasting with convolutional neural network and long short-term memory network algorithms. Applied Energy, 253, 113541.

Chapter 12

Consideration of Pumice Sand-Concrete Interface Friction in Pile Modeling

İbrahim Yiğit[1]

Abstract

In geotechnical engineering designs, it is necessary to know the friction mechanism on the soil-structure contact surface as well as the mechanical properties of the soil. Geotechnical structures, such as friction piles derive their reaction force entirely from this mechanism. For this reason, there are many studies in the literature examining the soil interface friction with building materials such as wood, steel and concrete, on which geotechnical structures can be built. However, there is a deficiency in the literature on examining the interface friction of pumice sand and building materials. Nevetheless, there are settlements built on pumice soil sections and this behavior should be known in the design of geotechnical structures in these regions. The most characteristic feature of pumice soil grains is that they have a very large internal void ratio and therefore they can be easily crushed under external loads. In terms of these properties, they can be expected to exhibit a different mechanical behavior than other granular soils. The most important factors affecting the interface friction of granular soils and building materials are stress level, soil fabric, soil particle size distribution, shape-texture of soil grains and surface roughness of the building material. The most widely used test in the laboratory for the investigation of soil and building materials interface friction has taken its place in the literature as the direct shear box test. The advantage of this test is that both the internal friction angle of the soil and the interface friction angle of the soil with the building material can be obtained under similar boundary conditions. Thus, the strength parameters of the material are obtained. Definitely, more comprehensive tests such as triaxial tests are needed to obtain elastic material parameters. By using all these material parameters, stress strain analysis of geotechnical structures can be performed with numerical methods such as the finite element method. In this context, the stress strain analysis of a single pile was investigated by the finite element method, strength parameters and the pumice sand concrete interface friction angle, which were obtained in the laboratory of the loosely prepared pumice sand.

1 Dr., Isparta University of Applied Sciences, ibrahimyigit@isparta.edu.tr, Orcid: 0000-0001-5485-9222

https://doi.org/10.58830/ozgur.pub130.c671

1. Introduction

In the design of geotechnical structures, it is necessary to know the interface friction angle between the soil and the construction material. There are many studies on the determination of the interface friction angle between the construction materials and soils. The main studies can be listed as; Potyondy (1961), Uesugi and Kishida (1986), Uesugi et al. (1990), and Jardine et al. (1993).

Potyondy (1961) presented a very comprehensive study examining the interface friction of dry and saturated sand with wood, concrete and steel materials. Tests were carried out in a direct shear box with a square section of 60x60 mm. Author stated that the interface friction angle (δ') varies depending on the water content, the particle size distribution, the density of the soil, the stress level, and the surface roughness of the construction material used. Author concluded that on very rough surfaces, the interface peak friction angle (δ'_{pik}), approaches the peak value of the internal friction angle of the soil (ϕ'_{pik}), but in all cases it is obtained as $\delta' < \phi'$.

Uesugi and Kisihida (1986) studied a range of dry sand and steel interface frictions with simple shear test. Authors stated that the type of sand used and the steel surface roughness were very effective on the interface friction, whereas the normal stress and mean grain size had less effect. Authors also concluded that if the steel surface is smooth enough, sliding occurs at the steel-sand interface, but if the steel surface is sufficiently rough, shear failure occurs in the sand mass.

Uesugi et al. (1990) investigated the sand-concrete interface friction under cyclic loading with a simple shear test. They noted that under monotonic loading, tangential displacement mostly occurs in the sand mass at the yielding condition. They emphasized that the tangential displacement after yielding is mostly due to interface sliding. They stated that a shear band is formed at the sand-concrete interface and the shear stress ratio occurring in this shear band is smaller than that of the dense sand sample. However, they concluded that the friction at the sand-concrete interface is characteristically similar to that at the rough steel-sand interface.

Jardine et al. (1993) performed a series of direct shear interface tests in which they examined the interface friction of steel and various cohesionless soils. In the experiments, the effects of relative density, mean grain size and stress level on shear resistance were investigated. 10° higher internal friction angle was obtained in dense sand samples than loose samples, and that the initial void ratio and relative density of the sand had a significant

effect on the peak internal friction angle. In all cases, the internal friction angle tends to a similar critical state value of 33° after the dilation stops and the shear stresses are balanced. Interface friction tests on the smooth steel and smoother teflon materials, gave similar trends with the internal friction tests on sand. Authors concluded that for each particular interface, the initial relative density affects the amount of expansion and δ'_{pik}, but not the critical state interface friction angle (δ'_{CS}). The δ'_{CS} decreases inversely with D_{50} and has the upper limit of the critical state internal friction angle (ϕ'_{CS}). The sand samples tend to compress after yielding when the relative density is less than 60% and to expand when it is greater than 70%. When the relative stiffness is greater than 70%, mobilized δ'_{pik} angles exceeding δ'_{CS} with a margin increasing with relative density.

In this study, the internal friction angle of the pumice sand and the interface friction angle between the pumice sand and the concrete were investigated by direct shear box test in the laboratory. By using the test data obtained for these materials, the stress strain analysis of the direct shear box test was carried out using the finite element method. Thus, the test calibration was done. Following this, the axial loading of the single pile in the pumice soil was carried out again using the finite element method.

2. Materials and Methods

In this section, stress strain analysis of the friction pile in pumice soil using the finite element method will be discussed. However, firstly, the pumice soil internal friction angle and pumice soil concrete interface friction angle obtained by direct shear box test in the laboratory will be explained. In addition, the same shear box test will be numerically modeled with the finite element method and parameter calibration will be performed.

2.1. Obtaining Pumice Sand Internal Friction Angle and Pumice Sand Concrete Interface Friction Angle by Direct Shear Box Test

As mentioned before, the gradation curve has a significant effect on the internal friction angle and the interface friction angle. The gradation curve of the pumice sand used in this study is given in Figure 1. The pumice sand has a well-graded structure. In addition, the chemical properties of the pumice sand are given in Table 1.

The concrete slab manufactured to be used in this study is given in Figure 2.a. The 28-day compressive strength of concrete was obtained as 25 MPa from the results of the one-dimensional loading test performed on the cube

specimens produced from the same concrete mixture. The concrete slab, which has a very rough surface, placed in the lower cell of the shear box is given in Figure 2.b. The top cell of the shear box is added to this is given in Figure 2.c. The pumice sand placed in the upper cell of the shear box is given in Figure 2.d. Shear box tests were carried out according to ASTM D3080 standard. Internal and interface friction tests were conducted under 100, 200 and 400 kPa normal stresses. The results of internal friction and interface friction tests were given in Figure 3.a and b. Using this test results internal friction and interface friction angle was found 36° and 33° respectively.

Table 1 Chemical properties of pumice sand (Çimen et al. 2020)

Content	Na_2O	MgO	Al_2O_3	SiO_2	P_2O_5	K_2O	CaO	TiO_2	MnO	Fe_2O_3
%	5.3	1.1	17.1	60.9	0.2	5.0	3.0	0.3	0.1	3.2

2.2. Finite Element Modeling of Direct Shear Box Test

Shear box tests were modeled using the finite element method, similar to Hegde and Roy (2018). In the analysis, the hardening soil model for pumice sand and the Mohr Coulomb model for concrete were used. The material parameters used in the analyzes for both materials are given in Table 2 and the analysis results are given in Figure 4. The geometric models, loading state and boundary conditions are given in Figure 4.a-1 for the pumice sand internal friction angle test and in Figure 4.b-1 for the pumice sand concrete interfacial friction angle test. Although the boundary conditions and loading conditions are the same in both experimental models, the materials in the base geometry in the first and second experiments are pumice sand and concrete, respectively. However, the interface element is defined between materials in the interface friction angle test model. Horizontal displacement values for both experimental models are given in Figure 4.2 and 3 as shading and vectors. Finally, the relative shear stresses were obtained as given in Figure 5.3.

Figure 1 Gradation curve of pumice sand

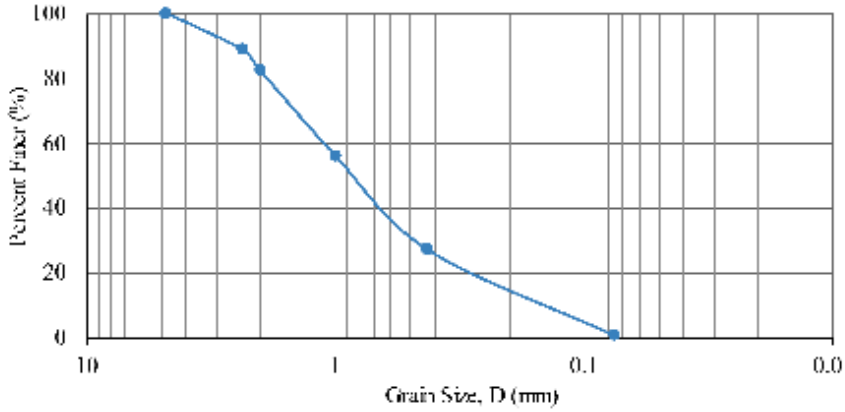

Figure 2 a) Concrete plate, b) Concrete plate in base cell, c) Concrete plate in base cell and top cell, d) Top cell filled with pumice sand

Figure 3 a) Direct shear internal friction angle test results of pumice sand, b) Direct shear interface friction angle test results of pumice sand and concrete

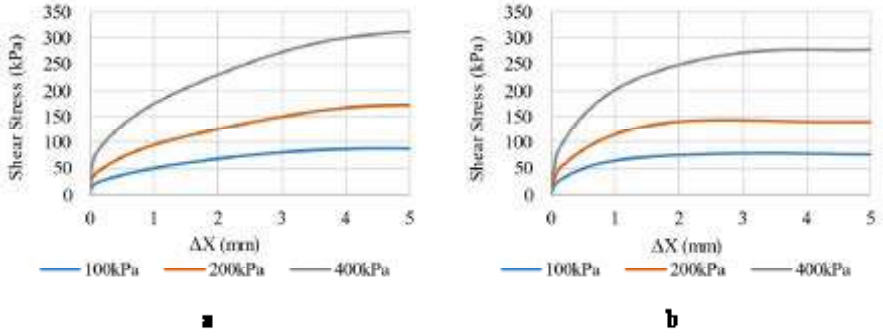

2.3. Modeling of Friction Pile in Pumice Sand

The material parameters of pile and pumice sand are given in Table 2. The geometric model was chosen as axisymmetric and the pile diameter was used as 1m. The pile is modeled as a linear elastic material. Groundwater is not considered. In the model, an interface element is used between the soil and the pile. A reduction in the internal friction angle, which is the soil shear strength parameter, is applied on the interface element and the pile-soil contact surface. From the previously mentioned shear box tests, the pumice soil internal friction angle $\phi = 36°$ and the pumice sand-concrete interface friction angle $\delta = 33°$. For the pumice sand, the interface reduction factor is $R = \tan\delta / \tan\phi \approx 0.9$. However, this value is generally used in the literature for sands in the range of 0.8 - 1.0. Therefore, analyzes were performed for the 0.8 and 0.9 values of the R reduction factor. The vertical displacement values of the pile are given in Figure 5.b and c. Pile loading values and corresponding maximum vertical displacement values are obtained as given in Figure 6. The interpretation of these graphs will be discussed in the results and conclusions section.

Table 2 Model parameters

Parameter	Pumice Sand	Concrete	Pile
Model Type	Hardening	Mohr Coulomb	Linear Elastic
E (kN/m^2)	10^4	$30x10^6$	$30x10^6$
m	0.8	NA	NA
v	0.3	0.2	0.2
ϕ ◦	30	35	NA
c (kN/m^2)	1	365	NA
ψ ◦	1	0	NA
γ (kN/m^3)	16	25	25
R	0.8 – 0.9	1	1

Figure 4 1) Geometry, materials, loads and boundary conditions, 2) Horizontal displacements (shading), 3) Horizontal displacements (vectors), 4) Relative shear stresses

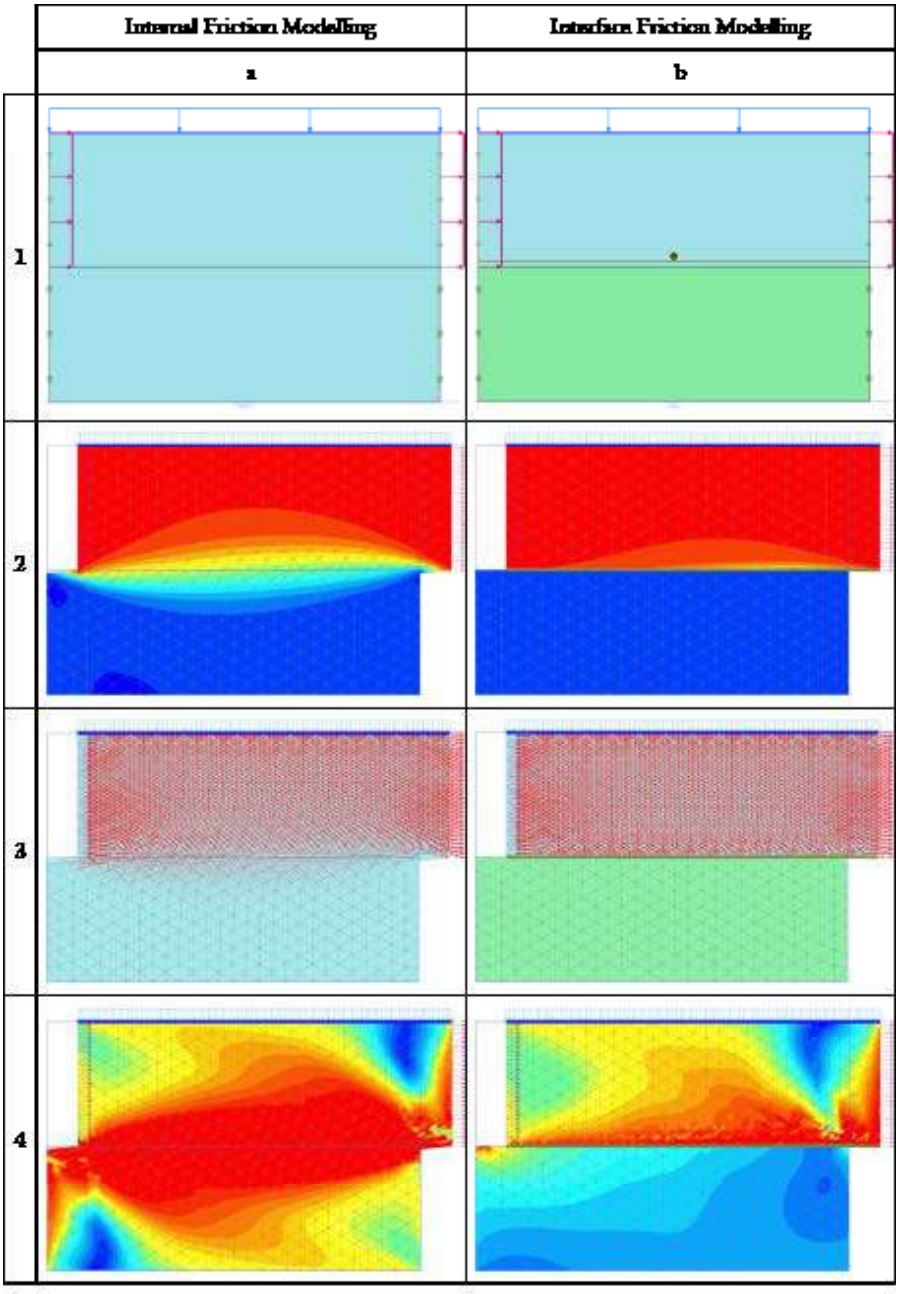

Figure 5 a) Geometry and mesh b) Vertical displacement (R=0.9) c) Vertical displacement (R=0.8)

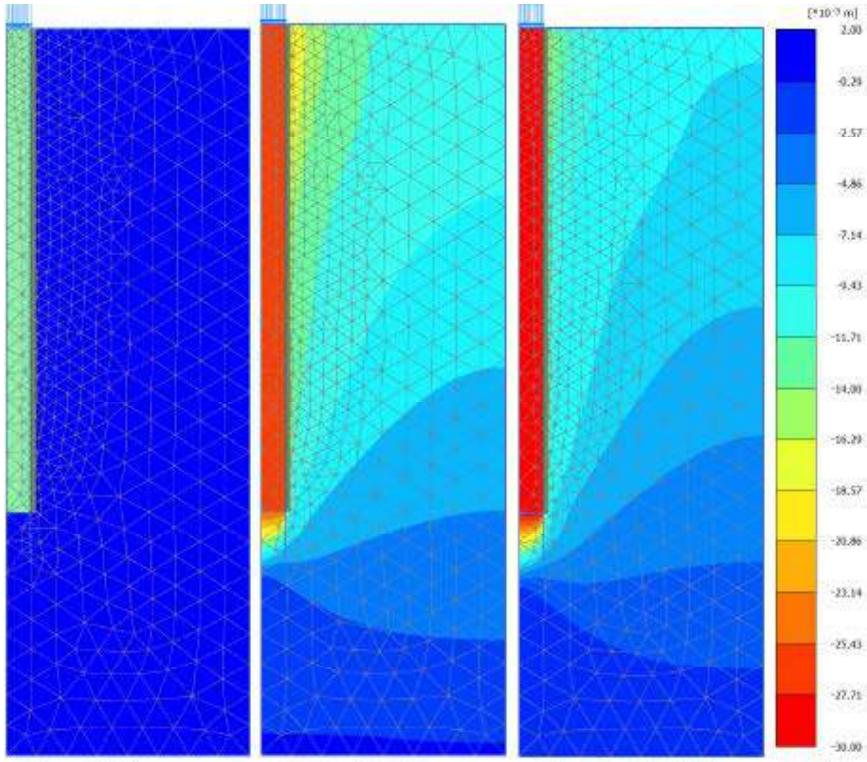

Figure 6 Pile load – vertical displacement curve.

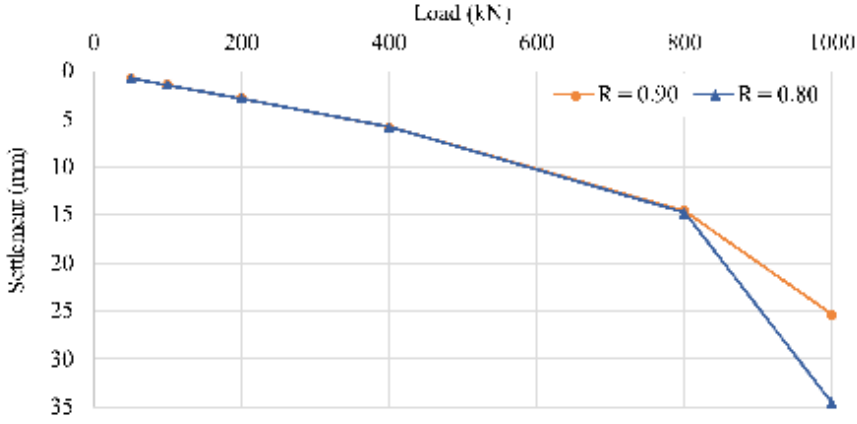

3. Results and Conclusions

Interface friction of concrete with pumice sand was investigated. Both pumice sand internal friction angle and pumice sand concrete interface friction angle were obtained in 60x60 mm square section direct shear box tests. With the obtained test data, a direct shear box finite element model was created and parameter calibration was done. In the internal friction angle test model, horizontal displacements occur in both the upper and lower parts (Figure 4.2.a), while in the interface friction angle test model, horizontal displacements are only seen in the upper part (Figure 4.2.a). A similar situation is also valid for the relative shear stresses given in Figure 4.4.a-b.

Using the parameters obtained from the shear box laboratory tests and finite element modelling, a pile model was created in the pumice sand. The geometry, loading condition, boundary conditions and finite element mesh of the created model are given in Figure 5.a. Analyzes were made by taking the strength reduction coefficients of 0.9 and 0.8 in the interface element used between the soil and the pile in the model. The maximum vertical displacement values of the pile are given in Figure 5.b and c for R = 0.9 and 0.8, respectively. R coefficient controls the shear strength in pile-soil interface. The load values used in the pile model and the corresponding vertical displacement values are shown in Figure 6. While both curves were approximately coincident until the load value of 800 kN, a large deviation was observed after this value. Following conclusion can be drawn from here; At the pile-soil interface, yielding occurred at this loading level, plastic deformations developed faster and settlement values were higher in the case of R = 0.8 than in the case of R = 0.9. This result is consistent with the result presented by Uesugi et al. (1990).

References

ASTM, D. (2011). Standard test method for direct shear test of soils under consolidated drained conditions. D3080/D3080M, 3(9).

Çimen, Ö., Dereli, B., & Keleş, E. (2020). Üç farklı bölgeye ait pomzanın yüksek plastisiteli kile etkisinin karşılaştırılması. Bitlis Eren Üniversitesi Fen Bilimleri Dergisi, 9(1), 427-433.

Hegde, A., & Roy, R. (2018). A comparative numerical study on soil–geosynthetic interactions using large scale direct shear test and pullout test. International Journal of Geosynthetics and Ground Engineering, 4, 1-11.

Jardine, R. J., Lehane, B. M., & Everton, S. J. (1993). Friction coefficients for piles in sands and silts. In Offshore Site Investigation and Foundation Behaviour: Papers presented at a conference organized by the Society for Underwater Technology and held in London, UK, September 22–24, 1992 (pp. 661-677). Springer Netherlands.

Potyondy, J. G. (1961). Skin friction between various soils and construction materials. Geotechnique, 11(4), 339-353.

Uesugi, M., & Kishida, H. (1986). Influential factors of friction between steel and dry sands. Soils and foundations, 26(2), 33-46.

Uesugi, M., Kishida, H., & Uchikawa, Y. (1990). Friction between dry sand and concrete under monotonic and repeated loading. Soils and Foundations, 30(1), 115-128.

Bölüm 13

Zararlı Bitkilerin İlaçlanması için Tarımsal bir İnsansız Kara Aracı

Sinan Akdan[1]

İsmail Öner[2]

Nevzat Akdeniz[3]

Ahyet Bingöl[4]

Salih Ensar Şimşek[5]

Emrehan Yavşan[6]

Özet

Tarımda yapay zekâ destekli insansız kara araçlarının tercih edilmesiyle aşırı kimyasal kullanımı ve çevre kirliliği ciddi oranda azaltılabilir. Tüm arazinin ilaçlanması yerine tarımsal insansız kara araçlarıyla lokal müdahalelerde bulunulabilir. İstenmeyen zararlı bitkiler lokal ilaçlama yapılarak ortadan kaldırılabilir. Aynı zamanda karadan yapılan ilaçlamalarda havadan yapılan ilaçlamalara kıyasla ilaç havada dağılmayacağından daha etkili ve sağlıklı sonuçlar alınabilir. Böylece zararlı kimyasalların tarım arazilerine etkileri en aza indirgenir, daha verimli ilaçlama yapılır ve kullanılan ilaç miktarı düşeceğinden maliyet azalır. Bu çalışmada tarım arazilerindeki zararlı bitkilerin lokal olarak ilaçlanabilmesi için özgün tasarıma sahip otonom bir tarımsal kara aracı geliştirilmiştir. Araç doğadan esinlenerek tasarlanmış ve hafiflik için üretiminde alüminyum profiller tercih edilmiştir. Aracın tarım arazilerindeki hareketini kolaylaştırmak için yenilikçi bir süspansiyon sistemi geliştirilmiştir. Bu sistemle bozuk zemin etkilerini en aza indirmek hedeflenmiştir. Araca

1 Necmettin Erbakan Üniversitesi, Mühendislik Fakültesi, Mekatronik Mühendisliği Bölümü, Konya, Türkiye, sinanakdan@ogr.erbakan.edu.tr Orcid: 0000-0001-7797-5824.

2 Necmettin Erbakan Üniversitesi, Mühendislik Fakültesi, Mekatronik Mühendisliği Bölümü, Konya, Türkiye, ismail.oner@ogr.erbakan.edu.tr Orcid: 0000-0002-0456-8424.

3 Necmettin Erbakan Üniversitesi, Mühendislik Fakültesi, Mekatronik Mühendisliği Bölümü, Konya, Türkiye. nevzatakdeniz@ogr.erbakan.edu.tr Orcid: 0000-0002-3773-7044.

4 İstanbul Teknik Üniversitesi, Bilgisayar ve Bilişim Fakültesi, Bilgisayar Mühendisliği Bölümü, İstanbul, Türkiye. bingol19@itu.edu.tr Orcid: 0000-0001-5623-3856.

5 Necmettin Erbakan Üniversitesi, Mühendislik Fakültesi, Mekatronik Mühendisliği Bölümü, Konya, Türkiye. salihensarsimsek@ogr.erbakan.edu.tr Orcid: 0000-0002-5465-1891.

6 **Sorumlu Yazar/Corresponding Author:** Emrehan Yavşan, Tekirdağ Namık Kemal Üniversitesi, Teknik Bilimler MYO, Elektronik ve Otomasyon Böl. Mekatronik Prog. Tekirdağ, Türkiye, eyavsan@nku.edu.tr Orcid: 0000-0001-9521-4500.

https://doi.org/10.58830/ozgur.pub130.c543

yerleştirilen derinlik kamerasından alınan verilerle robot işletim sistemi üzerinden eş zamanlı yol haritası oluşturulmaktadır. Tarım arazisindeki zararlı bitkilerin tespit edilebilmesi için evrişimsel sinir ağları temelli bir tespit algoritması kullanılmıştır. Zararlı bitkinin tespit edildiği anda ilaçlanması önemlidir. Aksi halde yanlış ya da verimsiz ilaçlama yapılmış olur. Kullanılan tespit algoritmasıyla bu darboğazın üstesinden gelinmiş ve gerçek zamanda en az gecikmeyle otonom ilaçlama sağlanmıştır. Geliştirilen kara aracıyla yapılan saha testlerinde 40 cm yüksekten %90 doğrulukla tarım arazisindeki zararlı bitki tespit edilip anlık olarak başarılı bir şekilde ilaçlanmıştır. İlaçlama süresince aracın konumu, pil tüketimi ve ilaç durumu gibi kritik parametreler harici bir yer istasyonu üzerinden geliştirilen kontrol ve takip arayüzüyle eş zamanlı izlenmektedir. Aracın güç besleme bileşenleri aracın düz bir arazide 1.5 – 2 saat süresince görev yapılabileceği şekilde seçilmiştir. Bunun yanında araca yerleştirilen güneş pilleriyle aracın görev süresinin uzatılması amaçlanmıştır.

1. GİRİŞ

Çeşitli sektörlerdeki insansız araç kullanımındaki artış tarımda da kendini göstermektedir. Özellikle şehirlere göçlerin artması ile çiftçilikle uğraşan insan nüfusu azalmıştır. Bunun yanı sıra işçi maliyetlerindeki artışla tarımda otonom ve insansız araçlara geçilmeye başlanmıştır. Tarımda iş gücü gerektiren ciddi uygulamalardan birisi zararlı bitkilerin ilaçlanmasıdır. Ekinlerin ilaçlanmaması halinde tarım arazilerine ekilen bu ürünlerin gelişim süreci olumsuz etkilenmektedir (Çınar, Halipoğlu, & İnal, 2014; Kara & Ata, 2021; Yazlik et al., 2019). Bunun yaşanmaması ve daha verimli ilaçlamının yapılamabilmesi için insansız kara araçlarıyla ilaçlama yapılabilir. Bu sayede artan ilaç maliyetleri de düşürülür ve fiyat-performans açısından daha dengeli bir süreç yürütülmüş olur (Karadöl, 2017).

Coğrafi koşulların uygun olmadığı bölgelerde insanların tarım arazilerine erişimi sınırlıdır. Hasat ve ekimin zor olduğu bu yerlerde ilaçlama yapmak haliyle zor olacaktır. Bu zorluğun üstesinden gelmek için insansız hava araçları (İHA) sıklıkla kullanılmaktadır (Şin & Kadioğlu, 2019; Türkseven et al., 2016). İHA kullanımıyla birlikte daha rahat ilaçlama ve bitkiye ulaşım sağlanmıştır. Fakat hava araçlarındaki taşıma kapasitesi sınırlıdır ve bu araçların aktif kullanım süreleri azdır (Ay & Ince, 2015). Bunlar artırılabilir fakat bu sefer de maliyet ciddi oranda artacaktır. Kullanım süresi ve taşıma kapasitesinin yanı sıra tarımda kullanılan genel bir İHA'nın bir kara aracına göre fiziksel dayanımı düşüktür (Ay & Ince, 2015). Ayrıca havanın rüzgârlı olduğu günlerde hava aracının kullanımı pek mümkün olmayacaktır ve havadan sıkılan zirai ilaç bitkiye ulaşmadan dağılabilir. Böylece verimsiz bir ilaçlama yapılmış olur. Burada sayılan olmusuzlukların üzerinden gelmek ya da bu

olumsuzlukları en aza indirmek için insansız kara araçları tercih edilebilir. Çünkü insansız kara araçları bir hava aracına göre hava koşullarından daha az etkilenerek daha kararlı çalışabilir.

Karadan ilaçlama üzerine yapılan çalışmalardan biri Kadir ve Cevat tarafından gerçekleştirilmiştir (Sabancı & Aydın, 2014). Onlar yaptıkları çalışmada sabit bir platform kurmuşlardır. Belirledikleri pancar bitkisi arasındaki yabancı bitkilerin tespitini görüntü işlemeyle gerçekleştirmişlerdir. Görüntü işleme sayesinde platformun altına gelen bitki tanınmış ve ilaçlama yapılmıştır. Fakat platformun ray benzeri bir sistem üzerinde hareket etmesinden dolayı sabit olması sunulan sistemin tarım arazilerindeki kullanımını zorlaştıracaktır. Görüntü işleme tekniğiyle bitkilerin tanınması kullanışlı ve etkili bir yöntem olmasına rağmen sunulan platformun çoğu tarım arazisine uygulanması zordur. Raza ve arkadaşları (Saeed, Tomasi, Carabin, Vidoni, & von Ellenrieder, 2022) insansız kara araçlarının tarıma entegre edilmesi üzerine çalışmışlardır. Onlar bir benzetim (simülasyon) ortamında çalışmalarını gerçekleştirmişlerdir. Kapalı alanda sanal bir ortam kurmuşlardır. Kapalı alan olmasından dolayı çıkarılan haritada lidar kullanılmıştır (Zou, Sun, Chen, Nie, & Li, 2022). Lidar ile sınırları belirli bir alan taranmış ve harita çıkarılmıştır. Çıkarılan bu haritayı gerçek sistem üzerinde kullanmışlardır. Sunulan sistem geniş tarım arazilerinde uygulanacak şekilde geliştirilebilir.

Yuanyuan ve arkadaşları (Song, Sun, Li, & Zhang, 2015) zararlı bitkilerin tespiti ve ilaçlanması üzerine çalışmıştır. Yaptıkları çalışmada ilaçlama işlemlerini iki kısımda incelemişlerdir. Bu kısımları bitki tespiti ve ilaçlama olarak ele almışlardır. Bitki tespiti; makine görüşü (machine vision) ile spektral algılama (spectral detection) üzerine yapılmıştır. Bitkileri etkisiz hale getirme işlemi için ise mikro ilaçlama (micro-spray), kesme (cutting), ısıl işlem (thermal) ve elektrikle öldürme (electrocution) tekniklerini önermişlerdir (Song et al., 2015). Kendileri mikro ilaçlama üzerine yoğunlaşmışlardır. Kullandıkları bu ilaçlama sistemi ile üç tür ilaçlama üzerinde durmuşlardır; 1) alansal ilaçlama, 2) sütun ilaçlama ve 3) bitkinin doğrudan konumu üzerinden ilaçlama (Slaughter, Giles, & Downey, 2008). Fakat alansal veya sütun ilaçlama diğer bitkilere ve toprağa zarar vereceği için çok tercih edilmemiştir. Bizler de bu uygulamaları göz önünde bulundurarak nozzle sistemi kullandık. Böylece daha rahat ve elverişli bir ilaçlama sağlamış olduk. Ayrıca geliştirilen ilaçlama sistemiyle ilaç tasarrufu sağlamanın yanında ilaçlanmaması gereken diğer bitkileri de korumuş olduk.

Bu çalışmada insansız kara araçlarının tarımda daha efektif kullanılmasına yoğunlaşılarak özgün bir insansız kara aracı geliştirilmiştir. Araç geliştirilirken çeşitli tarım arazileri göz önünde bulundurulmuştur. Aracın tarım arazi-

lerine uygunluğuyla kullanım alanı genişletilmiştir. Bu sayede çeşitli bitkilerin daha verimli ilaçlanması ve tespiti için zemin hazırlanmıştır. Geliştirilen ve araç üzerinde gerçek zamanda çalışan tespit sistemiyle bitkiler başarıyla tespit edilmiştir. Tespit edilen bitkiler otonom bir şekilde ilaçlanmıştır. İlaçlama işlemi görüntü işleme ile eş zamanlı çalışmaktadır. Tespit işleminin rahatlıkla yapılabilmesi için aracın üzerine bir kamera yerleştirilmiştir. Ayrıca araç üzerine paneller konulmuş ve bu panellerle güneş enerjisinden faydalanılmıştır. Böylece çalışma süresinin uzatılması hedeflenmiştir. Aracın boyutunun orta düzeyde olması küçük tarım arazileri ve bahçeler için uygunluğu artırmaktadır. Bu sayede aracın kullanım alanının genişletilmesine katkı sağlanmıştır.

2. MATERYAL VE METOT

2.1. Tarımsal İnsansız Kara Aracının Mimarisi

Araç ekipmanları aracın engebeli ve kötü hava koşullarında verimli çalışmasını sağlayacak şekilde seçilmiştir. Bu nedenle araç 4x4 hareket sistemine sahiptir. Aracın tekerleklerine entegre edilen her elektrik motoru yaklaşık 200 W güç üretmektedir. Bu motorlar bir kontrol kartı üzerinden elektronik hız kontrolcüleriyle (ESC) sürülmektedir. Kontrolcü olarak 168 MHz hıza ve 2 MB hafızaya sahip Pixhawk kontrol kartı tercih edilmiştir (ArduPilot, 2021). Kart içinde GPS, IMU, jiroskop, barometre ve pusula sensörleri barındırmaktadır. Aynı zamanda bu özellikleri anlık olarak takip edebilecek arayüze sahiptir. Aracın otonom hareketi için Nvidia Jetson Nano kartı (NVDIA, 2022) ile motorlar arasında köprü görevi görmektedir. Otonom hareket haricinde uzaktan kumanda kontrolü de Pixhawk kartıyla sağlanmaktadır.

Hareket ve görüntü işleme algoritmaları 2.1 GHz hıza ve 4 GB hafızaya sahip 40 giriş pinli Nvidia Jetson Nano kartında gerçekleşmektedir. Bu kart ile z ekseninde 28 mm derinlik oluşturabilen ve 30 FPS yayın yapabilen Intel RealSense D435i kamerası kullanılmaktadır (Intel, 2022). Ayrıca görüntü algılama için kullanılan 78 dereceye kadar diyagonal yayın yapabilen 1080p/30 FPS görüntü özelliklerine sahip Logitech G920 Pro kamerası kullanılmaktadır (Logitech, 2019). Aracın bu bileşenlerinin yanında elektronik bileşenlerinin tamamı Şekil 1'deki şemada verilmiştir.

Şekil 1. İnsansız kara aracının elektronik bileşenleri

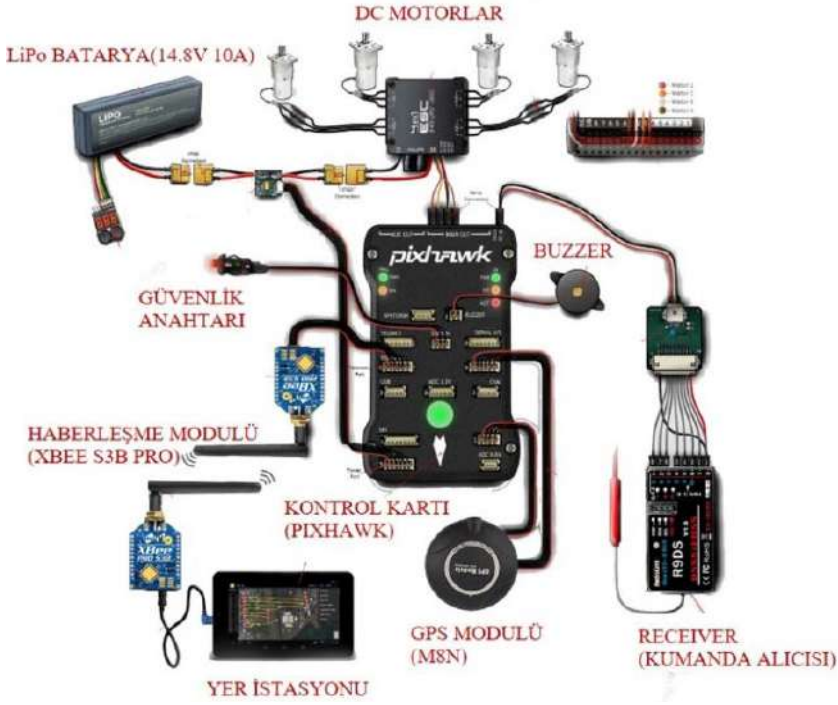

Araç üzerinde ana ve yardımcı olmak üzere iki adet kart bulunmaktadır. Bu kartlardan ilki Nvidia Jetson Nano kartıdır. Bu kart ana kart olarak görev yapmaktadır ve bitki tespiti için geliştirilen algoritma bu ana kart üzerinde koşmaktadır. Görüntü işleme için kullanılan kamera Logitech G920 Pro'dur. G920 Pro'nun tercih edilme amacı; 78 derece geniş açı ve görüntü netliği sunmasıdır. Otonom sürüş için ise Intel RealSense D435i derinlik kamerası kullanılmıştır. Kullanılan D435i kamerayla 28 mm derinlik algılaması ile sınırları belirli olmayan yerlerde harita çıkarımı yapılabilmektedir.

Otonom bir şekilde ilaçlama yapmak için doğrudan ana kart üzerinden su pompasına çıkış verilmiştir. Diğer kart olan Pixhawk ile ana karttan gelen komutlar kontrol edilmiştir. Kontrol edilen kısım motorlardır. Pixhawk kartı ile motor kontrolü ve aracın manuel olarak uzaktan kontrolü sağlanmıştır. Uzaktan kontrol için Xbee S3b Pro haberleşme modülleri kulanılmıştır.

Aracın sunulan elektronik bileşenlerinin güç beslemeleri Li-Po bataryalarla sağlanmıştır. Bu bataryalar ayrıca 420x360 mm boyutlarındaki 20 Watt güç üretebilen güneş panelleriyle desteklenmektedir. Bu sayede yenilenebilir enerjiyle aracın güç tüketiminin belirli bir kısmı karşılanabilmektedir. İlaçlama için araç üzerinde yaklaşık 3 lt'lik bir ilaçlama deposu bulunmaktadır. Bu

depodan bir su pompasıyla saniyede 0.07 lt'lik ilaç aracın ön kısmındaki 4 yollu ilaçlama sistemine iletilmektedir.

3. TARIMSAL İNSANSIZ KARA ARACININ MODELLENMESİ VE ÜRETİMİ

Aracın mekanizmasının dayanıklı ve daha hafif olması için şasi alüminyum sigma profilden imal edilmiştir. Seçilen malzemelerin dayanımları Şekil 2'deki stres analizleri yapılarak doğrulanmıştır. Bu analizler dayanım testleri olarak adlandırılmaktadır. Dayanım testleriyle aracın dayanıklılığı üretimden önce test edilmiştir. Böylece olası harici harcamaların önüne geçilerek maliyet düşürülmüştür.

Şekil 2. Dayanım testleri adı altında aracın çeşitli mekanik bileşenleri (a) şasi, (b) jant, (c) süspansiyon ayar parçası ve (d) süspansiyon gövde için gerçekleştirilen stres analizleri

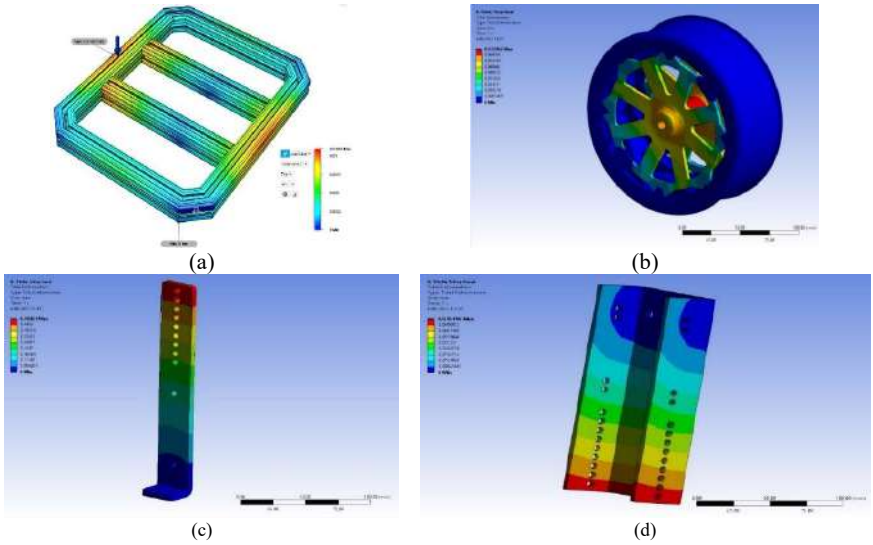

Aracın süspansiyon sisteminde üretim ve montajda kolaylık sağlanmasının yanı sıra istenen yumuşaklığı vermesi için çekme yay sisteminden oluşan bir yapı kullanılmıştır. Bu sayede araçtaki bileşenlerin maruz kalacağı titreşim düşük seviyelerde tutularak olası yorulmaların önüne geçilmeye çalışılmıştır.

Aracın jantlarının hafif ve dayanıklı olması için ABS türü filament kullanılarak 3 boyutlu bir yazıcıdan basım yapılmıştır. Jantın iç yapısı içerisine kaçabilmesi muhtemel kumları hareket ettikçe dışarı atacak şekilde tasarlan-

mıştır. Lastik olarak kauçuk lastikler tercih edilmiş ve lastiklerin zemine tutunmasını kolaylaştırmak için balıksırtı desenli plastik zincirler kullanılmıştır.

Aracın toprak zeminde rahat hareket edebilmesi ve toprağa saplanmaması için Tablo 1'deki parametreler üzerinden motor seçimleri yapılmıştır. Böylelikle araç ufak toprak veya taş parçalarıyla karşılaştığında sıkıntısız olarak ilgili engeli aşabilecektir. Bu yüzden motor seçimi esnasında aracın kütlesi, teker çapı, ağırlığı, gidilecek yolun eğim bilgisi ve maksimum ivme belirlenmelidir.

Tablo 1. Motor seçiminde kullanılan parametreler ve bu parametrelerin değerleri

Parametreler	**Parametrelerin Değerleri**
Aracın Kütlesi	30 kg
Teker Çapı (R)	0.22 m
Aracın Yere Uyguladığı Kuvvet	30 x 9.81 = 294.3 N
Güvenlik Katsayısı	3
Motor Verimi	%60
Eğim Açısı	%10 $eğim$ = arctan(%$eğim$) = arctan(10/100) = 5.7° →α= 5.7°
Maksimum İvme	0.2 m-s^2
Yuvarlanma Direnç Katsayısı (f)	0.035
Kütle Katsayısı (c)	0.9

Aracın kara yüzeyinde hareket ederken karşılaşacağı engellerden biri de yuvarlanma direnci (R_y)'dir. R_y, Eş. 1 üzerinden hesaplanmıştır. Aracın kalkışı ve düzgün bir şekilde seyri için R_y'nin hesaplanması kritiktir. Araca gösterilen dış dirençlerden bir tanesi ise meyil direnci ($R_{m)}$'dir. R_m, Eş. 2 üzerinden hesaplanmıştır. Aracın motor seçimi için motor gücünün ne kadarlık bir eğime karşı direnç göstereceği önemlidir. Gösterilen dış etkenlerden bir diğeri ivmelenme direnci (R_i)'dir. R_i, Eş. 3 üzerinden hesaplanmıştır. Aracın ivmelenmesi ise aracın belirli ve ideal bir ivme ile gitmesi için önemlidir. Sonuç olarak gösterilen dirençlerin toplamı (R_{toplam}) ile gerekli motor kuvveti hesaplanmıştır. Hesaplanan toplam motor kuvveti üzerinden tekerleklerin üzerine düşen kuvvet Eş. 5 ile hesaplanmıştır. Hesaplanan tek motor kuvveti üzerinden Eş. 6 kullanılarak motor başına düşen tork bulunmuştur. Bulunan tork ile Eş. 7 üzerinden kullanılabilir tork değeri hesaplanmıştır. Son olarak

Eş. 8 ile %60 verimlilikte gerekli olan güç ve toplam tork değerleri hesaplanmıştır.

$$R_y = G.f \qquad \text{Eş. 1}$$

$$(294.3)\ \text{x}\ (0.035) = 10.3\ \text{N}$$

$$R_m = G.\sin(\alpha) \qquad \text{Eş. 2}$$

$$(294.3)\sin(5.7°) = 29.22\ \text{N}$$

$$R_i = c.G.a.g \qquad \text{Eş. 3}$$

$$(0.9)\text{x}(294.3)\text{x}(0.2)/(9.81) = 11.2\ \text{N}$$

$$R_{toplam} = R_y + R_m + R_i \qquad \text{Eş. 4}$$

$$(10.3)+(29.22)+(11.2) = 50.72\ \text{N}$$

$$R_{1,2,3,4} = \frac{R_{toplam}}{4} \qquad \text{Eş. 5}$$

$$\frac{(50.72)}{4} = 12.68\ \text{N}$$

$$T = (R_{1,2,3,4}) x\ (\frac{R}{2}) \qquad \text{Eş. 6}$$

$$12.68\ x\ 0.11 = 1.4\ N.m$$

$$\textit{Kullanılabilir Tork Değeri} = T\ x\ \textit{Güvenlik Katsayısı} \qquad \text{Eş. 7}$$

$$1.4\ x\ 3 = 4.2\ Nm$$

$$P = \frac{T\ x\ n}{9554} \qquad \text{Eş. 8}$$

$$\frac{4.2\ x\ 36}{9554} = 15.82\ W,\ P_{\%60\ verim} = 26.36\ W,\ T = \frac{0.2\ x\ 9554}{36} = 53.07\ Nm$$

4. GÖRÜNTÜ İŞLEME VE YABANCI BİTKİ TESPİTİ

Çalışmanın görüntü işleme kısmında kameradan veri almak, bu görüntüleri dönüştürüp çeşitli işlemlere sokmak için OpenCV kütüphanesi tercih edilmiştir. Yabancı bitkilerin tespiti için gerçek zamanlı nesne tespitinde kullanılan ve diğer algoritmalara göre daha hızlı ve daha yüksek ortalama kesinlik değerine sahip olan Yolo algoritması tercih edilmiştir. Ayrıca bitkinin tespit edildiği anda ilaçlanması önemlidir. Bu nedenle kullanılan tespit algoritmasının yüksek FPS vermesi gerekmektedir. Yolo algoritması Şekil 3'teki grafiğe göre diğer algoritmalara nazaran daha yüksek FPS sağlamaktadır. Bunun yanında sunulan çalışma için YOLOv3 ve YOLOv4-tiny modellerini karşılaştırmak adına 200 adet resimden oluşan küçük boyutlu bir veri seti hazırlanmıştır. Hazırlanan veri seti eğitim ve test verilerine ayrılarak önerilen Yolo modelleri üzerinden eğitimler yapılmıştır. Modeller karşılaştırıldığında daha hızlı olması sebebiyle bu çalışmada YOLOv4-tiny modelinin kullanılmasına karar verilmiştir.

Şekil 3. Nesne tespit algoritmalarının FPS parametresi üzerinden karşılaştırılması (Aleksey Bochkovskiy, 2020)

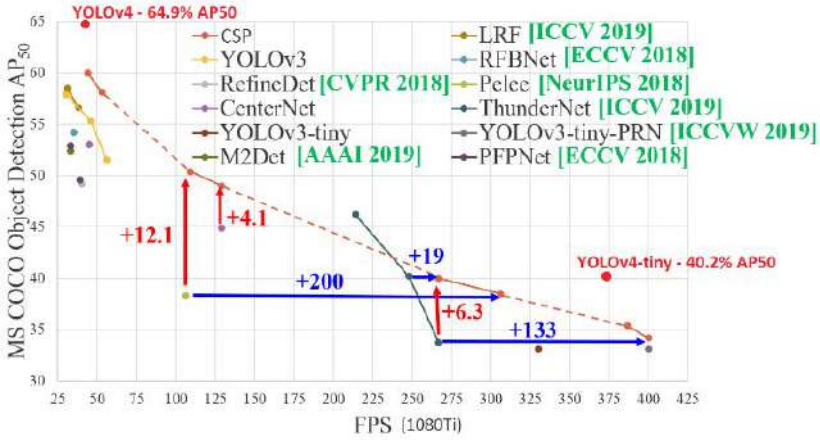

Yabancı bitkilerin tespiti için veri seti oluşturulurken bitkinin farklı açılardan ve birden fazla zeminde videoları çekilmiştir. Çekilen videolardan gerekli resimler boyutlandırılıp ayrıştırılmıştır. Ardından OpenCV kütüphanesi kullanılarak resme döndürme, tuz-biber gürültüsü ekleme, bulanıklaştırma, parlaklık ayarı değişimi, kaydırma işlemleri uygulanarak veri seti genişletilmiştir. Çalışma süresince 2 farklı veri seti hazırlanmıştır. Toplanan 3720 adet bitki görseli labelImg programı kullanılarak Yolo modeline uygun olarak etiketlenmiştir. Eğitim ve test için kullanılacak veriler; %10'u test, %90'ı eğitim olacak şekilde ayrıştırılmış ve eğitim için hazırlanmıştır. Bu işlem tamamlan-

dıktan sonra C ve CUDA ile yazılmış açık kaynaklı bir sinir ağı çerçevesi olan Darknet kurulmuş ve kendi veri setimizin eğitimi için YoloV4-tiny'e göre düzenlenmiştir. Düzenlenen Darknet Google Drive kullanılarak Google Colab programlama ortamına dahil edilmiştir. Google Colab üzerinden eğitim işlemi gerçekleştirilmiştir. Eğitim sırasında doğruluk ve kayıp değerlerinin değişimini gösteren grafik Şekil 4'te verilmiştir.

Şekil 4. Doğruluk ve kayıp grafiği

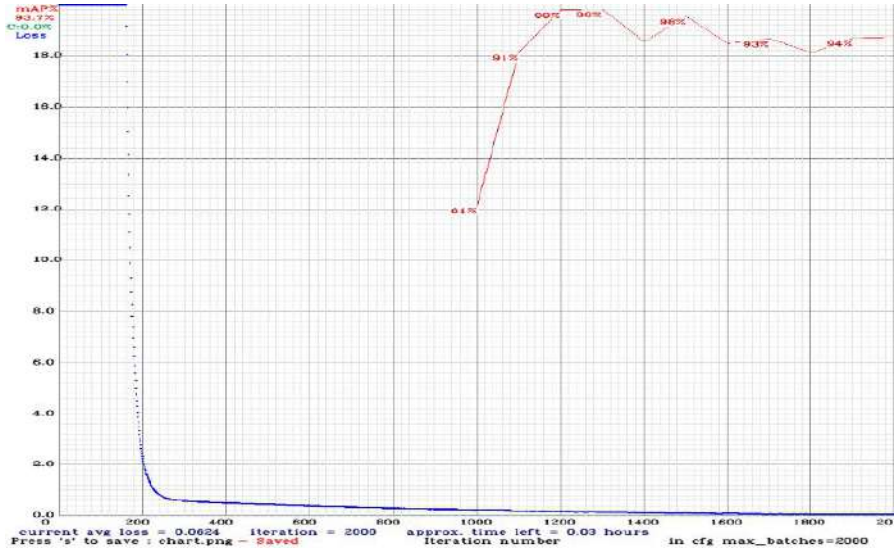

Şekil 4'teki grafiğin y ekseninde kırmızı renkle doğruluk değeri, yine aynı eksende mavi renk ile kayıplar gösterilmektedir. Doğruluk değeri mAP ile sembolize edilmiştir. Grafiğin x ekseni iterasyon sayısını göstermektedir. Toplamda 2000 adet iterasyon yapılmıştır. En yüksek doğruluk değerinin elde edildiği iterasyondaki ağırlıklar alınarak eğitim tamamlanmıştır. Eğitimden elde edilen ağırlık dosyaları kullanılarak Python dilinde, OpenCV'nin DNN modülü kullanılarak bir tespit algoritması hazırlanmıştır. Bu algoritma test için çekilen resimler, videolar ve gerçek zamanlı alınan görüntüler kullanılarak test edilmiştir. Test aşamasından elde edilen sonuçlardan bazıları Şekil 5'te verilmiştir.

Şekil 5. Eğitilen modelle yüksek doğrulukla tespit edilen bitki

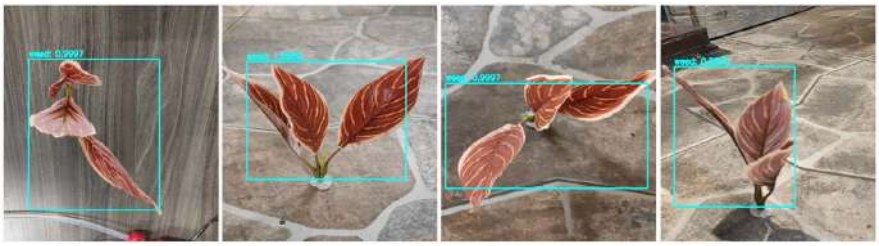

Çalışma süresince karşılaşılan problemlerden biri algoritmanın yabani bitkiyi tanımasında harcadığı süredir. Araç hareket ederken tanıma işlemi gerçekleştireceğinden 2-3 saniyelik tanıma için harcanan süre bitkinin tanınmasına imkân tanınmadan aracın üzerinden geçip gitmesine sebep olmaktadır. Bu ciddi bir sorundur. Bu aşamada veri setinin kalitesi ve algoritmanın verimli bir şekilde hazırlanması önemlidir. Seçilen YOLO v4-tiny algoritma modeli ile benzer içeriklerin yer aldığı veri setinde temizleme yaparak veri boyutunun azaltılmıştır. Verinin daha hızlı şekilde tanımlanması için veri setinin her bölgesinin incelenmesi yerine tanımlanacak cismin olabilecek pixel aralığında incelenmesi sağlanmıştır. Böylece tanımlama işlemi daha kısa süreye indirilmiştir. Bu konuda yaptığımız iyileştirmeler sayesinde araç hareket ederken durmaksızın bitkiyi tanıma ve imha etme işlemini hatasız bir şekilde gerçekleştirebilmektedir.

Şekil 6. Geliştirilen tarımsal insansız kara aracının farklı açılardan görünümü

5. ARAŞTIRMA SONUÇLARI VE TARTIŞMA

Çalışmanın sonunda aracın anlık durumunu görebilmek ve kontrol edilebilmek için Şekil 7'deki arayüz geliştirilmiştir. Geliştirilen arayüz sayesinde bir yer istasyonu üzerinden aracın uzaktan kablosuz kontrolü sağlanmaktadır. Arayüz üzerinde aracın anlık konumu, tespit edilen yabancı bitkinin görüntüsü, aracın hareket kontrol paneli, aracın hız-durum göstergeleri ve sürüş için otonom ve manuel mod seçenekleri bulunmaktadır. Buradaki arayüzden yapılan saha testleri sonucunda elde edilen veriler görülebilir.

Geliştirilen araçla yapılan saha testlerinden sonra aracın gövdesi ile tekerlekleri arasındaki bağlantının tek taraflı yataklı olmasından kaynaklı aracın yürür sisteminde sıkıntılar tespit edilmiştir. Tekerlekler tek taraflı yataklandığından zamanla lastikler yere açılı basmaktadır. Bunun önüne geçmek için ilerleyen çalışmalarda tekerleklerin çift taraflı yataklanması düşünülmektedir. Ayrıca araç daha iyi bir GPS modülüyle desteklenecektir. Bu sayede daha kesin konum bilgilerinin elde edilmesi amaçlanmıştır.

Şekil 7. Aracın uzaktan kontrolü ve izlenmesi için geliştirilen arayüz

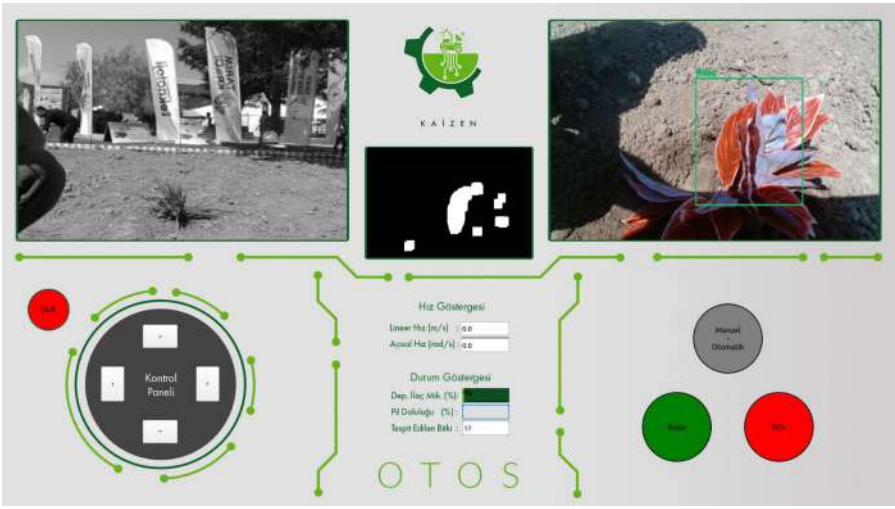

6. SONUÇ

Bu çalışmada tarımdaki fazla ilaç kullanımının önüne geçmek ve lokal olarak daha verimli bir ilaçlama yapabilmek için özgün tasarıma sahip insansız bir kara aracı geliştirilmiştir. Araç üzerinde tarım alanlarındaki istenmeyen yabani bitkilerin algılanması için bir tespit sistemi bulunmaktadır. Bu tespit sistemiyle istenmeyen yabani bitkiler yüksek doğrulukla tespit edilmiştir. Bitkilerin tespiti gerçek zamanda ve hızlı bir şekilde yapıldığından ilaçlama esnasındaki gecikmeler en aza indirilmiştir. Bitkiler, tespit edildikleri anda yine araç üzerindeki ilaçlama sistemiyle anlık ve lokal olarak ilaçlanabilmiştir. İlaçlama işlemi otonom yapılmıştır. Araç gerçek saha şartlarında test edilmiştir. Geliştirilen kara aracıyla yapılan saha testlerinde 40 cm yüksekten %90-95 doğrulukla tarım arazisindeki zararlı bitki tespit edilip anlık olarak başarılı bir şekilde ilaçlanmıştır. Bu testler sırasında yabani bitkiler başarıyla tanınmış ve aracın lineer-açısal hız verileri, araçta depolanan ilaç miktarı, bataryaların doluluk oranları ve tespit edilip ilaçlanan bitki sayıları gibi kritik parametreler harici bir yer istasyonu olarak geliştirilen arayüz üzerinden gerçek zamanda izlenmiştir.

KAYNAKLAR

Aleksey Bochkovskiy. (2020). YOLO v4 tiny Algorithm Model to Compare. Retrieved 21 March 2022, from pythonrepo.com

ArduPilot. (2021). Pixhawk Overview. Retrieved 4 March 2022, from https://ardupilot.org/copter/docs/common-pixhawk-overview.html

Ay, F., & Ince, G. (2015). Application of pesticide using unmanned aerial vehicle. *2015 23rd Signal Processing and Communications Applications Conference, SIU 2015 - Proceedings*, (June), 1268–1271. Retrieved from https://doi.org/10.1109/SIU.2015.7130069

Çınar, S., Halipoğlu, R., & İnal, İ. (2014). Effects of Some Weed Control Methods on Yield, Botanical Composition and Forage Quality in Subirrigated Grasslands of Cukurova. *Journal of Tekirdag Agricultural Faculty*, 1.

Intel. (2022). Intel RealSense D435 Camera. Retrieved 20 May 2022, from https://dev.intelrealsense.com/docs/stereo-depth-camera-d400

Kara, A., & Ata, E. (2021). Determination of Weed Species, Density and Frequency of Occurence in the Vineyards of Tekirdağ Province. *Journal of Tekirdag Agricultural Faculty*, 18(May), 333–343. Retrieved from https://doi.org/10.33462/jotaf.799731

Karadöl, H. (2017). Mısır Arazisinde Yabancı Otların Belirlenmesine Yönelik Matlab ve PLC Arası OPC Haberleşme Kullanılarak Geliştirilen Bir Kontrol Sistemi A Developed Control System by Using OPC Communication Between Matlab and PLC for Determination of Weeds in Corn Field. *Journal of Tekirdag Agricultural Faculty*, 14(02).

Logitech. (2019). Logitech C920 Pro. Retrieved 25 February 2022, from https://www.logitech.com/tr-tr/products/webcams/c920-pro-hd-webcam.960-001055.html

NVDIA. (2022). NVDIA Jetson Nano. Retrieved 1 January 2022, from https://developer.nvidia.com/embedded/downloads#?search=Jetson Nano

Sabancı, K. & Aydın, C. (2014). Görüntü İşleme Tabanlı Hassas İlaçlama Robotu. *Journal of Agricultural Sciences Journal*, 406–414. Retrieved from https://doi.org/10.1501/Tarimbil

Saeed, R. A., Tomasi, G., Carabin, G., Vidoni, R., & von Ellenrieder, K. D. (2022). Conceptualization and Implementation of a Reconfigurable Unmanned Ground Vehicle for Emulated Agricultural Tasks. *Machines*, 10(9), 1–20. Retrieved from https://doi.org/10.3390/machines10090817

Şin, B., & Kadioğlu, İ. (2019). İnsansız Hava Aracı (İHA) ve Görüntü İşleme Teknikleri Kullanılarak Yabancı Ot Tespitinin Yapılması. *Turkish Journal of Weed Science*, 20(2), 211–217. Retrieved from https://dergipark.org.tr/tjws

Slaughter, D. C., Giles, D. K., & Downey, D. (2008). Autonomous robotic weed control systems: A review. *Computers and Electronics in Agriculture*, 61(1), 63–78. Retrieved from https://doi.org/10.1016/j.compag.2007.05.008

Song, Y., Sun, H., Li, M., & Zhang, Q. (2015). Technology Application of Smart Spray in Agriculture: A Review. *Intelligent Automation and Soft Computing*, 21(3), 319–333. Retrieved from https://doi.org/10.1080/10798587.2015.1015781

Türkseven, S., Zeki KIZMAZ, M., Behiç TEKİN, A., Urkan, E., Tansel SERİM, A., Üniversitesi Ziraat Fakültesi Bitki Koruma Bölümü, E., … Tarihi, G. (2016). Tarımda Dijital Dönüşüm; İnsansız Hava Araçları Kullanımı. *Journal of Agricultural Machinery Science*, 12(4), 267–271.

Yazlik, A., Çöpoğlu, E., Özçelik, A., Tembelo, B., Yiğit, M., Albayrak, B., Aydinli, V. (2019). Weed species and their impacts: Fruit nursery area sample in düzce. *Journal of Tekirdag Agricultural Faculty*, 16(3), 389–401. Retrieved from https://doi.org/10.33462/jotaf.578999

Zou, Q., Sun, Q., Chen, L., Nie, B., & Li, Q. (2022). A Comparative Analysis of LiDAR SLAM-Based Indoor Navigation for Autonomous Vehicles. *IEEE Transactions on Intelligent Transportation Systems*, 23(7), 6907–6921. Retrieved from https://doi.org/10.1109/TITS.2021.3063477

Bölüm 14

Yaprak Yaylarda Yorulma Analizi

Güven Ege Erkman[1]

Özet

Bu çalışma, yaprak yayların bir diğer ismiyle makas yaylarının bilgisayar ortamında SolidWorks 2018 programından yardım alarak tasarlanıp ardından yine bilgisayar ortamında Ansys Workbench 18.1 programından yardım alarak analizlerinin yapılmasını amaçlanmıştır. Yapmış olduğumuz bu çalışmada gerçekte üretilmiş (Tip – 1) olan parabolik yaprak yay numunesini bilgisayar ortamında tasarlayıp ardından sonlu elemanlar analizi yaparak gerekli incelemeler yapılmıştır. Ayrıca aradaki farkı daha net görebilmek amacıyla numunenin ölçülerini değiştirilmiş versiyonla (Tip – 2) analiz yapılmıştır. Yapılan incelemeler de alt başlıklar halinde yazılmıştır. Bu çalışmanın temel amacı kısa bir süre içerisinde yaprak yayın hem tasarımını yapmak hem de üretilen yaprak yayların fiziki testlere ihtiyaç duymamıza gerek kalmadan seri üretime başlayabilmemizdir.

1.Giriş

Yaprak yaylar halk arasında bilinen adı makas yaylar, motorlu taşıtların arka süspansiyon donanımlarında kullanılan bir materyaldir. Günümüzdeki otomobillerde çok kullanılmamaktadır. Günümüzde daha çok iş makinelerinde veya ticari araçlarda sıklıkla kullanıldığı görülmektedir. [1]

Yaprak yaylar, tekerlek ve araç sistemleri arasında bağlantıdan sorumlu olan bir elemandır. Aynı zamanda yolda oluşan bozukluklara karşı titreşimleri sönümlemekle görevli olan bir sistemdir. Diğer bir değişle yaprak yaylar sürüş konforunu korumaya yardımcı olmaktadır. Yaprak yaylar yassı çelikten bant şeklinde kıvrılarak yapılmaktadır. İnce yaprağın uzundan kısaya doğru üst üste gelmesiyle oluşmaktadır ve bunda da büküm adı verilmektedir. Bu bağlamanın amacı yaprak yayların esnemesi durumunda kırılmaması, eğilmeğe zorlanmasıdır.[2]

Yaprak Yayların parçaları Şekil-1 de gösterilmiştir.

1 Yüksek Lisan Öğrencisi, Kırşehir Ahi Evran Üniversitesi, Makine Mühendisliği Bölümü, Kırşehir, Türkiye, egeerkman95@gmail.com, Orcid: 0000-0003-4804-5753

https://doi.org/10.58830/ozgur.pub130.c605

Şekil 1- Yaprak Yay Bağlantı Elemanları

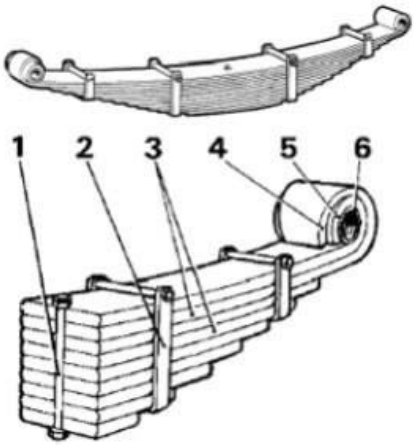

Yaprak Yay parça listesi aşağıda liste halinde mevcuttur;

1. Merkez Cıvata
2. Kelepçe
3. Yaprak Yay ya da Büküm
4. Bağlantı Küpesi
5. Yay Gözü
6. Lastik Burç

Yaprak Yaylar bir diğer adıyla makaslar, merkez cıvata tarafından birbirine bağlanır. Merkezden uçlara doğru kaymayı engelleyen kelepçeler yardımıyla yapraklar yani bir diğer adı bükümler birbirine tutturulur. Kelepçenin görevi yaprakların yani bükümlerin düzgün bir hizada tutmaya çalışmaktadır. Bunun dışında kelepçelerin görevi yaprak yayların yaylanma hareketi esnasından yaprakların yani bükümlerin birbirinden ayrılmasını engellemektedir. Bazı yaprak yayların yani makasların içine pul konularak eğilme esnasında üst üste olan bükümlerin kayma imkânı sağlanmaktadır. Bunun sebebi ise yaprak yayların kırılmasını önlemektedir. Ayrıca yaprak yayların sayısı arttıkça yük miktarı da artmaktadır. Şekil – 2'de yaprak yayın yüksüz ve tam yüklü halleri gösterilmiştir.

Şekil 2 – Yaprak yayın yüksüz ve ve tam yüklü halleri gösterilmiştir.

Yaprak yayların yani makasların en uzun yayın uçlarına kıvrımlı bir şekilde yay gözü oluşturulmuştur. Yay gözünden yay askısına kadar olan kısım bir cıvata yardımıyla asılmıştır ardından cıvata ve askıdaki yuvanın arasına kauçuk burçlar monte edilmiştir. Bu işlem sayesinde metallerin birbirlerine olan teması engellenmiş olur. Kauçuk burçların bir özelliği daha vardır. Bu özellik, kauçuk burçlar titreşimleri üzerlerine çeker yani titreşimleri üzerine alır ardında yapısı gereği kendi yapılarında üzerlerine almış olduğu titreşimleri sönümlerle yani titreşimleri yok ederler. Kauçuk burçlar titreşimleri yok ettiklerinden dolayı şasiye titreşimi iletmesine engel olmaktadır. Bunun dışında kauçuk burçlar yay eğilme çalışırken yay gözünün ileri geri bükülmesine müsaade etmektedir.[1]

Yaprak yaylar (makaslar) kullanım alanlarına göre aşağıda sıralanan özellikleriyle bilinmektedir bahsi geçen özellikler aşağıda maddeler halinde sunulmuştur;

- Yaprak yaylar sabittir. Uygun pozisyonda aksın içerisine aldıklarından bağlantı parçalarına gerek yoktur. Fakat büyüklüğü nedeniyle çok yer kaplamaktadır.
- Ağır hizmet kullanımı yani iş makineleri için oldukça dayanıklıdır, fakat üretimi zordur.
- Yaprak iç sürtünmeleri nedeniyle yol yüzeyinden meydana gelen küçük titreşimleri sönümlemeleri zordur.
- Sürüş konforu diğer süspansiyon sistemler ile karşılaştırdığımızda iyi değildir. Bu sebeple yaprak yaylar büyük ticari araçlarda kullanılmaktadır.
- Kalkış ve duruş sarsıntılarını kolay bir şekilde sönümlenmektedir.
- Yaprakların sürtünmesinden dolayı düzenli bakım gerektirmektedir. [3]

2. Yorulma

Makine elamanları çalıştıkları koşullara göre dinamik yüklere ve vibrasyonlara maruz kalabilmektedirler. Bu maruz kaldığı durumlar belirli gerilmelere maruz kalmaktadırlar. Bu gerilmeler sonucunda makine elemanlarının yüzeyinde çatlamalar ve daha sonrasında yüzeyinde parça ayrılması şeklinde hasara yol açmaktadır. Bu olaya da yorulma denilmektedir.[4]

2.1. Yorulma Literatür

Malzemelerin yorulma davranışı, 150 yıldan fazla bir süredir araştırma çalışmalarında konu olmuştur. Günümüzde teknolojinin ilerlemesi sayesinde makine elemanlarının ömrünü tahmin etmek geçmiş yıllara göre daha kolaydır. Yorulmadan kaynaklı olarak düşünülen ilk kazalar 1840'lı yıllarda meydana gelen demir yolu kazalarıydı. Bu kazaların sebebi demiryolu raylarını birbirine bağlantılı olan bağlantı parçalarının düzenli aralıklarla hasara maruz kalmasıydı ve daha kullanılamayacak halde olduğunu fark edilmesiydi. Bu kazaların sebebi anlaşıldıktan sonra 1840 ve 1850 yılları arasında "yorulma" kelimesi tekrar eden gerilmelerden kaynaklı olan arızaların tanımlamak için denilmiştir. Ardından tekrarlanan gerilimler nedeniyle oluşan kırılmalara ya da hasarları tanımlamak amaçlı günümüze kadar yorulma olarak kullanılmıştır.

1850 ile 1860 yılları arasında yorulmaların öncülerinden olan August Wöhler laboratuvar koşullarında tekrarlanan gerilmeler altında birçok yorulma testi yapmıştır. Bu deneyler ise 1840'lı yıllarda meydana gelen demir yolu kazaları ile ilgiliydi. August Wöhler demir yolu kazalarını araştırma amaçlı kendine yorulma test düzeneği kurmuştur. August Wöhlerin yorulma test düzeneği Şekil-3'de gösterilmiştir.

Şekil 3 - Agust Wöhler yorulma test düzeneği

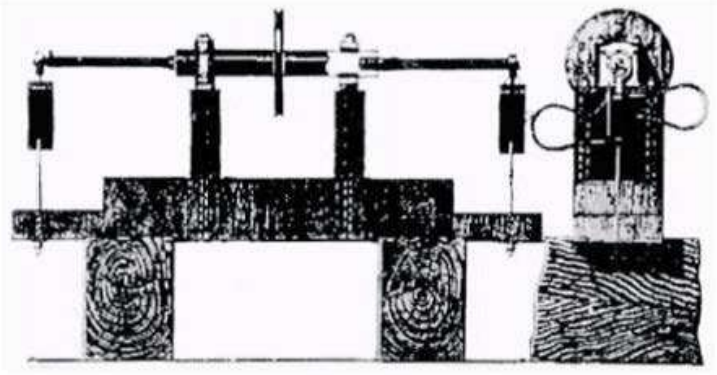

Agust Wöhler, gerilme ve ömür diyagramları kullanarak yüksek gerilme genlikleri ile yorulma ömrünün nasıl azaldığını gösterebilmiştir ayrıca gerilme genliği altında test numunelerinin kırılmadığını gösterebilmiştir. Bu ispatı sayesinde Agust Wöhler yorulma için gerilme aralığının maksimum gerilmeden çok daha önemli olduğunu gösterebilmiştir. Agust Wöhler den sonra gelen araştırmacılar Wöhlerin çalışmalarını doğruladı ve çalışmalarını genişletmişlerdir. Çalışmaları devam ettiren araştırmacılardan biri olan Gerber ekibinin yardımı ile gerilmenin etkisini araştırmışlardır. Bir diğer araştırmacı olan Goodman'da ortalama gerilme ile ilgili basitleştirilmiş bir teori önerebilme başarısını gösterebilmiştir. 1870 ile 1890'lı yıllar arasında geçen süre zarfında Gerber ve Goodman gibi birçok araştırmacı Agust Wöhlerin ışık tuttuğu bu araştırma konusunu genişletmişlerdir ve her biri gelecekteki insanlara bu bilgileri miras bırakmışlardır.

Bu mirasın parçalarından biri olan Bauschinger 1886 yılında elastik olmayan ve deformasyona neden olan zıt yönde bir yük uygulamıştır daha sonra çeki ve basıdaki akma dayanımının azaldığını gösterebilmiştir. Bauschinger'ın yarattığı bu olay bize elastik olmayan gerinimin metallerin gerilme – gerinim davranışını değiştirebileceğinin ilk göstergesiydi. Bu araştırmacılara ek olarak 1900'lü yılların başında Ewing ve Humpfrey ekleyebiliriz. Ewing ve Humpfrey yorulma mekanizması çalışmalarını devam ettirebilmek amacıyla optik bir mikroskop kullanmışlardır. Bunun sebebi ise lokalize çizgileri ve mikro çatlak oluşumuna neden olan kayma bantlarını gözlemlemeyi amaçlamışlardır.

1910 yılında günümüzde de sıkça karşılaştığımız Basquin'in sonlu ömür bölgesindeki değişken gerilme sayısı ve hasar çevirim sayısıdır (günümüzde S-N olarakta bilinmektedir). Basquin gerilme ve hasar çevirim sayısı arasında logaritmik doğrusal bir ilişki olabileceğini bilim dünyasında göstermiştir. Basquin bulduğu denklem güncellemeler ile günümüzde sonlu ömür yorulma davranışlarını temsil edecek bir şekilde hala kullanılmaktadır. 1924 yılında ise araştırmacılardan biri olan Palmgren değişken genlik yüklemesi için doğrusal bir kümülatif hasar modeli meydana getirmiştir. Palmgren meydana getirmiş olduğu modeli küresel yatak tasarımı için istatiksel dağılımlarına dayanarak kullanımını gerçekleştirmiştir.

1930'lu yıllara geldiğimizde bazı yorulma otomobil endüstrisi sayesinde ilerleme göstermiştir. Bunun nedeni ise otomobil endüstrisinde bilya püskürtme yöntemi bulunmasından dolayı.[5] Bilya püskürtme yöntemi, malzemelerin üzerinde yapılan inovatif yani bir diğer adıyla yenilikçi çalışmalar ışığında günümüze kadar geniş bir kullanım alanına sahip olmuşturlar. Bilya püskürtme yöntemi ilk olarak otomobil endüstrisinde kullanılması rağmen

günümüzde ise hava taşıtlarında da kullanılmaktadır. Eski zamanlarda mesleği demirci olan insanlar çekiç darbeleriyle metallere şekil veremeye çalışırlarmış hem de iyileştirmeye çalışmışlardır. Günümüzde ise bu olaya bilya püskürtme (shot peening) denmektedir.[6]

Şekil 4 – Bilya püskürtme işlemi

Bilya püskürtme işleminin öncülerinden olan Almen, parçaların yüzeye yakın tabakalarında bası artık gerilme oluşturulmasıyla beraber bu alandaki geliştirmeleri doğru bir şekilde açıklamıştır bu olay sonucunda ise artık gerilme üreten diğer proseslerin yani süreçlerin ve bilya püskürtme yönteminin kullanımının destekçilerinden biri olmuştur.[5]

1937 yılında Neuber adındaki bilim insanı çentiklerin gerilme gradyan etkilerini ve temel blok konseptini dünyaya tanıtmıştır. Neuberin yarattığı bu çalışma çentiğin kökündeki küçük bir hacim üzerinde oluşan gerilmenin çentikteki maksimum gerilmeden çok daha önemli olduğunu göstermeyi amaçlamıştır. Neuber'in yapmış olduğu çalışmanın yorulma konusuna olan katkısı ise kapalı döngü servo hidrolik test sistemlerinin tanıtılmasıyla yapılmıştır. Kapalı döngü servo hidrolik test sistemi mekanik sistemlerdeki, parçalardaki ve test numunelerindeki yük geçmişini daha iyi simüle edilmesini sağlamaktadır.

1970 yıllarına geldiğimizde ise Elber yorulma çatlağı büyümesinin, uygulanan bir gerilme yoğunluğu faktörü aralığı yerine efektif bir gerilme yoğunluğu faktörü aralığıyla kontrol edildiğini gösteren bir model yaratmayı başarmıştır. Geçmişten günümüze birçok bilim insanı yorulma konusunda araştırma yapmışlardır. Bu zaman zarfında küçük çatlakların davranışını incelemişlerdir. Yük altında küçük çatlakların büyümesi büyük çatlaklara göre daha hızlı meydana geldiğinden dolayı küçük çatlak problemlerinin karmaşık

ve daha önemli olduğu göz ününe serilmiştir. Küçük çatlak ve büyük çatlak arasındaki farkı daha net anlamak için ikisine de aynı yük altında bakılması gerekmektedir. Yorulmadan dolayı kaynaklanan mekanik hasarlarla günümüzde her alanda karşımıza çıkabilecek bir durumdur. Geçmişte çalışmalarıyla günümüze ışık tutan bilim insanlarının bize verdiği bilgiler ve günümüz teknolojisini birleştirdiğimizde gelişmiş olanaklar sağlamaktadır bu olanakları değerlendirilerek günümüzde halen yorulma konusu incelenmeye devam etmektedir. [5]

2.2 Yorulma Deney Cihazları

Teknolojinin ilerlemesiyle birlikte yorulma cihazları da teknolojiye adapte olabilmiştir. Günümüzde yorulma cihazlar malzemeleri çekme, çekme – basma, çevresel eğme, ileri – geri eğme, burma gibi zorlamayı başarabilmişlerdir. Bu makinaların çalışma frekansları farklılık gösterirler.

2.2.1 Döner Mil Deney Cihazı

Malzemeleri yorulma cihazlarında test edilirken basit bir numune şeklinde test edilmektedir. Özellikle döner mil deney cihazıyla test edilecekse küçük bir numune iş görmektedir. Döner mil deney cihazında dönerken birbiri arkasına, eşit genlikte çekme ve basma gerilmelere maruz kalmasını sağlamaktadır. Test esnasında numunede ortalama gerilme etrafında titreşen ve değişen eğme gerilmeleri meydana gelmektedir. Bu test için gerekli parametreli girip numune kırılana kadar aynı döngüyü uygulamaktadır.

Şekil 5 – Döner Mil Deney Cihazı

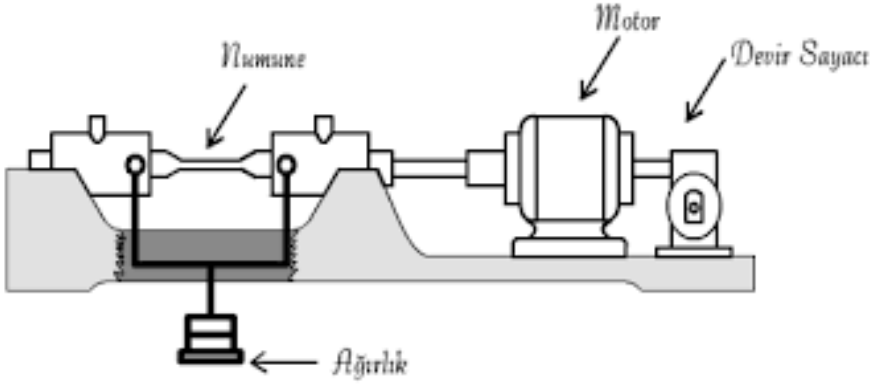

Döner mil deney cihazında uçlarını rijit olarak yerleştirilmiş olduğu numune sadece eğilme etkisine maruz kalmaktadır. Numune dönerken üst kısım basıya alt kısım ise çekiye çalışmaktadır. Cihaza takılı olan numuneyi

mil olarak düşünürsek her iki noktadasın da sinüzoidal değişen bir gerilme doğmaktadır. Bu yüklemeler statik olduğundan dolayı sabit bir yükleme yapılmasına mümkün kılmaktadır ve ortalama gerilme sıfır olmaktadır.[7]

2.2.2. Eksenel Gerilmeli Yorulma Deney Cihazı

Eksenel gerilmeli yorulma deney cihazı yorulma test cihazları arasında olan en basitte yakın cihazdır. Bu test cihazı numunenin uzunluğu boyunca çekme ve basma gerilmelerine maruz bırakmaktadır. Test cihazının uyguladığı gerilme numune boyunca dağılmaktadır. [8]

Şekil 6 – Eksenel çekme – basma test cihazı

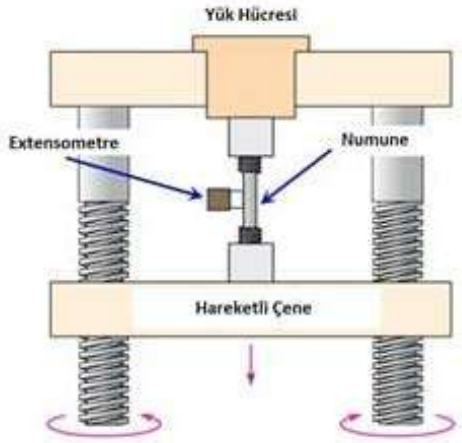

Eksenel gerilmeli yoruma test cihazının amacını daha ayrıntılı bir şekilde anlatacak olursak, malzemelerin statik yük altındaki elastik ve plastik deformasyonunu görebilmek için yapılmaktadır. Numunenin elastik ve plastik davranışlarını görebilmek için numuneyi standartlara uydun bir şekilde kesilmesi (daire veya dikdörtgen kesit haline getirilmiş parçalar) gerekmektedir. Bu kesilen numuneler daha sonra test cihazına girip test edilmelidir. Bu cihaz aşağı ve yukarı hareket edebilen bir cihazdır. Deney parçasının bağlandığı iki çene ve standartlara göre kesilen numunelere hareket veya kuvvet verebilen ayrıca bu iki olayı da (hareket ve kuvvet) ölçebilen ünitelerden oluşmaktadır. [9]

2.2.3. Burma Gerilmeli Yorulma Deney Cihazı

Burma gerilmeli yorulma deneyi sabit bir eksene göre tekrarlanan burma bir diğer adı dönme işlemi uygulanmaktadır. Burma gerilmeli deney daha çok araçların süspansiyon yaylarında veya çekme – basma kuvvetine maruz

kalmış olan tüm helisel yaylarda burma gerilmeli yorulma deneyi yapılmaktadır.[8]

2.2.4. Birleşik Gerilmeli Yorulma Deney Cihazı

Birleşik gerilmeli yorulma deney cihazı, en az iki tane yorulma cihazının bir araya gelmesiyle oluşan cihazlara birleşik gerilmeli yorulma cihazı olarak adlandırılmaktadır. Birleşik gerilmeli yorulma deney cihazının günümüzde en çok rastladığımız modeli eğme – burulma gerilmelerinin bir arada bulunduğu durum ile eksenel – burma gerilmelerinin olduğu cihazlardır. [8]

3. Metodoloji

Yaprak yaylar yassı çelikten bant şeklinde kıvrılarak yapılmaktadır. İnce yaprağın uzundan kısaya doğru üst üste gelmesiyle oluşmaktadır. Yaprak yayların tasarlanırken esnemesi durumunda kırılmaması, eğilmeğe zorlanması amaçlanmaktadır. Tasarlanmış olan yaprak yayların teknik çizimleri SolidWorks 2018 programı tarafından çizilmiştir. Tasarlanan bu yaprak yay günümüzden kullanılan yaprak yay çeşitlerinden sadece bir tanesidir. Tasarlanmış olan yaprak yay bire bir gerçeği ile aynıdır. Aşağıdaki şekil 7, şekil 8, şekil 9, şekil 10, şekil 11'da gösterilmiştir.

Şekil 7 – Yaprak yay teknik çizim

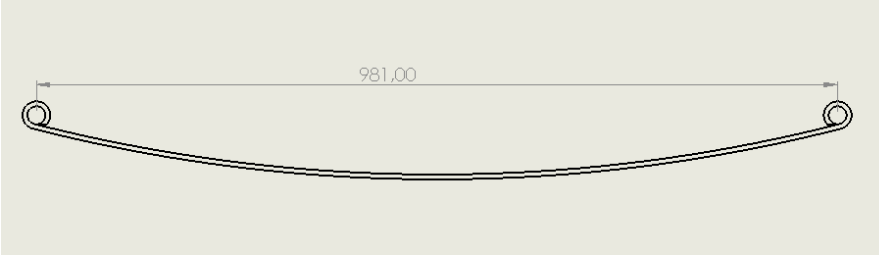

Yaprak yayın uçlarında olan bağlantı elemanlarının merkezden merkeze olan uzaklığı 981 mm olarak tasarlanmıştır.

Şekil 8 – Yaprak yay teknik çizim

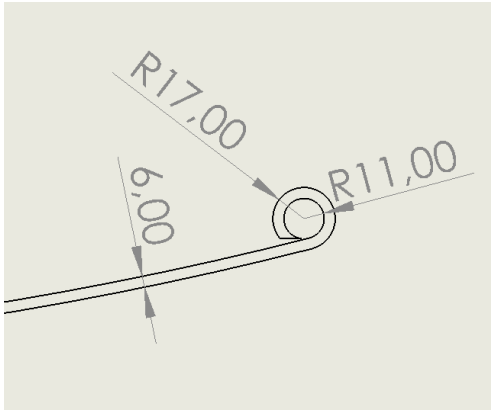

Yaprak yayın et kalınlığı 6 mm olacak şekilde tasarlanmış olup araca bağlanacak olan yerlerin iç çapı 22 mm dış çapı ise 34 mm şeklinde tasarlanmıştır.

Şekil 9 – Yaprak yay teknik çizim

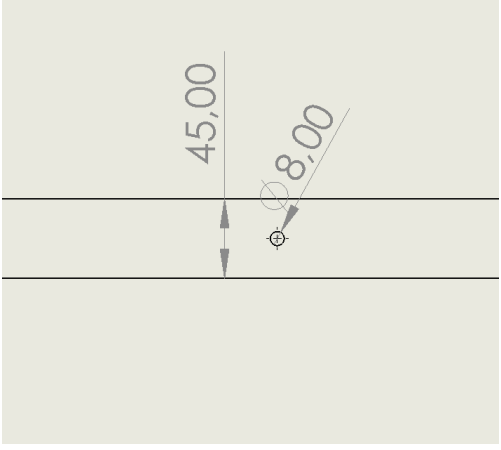

Yaprak yayın genişliği 45 mm olacak şekilde tasarlanmıştır. Yaprak yayın yani bir diğer adıyla makas yayların ortasında olan deliğin çapı 8 mm olarak belirlenmiştir. Yaprak yayın ortasındaki delik ise yaprak yayların üst üste getirilmesini sağlayan bağlantı boşuğudur.

Şekil 10 – Yaprak yayın 3 boyutlu (3D) çizimi.

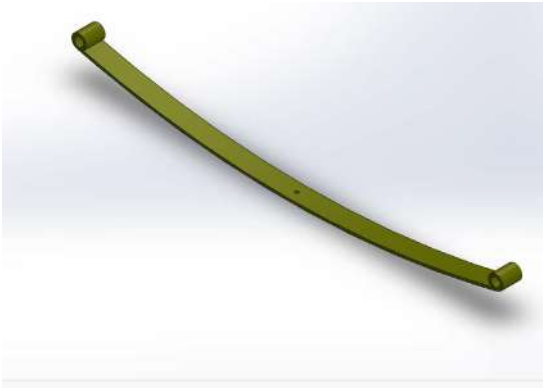

Yaprak yayın çizimi daha öncede bahsedildiği üzere SolidWorks 2018 programı sayesinde tasarlanmıştır.

3.1. Yaprak Yay Analizi

Yaprak yayın analiz işmelerini Ansys Workbench 18.1 programını kullanarak yapılmıştır. Analiz methotlarını yaprak yay analiz konusunun altbaşlıklar haliden adım adım anlatılmaktadır.

3.1.1 Sonlu Elemanlarda Analiz

Sonlu elemanlar analiz türleri yük – zamana göre değişim ve yapıların yüke verdiği reaskyonlara göre iki temel kategoride sınıflandırılabilmektedir. Yük ve zamana göre analiz türleri; statik analiz, dinamik analiz ve harmonik analiz olarak adlandırılmaktadır. Yapıların uygulanan yüke verdilleri tepkilere göre analiz türleri; lineer analiz ve lineer olmayan analiz olarak adlandırılmaktadır.

Statik Analiz: Uygulanan yükün ve sınır şartlarının zamana bağlı olarak sabit kaldığı ve değişmediği durumlarda gerçekleştirilen analiz olarak adlandırılmaktadır.

Şekil 11 – Statik analiz örnek grafik

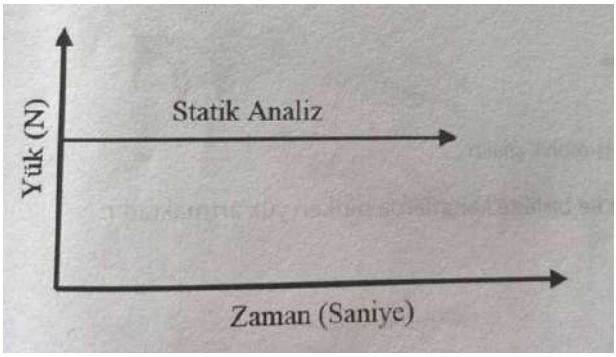

Statik analizin kullanım alanlarına örnek verecek olursak, çelik konstrüksiyonlda kolonlarda oluşan gerilmenin belirlenmesinde yardımcı olmaktadır.

- **Lineer Analiz:** Lineer analiz malzemelerin yükün etkisi altında elastik sınırlar içinde kaldığı durumda gerçekleşen analiz türü olarak adlandırlmaktadır.

Şekil 12 – Gerilim ve gerinim grafiği (elastik bölgesi)

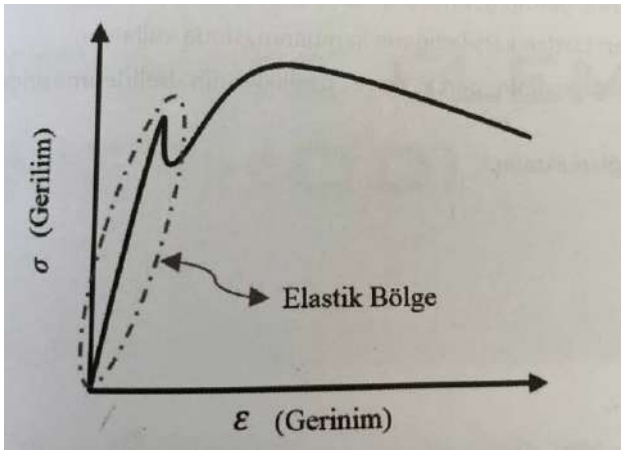

Bir malzemeye etki eden kuvvet ortadan kalktığında malzeme eğer kendi şekline geri dönüyorsa değişimi kalıcı değildir. Bu olaya ise **elastik deformasyan** olarak adlandırlmaktadır.

- **Lineer Olmayan Analiz:** Lineer olmayan analiz malzemeye uygulanan yükünün genellikle plastk deformasyon bölgesinde kalmasından dolayı gerçekleştirilen bir analiz türüdür.

Şekil 13 – Gerilim ve gerinim grafiği (plastik deformasyon bölgesi)

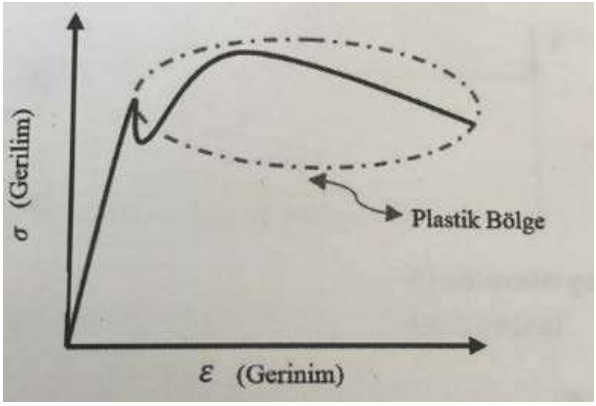

Bir malzemeye etki eden kuvvet ortadan kalktığında malzeme eğer kendi şekline geri dönmüyorsa bu malzemenin şekil değişimi kalıcıdır. Bu olaya ise **plastik deformasyan** olarak adlandırlmaktadır. Bu çalışmada yaprak yayların yük taşıma kapasiteleri ve yorulma dayanımları hesaplanmıştır. Yaprak yayların analizi sonucu güvenlik faktörleri ve kullanılacak standartlar belirlenmiş olup sonlu elemanlar analizi (FEA) metodu uygulanmıştır. Analiz her yaprak yay modeli için alınan teknik resimler kullanılarak ANSYS Workbench 18.1 yazılımında gerçekleştirilmiştir.

Bu analizi TS EN 15620 Standardı (Ayarlanabilir Palet Raf Sistemleri - Çarpılma Ve Aralık Toleransları) referans alınarak yapılmaktadır.

- Maksimum yükte, izin verilen maksimum sehim, köprü kirişlerde travers boy uzunluğunun 200'e oranını geçemez. ($y < L/200$)
- Maksimum yükte, izin verilen maksimum sehim, konsol kirişlerde travers boy uzunluğunun 100'e oranını geçemez. ($y < L/100$)

Şekil 14 – Maksimum sehim oranları

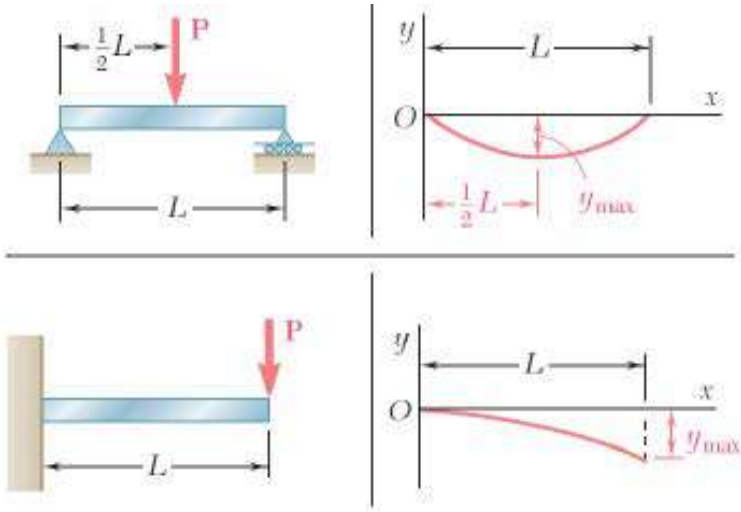

3.1.2. Deney Öncesi Kabuller ve Varsayımlar

Analiz sürecinde ve sonuç değerlendirmesinde EN 15620 standardı kabul edilmiştir. Yaprak yayların geometrisi analize tâbi tutulmuştur. Malzemenin bükülmesi asıl taşıyıcı elemanlar kabul edilip profil indirgemesi yapılmıştır. TS EN 15635 (Saklama Ekipmanlarının Uygulama Ve Bakımı) standardı gereği uygun yükleme yapıldığı ve komponentlerinin hasar almadığı varsayılmış olup yükün profillere homojen dağıldığı kabul edilmiştir.

Yayların topolojisi gereği kapasite analiz sürecinde temel olarak travers sehim kontrolü ve güvenlik faktörü seçimi yapılmıştır. Yaprak yay sistemlerinde yaygın olarak sehim kontrolünün elzem olması sebebiyle standartlara verilen örnek güvenlik faktörleri genelde 1.5 – 1.75 mertebelerinde olmaktadır. Malzemeyi yapısal çelik olan St37 olarak belirlenmiştir. Bu malzeme için izin verilen maksimum yükleme 140 MPa civarında alınmış olup güvenlik faktörü 1.68 mertebelerinde tutulmuştur. Bazı durumlarda sehim sınırlayıcı faktör olurken bazı bölgelerde birleştirilmiş stres baskın parametre haline gelmektedir. Analiz boyunca her iki kontrol de yapılacaktır.

Burkulma kontrolü için kritik yükleme Yük Çarpanı ile belirlenecektir. Genel kabul gören bir prensip olarak kritik yükün izin verilen maksimum yüklemenin en az 3 katı mertebelerinde olması beklenmektedir. Dolayısıyla Yük Çarpanı'nın 3 civarı veya 3'ten büyük bulunması durumunda burkulma açısından güvenlik sağlanmış olacaktır. Kullanılan yapı elemanlarının uygun yöntemler (civata, tırnak vs.) ile kolon kirişlere bağlandığı göz önünde bu-

lundurulduğunda profil birleşim yerlerine çarpılma serbestliği verecek bir rijitlik tanımlanmıştır. Bu özellikle burkulma analizi için elzemdir.

3.1.3. Mesh

1D doğrusal modele sahip profiller 3D versiyonlarına kıyasla çok daha az mesh sayısı gerektirmektedir.

Şekil 15 – Meshleme

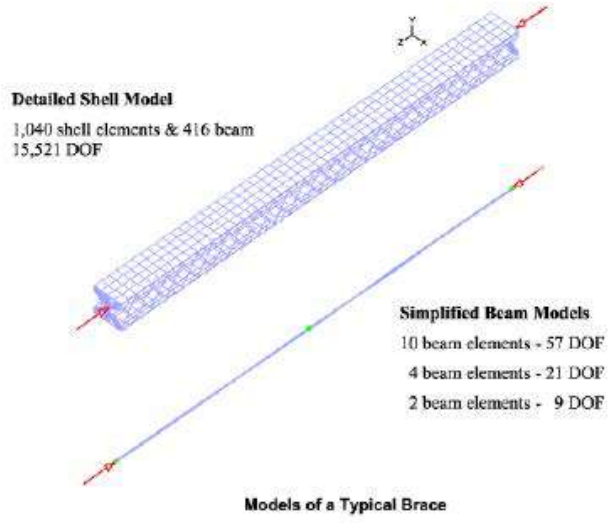

Her bir doğrusal eleman bağlı olduğu ve temsil ettiği profilin mekanik özelliklerini taşımaktadır. Bu mekanik özelliklerin en başında profil kesiti geometrisi gelmektedir. Benzer durum düzlemsel elemanlar için de geçerli olup mekanik olarak bağlı oldukları sacın kalınlığını analize yansıtmaktadırlar.

Uzunluk olarak metreler arası değişen raf bölmeleri için mesh boyutları göreceli olarak seçilmelidir. Profiller için 1D doğrusal mesh boyutu 7.5 mm seçilmiştir. Yani her bir doğrusal profil 7.5mm'lik segmentlere bölünmüştür. 7.5mm'lik mesh boyutu analiz doğruluğu için göreceli olarak yeterli seviyededir. Yaprak yay için 2D düzlemsel mesh boyutu tanımlanmamıştır. Yazılımın adaptif mesh yöntemi gerekli düzlemsel mesh boyutlarını kenarlara göreceli olarak ayarlamaktadır. Aşağıda analizde kullanılan örnek bir hibrit doğrusal ve düzlemsel mesh gösterilmiştir.

3.1.4. Yükleme ve Sınır Şartları

Yükleme her bir kompartımana homojen olarak dağıtılmış olup yük miktarı maksimum izin verilen sehim ve izin verilen stres sınırına ulaşılana kadar iteratif bir şekilde arttırılmıştır.Yüksek travers uzunluğuna sahip olan yaprak yaylar kendi ağırlığı da deplasman yaratacaktır. Bu etkiyi modellemek adına analiz ortamına aşağı yönde yer çekimi tanımlanmıştır.Yaprak yaylar uçlarından sabitlenmiş olup zemine basma şartını yerine getirmekiçin yere özellikle temas eden yaprak yay uçlarına yükseklik değişimi ve rotasyon izni verilmemiştir.

3.1.5. Tip – 1 Yaprak Yay ve Tip – 2 Yaprak Yay Analiz Tablosu

Tablo – 1 Analiz Tablosu

ANALİZ SONUÇ TABLOSU	Tip - 1	Tip - 2
Kuvvet (N)	7920	30250
Maksimum Sehim (mm)	1,21	0,41
İzin verilen Maksimum Sehim (L/200 mm)	4,9	3,3
Maksimum Stres (von-Mises MPa)	140,03	139,93
Yük çarpanı (1) > 3	1598,4	1623,3
Yük çarpanı (2) > 3	1609,9	1680,7
Yük çarpanı (3) > 3	1620,5	1734,9
Yük çarpanı (4) > 3	1635,1	1830,8
Malzeme Adı	St 37 Çeliği	St 37 Çeliği
Yaprak yay taşıma kapasitesi (kg)	807	3080
Malzemenin akma mukaveti (MPa)	235	235
Emniyet Katsayısı (Akma Mukavemeti / Maksimum Stres)	1,68	1,68
Yorulma Döngü Sayısı	10000000000	10000000000
En çok darbe alınan bölge	Yaprak Yay Ağırlık Merkezi	Yaprak Yay Gözleri

Tip – 2 teknik ölçüleri; uzunluk 666 mm, genişlik 65 mm, ek kalınlığı 10mm, yaprak yay göz çapı 14mm olarak ayarlanıp analiz işlemine sokulduğunda. Tablo – 1'de ki gibi sonuçlar elde etmekteyiz.

SONUÇ VE ÖNERİLER

Deneylerin sonucunda, Tablo – 1'de yaprak yaylarında yükleme miktarları belirlenirken sehim ve stres bakımından güvenli kalacak şekilde sınır değerlerine ulaşılana kadar iterasyon yapılmıştır. Sonuç bölümünde yaprak yayları için bahsi geçen yüklemelerin kilogram karşılıklarını tip -1 için 807 kg olarak tip – 2 için ise 3080 kg olarak bulunmuştur. Yaprak yayın kapasitesinin arttırması için gereken değişiklikler yaprak yayın kalınlığını arttırmak, uzunluğunu kısaltmak, genişliğini arttırmak olmuştur. Yaprak yayın ölçülerini bu parametrelerle değiştirmemizin sonucunda burkulma katsayımızın arttığını gözlemlemiş bulunmaktayız. Yaprak yayın bağlı olan araçlarda tek katlı ve ya çok katlı yaprak yayların sürücünün konforuna göre değişiklik gösterebilir. Bu çalışmanın sonucunda yaprak yayların sürücünün konforuna göre değişkenlik gösterebildiğini gözlemlemiş bulunmaktayız.

Yorulma ömrü hesaplarının girmiş olduğumuz parametrelere bağlı olduğunu ve yaprak yayın ölçülerinin değişkenliğine göre yorulma ömrününde değişebileceğini gözlemlemiş bulunmaktayız. Numunenin ölçüleri değiştiği taktirde numuneye uygulanan hasarında değişebildiğini gözlemleyebiliriz. Seri üretim yapan firmalar analiz için uygun parametrelere girmesi halinde yaprak yayın birden fazla versiyonda deneme imkanları olacaktır. Bu durum ise üreticiye ciddi anlamda kar ve zaman kazandırmaktadır.

KAYNAKÇA

[1] Polat, O. (2012). *Yaprak yayların bilgisayar destekli yorulma analizi* (Master's thesis, Balıkesir Üniversitesi Fen Bilimleri Enstitüsü).

[2] Tokgönül, G., Kulaç, G., Şenocak, Ç., & Başalan, E. Ağır Ticari Kamyondaki Tek Katlı Parabolik Yaprak Yayın Bilgisayar Destekli Tasarımı, Analizi Ve Fiziksel Doğrulaması. *Soma Meslek Yüksekokulu Teknik Bilimler Dergisi*, *2*(26), 55-61.)

[3] Bakanlığı, M. E. (2013). Motorlu Araçlar Teknolojisi İş Makineleri. *Milli Eğitim Bakanlığı, Ankara*.

[4] Başkent Üniversitesi Makine Mühendisliği Bölümü, Yorulma Testi Deney MAK – 402

[5] Zerkin, D. (2019). *Binek Araçlardaki Rot Başlarında Yorulma Davranışının İncelenmesi* (Master's thesis, Dokuz Eylül Üniversitesi Fen Bilimler Enstitüsü).

[6] Karahan, B., & Ince, U. (2015). Bilya Püskürtmenin (Shot Peening) Teknik-Teknolojideki Yolculuğu ve Soğuk Dövme Prosesine Adaptasyonu. *Derin Ekim*, *74*, 90.

[7] Gök, G ve Aslaner, T.. (2021). *Dönel Eğmeli Korozyonlu Yorulma Deney Düzeneği* (*Project Study*, Karadeniz Teknik Üniversitesi Makine Mühendisliği Bölümü).

[8] Başuslu, O. (1999). *1.2080 (X210Cr12), 1.7225 (42CrMo4) ve Ck45 çeliklerinin Yorulma Dayanımı Açısından Optimum ısıl İşlem Parametrelerinin Belirlenmesi* (Doctoral dissertation, Bursa Uludag University (Turkey)).

[9] Uludağ Üniversitesi, Çekme ve Basma Deney Föyü 2018

Bölüm 15

Minimum Miktarda Yağlama Yöntemi İçin Farklı Uygulama Mesafelerinin ve Farklı Kesme Parametrelerinin St37 Çelik İşlenebilirliğine Etkilerinin İncelenmesi

Üsame Ali Usca[1]

Özet

İmalat endüstrisinde sıklıkla tercih edilen St37 çeliğinin işlenebilirlik özelliklerinin geliştirilmesi ve araştırılması oldukça önemlidir. Bu malzemelerin frezelenmesi esnasında minimum miktarda yağlama (MMY) soğutma/yağlama sisteminin kullanılması gün geçtikçe artmakta fakat bu sistemin içerdiği değişken parametrelerin frezeleme işlemine olan etkileri yeterince araştırılmamıştır. Ayrıca bu sistemin değişken parametrelerinden olan püskürtme mesafelerinin işlenebilirlik parametrelerine olan etkisi de ayrı bir inceleme konusudur. Bundan dolayı, bu çalışmada yaygın bir kullanım alanına sahip St37 sade karbonlu çeliğin kesme derinliği (1 mm) sabit tutularak farklı kesme (140-210 m/dk) ve ilerleme hızlarında (0,14-0,21 mm/dev) MMY destekli soğutma yapılarak CNC frezeleme işlemi gerçekleştirilmiştir. Yapılan çalışma ile farklı kesme ve ilerleme hızları ile farklı MMY püskürtme mesafelerinin (50-250 mm) işlenebilirlikteki çıktı parametreleri (Yüzey pürüzlülüğü, takım aşınması ve kesme sıcaklığı) üzerindeki etkileri araştırılmıştır. Elde edilen bulgulara göre uzun mesafeden uygulanan MMY sıvısı takım aşınması ve kesme sıcaklığı üzerinde olumlu etki yaptığı görülmüştür. MMY uygulama mesafesinin yüzey pürüzlülüğü üzerindeki etkisi ise kesme hızına bağlı olarak değişkenlik gösterdiği tespit edilmiştir.

1. Giriş

Dünyada yer alan sanayi kuruşlarının üretim aşamasında en çok ihtiyaç duyduğu ve kullandığı malzemelerden biri St37 çeliği olup yapısında maksimum %2 oranında karbon bulunan ve çekme dayanımı en az 37 kg/mm

1 Dr. Öğr. Üyesi, Makine Mühendisliği Bölümü, Mühendislik ve Mimarlık Fakültesi, Bingöl Üniversitesi, Bingöl, Türkiye; ausca@bingol.edu.tr, Orcid: 0000-0001-5160-5526

https://doi.org/10.58830/ozgur.pub130.c798

olan sade karbonlu bir çeliktir. Gerek ucuz olmaları gerekse de maliyetlerine kıyasla iyi mekanik özellik göstermeleri nedeni ile otomotiv, inşaat ve tekstil sektörleri başta olmak üzere pek çok imalat sanayisinde tercih edilmektedir [1]. Tüm bu yaygın kullanım alanları nedeni ile St37 sade karbonlu çeliğin işlenebilirliği ve yüzey özelliklerinin geliştirilmesi önemli bir araştırma alanıdır. Talaşlı imalat sırasında kesici takımın zarar görmemesi ve kaliteli bir yüzey elde etmek için kesme sıvıları yaygın bir şekilde kullanılmaktadır [2-7]. Ayrıca kesme sıvıları talaşın kırılmasını ve kesme bölgesinden taşınmasını da kolaylaştırmaktadır [8]. Fakat geleneksel kesme sıvılarının kullanımı birçok sağlık sorunlarına yol açarak endişeye sebep olmaktadır [9]. Aynı zamanda maliyet açısından kesme sıvıları oldukça yüksek rakamlara çıkabilmektedir. Bu sebeple son zamanlarda alternatif soğutma/yağlama seçenekleri oldukça popüler bir hal almaktadır [2, 10-13]. Özellikle MMY ile soğutma seçeneği birçok araştırmacının odağı haline gelmektedir [14-16]. MMY ile soğutma yönteminde çok az sıvı tüketimi sağlandığı için oldukça çevreci bir yöntemdir. Minimum seviyede püskürtülen yağ kesme bölgesindeki sürtünmenin azalmasını sağlayarak malzemenin kesici takıma yapışmasını önleyebilmektedir [17]. Ayrıca kesme bölgesinde ve kesici takımda kalıntı bırakmadan ortalama 5-500 ml/saat aralığında yağlama hızı sayesinde kuru işlemeye alternatif bir seçenektir [18]. MMY ile soğutma işleminde kullanılan yağ basınçlı hava yardımıyla pulverize şekilde kesme bölgesine iletilerek sıcaklıklar azaltılmaktadır. Bu nedenle MMY koşulları kullanılarak takım aşınmasının ve yüzey pürüzlülüğünün iyileştirilmesine yönelik yapılan birçok çalışma bulunmaktadır. Bu çalışmalara örnek olarak Danish et al. [19] havacılık sektöründe yaygın bir şekilde kullanılan Inconel 718 alaşımının tornalanması için kriyojenik ve MMY teorisini içeren bir soğutma/yağlama ortamı önermişlerdir. Hadad and Sadeghi [20] AISI 4140 çelik alaşımında MMY koşulları altında işleme kuvvetleri, yüzey pürüzlülüğü ve sıcaklık gibi malzeme performanslarını araştırdılar. Khanna et al. [21] 15-5 PH SS çeliğinin kuru, taşma, LCO_2 ve MMY koşulları altında takım aşınması açısından analiz ettiler. Ayrıca farklı soğutma/yağlama stratejilerinin güç tüketimi ve yüzey pürüzlülüğü üzerindeki etkilerini araştırdılar. Mia et al. [22] kuru kesme, MMY ve basınçlı hava soğutmalı katı yağlama sistemi gibi üç sürdürülebilir işleme teknolojisi kullanarak soğutma yağlama sıvılarının işlenebilirlikteki etkilerini incelemişlerdir. Yapılan çalışma sonucunda MMY'nin iyileştirmeye yardımcı olduğu, çevre dostu ve daha temiz üretim sağladığı bulunmuştur. Bir diğer çalışmada Aslantaş ve Cicek [23] Inconel 718 süper alaşımının mikro frezelenmesinde MMY, etanol ve yağ-su emülsiyonu) gibi farklı soğutma/yağlama tekniklerinin yüzey pürüzlülüğü, takım aşınması ve çapak oluşumu üzerindeki etkileri araştırmıştır. Yüzey kalitesi ve takım aşınması göz önüne

alındığında MMY'nin daha iyi sonuçlar verdiği bulunmuştur. Korkmaz et al. [24] Ni tabanlı bir alaşım olan Nimonic 80A'nın farklı soğutma koşullarının ve mesafelerinin işlenebilirlik parametreleri (Takım aşınması, yüzey pürüzlülüğü, güç tüketimi) üzerinde olan etkilerini araştırmışlardır. Muaz and Choudhury [25] TiCN/Al2O3/TiN kaplı kesici uçlar kullanarak AISI 4340 çeliğinin MMY destekli frezelenmesinde kesme kuvvetlerinin ve yüzey pürüzlülüğünün etkilerini araştırdılar.

2. Materyal ve metot

Bu çalışmada test malzemesi olarak pek çok imalat sanayinde yaygın olarak kullanılan St37 çeliği kullanılmıştır. Tablo 1, kullanılan çeliğe ait ağırlıkça kimyasal bileşimini göstermektedir.

Tablo 1. St37 çeliğinin kimyasal bileşeni.

C	Si	Mn	P	S	Cr	Ni
% 0,11	% 0,03	% 0,56	% 0,007	% 0,005	% 0,07	% 0,03

Deneylerde kullanılacak iş parçaları, 50 mm x 50 mm genişlik ve 15mm kalınlığa sahip olacak şekilde kare kesitli levhalar şeklinde temin edilmiştir. DAHLIH MCV-860 marka CNC freze tezgahı kullanılarak MYY soğutma/yağlama sıvısı altında numunelerin frezeleme işlemi gerçekleştirilmiştir. Kesme işlemi için AlTiN kaplı ISO 13399 kodlu kesici takım uçları kullanılmıştır. Kesici uçlar tek ağızlı yüzey tarama frezesine takılmıştır. Deneylerde kesme derinliği sabit ve 1 mm olarak seçilmiştir. Kesme hızı (140-210 m/dk) ve ilerleme hızı (0,14-0,21 mm/dev) ise değişken parametreler olarak seçilmiştir. Tablo 2, deney sistemini göstermektedir.

Tablo 2. İşlenebilirlik deney tasarım sistemi.

Deney no	**Kesme hızı (m/dk)**	**İlerleme hızı (mm/dev)**	**MMY nozül uzaklığı (mm)**
1	140	0,14	50
2	140	0,14	250
3	140	0,21	50
4	140	0,21	250
5	210	0,14	50
6	210	0,14	250
7	210	0,21	50
8	210	0,21	250

MMY soğutma/yağlama sıvısı ile işlenebilirlik deneyleri yapılarak yüzey pürüzlülüğü, takım aşınması ve kesme sıcaklığı incelenmiştir. İlgili deney şeması Şekil 1'de görülmektedir.

Şekil 1. İşlenebilirlik deney şeması.,

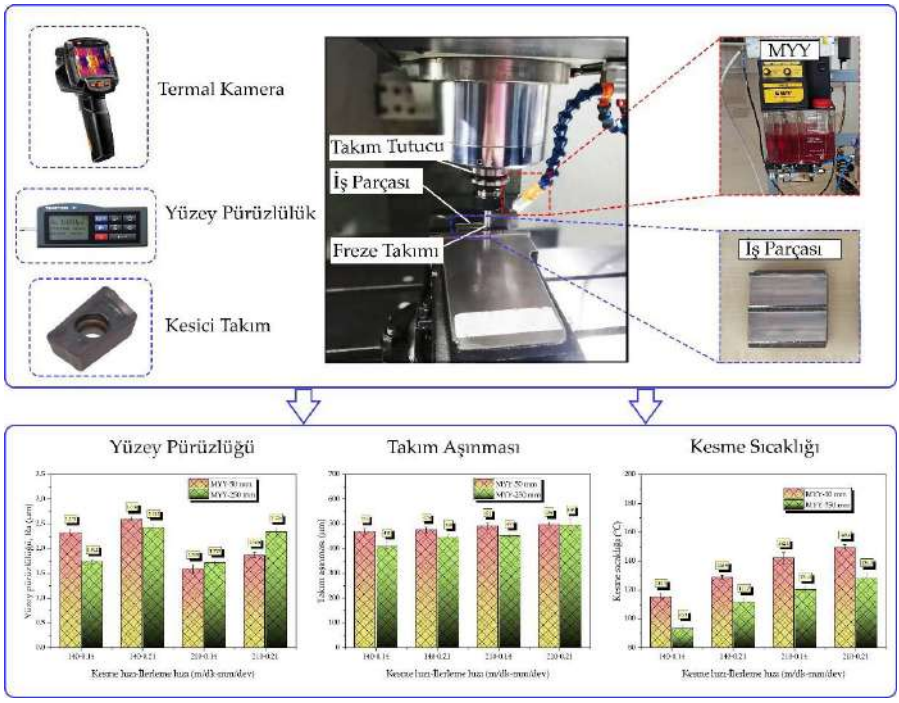

MMY yağı sisteme Werte Micro Stn-15 marka potansiyometre kontrollü bir sistem kullanılarak uygulanmıştır. MMY kesme sıvısı olarak Cuttex Syn 5 sıvısı kullanılmış bu sıvı basınçlı hava yardımıyla kesici takım ve iş parçası üzerine püskürtülmektedir. Uygulanan MMY'nin akış debisi 35 mL/saat, püskürtme basıncı 6,5 bar ve püskürtme açısı 45° dir. MMY'nin çıkış nozulu ise 5 mm çapa sahiptir. Bu çalışmada MMY sıvısının kesme bölgesine uygulanma mesafesinin işlenebilirlik parametreleri üzerindeki etkileri araştırılmak istendiğinden 50 mm ve 250 mm olmak üzere iki farklı uygulama mesafesi seçilmiştir. Kesme sıcaklıkları 650 °C sıcaklığa kadar ölçüm yapabilen Testo-871 model bir termal kamera kullanılarak ölçülmüştür. Ölçümler sabit bir mesafede konumlandırılarak gerçekleştirilmiştir. Kesme işlemi sonrasında numunelerin yüzey pürüzlülük değerleri TIME3200 test cihazı ile ölçülmüştür. Ölçüm parametreleri olarak Cutoff: 0,25 mm, n*cutoff: 5l, Standart: ISO, Range: ± 80 μm, Filter: RC, Display: Ra değerleri referans alınmıştır. Hata payını en aza indirerek doğru ölçüm değerleri elde etmek için cihaz kalibrasyonu yapıldıktan sonra ölçümler farklı noktalardan 5 kez tekrarlan-

mıştır. Bu değerler içerisinden yüksek sapma yapan değerler çıkartılarak kalan değerlerin ortalaması alınmış ve nihai yüzey pürüzlülüğü değerleri elde edilmiştir. Kesici takım aşınma değerleri Insize ISM-PM200SB cihazı kullanılarak ölçülmüştür. En fazla aşınan alan dikkate alınarak kesici takımın yan bölgesinden alınmıştır.

3. Bulgular ve tartışma

St37 çeliği farklı kesme hızında (140-210 m/dk), farklı ilerleme hızında (0,14-0,21 mm/dev) ve farklı nozul uzaklıklarında (50-250 mm) frezelenmiştir. Deney esnasında ve sonrasında kesici takım aşınması, kesme sıcaklığı ve yüzey pürüzlülüğü sonuçları kayıt altına alınarak analiz edilmiştir.

3.1. Kesici takım aşınması

Takım aşınması bitmiş parça yüzey kalitesi, parça maliyeti ve işlenebilirlik sürecinin sürdürülebilirliği üzerinde etkisi olan çok önemli bir işlenebilirlik metriğidir [26]. Frezeleme esnasında kesici takımın maruz kaldığı mekanik ve termal yükler takım ömrünü azaltır. Hem ürün kalitesi hem de üretim verimliliği açısından takım ömrünü analiz etmek kritik bir durumdur [27]. Bu sebeple, kesici takımın ömrünü tamamlayıp parçaya zarar vermeden değiştirilmesi önemlidir. Şekil 2, farklı işlenebilirlik parametrelerinin takım aşınması üzerinde etkisini göstermektedir. Kesme hızı ve ilerleme hızının artışıyla birlikte takım aşınmasının arttığı görülmektedir. En düşük takım aşınması değeri (0,411 mm) düşük kesme parametrelerinde ve uzak mesafe MMY uygulamasında elde edilmiştir. En yüksek takım aşınma değeri (0,499 mm) ise yüksek kesme parametrelerinde ve yakın mesafe MMY uygulamasında elde edilmiştir. Artan kesme hızının takımda meydana gelen plastik deformasyonu artırdığı ve artan ilerleme hızının da kesici takım-iş parçası temas süresini artırarak daha fazla kuvvet ve ısı oluşumuna yol açtığı bilinmektedir [27]. Bu sebeple takım aşınmasında artış meydana geleceği açıktır. MMY uygulama mesafesinin artmasında takım aşınmasın azalmasının iki farklı nedeni olabilir. Birincisi, uygulama mesafesi arttığında yağlama akışkanı iş parçası-takım bölgesini daha etkili kapsayabilir. Böylelikle ısıyı daha etkin dağıtarak kesici takımın aşırı ısınmadan kaynaklanan aşınma sürecini geciktirebilir. İkincisi ise uzak mesafede yağlama akışkanı, daha fazla alana homojen bir şekilde dağıldığından dolayı takım yüzeyinin daha etkin bir şekilde temizlenmesini ve takım-iş parçası yüzeyinde daha etkin bir yağlama filminin oluşmasına neden olduğundan dolayı sürtünmeyi azaltabilir. Bu sebeple daha takım aşınması azalarak takım ömrü artabilir.

Şekil 2. Farkı işlenebilirlik parametrelerinin takım aşınması üzerindeki

etkisi.

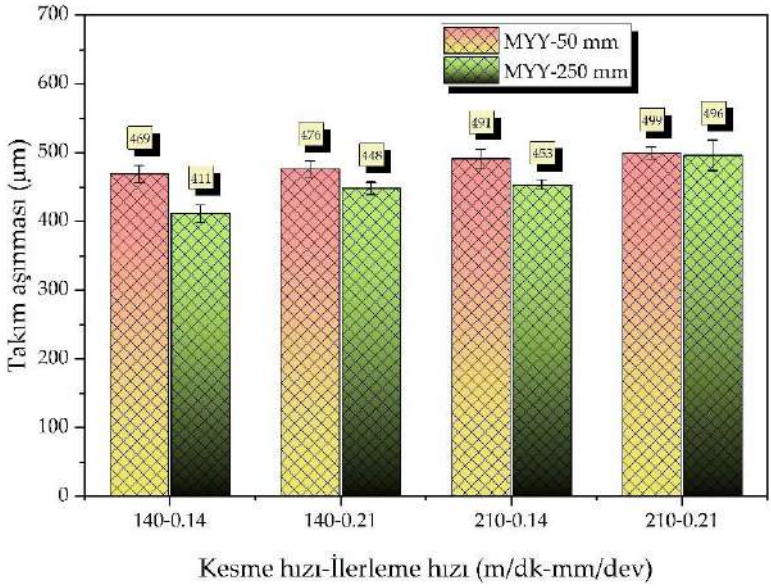

3.2. Kesme sıcaklığı

Frezeleme esnasında kesici takım-iş parçası arasında kesme, sürtünme, plastik deformasyon gibi bazı mekanik olgulardan dolayı ısı enerjisi açığa çıkmaktadır. Bu ısı enerjisi iş parçası, kesici takım ve talaşa yayılarak kesme sıcaklığına neden olabilir. Frezeleme ile birlikte oluşan talaşlar ise ısının büyük bir bölümümü kesme ortamından uzaklaştırırlar [28]. Kesme sıcaklığı kesici takım kenar keskinliğini, iş parçası kalitesini ve talaş geometrisini önemli derecede etkilemektedir [29]. Yüksek kesme sıcaklıkları düşük yüzey kalitesi ve düşük takım ömrü ile işleme sürecini olumsuz etkileyebilir [30]. Bu sebeple kesme sıcaklığını kontrol altına alabilmek önem arz eder. Şekil 3, farklı kesme parametreleri ile farklı MMY uygulama mesafelerinin kesme sıcaklığına olan etkisini göstermektedir. Kesme parametrelerinin artmasıyla birlikte kesme sıcaklıklarının arttığı gözlemlenmiştir. Bu durumun birim zamandaki kinetik enerji, sürtünme ve plastik deformasyondaki artışlara bağlı olduğu söylenebilir [22]. En düşük (93,4 °C) ve en yüksek (149,4 °C) kesme sıcaklıkları buna bağlı olarak sırasıyla en düşük ve en yüksek kesme parametrelerinde meydana gelmiştir. Takım aşınmasına durumuna benzer şekilde uzak mesafeden uygulanan MMY sıvısı daha fazla alana yayılarak daha etkin bir şekilde homojen yağlama yapmaktadır. Böyle daha etkin bir soğutma yapabildiğinden dolayı uzak mesafeden yağlama durumunda daha iyi kesme sıcaklık sonuçları elde edilmiştir.

Şekil 3. Farkı işlenebilirlik parametrelerinin kesme sıcaklığı üzerindeki etkisi.

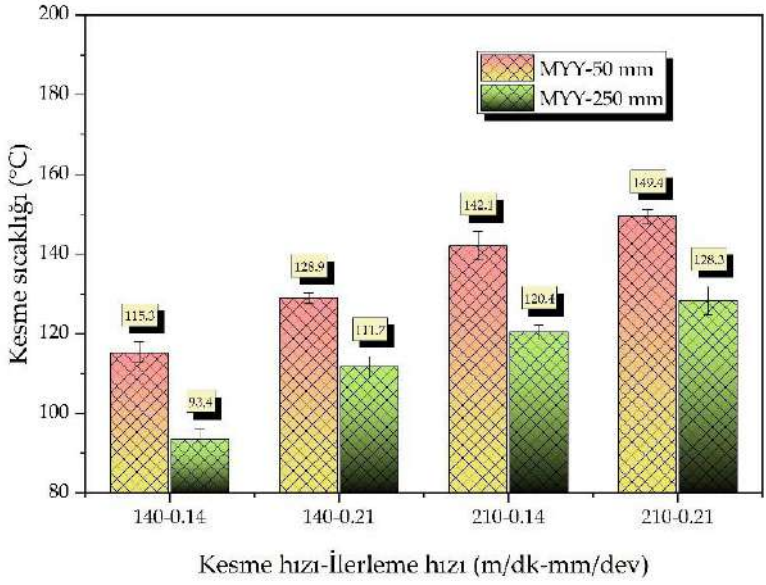

3.3 Yüzey pürüzlülüğü

Yüzey kalitesi, işlenebilirlik işlemlerinden sonra elde edilen en önemli parametrelerden bir tanesidir. Ayrıca yüzey kalitesi parçanın çalışacağı ortamda tribolojik ve mekanik özellikleri etkileyebilmektedir. [8]. Yüzey pürüzlülüğü, yüzey kalitesi için önemli parametrelerden birisidir. Yüzey pürüzlülüğü fazla olan parçalar daha fazla aşınabilmekte ve bulunduğu yerdeki işlevini daha hızlı kaybedebilmektedir. Bu yüzden istenilen yüzey kalitesini elde edebilmek için yüzey pürüzlülük değerleri istenilen değer içerisinde kalması gerekmektedir [31]. R_a değeri, iş parçası örneklem uzunluğundaki yüzey profili yüksekliğinin aritmetik ortalaması olarak bilinen bir yüzey pürüzlülük değerini yansıtmaktadır. Bundan dolayı örneklem uzunluğundaki ani değişikliklere duyarlı olmayıp, bütün yüzey profillerinden etkilenmektedir. Bu nedenle diğer yüzey pürüzlülük değerlerine göre daha çok kullanılmaktadır [32, 33]. Yüksek-düşük kesme hız ve ilerleme hızlarında ve yakın-uzak MMY uygulama mesafesinin yüzey pürüzlülüğüne etkisi Şekil 4'te gösterilmiştir. İlerleme hızının yüzey pürüzlülüğüne etkisi bilinmektedir [34]. Literatür bilgisi doğrultusunda artan ilerleme hızı ile yüzey pürüzlülüğünün düştüğü gözlemlenmiştir. Kesme hızının artması ile birlikte yüzey kalitesinin önemli şekilde iyileştiği tespit edilmiştir. Yapılan bir çalışmada artan kesme hızı ile birlikte kesme sıcaklığının artacağı ve bununla birlikte kesme bölgesinin yumuşayarak kesici takım üzerinde daha az talaş yığılmasına sebep olacağı belirtilmiş-

tir. Böylece takım daha geç aşınacağı için iş parçası yüzeyinin daha kaliteli olacağı vurgulanmıştır [27]. Literatürdeki başka çalışmaların da [35, 36] bu kanıyı desteklediğini belirtmişlerdir. MMY uygulama mesafelerinin çalışmada farklı kesme hızları için farklı davranışlar sergilediği gözlemlenmiştir. Düşük kesme hızına göre yüksek kesme hızında yüzey kalitesinin yaklaşık % 29 iyileştiği görülmüştür. Yüksek kesme hızında artan MMY uygulama mesafesi, talaş kontrolünü zorlaştırabilir. Kontrolsüz talaşın yüzey üzerine çarpma etkisiyle birlikte yüzey kalitesini azaltabileceği düşünülmektedir.

Şekil 4. Farkı işlenebilirlik parametrelerinin yüzey pürüzlülüğü üzerindeki etkisi.

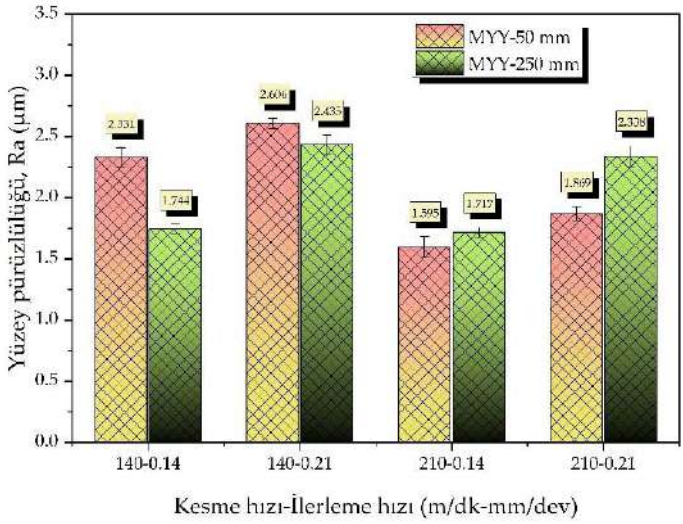

4. Sonuçlar

Bu çalışmada farklı kesme parametrelerinin ve farklı MMY uygulama mesafelerinin St37 çeliği üzerindeki işlenebilirlik etkileri araştırılmıştır. Bu kapsamda iki farklı kesme hız (140-210 m/dk) ve iki farklı ilerleme (0,14-0,21 mm/dev) hızı kullanılmıştır. Ayrıca iki farklı MMY uygulama mesafesi (50-250 mm) tercih edilmiştir. 2^3 deney tasarım sistemine göre toplam 8 deney gerçekleştirilmiştir. Deney sonuçlarına göre kesme sıcaklığı, takım aşınması ve yüzey pürüzlülük sonuçları irdelenmiştir. Bu sonuçlara göre;

- Artan kesme ve ilerleme hızlarıyla birlikte takım aşınmasında maksimum %20 oranında artış meydana geldiği görülmüştür. Ayrıca MMY uygulama mesafesinin artmasıyla birlikte tüm kesme parametreleri için takım aşınmasında azalma meydana geldiği tespit edilmiştir.

- Uzak mesafe MMY uygulaması, işlenebilirlik üzerinde pozitif etki oluşturmuş ve kesme sıcaklığının düşmesinde önemli rol oynamıştır. Farklı kesme parametrelerinin artışı ile kesme sıcaklığının arttığı görülmüştür.
- Farklı MMY uygulama mesafelerinin yüzey pürüzlülüğü sonuçlarına etkisi kesme hızına göre değiştiği tespit edilmiştir. Yüksek kesme hızlarında yakın mesafeden uygulanan MMY sıvısı iş parçası yüzey kalitesi üzerinde pozitif etki yaparken düşük kesme hızlarında uzak mesafeden uygulanan MMY sıvısı pozitif etki yaptığı görülmüştür. Kesme parametreleri için, artan ilerleme hızı ile yüzey pürüzlülüğünün arttığı, artan kesme hızı ile yüzey pürüzlülüğünün azaldığı tespit edilmiştir.

Kaynakça

[1] O. Altay, T. Gürgenç, St37 çeliğinin tornalanmasında yüzey pürüzlülüğünün destek vektör regresyonu kullanılarak tahmini, Fırat Üniversitesi Mühendislik Bilimleri Dergisi, 2022.

[2] I.S. Jawahir, H. Attia, D. Biermann, J. Duflou, F. Klocke, D. Meyer, S.T. Newman, F. Pusavec, M. Putz, J. Rech, V. Schulze, D. Umbrello, Cryogenic manufacturing processes, CIRP Annals, 65 (2016) 713-736.

[3] H.-J. Kim, K.-J. Seo, K.H. Kang, D.-E. Kim, Nano-lubrication: A review, International Journal of Precision Engineering and Manufacturing, 17 (2016) 829-841.

[4] S. Amiril, E. Rahim, S.J.J.o.C.P. Syahrullail, A review on ionic liquids as sustainable lubricants in manufacturing and engineering: Recent research, performance, and applications, 168 (2017) 1571-1589.

[5] Ç.V. Yıldırım, T. Kıvak, F.J.A.J.f.S. Erzincanlı, Engineering, Influence of different cooling methods on tool life, wear mechanisms and surface roughness in the milling of nickel-based waspaloy with WC tools, 44 (2019) 7979-7995.

[6] C. Cai, X. Liang, Q. An, Z. Tao, W. Ming, M. Chen, Cooling/Lubrication Performance of Dry and Supercritical CO2-Based Minimum Quantity Lubrication in Peripheral Milling Ti-6Al-4V, International Journal of Precision Engineering and Manufacturing-Green Technology, 8 (2021) 405-421.

[7] Q.L. Niu, L. Jing, Z. Yu, C.P. Li, X.Y. Qiu, T.J. Ko, Experimental study on cryogenic milling performance of SiCp/Al composites with liquid nitrogen, Machining Science and Technology, 26 (2022) 1-17.

[8] S. Şap, M. Uzun, Ü.A. Usca, D.Y. Pimenov, K. Giasin, S. Wojciechowski, Investigation of machinability of Ti–B-SiCp reinforced Cu hybrid composites in dry turning, Journal of Materials Research and Technology, 18 (2022) 1474-1487.

[9] T. Tawakoli, M.J. Hadad, M.H. Sadeghi, A. Daneshi, S. Stöckert, A. Rasifard, An experimental investigation of the effects of workpiece and grinding parameters on minimum quantity lubrication—MQL grinding, Int. J. Mach. Tools Manuf., 49 (2009) 924-932.

[10] G. Singh, C.I. Pruncu, M.K. Gupta, M. Mia, A.M. Khan, M. Jamil, D.Y. Pimenov, B. Sen, V.S. Sharma, Investigations of Machining Characteristics in the Upgraded MQL-Assisted Turning of Pure Titanium Alloys Using Evolutionary Algorithms, Materials, 12 (2019) 999.

[11] Y.S. Liao, H.M. Lin, Mechanism of minimum quantity lubrication in high-speed milling of hardened steel, International Journal of Machine Tools and Manufacture, 47 (2007) 1660-1666.

[12] S.A.S. Amiril, E.A. Rahim, S. Syahrullail, A review on ionic liquids as sustainable lubricants in manufacturing and engineering: Recent research, performance, and applications, Journal of Cleaner Production, 168 (2017) 1571-1589.

[13] M. Mia, M.K. Gupta, J.A. Lozano, D. Carou, D.Y. Pimenov, G. Królczyk, A.M. Khan, N.R. Dhar, Multi-objective optimization and life cycle assessment of eco-friendly cryogenic N2 assisted turning of Ti-6Al-4V, Journal of Cleaner Production, 210 (2019) 121-133.

[14] Y. Touggui, A. Uysal, U. Emiroglu, S. Belhadi, M. Temmar, Evaluation of MQL performances using various nanofluids in turning of AISI 304 stainless steel, Int. J. Adv. Manuf. Technol., 115 (2021) 3983-3997.

[15] E. Salur, M. Kuntoğlu, A. Aslan, D.Y. Pimenov, The Effects of MQL and Dry Environments on Tool Wear, Cutting Temperature, and Power Consumption during End Milling of AISI 1040 Steel, Metals, 11 (2021) 1674.

[16] R.L. Rodriguez, J.C. Lopes, M.V. Garcia, F.S. Fonteque Ribeiro, A.E. Diniz, L. Eduardo de Ângelo Sanchez, H. José de Mello, P. Roberto de Aguiar, E.C. Bianchi, Application of hybrid eco-friendly MQL+WCJ technique in AISI 4340 steel grinding for cleaner and greener production, J. Clean. Prod., 283 (2021) 124670.

[17] S. Ekinovic, H. Prcanovic, E. Begovic, Investigation of Influence of MQL Machining Parameters on Cutting Forces During MQL Turning of Carbon Steel St52-3, Procedia Eng., 132 (2015) 608-614.

[18] V.S. Sharma, M. Dogra, N.M. Suri, Cooling techniques for improved productivity in turning, Int. J. Mach. Tools Manuf., 49 (2009) 435-453.

[19] M. Danish, M.K. Gupta, S. Rubaiee, A. Ahmed, M.E. Korkmaz, Influence of hybrid Cryo-MQL lubri-cooling strategy on the machining and tribological characteristics of Inconel 718, Tribol. Int., 163 (2021) 107178.

[20] M. Hadad, B. Sadeghi, Minimum quantity lubrication-MQL turning of AISI 4140 steel alloy, J. Clean. Prod., 54 (2013) 332-343.

[21] N. Khanna, P. Shah, Chetan, Comparative analysis of dry, flood, MQL and cryogenic CO2 techniques during the machining of 15-5-PH SS alloy, Tribology International, 146 (2020) 106196.

[22] M. Mia, M.K. Gupta, G. Singh, G. Królczyk, D.Y. Pimenov, An approach to cleaner production for machining hardened steel using different cooling-lubrication conditions, Journal of Cleaner Production, 187 (2018) 1069-1081.

[23] K. Aslantas, A. Çiçek, The effects of cooling/lubrication techniques on cutting performance in micro-milling of Inconel 718 superalloy, Procedia CIRP, 77 (2018) 70-73.

[24] M.E. Korkmaz, M.K. Gupta, M. Boy, N. Yaşar, G.M. Krolczyk, M. Günay, Influence of duplex jets MQL and nano-MQL cooling system on machining performance of Nimonic 80A, Journal of Manufacturing Processes, 69 (2021) 112-124.

[25] M. Muaz, S.K. Choudhury, Experimental investigations and multi-objective optimization of MQL-assisted milling process for finishing of AISI 4340 steel, Measurement, 138 (2019) 557-569.

[26] N. Khanna, J. Airao, G. Kshitij, C.K. Nirala, H. Hegab, Sustainability analysis of new hybrid cooling/lubrication strategies during machining Ti6Al4V and Inconel 718 alloys, Sustainable Materials and Technologies, 36 (2023) e00606.

[27] M.N. Babu, V. Anandan, Ç.V. Yıldırım, M.D. Babu, M. Sarıkaya, Investigation of the characteristic properties of graphene-based nanofluid and its effect on the turning performance of Hastelloy C276 alloy, Wear, 510-511 (2022) 204495.

[28] S. Şap, Understanding the Machinability and Energy Consumption of Al-Based Hybrid Composites under Sustainable Conditions, Lubricants, 2023.

[29] N.A. Abukhshim, P.T. Mativenga, M.A. Sheikh, Heat generation and temperature prediction in metal cutting: A review and implications for high speed machining, International Journal of Machine Tools and Manufacture, 46 (2006) 782-800.

[30] Ç.V. Yıldırım, Ş. Şirin, T. Kıvak, M. Sarıkaya, The effect of nanofluids reinforced with different surfactants on the machining and friction-wear properties of Waspaloy, Tribology International, 181 (2023) 108316.

[31] W. Akhtar, J. Sun, P. Sun, W. Chen, Z. Saleem, Tool wear mechanisms in the machining of Nickel based super-alloys: A review, Frontiers of Mechanical Engineering, 9 (2014) 106-119.

[32] E.S. Gadelmawla, M.M. Koura, T.M.A. Maksoud, I.M. Elewa, H.H. Soliman, Roughness parameters, Journal of Materials Processing Technology, 123 (2002) 133-145.

[33] N. Khanna, N.M. Suri, P. Shah, H. Hegab, M. Mia, Cryogenic turning of in-house cast magnesium based MMCs: A comprehensive investigation, Journal of Materials Research and Technology, 9 (2020) 7628-7643.

[34] G.S. Samy, S. Thirumalai Kumaran, M. Uthayakumar, An analysis of end milling performance on B4C particle reinforced aluminum composite, Journal of the Australian Ceramic Society, 53 (2017) 373-383.

[35] D. Umbrello, Investigation of surface integrity in dry machining of Inconel 718, The International Journal of Advanced Manufacturing Technology, 69 (2013) 2183-2190.

[36] A. Thakur, S. Gangopadhyay, State-of-the-art in surface integrity in machining of nickel-based super alloys, International Journal of Machine Tools and Manufacture, 100 (2016) 25-54.

Interdisciplinary Studies on Contemporary Research Practices in Engineering in the 21st Century-III

Editor: Prof. Dr. Kamil Kaygusuz

ÖZGÜR YAYINLARI

ISBN 978-975-447-644-6